Combined Spoiler and Split Flap Effects on the Flying V

MSc Thesis Report

Alexander DeWerff

Delft University of Technology

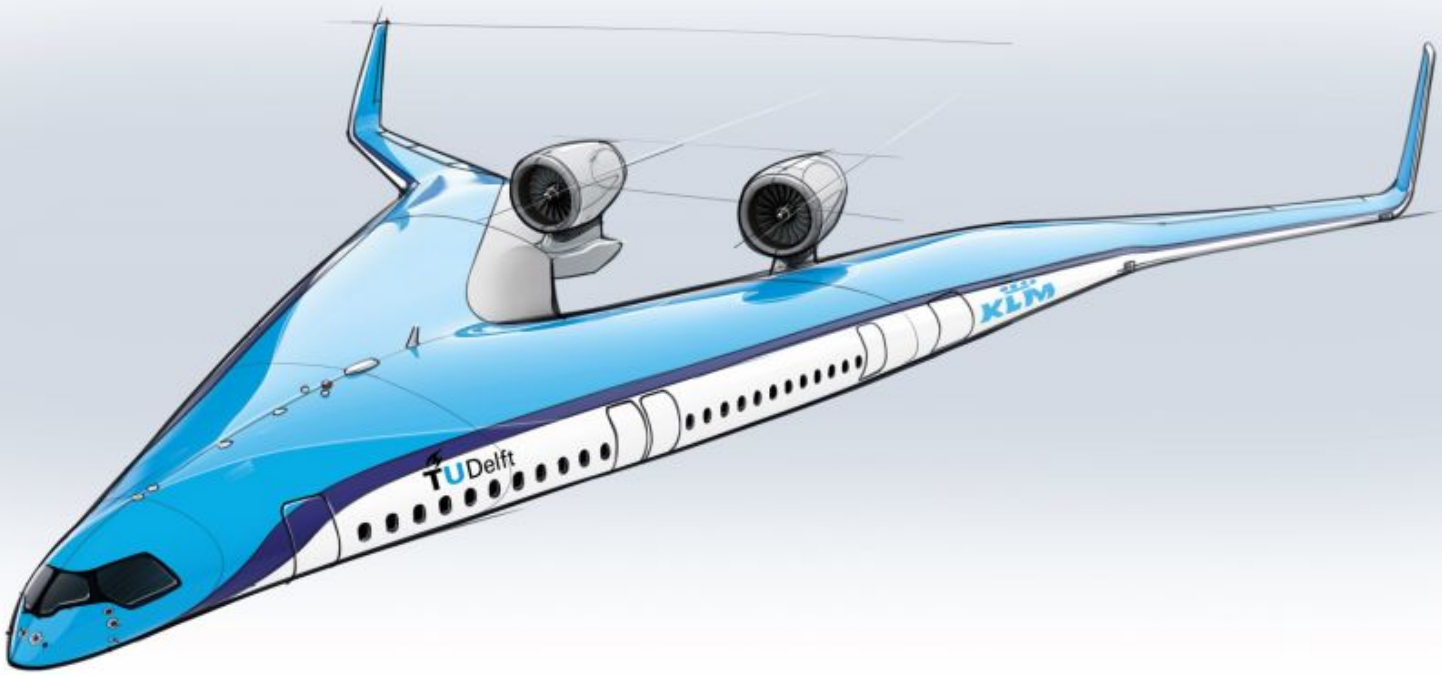

TU Delft

Combined Spoiler and Split Flap Effects on the Flying V

MSc Thesis Report

by

Alexander DeWerff

to obtain the degree of Master of Science
at the Delft University of Technology,
to be defended publicly on Thursday, August 28, 2025 at 1:00 PM.

Student number:	5956048	
Project duration:	December, 2024 – August, 2025	
Thesis committee:	Dr. ir. R. Vos,	TU Delft, Supervisor
	Dr. ir. T. Sinnige,	TU Delft, Chair
	Dr. N.A.K. Doan,	TU Delft, Examiner

Cover: Image credit: CNN (2020), ”Futuristic ‘Flying-V’ airplane makes successful maiden flight”

An electronic version of this thesis is available at `http://repository.tudelft.nl/`.

TU Delft

Preface

This report details the outcomes of my MSc thesis project, and it marks the culmination of my MSc degree in Aerospace Engineering at Delft University of Technology.

First and foremost, I thank my supervisor, Roelof Vos, for his insight, encouragement, and support throughout the duration of this project. His encouragement to ”do more than a simple wind tunnel test” sparked an exciting investigation that pushed me to grow both as a researcher and as an engineer. I greatly enjoyed our regular meetings and the excitement and curiosity with which he approached each new set of results, always eager to explore what the results might reveal about this novel aircraft design.

I also must thank Salvatore Asaro, Nikki van Luijk, and Malcom Brown for their advice, input, and assistance in all things from experiment and part design to test execution and interpretation. You guys are great, and you have all been a pleasure to work with.

A huge shout-out goes to my fellow MSc student Surya Saravan, without whose help I wouldn’t have been able to finish my experiment on time, given how time-consuming the configuration changes were.

I am grateful for all of the colleagues and friends that I have found here in Delft over the last two years, especially those from ICF and University Church Delft. They were an amazing and supportive community, and my time here was made all the better because of them.

I also acknowledge Logan Mauch for being a pretty cool guy all around. He’s the youngest engineer I know to have impressed Mr. Barlow himself.

Most importantly, however, my deepest thanks belong to my loving and supportive wife, Savannah, who has been my biggest cheerleader during my whole MSc program. I also have much gratitude for the rest of my family, especially Grandma and Grandpa Miller. Without their support, I never would have been able to even dream of coming to Delft.

It’s bittersweet to close this chapter of my life, both in academia and in Delft, but I am excited for what lies ahead and know that my time here in Delft has helped prepare me to leave the world in a better place than where I found it. Delft has broadened my outlook on life, introduced me to new lifelong friendships, and driven home the fact that seasonal depression is real: I’m happy to be moving back to Kansas, where there’s at least proper sunshine during the winter.

I hope others will be able to stand on the shoulders of my work and reach higher accomplishments than I, and I hope that this contribution is but one of many steps on the road to innovative aircraft design.

Soli Deo Gloria

Alexander DeWerff
Delft, August 2025

Summary

This report highlights the outcomes of the project Combined Spoiler and Split Flap Effects On the Flying V. The project consisted of the design, execution, and analysis of a wind tunnel experiment in the Delft University of Technology's Low Turbulence Tunnel (LTT) using the 1.84% scaled full-span Flying V wind tunnel model.

First, a review of the literature on the Flying V and modern experiment and wind tunnel testing techniques was conducted to inform the research objective and questions. The knowledge gathered was used to select experimental design variables, choose a testing and analysis methodology–namely, Modern Design of Experiments and Response Surface Methodology–and design the spoiler and split-flap parts for the 1.84% wind tunnel model. The spoiler and flap designs were dictated by previous design research, using the suggested final designs in both studies and scaling and modifying the geometry as needed from the 4.8% scale Open Jet Facility (OJF) semi-span model to interface with the present 1.84% LTT model.

The test matrix was assembled in a split plot fashion, achieving a semi-randomized, modified Central Composite Design (CCD) for six independent variables over two subranges. The four configuration variables, dictating the flap and spoiler deflections, were designated as whole plot factors, and the angles of attack and sideslip were designated as subplot factors. The specific CCD design was inscribed within the independent variable limits, and an extra Full Factorial Design was superimposed and scaled such that the added points occupied the sample space corners in the subplot variables (angles of attack and sideslip). This design was chosen to test five levels in each of the configurations, allowing for squared and even up to cubic main effects to be fit if enough data is available.

The flap and spoiler parts were manufactured using flat aluminum plates around 1 mm to 2 mm thick, which were mounted to 3D printed offsets that set the angle of the plates with respect to the model surface and also interfaced smoothly with the complicated model curvature. The parts were fixed to the model using double-sided tape, and their positioning on the model was guided by printed alignment blocks, enabling repeatable installation.

In addition to the measurements planned for the response surface model fitting, specific configurations were planned for testing using conventional sweeps. These sweeps at fixed angle of attack or sideslip would provide validation data to assess the quality of the fitted models and a conventional counterpart to assess the flap and spoiler effects in case the models were shown to be insufficient.

After the successful wind tunnel experiment, the data was processed but left uncorrected for strut or wind tunnel effects. The processed data was then used to fit variations of 48 different regression models using stepwise regression with Ordinary Least Squares and Generalized Least Squares for both the full measured coefficient data and for the deltas calculated with respect to the clean wind tunnel model. These models were all assessed for validity using the measured validation data that was held separate during the model fitting, and the significant variables and interactions were identified for each force and moment coefficient.

The primary findings from this project show that there are indeed significant interaction effects when the split flaps and spoilers are deflected together, meaning that predictions for any combined deflection configuration ought to be measured explicitly and not approximated by superimposing the flap-alone and spoiler-alone effects. Furthermore, it was observed that the flap-alone effects and the spoiler-alone effects differ in magnitude from their estimated performance in past research when considered on the 1.84% scaled LTT Flying V model with the updated geometry. This difference in effects can be attributed to a number of factors, including lack of tunnel corrections, different scaled model geometry, and different model installation methods.

Contents

List of Figures

List of Tables

Nomenclature

Abbreviations

Abbreviation	Definition
AIC	Akaike Information Criterion
ANOVA	Analysis Of Variance
AoA	Angle of Attack
AoS	Angle of Sideslip
BBD	Box Behnken Design
BIC	Bayesian Information Criterion
CCD	Central Composite Design
CG	Center of Gravity
CI	Confidence Interval
DOE	Design of Experiments
FA	Flow Angularity
FCD	Face Centered central composite Design
FFD	Full Factorial Design
GLS	Generalized Least Squares
IB	Inboard
LE	Leading Edge
LEE	Lift Enhancing Effector
LHS	Left Hand Side
LMM	Linear Mixed (Effects) Model
LTT	Low Turbulence Tunnel
MAC	Mean Aerodynamic Chord
MDOE	Modern Design of Experiments
ML	Maximum Likelihood Estimation
MRC	Moment Reference Center
MS_R	Regression Mean Square Error
MS_E	Residual Mean Square Error
NASA	National Aeronautics and Space Administration
OB	Outboard
OFAT	One Factor At a Time
OJF	Open Jet Facility
OLS	Ordinary Least Squares
PDF	Probability Density Function
PRESS	Predicted Residual Error Sum of Squares
RANS	Reynolds Averaged Navier-Stokes
REML	Restricted Maximum Likelihood
RHS	Right Hand Side
RMSE	Root Mean Square Error
RSM	Response Surface Methodologies
SS	Sum of Squares
SS_T	Total Sum of Squares
SS_R	Regression Sum of Squares
SS_E	Residual Sum of Squares
SSFT	Sub-Scale Flight Test
TE	Trailing Edge

Symbols

Symbol	Definition	Unit
a	Aerodynamic reference system	[-]
b	Body reference system	[-]
C_{Fn}	Normal force coefficient in body axis	[-]
C_{Ft}	Tangential force coefficient in body axis	[-]
C_{Fs}	Sideforce coefficient in body axis	[-]
$C_{l,\beta}$	Lateral stability derivative	[deg^{-1}]
$C_{l,\text{ body}}$	Rolling moment coefficient in body axis	[-]
$C_{\ell,\delta_{sp,2l}}$	Roll control derivative with outboard port spoiler deflection	[deg^{-1}]
$C_{\ell,\delta_{sp,2r}}$	Roll control derivative with outboard starboard spoiler deflection	[deg^{-1}]
$C_{m,\text{ body}}$	Pitching moment coefficient in body axis	[-]
$C_{n,\text{ body}}$	Yawing moment coefficient in body axis	[-]
$C_{n,\beta}$	Directional stability derivative	[deg^{-1}]
C_L	Lift coefficient in wind axis	[-]
C_D	Drag coefficient in wind axis	[-]
C_Y	Sideforce coefficient in wind axis	[-]
$C_{l,\text{ wind}}$	Rolling moment coefficient in wind axis	[-]
$C_{m,\text{ wind}}$	Pitching moment coefficient in wind axis	[-]
$C_{n,\text{ wind}}$	Yawing moment coefficient in wind axis	[-]
C_{FX}	Axial force coefficient in aerodynamic axis	[-]
C_{FY}	Lateral force coefficient in aerodynamic axis	[-]
C_{FZ}	Vertical force coefficient in aerodynamic axis	[-]
C_{MX}	Moment coefficient about X-axis in aerodynamic axis	[-]
C_{MY}	Moment coefficient about Y-axis in aerodynamic axis	[-]
C_{MZ}	Moment coefficient about Z-axis in aerodynamic axis	[-]
$C_{MX,bal}$	Moment coefficient about X-axis in aerodynamic axis at moment reference center	[-]
$C_{MY,bal}$	Moment coefficient about Y-axis in aerodynamic axis at moment reference center	[-]
$C_{MZ,bal}$	Moment coefficient about Z-axis in aerodynamic axis at moment reference center	[-]
C_{m_α}	Pitching moment derivative with respect to angle of attack	[deg^{-1}]
C_{m_o}	Pitching moment intercept at angle of attack $\alpha = 0°$	[-]
d	Polynomial order	[-]
df	Degrees of freedom	[-]
F	F-statistic	[-]
$\mathbf{G}$	Random grouping effects covariance matrix	[-]
k	Number of independent variables	[-]
$\mathbf{K}$	Linear combinations selection matrix	[-]
M	Mach number	[-]
n	Number of data points (scaled)	[-]
p	Number of parameters, usually in a polynomial	[-]
$\mathbf{R}$	Residual error covariance matrix	[-]
R^2	Coefficient of Determination	[-]
R^2_{adj}	Adjusted Coefficient of Determination	[-]
V	Velocity	[m/s]
V_{SR1}	Reference stall speed in landing configuration	[knot]
w	Wind reference system	[-]

Symbol	Definition	Unit
x_{ac}	X-coordinate of Aerodynamic Center in percent chord	[-]
x_{bal}	X-coordinate of model reference center wrt moment reference point in percent chord	[-]
x/c	X-coordinate in percent chord	[-]
$(x/c)_{loc}$	X-coordinate in percent local chord	[-]
y	Measured observation	[*]
y_{bal}	Y-coordinate of model reference center wrt moment reference point in percent chord	[-]
$\hat{y}$	RSM model prediction	[*]
z_{bal}	Z-coordinate of model reference center wrt moment reference point in percent chord	[-]
$\mathbf{Z}$	Random effects design matrix	[-]
α	Angle of attack	[deg]
β	Angle of sideslip	[deg]
β_{fa}	Angle of sideslip flow angularity offset	[deg]
β_{max}	Maximum angle of sideslip	[deg]
Δ	Change in quantity	[*]
δ_f	Angle of flap deflection	[deg]
δ_{sp}	Angle of spoiler deflection	[deg]
$\delta_{sp,1}$	Angle of inboard spoiler deflection	[deg]
$\delta_{sp,2\ell}$	Angle of left (port) outboard spoiler deflection	[deg]
$\delta_{sp,2r}$	Angle of right (starboard) outboard spoiler deflection	[deg]
ϵ	Random error	[*]
θ_k	Regression coefficient of kth term	[-]
μ	Mean value	[*]
σ	Standard deviation	[*]
σ_{balance}	Estimated balance uncertainty	[*]
$\sigma_{\text{block effect}}$	Estimated repeatability error due to block effects	[*]
ρ	Density	[kg/m^3]
ξ	Factor level being transformed	[*]
ψ	Turntable yaw angle	[deg]

1

Introduction

All models are wrong; some are useful.
G. E. P. Box, “Statistics for Experimenters”

Flying wings have been the ever-elusive aerodynamic solution to the aircraft designer’s quest for an optimal aircraft design [1]. In a flying wing, every component is multi-functional, offering lift-generation and cargo space together in one product that promises incredible drag reductions when compared to the traditional tube-and-wing aircraft that dominate the skies today. The Flying V represents a potential shift in the current paradigm, offering a bold step away from incremental improvements and towards a more sustainable and efficient transport.

The Flying V is a novel flying wing aircraft design that was conceived by Justus Benad at Airbus in 2013, and the design has been the object of much research, collaboration, and optimization between Airbus, KLM Royal Dutch Airlines, and the Aerospace Engineering faculty at the Delft University of Technology [2], [3]. Recently, the Flying V has been carefully researched in approach and landing conditions, as it matters little if a design boasts improved cruise performance if it cannot be safely or competitively returned to the ground. To this end, different split flap and spoiler designs were separately designed and optimized for the Flying V geometry optimized by Faggiano [3]–[5]. These designs and their performance improvements have led to improved landing and approach handling predictions [6].

However, the Flying V geometry has been steadily improved upon and optimized for cruise conditions and operability in parallel efforts [7]–[10]. With an updated Flying V design and a full-span wind tunnel model to experimentally investigate it, predictions on the flight performance can be made that are more relevant to the final Flying V design. Several questions are introduced by this new design, such as ”do the flaps and spoilers, designed and optimized for the old Flying V geometry, still perform as well on the new geometry?” and ”how does the Flying V’s performance change in sideslip?” Research is now needed to bridge the gap between the body of research performed on the Faggiano’s Flying V geometry and that performed on the most recent design iteration, research that will pave the way for the final design to soar through the sky.

1.1. Research Objective

The goal of this project is to better understand how the Flying V split flap and spoiler surfaces, which were designed separately and on old geometry, perform on the new model geometry and in combination with each other. Furthermore, it is desired to understand how the individual and combined effects change with sideslip, as this is necessary for predicting the handling performance needed to meet regulations, such as in take-off and landing conditions. The Modern Design of Experiments (MDOE) methodology is aptly suited for identifying the significant effects and relationships between experimental variables. Therefore, the research objective for this thesis is to

Experimentally characterize the Flying V’s split flap and spoiler aerodynamic and interaction effects in sideslip conditions using Modern Design of Experiment techniques in a wind tunnel.

1.2. Research Questions

The research objective is to be met through an experimental investigation of the 1.84% scaled Flying V model using the Low Turbulence Tunnel of the Delft University of Technology's Faculty of Aerospace Engineering. To this end, a literature study was conducted to survey the state-of-the-art and the specific gaps to be addressed. Examining past research on the Flying V's split flap and spoiler designs, wind tunnel testing, and strategic experiment design led to the formulation of the following research question.

What is the combined effect of split flap and spoiler deflection on the subscale Flying V's force and moment coefficients, and how does that effect change in sideslip conditions?

To answer this query, the question is divided into sub-questions which will aid in specifying the research to be done. The main research question can be satisfactorily answered and the research objective met by answering the following sub-questions.

- What is the mathematical relationship between flap deflection angle, inboard spoiler deflection angle, outboard spoiler deflection angle, angle of attack, and sideslip angle on each of the Flying V's force and moment coefficients?
- To what extent is the spoiler effectiveness changed when combined with flap deflections?
- How do full-span flap and spoiler effects compare with the semi-span flap and spoiler effects?

1.3. Thesis Outline

In the following chapters, the work conducted during the project Combined Spoiler and Split Flap Effects on the Flying V is described. First, a literature study was conducted, and the gathered background information on the Flying V and experimental methods is provided in chapter 2. Next, the methodology used to design and conduct the experiment and analysis is discussed in chapter 3. This is followed by a presentation of the verification and validation of the methodology used in chapter 4 and a presentation and discussion of the results in chapter 5. The report is concluded in chapter 6 along with recommendations for future research and next steps.

2

Background

This chapter summarizes the literature review conducted in the beginning of this thesis project. Section 2.1 discusses some of the Flying V development and highlights the design of the split flaps and spoilers, discussing the limitations of the previous research and opportunities for further study. Next, Section 2.2 covers information on wind tunnels, their usage in aircraft design research, and their limitations. Last, this chapter is concluded with Section 2.3, which introduces the concept of modern experiment design and examines how the use of statistics-driven techniques can maximize the value of wind tunnel experiments.

2.1. Flying V

The Flying V is an unconventional flying wing aircraft design that boasts predictions of better efficiency and less fuel usage than modern passenger aircraft, like the A350-900 [11]. Studies and improvements on the initial design have produced estimates of reducing fuel by 10% and reducing long-term climate effects by 36% compared to conventional aircraft [12]. These gains and improvement primarily come from the benefits associated with tailless, flying wing designs: a lower wet surface area due to less aircraft parts and lower structural weights due to better load distributions [1].

With a similar passenger capacity and wing span, the Flying V is designed to easily compete with aircraft like the A350-900 or A350-1000 [7], [11]. It can use the same existing airport infrastructure that conventional aircraft use, which makes the adoption of this design easier [11]. However, subsequent design iterations and investigations since the initial design have revealed aerodynamic challenges that need to be better understood and remedied before this promising concept can be realized.

Aerodynamic Challenges

The Flying V has a highly swept-back and cranked wing, a design that introduces highly vortical and non-linear flow at moderate to high angles of attack. This can be simultaneously an advantage and a source of concern, as will be discussed in the following presentation of some past research.

An experimental and numerical study was done on the half-span model in the Open Jet Facility at TU Delft by Palermo where the longitudinal static stability of the Flying V was investigated [13]. Although Benad's initial work showed the Flying V displays longitudinal static stability at low angles of attack [11], Palermo found that an unstable pitch break was observed around 20° angle of attack due to a forward-moving aerodynamic center x_{ac}. This change in x_{ac} was due to the changing pressure distribution over the wing due to the change in the vortical flow over the Flying V with increasing angle of attack. Through the numerical investigation, it was seen that at as early at 10° angle of attack many vortices started to develop [13]. As many as seven different vortices were observed at once over the range of angles of attack considered.

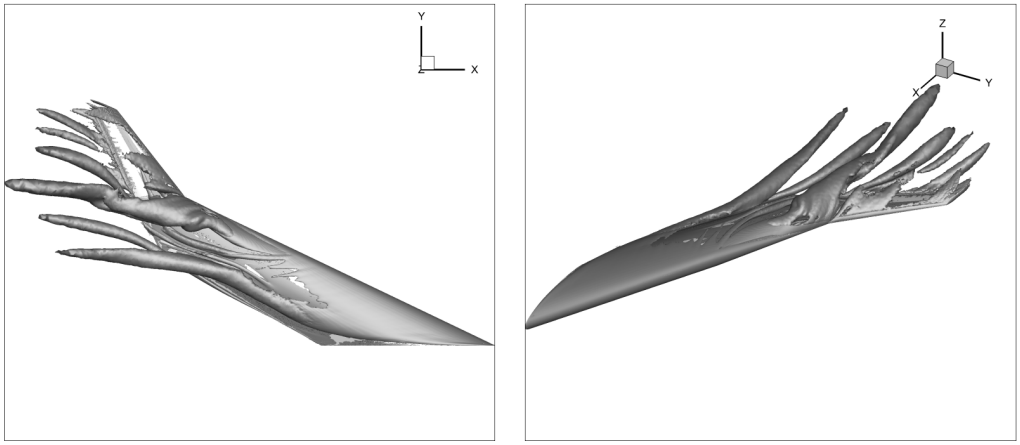

Figure 2.1: Simulated vortical flow development over the Flying V at $\alpha = 20°$; top view left, isometric view right [13]

The vortical structures identified at $\alpha = 20°$ using RANS and the Spalart-Allmaras one equation eddy viscosity model can be seen in Figure 2.1. In the images, the primary vortex over the inboard wing can be seen rolling over the wing and concentrating near the trailing edge before following the wake behind the wing. Also, a large vortex is seen developing counter-clockwise to the streamwise-flow, starting just inboard of the leading edge kink. There are more vortical structures seen in this image, and all these vortices start, develop, and break down differently across different angles of attack.

Using the same semi-span model and wind tunnel facility, another study done around the same time investigating the Flying V at approach speeds while also using flow visualization methods to characterize the flow over the model [14]. This study tested the Flying V over a very large range of angles of attack, from 0° to 60°, and the same unstable pitch break was observed at around 20° angle of attack. The interaction and formation of the different vortices were also documented through the use of tufts, smoke, and oil flow visualization.

Vortical flow has a core of low pressure, so vortices forming over a wing surface can be beneficial by introducing a region of low pressure in an area that would otherwise separate due to high pressure. In this way, the vortical flow over the Flying V enables it to reach high angles of attack before reaching maximum lift at 40° angle of attack [14]. However, the consequence of this flow is that the change in vortex development location and strength with angle of attack changes the pressure distribution over the wing such that the aircraft is longitudinally statically unstable past 20° angle of attack [13].

It is important to note that the vortical flow development characterized in the above research was characterized with respect to the geometry optimized by Faggiano [3]. Both the CFD and wind tunnel models shared this geometry, thus the exact vortical development and formation over this geometry are not expected to occur in precisely the same way over the more recent versions of the Flying V geometry. For example, at some angles of attack, vortex separation and attachment lines were affected by the presence of the stream-wise airfoil section in the old inboard wing trunk; newer geometries not exhibiting such a sharp transition will likely induce different vortical development over that section. There will surely be vortical flow over any version of the Flying V that exhibits its characteristic high inboard sweep.

The Flying V's vortical flow also invalidates the use of much of the textbook wind tunnel corrections, as demonstrated by Jorge's numerical analysis that quantified the wind tunnel effects on the Flying V [15]. Modeling the Flying V geometry numerically, Jorge added the effects of tunnel walls next to the geometry and the struts supporting it and compared the setup to a free-flight case. He also compared the results given by classical wind tunnel corrections. With the numerical analysis in hand, it was discovered that the classical wind tunnel corrections, which are founded in potential flow theory and the method of images, cannot adequately account for the walls' effects on the vortical flow over the Flying V [15]. Additionally, special corrections for highly swept wings and delta wings are invalid as most were developed empirically for geometries with sharp leading edges, which the Flying V does not employ [16].

Recent Developments

Other studies have been done to investigate the Flying V design and improve both the design and the models available to analyze and predict its performance. Many optimization and parametrization studies have been conducted since the first design, seeking to iteratively optimize the design for aerodynamic performance, structural constraints, climate effects, and cost [3], [7], [8], [12], [17]–[20]. Other studies have investigated the performance of the Flying V, taking steps to develop new models and methods to characterize and test its behavior [15], [21]–[23]. These research efforts are crucial for the Flying V's design due to its unconventional nature and complicated flow field: most empirical methods and rules of thumb don't apply or are insufficient.

When considering the flight performance characteristics of the Flying V, the pitch break causes some difficulty. It was found in an investigation by Viet that the Flying V must sustain a high angle of attack in landing, around 15.9° [14]. This is undesired since an upward gust at this attitude and low speed could suddenly increase the angle of attack and tip the Flying V into instability. The benefits of enabling a lower landing angle of attack extend beyond increased margin with respect to the pitch break: it also improves other flight performance parameters like required runway length, pilot visibility, and the amount of rotation the plane must make upon contact with the runway. Due to the benefits to be gained, research has been done to search for ways to delay the onset of the pitch break to higher angles of attack and to lower the needed angle of attack at landing.

A few studies have taken place to investigate how adding to or changing the design of the Flying V could help alleviate or delay the pitch break. Notably, van Uitert tested a variety of trip strips, vortilons, and fences on the half-span model of the Flying V in the OJF in 2021 [24]. The trip strips were placed on the suction side at a constant chordwise position of x/c = 0.5 and on the pressure side at a chordwise position of x/c = 0.10. These trip strips extended along the entire span of the model. The locations of the fences and vortilons tested can be seen in Figure 2.2a and Figure 2.2b.

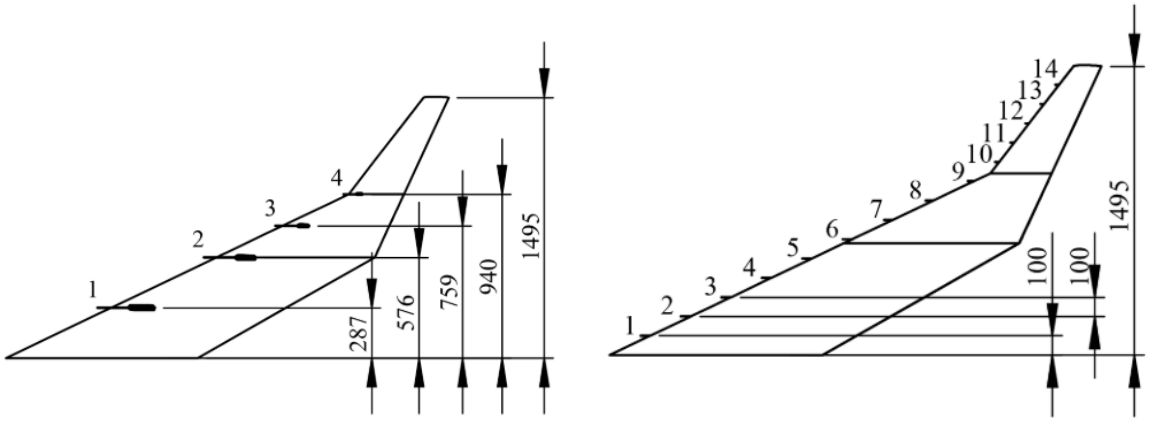

(a) Spanwise fence locations, dimensions in mm [24] **(b)** Equally spaced spanwise vortilon locations, dimensions in mm [24]

Figure 2.2: Spanwise fence and vortilon locations

The investigation revealed that the addition of trip strips actually brought down the maximum usable lift coefficient before the pitch break from $C_L = 0.95$ to 0.80. However, it was observed that the surface flow, as indicated by flow tufts applied, improved on the outboard wing due to the trip strips [24]. Adding vortilons to the Flying V showed some improvement to the pitching moment behavior, but it did not delay the pitch break [24]. The fences were found to be more effective, specifically the fence placed at location 4 in Figure 2.2a, which coincides with the leading edge kink. Some variations of fences were tested at that position, including ones that varied in height and one that was the length of the entire local chord. Through the addition of the fences, the pitch break was changed from an abrupt change to a gradual one, and an increase of $\Delta C_L = 0.35$ was gained in the maximum usable lift [24].

Further work was done in 2024 by van Meenen to investigate how changing the juncture design at the leading edge kink might impact the pitch break. The results, which as of writing are unpublished, indicated that, though some small incremental improvement might be gained, the pitch break still was

observed around 19°–20° angle of attack [25].

Other studies took a different approach to assessing the Flying V pitch break behavior; through refining prediction methods and incorporating more effects, more comprehensive predictions of the Flying V's longitudinal stability were made, especially for the approach and landing conditions. In 2020, Santosh considered what kind of impact the ground effect might have on the Flying V performance in takeoff and landing [26]. Initial predictions had shown that the Flying V required an landing angle of attack of 20°, but Santosh's consideration of ground effect in his numerical investigation showed that the increase in lift and decrease in drag allows for a 19° landing attitude.

Many modern passenger aircraft include a variety of high lift devices and lift dumping surfaces for improved landing and takeoff performance [27]. These allow the aircraft to take off and land over shorter runways, fly slower, and brake faster. The flap, spoiler, and other control surfaces can be seen on an example Boeing 707 aircraft in Figure 2.3. Due to the common use of flap and spoilers on airliners to improve take off and landing performance, both surface types were considered on the Flying V.

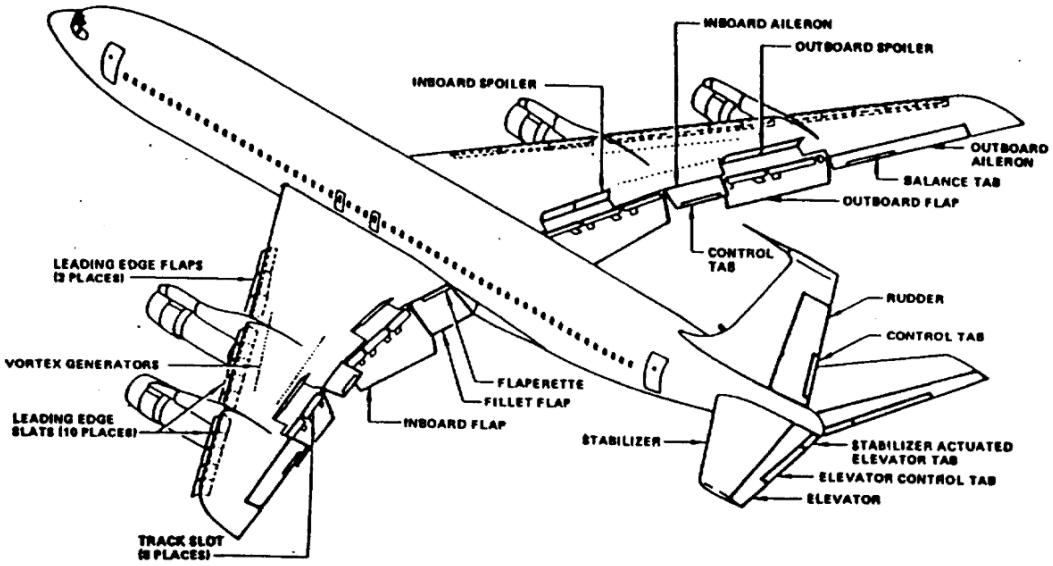

Figure 2.3: Boeing 707-320 control surfaces, high lift devices, and lift dumping devices [27]

In 2021, Erdinçler investigated how adding spoilers to the Flying V design could reduce ground roll and help with derotating and dumping lift at touchdown [5]. In his research, a parametric set of spoilers near the trailing edge were tested, varying in spanwise and chordwise location, along with a set of step spoilers. The spoiler locations tested can be seen in Figure 2.4a. It was found that two $0.1c$ spoilers at the $0.8c_{loc}$ chord line, one close to the the root and one at the trailing edge kink were the most effective at increasing drag and dumping lift for braking performance. One of the spoiler design iterations similar to the final design can be seen in Figure 2.5. These spoiler results were used to refine the preliminary rolling distance predictions, predicting the distance would be reduced 95 m from the initial 1300 m needed in typical conditions in addition to reducing the angle of attack at touch-down by 1.5°.

Considering the contributions of ground effect, spoilers, and landing gear, de Zoeten incorporated refined the landing attitude prediction further: 14°–17° and 72 m/s for the full scale design [6]. Additionally, the combined effects improved rolling distance predictions, showing the Flying V compared with the A350-1000 in required distance [28]. Lastly, adding split flaps to the design further decreased the pitch landing attitude prediction another 3° to around 13.5°–14.5° at landing at the most forward CG location [4]. The tested flap locations can be seen in Figure 2.4b.

Due to the promising results found by adding the spoilers and split flap surfaces to the Flying V, it is desired to incorporate them in the subsequent Flying V designs and models to improve the landing

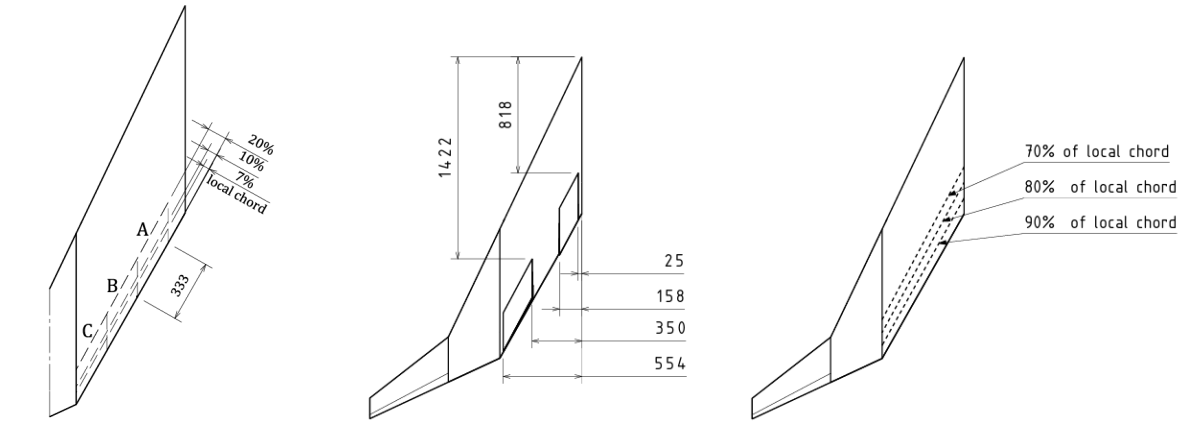

(a) Top view of spoiler locations on Flying V root section [5]

(b) Bottom view of flap locations [4]

Figure 2.4: Spoiler and flap locations tested on the OJF 4.8% scale Flying V model, all dimensions in mm

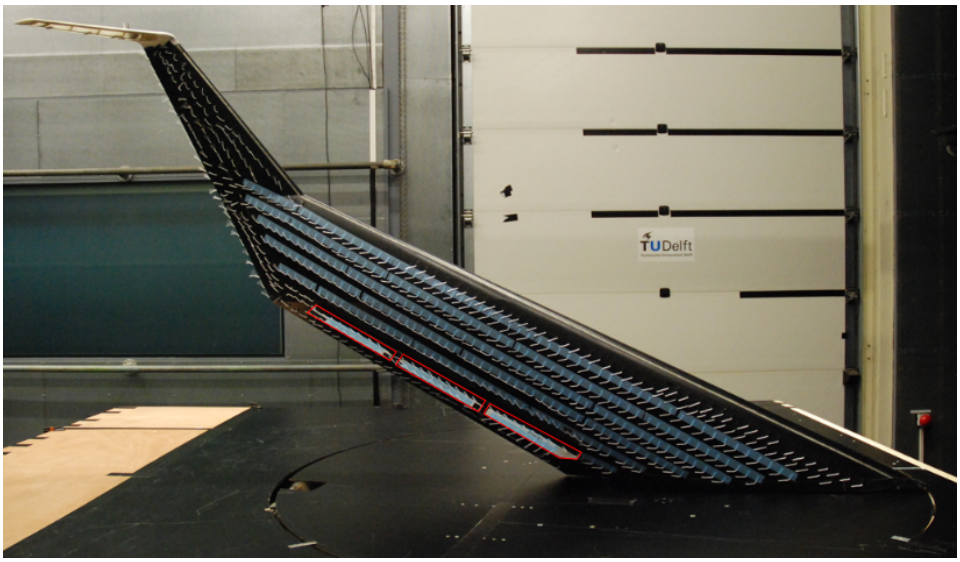

Figure 2.5: Top view of selected spoiler design on OJF 4.8% scale Flying V model with extra middle spoiler, spoilers outlined for visibility [5]

performance. A more in-depth overview of the split flap and spoiler designs, their behavior on the Flying V, and the relevant gaps in research are given the following subsections.

2.1.1. Split Flaps

Split flap designs were proposed as an alternative to delaying the pitch break; by allowing the Flying V to take off and land at lower angles of attack, flaps would increase the Flying V's safety margins. Split flaps were one of the first flap designs developed for aircraft, and they achieve the desired effect of increased lift and circulation over the wing though to a lesser extent than many modern flap designs and with higher penalties [29], [30]. Though split flaps tend to perform worse than nearly any other flap design, the simplicity of the design choice is appreciated given the multiple structural and geometric constraints in the Flying V. The difference between a split flap and a slotted flap can be seen in Figure 2.6, where the simplicity in flap linkages can be seen for the split flap.

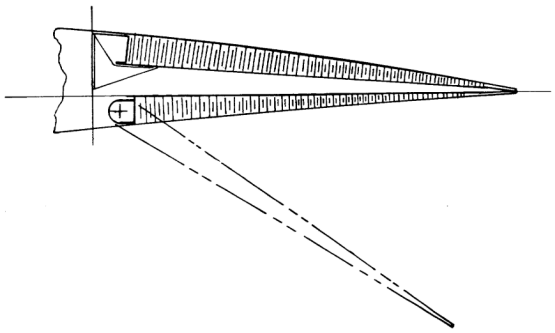

(a) Standard split flap cross section with flap deflection shown and upper spoiler surface stowed [27]

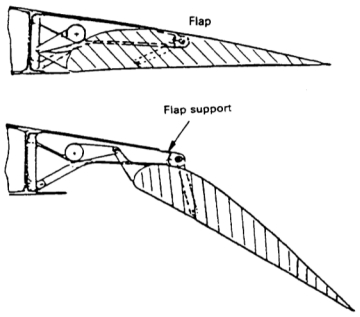

(b) Boeing 747SP single-slotted flap cross section [27]

Figure 2.6: Split flap and slotted flap cross sections and deflection mechanism comparison

As illustrated in Orville Wright's patent drawings of the split flap, seen in Figure 2.7a, the split flap acts as a high-lift device by increasing the pressure on the bottom wing surface, or the pressure surface. The large area of low pressure introduced behind the deflected flap, however, results in an increase in drag, achieving an increase in lift with high drag penalties. Other flap types can easily achieve equal or better lift generation without as large a drag penalty through a variety of alternative approaches, such as extending the wing chord, as seen in Figure 2.7b, introducing a slot to reinvigorate the boundary layer over the flap, and more [31].

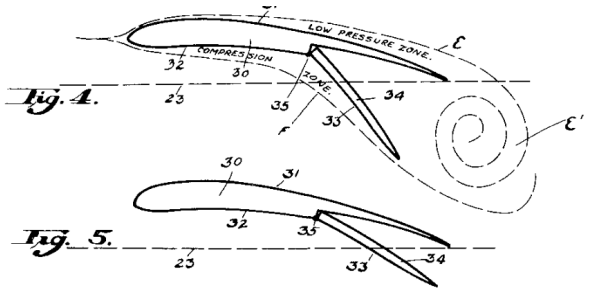

(a) Orville Wright split flap patent drawings [29]

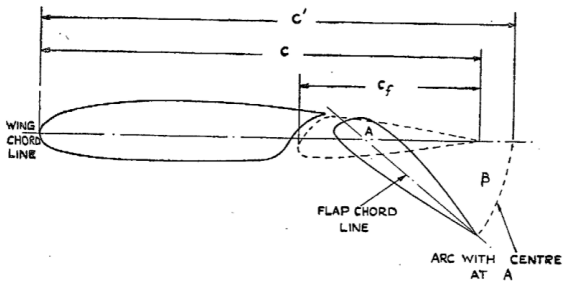

(b) Extended chord effect of deflected, slotted Flap [30]

Figure 2.7: Examples of different flap designs' lift generation approach

In Eftekhar's research on the split flap effectiveness on the Flying V, the selected design was shown to vary quadratically in effectiveness with increasing angle of attack, reaching a maximum effectiveness around angle of attack $\alpha = 10^\circ$ for most flap deflection angles [4]. The change in lift with this flap design can be seen in Figure 2.8. It can be seen that, at higher AoA, the flap effectiveness in changing the lift started to converge across flap deflections, with all deflections past 20° flap deflections performing roughly the same past $\alpha = 20^\circ$. The selected flap design induced a decrease in pitching moment coefficient with increasing flap deflection angle. The final design of the selected flap is seen on the Flying V model in Figure 2.9.

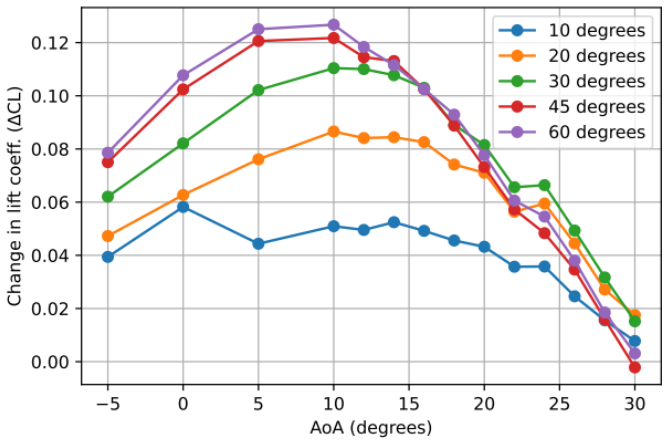

Figure 2.8: Final OJF flap design effects: change in lift coefficient due to flap deflection in comparison to clean wing [4]

Figure 2.9: Bottom view of final flap design selection on OJF 4.8% scale Flying V model [4]

These results, combined with the other force and moment data gathered, were used to refine the approach and landing predictions discussed earlier. Though insight was gained in Eftekhar's research, significant gaps exist in the predicted flap performance as no data has yet been gathered in sideslip conditions. Whereas a conventional swept wing will experience an increase in lift produced by the wing yawed into the wind, the Flying V experiences the opposite effect due to the weakening of the vortex formed over the windward wing [15]. Because the Flying V's windward wing is more susceptible to stall due to this effect, it is important to understand how the effects and benefits of the flaps might change in these sideslip conditions. Therefore, further work should be done to discover this relationship to enable further, more comprehensive predictions over the Flying V's flight envelope.

2.1.2. Spoilers

Spoiler panels were proposed as an another way to improve landing performance. Spoilers specifically help in landing due to their ability to "spoil" the flow over the wing and thereby "dump" the lift from the wings. This lift dumping is achieved by the same aerodynamic principle used by the split flap but on the opposite wing surface: the deflected spoiler surface increases the pressure over the top of the wing, over the suction side. This increased pressure over the wing pushes the wing down, and the decrease in pressure behind the spoiler surface increases the drag of the aircraft. Figure 2.10 shows an example flow field of the flow separation over a deflected spoiler surface, where the reversed flow velocity profile

indicates a decrease in pressure.

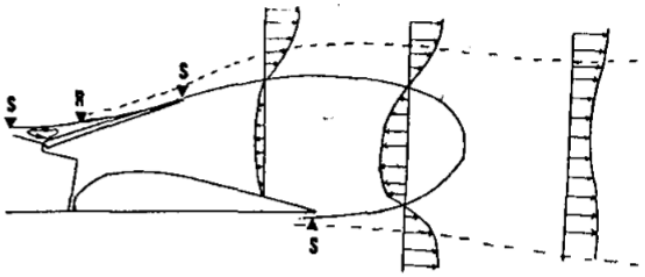

Figure 2.10: Example flowfield and flow separation (S) over a deflected spoiler surface [32]

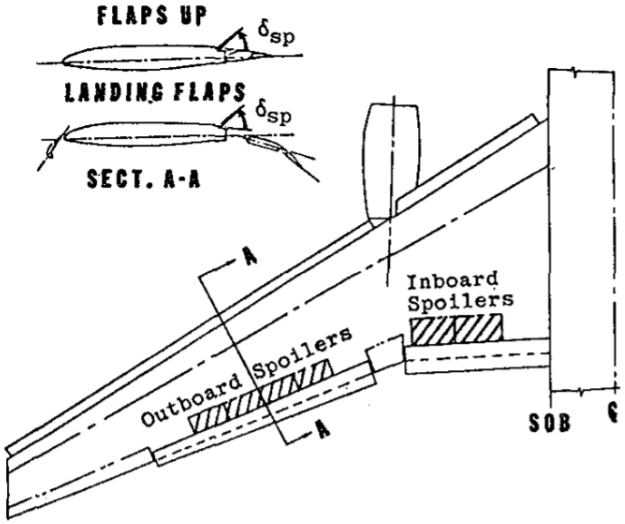

Figure 2.11: Typical transport airplane spoiler configuration [32]

Spoilers are typically located close to the fuselage to minimize the resulting change in bending moment at the wing root, as seen in Figure 2.3 and Figure 2.11. They are also typically located in front of the flaps, allowing the spoilers to nullify the lift generation of the flaps after the aircraft touches down. The change in spoiler effectiveness when paired with flap deflections on standard passenger aircraft can be seen in Figure 2.12, where the amount of lift dumped by a spoiler almost doubles when deflected in conjunction with a deflected slotted flap. Outboard spoilers, like those seen in Figure 2.3 and Figure 2.11 can be used for lift dumping and can also provide roll control at cruise conditions, where aileron roll-control reversal often occurs [31]–[33].

The spoiler lift dumping process allows an aircraft's wheels to be fully loaded sooner and increases the drag of the aircraft, improving and shortening the rolling distance needed for the aircraft to stop. In the landing procedure, spoiler deployment also helps derotate the aircraft, which reduces the likelihood of the aircraft bouncing up [31], [32], [35]. These benefits motivated Erdinçler's design and incorporation of the spoiler panels on the Flying V.

The results from the selected spoiler designs at max deflection, $\delta_{sp} = 60°$, showed a decrease in lift coefficient at all angles of attack, though the effectiveness decreases with angle of attack until around $\alpha = 15° - 17°$ [5]. No adverse lift was observed for the selected design at low spoiler deflection angles, though an adverse increase in pitching moment was observed. At angles of attack $\alpha > 7°$ and deflections greater than $\delta_{sp} = 20°$ showed a decrease in pitching moment.

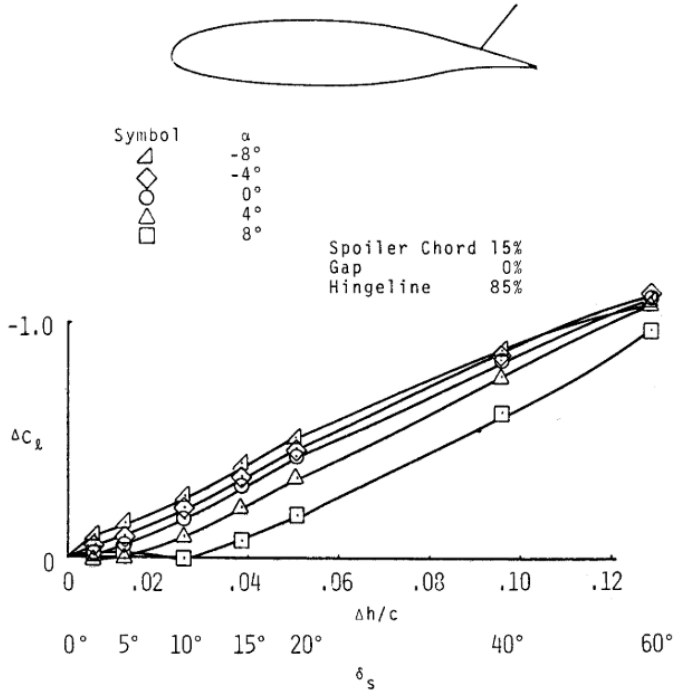

(a) Spoiler effectiveness with stowed flap, spoiler at 85% hingeline [34]

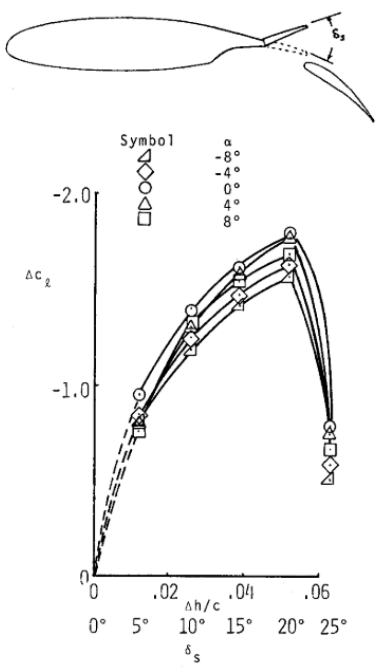

(b) Spoiler effectiveness with slot and 40° flap deflection [34]

Figure 2.12: Changes in spoiler effects on lift coefficient with flap deflection

The final spoiler design was effective at decreasing lift at all angles of attack, though there is a chance that this effectiveness at the lower to mid angles of attack was overpredicted due to the low Reynolds number tested at. It has been indicated that wind tunnels overpredict spoiler effectiveness at lower Reynolds numbers because the corresponding lower-energy flow over the wing is more easily disrupted when compared with full-scale Reynolds numbers [32]. This is also true of spoiler effectiveness in combination with flaps; spoilers tend to dump more lift when deployed simultaneously with flaps by inducing separation over the flaps [31]. As a result, there is often an interaction between flaps and spoilers, though this is also dependent on Reynolds number.

It is often observed that at very low spoiler deflections, the spoilers can sometimes increase the lift generated over the wing in combination with flap deployment [5], [32], [34], [36], and when the spoiler does dump the lift generated by the flaps (at moderate to high spoiler deflections), sharp changes can occur in the lift and the pitching moment, as seen in Figure 2.13 [32], [34], [37]. Erdinçler found a spoiler design that resulted in undesired lift generation at up to 30° spoiler deflections for the M ABC 2 spoiler on the Flying V, as seen in Figure 2.14. Furthermore, these adverse spoiler interactions are all subject to change in sideslip conditions. For example, one study by Abdelrahman *et al.* shows that spoilers on a 40° swept wing increased in effectiveness with increasing sideslip [38].

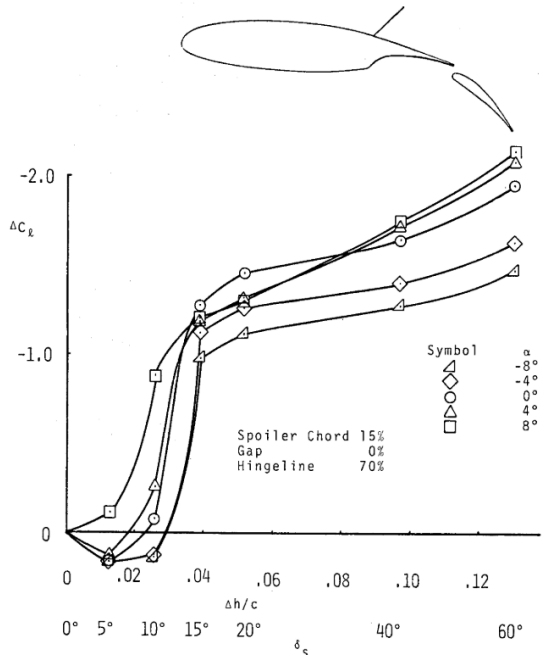

Figure 2.13: Adverse spoiler effects for low spoiler deflections of gap- and slot-less spoiler and a 40° flap deflection [34]

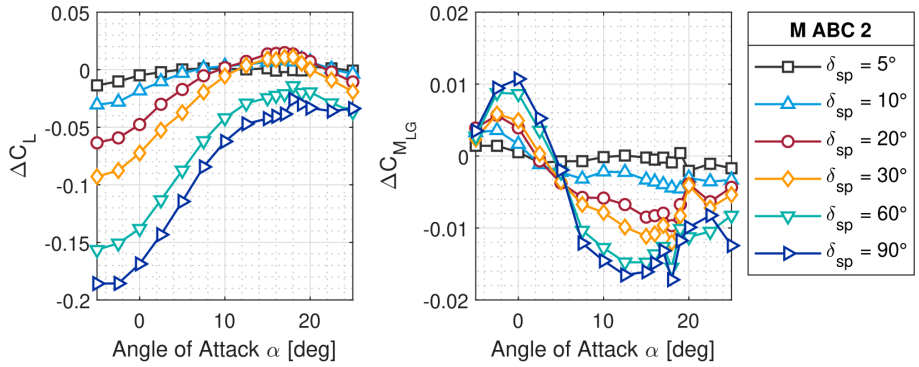

Figure 2.14: Spoiler deflection effects on lift and pitching moment coefficients on M ABC 2 spoiler on OJF 4.8% scale Flying V model [5]

2.1.3. Research Gaps

Initial designs for high lift flaps and lift dumping spoiler surfaces on the Flying V have been proposed and investigated, but much still remains to be understood about the combined effects of these devices and their performance in sideslip conditions. Spoiler effects tend to be very nonlinear in their behavior, and their deflections affect much of the flow around them, especially on highly swept wings like the Flying V, where the spoiler hinge line is swept back about 64°. Thus, predictions of how they perform in combination with flaps and control surfaces are nontrivial. Additionally, it is unknown how the benefit in reducing landing angle of attack given by the flaps or the rolling distance estimates provided by the spoilers might change in the presence of sideslip, especially given contradicting trends from literature and preliminary results from the Flying V. Knowing this sideslip dependency is important when considering flight regulations, which can require stable flight in up to 15° of sideslip at low speeds [39].

Lastly, the spoiler and split flaps designs were evaluated on the semi-span model founded in Faggiano's geometry optimization [13]. This geometry is now outdated as it was optimized from a strictly aerodynamic approach, and when considering structural constraints, it behaves poorly. The newly optimized

geometry that has been refined over the last few years is currently being investigated and characterized, and it remains to be seen how effective the flap and spoiler surfaces, which were designed for the old geometry, will perform on this geometry iteration. It is of great interest, therefore, to study the proposed split flap and spoiler designs together in side slip conditions so that these interactions can be measured and their effect on the stability and control of the Flying V be better understood.

2.2. Wind Tunnels

Wind tunnels are an important tool in simulating and investigating the aerodynamic behavior of an object, and they are particularly useful in assessing the performance and behavior of an aircraft design. Fundamentally, wind tunnel testing works by taking a object moving through still air and modeling it as a stationary object in moving air. Wind tunnels are a popular alternative to other forms of testing because if a wing fails in testing, the wind tunnel engineer only needs to turn off the tunnel while the flight test pilot finds himself still in the air. Not only are wind tunnels generally safer, they allow the aircraft designer to test a smaller model of the aircraft to predict the full-size performance, something that is much cheaper to do than building the full-size aircraft and running a test flight, especially during the iterative process that is aircraft design. Thus, it is said that compared to other forms of testing, wind tunnels are cheaper and save lives [40].

Wind tunnel experiments are often more attractive than Computational Fluid Dynamics (CFD) simulations due to the amount of data that can be gathered in a short time, notwithstanding the fact that tunnels don't need turbulence modeling approximations. Wind tunnels and CFD can go hand-in-hand in aerodynamic research, providing insight in different ways. For the time being, wind tunnels have a very real use in aircraft design today.

This section will cover the importance of similarity parameters in wind tunnels in Section 2.2.1, wind tunnel data sources and instrumentation in Section 2.2.2, the limitations and other considerations when using wind tunnels in Section 2.2.3. Lastly, a brief discussion of different wind tunnel models will be provided in Section 2.2.4

2.2.1. Similarity Parameters

Testings a smaller model and using the results to predict a larger model is possible in a wind tunnel due to the concept of similarity. If parameters of a flow such as the Reynolds number and Mach number are all the same, then the airflow over a geometrically similar shape can be modeled and be used to inform predictions for the full scale [40]. These similarity parameters serve as ratios between forces or effects. For example, the Reynolds number is effectively a ratio between inertial and viscous forces, and it serves as an indicator of flow regimes at a certain scale. Mach number is the ratio between a velocity and the speed of sound, and it serves as an indicator of the compressibility of a fluid or the ratio of inertia to elasticity [40].

If an aircraft design is to be examined in a wind tunnel, the full scale Reynolds and Mach numbers can be calculated and be used to set the proper conditions in the wind tunnel. A smaller version of the aircraft design can then be made, and if tested at flow conditions such that the ratios of inertial to viscous forces and flight velocity to sound velocity are matched, then the flow will move over the static, sub-scale model just as it would over the full scale design, just on a smaller scale.

Key to relating wind tunnel results to the full-scale predictions is the process of nondimensionalizing the results or expressing the modeled results in terms of coefficients. The similarity parameters are nondimensional ratios that allow a phenomena to be characterized at different scales. Coefficient results achieve the same thing, allowing the test engineer to express the forces and moments experienced by the model in terms of, often, the model reference area, flight speed, and air density. These nondimensional results, after some scaling and boundary corrections, can then be attributed to the full-scale geometry, where the full-scale size and flight speed can be used with the measured coefficient to predict the full-scale, dimensional force experienced. In this way, information can be inferred about a full-scale object from a measured, sub-scale model.

The exact match of similarity parameters in experimental conditions needed to accurately model the flow is rarely achieved, however, because achieving such exact similarity in Reynolds and Mach numbers simultaneously for a small model requires very fast flows and/or very cold temperatures. This mismatch

can be remedied by a number of testing techniques and approximations that are beyond the scope of discussion here. Ultimately, wind tunnel models are still *models*. All models have simplifications and shortcomings, but if used correctly, they can be valuable tools.

2.2.2. Data and Instrumentation

With a scaled wind tunnel model, the flow phenomena over it can be measured in the wind tunnel at various simulated flight conditions. Most tunnels are equipped with systems to position the model in the tunnel flow at different incidences to simulate the pitch, roll, and/or yaw attitude of a model. When in the tunnel flow, the model's reaction to the forces exerted on it by the flow can be numerically measured in a number of ways, usually by means of balance data or pressure data. Force and moment data is the most prevalent way to measure a model in a flow, and it is measured by a balance, either external or internal to the model. A wind tunnel balance is usually designed to decompose the overall reaction force of the model into six components using a collection of strain gauges or mechanical balances, meaning a single balance data point will return three forces and three moments for a six-axis balance [40].

When using a wind tunnel to observe the flow over the model, it is important to remember the model is in a wind tunnel. That is, the presence of the wind tunnel around the model will affect the flow over it to behave differently than if the tunnel were not there. As a result, special consideration needs to be taken before comparing wind tunnel data to the full-scale conditions. This process is referred to as *wind tunnel* (or *boundary*) corrections [40]. In this process, other factors, like the presence of the supports holding the model in the tunnel, are taken into account by treating and modifying the measured data.

2.2.3. Experiment Statistics and Sources of Error

When positioned inside the tunnel flow, a wind tunnel model isn't guaranteed to experience dynamically stable flow; at a minimum, fluctuations and vibrations due to turbulent flows, especially when any flow separation is present, are sure to occur. As a result, data points are often measured by sampling balance (or pressure) data over a set duration, on the order of a few seconds, to capture the fluctuating signal. The balance data is generated first in the form of an electric, analog signal which is output via the balance's strain gauges. This signal is often filtered and processed by the wind tunnel's data acquisition system, using analog-to-digital converters and techniques to process the data and output the sample mean and standard deviation [40]. This sampling process is but one source that introduces uncertainty in wind tunnel results. Due to its stochastic nature, wind tunnel testing is not deterministic and has different considerations compared to the results of a computer simulation [41].

In any experimental setup, if one were to repeat a measurement under seemingly or ostensibly identical conditions, the measured results would vary. This difference in measured results is referred to as random or experimental error, noise, or simply *error*, and its magnitude is often dependent on the precision of the instruments used [42]. This random error is present in any experiment done due to reasons not entirely clear, but it is the reason why much of the field of statistics exists today. Given a dataset of ostensibly identical data points, the variations between them due to the random error is called *variance*, and variance in data contributes to the *uncertainty* in which we present the data. There are many techniques to quantify this uncertainty and minimize the variance that causes it, and some of those techniques are discussed here.

Variance is often discussed in terms of random and systematic, or explained and unexplained components [40], [43]. The different sources then manifest as uncertainty in measurement precision or as a bias from the unknowable true value. Random variance will cause a measured value to be distributed around the true value. According to the Central Value Limit theorem, as more measurements are made in the absence of any bias or systematic variance the measurement distribution will approach a Gaussian or normal distribution around the true value [42]. The true value can then be reported as the average or mean of the data set, and the random error of that value is the amount by which each data point deviates from that mean, quantified as the standard deviation or referred to as the precision of the data set. If bias or systematic variance occurs, then the data set will be distributed around some value offset from the true value. Figure 2.15 illustrates some examples of measurement distributions with their mean and deviation values.

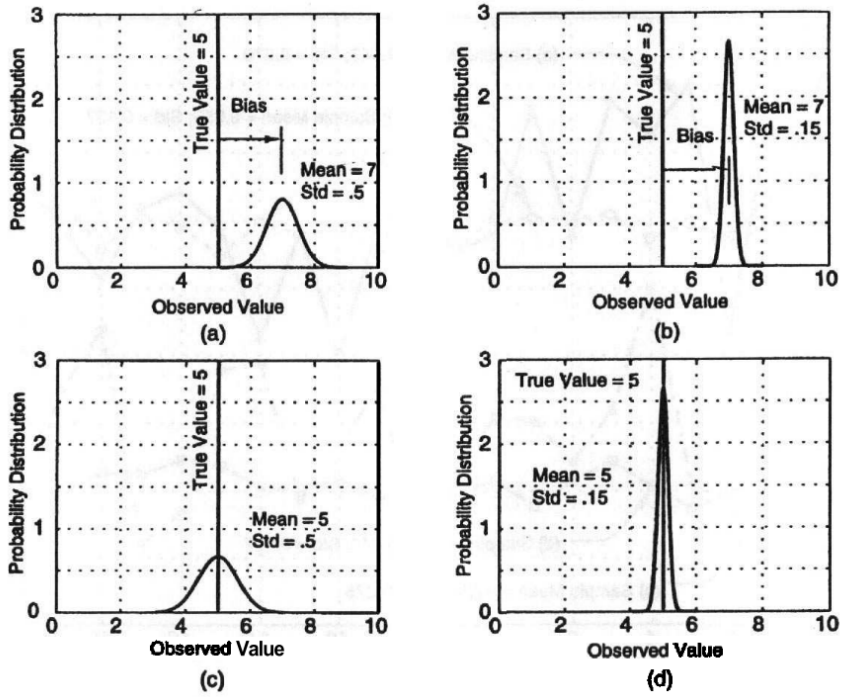

Figure 2.15: Examples of normal distributions of measurements with and without bias [40]

Given a number n of ostensibly identical data points y_i, the mean μ and standard deviation σ of the dataset can be calculated using the following equations:

$$\mu = \frac{1}{n}\sum_{i=1}^{n} y_i \tag{2.1}$$

$$\sigma = \sqrt{\sum_{i=1}^{n} \frac{(y_i - \mu)^2}{n-1}} \tag{2.2}$$

In the absence of bias, μ is considered an approximation of the estimator of some response that is a function of the design variables used to measure the data. The standard deviation is likewise an approximation of the first estimator of the same response given the measurements are normally distributed. The smaller the standard deviation, the greater the precision of the mean in describing that data set.

The area under a probability distribution curve is often used to indicate the probability of a new measurement's likelihood of belonging to the population. If a new measurement is more than one standard deviation away from the groups' mean, the area to the right of the mean and one standard deviation indicates the probability that the new measurement is a member of the group. Looking at Figure 2.16, the probability that a measurement more than two standard deviation from the mean in either direction belongs to the population is about 5%. Expressed in another way, if a data point is measured more than two standard deviations away, it can be said that, with 95% confidence, the new data point is distinct from the population [44].

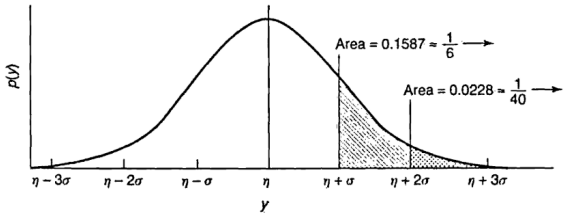

Figure 2.16: Area under the normal distribution [42]

Another type of observation distribution used is the Student's distribution, or t-distribution, and it is helpful for considering probabilities of distributions while considering the number of measurements available [42]. Specifically, with less data points or degrees of freedom, less is known about a sample's distribution, so the probabilities associated with the sample are more uncertain. Figure 2.17 shows how for lower degrees of freedom, shown in this graph as ν, the area under the curve is less centralized. Thus, the confidence levels change from a normal distribution depending on the number of samples taken, but the t-distribution approaches the normal distribution as the number of samples approach infinity [42].

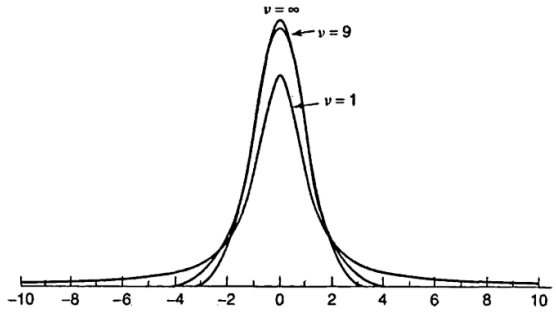

Figure 2.17: The t-distribution for different degrees of freedom (ν) [42]

Unexplained variance is the variance present in data that introduces a bias from the true value but is unidentified or unaccounted for [44]. This introduces error into the experimental results and is part of the difficulty in comparing between experimental data sets and making accurate predictions from experiments. In wind tunnel tests, unexplained variance can be caused by the drift of temperature, which is a common culprit as it often drifts throughout the duration of a wind tunnel test [45]. There can exist an underlying function of the forces and moments measured with respect to temperature, which in turn can change with time. This is often due to the sensitivity to temperature by the strain gauges often used in balances to measure these forces and moments, temperature dependence of different instrument calibrations, or even the varying of a model support structure's Young's modulus with temperature [45]. Additional sources of variance that can bias the measured data could come from difference in facility personnel experience and focus over the duration of a test, the movement of trip dots on the model, slop in the model as it is loaded and unloaded by the air flow, and more [44].

The prevalence of unexplained variance in wind tunnels is persistent, but there are ways to combat it. For example, many tunnels employ some form of heat-exchange or cooling system to attempt to maintain a constant temperature. This highlights the importance of mitigating unexplained bias in the experiment results, because, even biases of small magnitude can be relatively larger than the required error margin set for most experiments [44]. Sources of variance also can differ between wind tunnels, making it troublesome to directly compare results from one tunnel to another, even when testing an identical model in ostensibly identical conditions [44]. Just like most experimental environments, the wind tunnel laboratory is not an isolated environment and random experimental error will always be present in addition to unexplained or unidentified error. As a result, careful attention should be given in conducting a wind tunnel experiment to mitigate, identify, and report the resulting uncertainties in these tests. Methods used to do just this will be discussed in Section 2.3.

Beyond data quality, other sources of error can occur in wind tunnel testing that impact its accuracy. Differences between the test model and the full-scale design can have an appreciable impact, such as the difference in relative surface roughness, simplifications made to the model due to size (no antenna, hinges, or other excrescences that would be present on the full-scale model), and differences in structural design and the resulting model deformations due to the material used. All of these model differences and sources of error can significantly reduce the applicability of the tunnel results to the full-scale model, and they ought to be carefully considered when designing the test model.

2.2.4. Wind tunnel model types

The two primary types of wind tunnel models are full-span models and half-span reflection plane models. A full-span model is a test model that is usually scaled down to fit within the tunnel test section and resembles the true design. To maintain similarity in the flow over such a model, the flow's Reynold's number and Mach number must match the full-scale flow conditions, often meaning the smaller test model must be tested at higher wind speeds and very low temperatures. For small tunnels, testing a full-span model means the speeds required to match similarity parameters might be higher than achievable. To remedy this, a half-span model can be used to increase the size of the model while fitting in the same wind tunnel test section. The larger scale decreases the necessary test speed for flow similarity. The downside is that fewer conditions can be tested, such as sideslip, and an assumption of symmetry of the flow and results must be assumed across the model symmetry plane. Additionally, interaction effects of the model and the surface onto which the semi-span model is mounted are introduced and ought to be accounted for.

Up until 2024, the Flying V had only been tested in a wind tunnel using the 4.8% scale semi-span model developed using Faggiano's optimized geometry, shown in Figure 2.18 [13]. This geometry has been tested in TU Delft's Open Jet Facility (OJF). Recently, a full-span model of the Flying V has been manufactured using the latest Flying V design iteration, based on the geometry optimization of Laar [9]. This new model, a 1.84% scale model, has been made for wind tunnel testing at the TU Delft Low Turbulence Tunnel laboratory. This model can be tested in a more complete flight envelope than the OJF model as it can be tested at a combination of both sideslip and angle of attack, unlike the OJF model that could only set at different angles of attack. Whereas the OJF model was mounted to a plate at its root, the LTT model is supported by two struts on the wings and by a bar through its longitudinal centerline, allowing it to be pitched inside the tunnel. More information on the LTT Flying V model is provided in subsection 3.4.2.

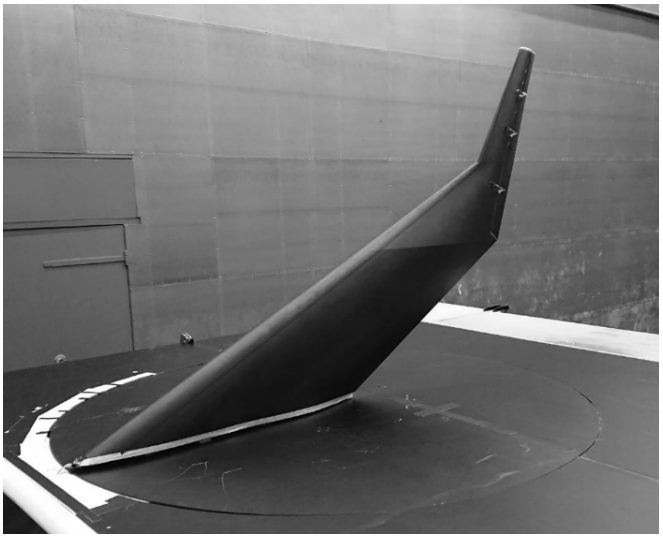

Figure 2.18: Flying V 4.8% semi-span OJF model [13]

This LTT setup introduces different interference effects than the OJF setup. On the OJF model, it was observed that the junction flow at the plate and model root traveled up the model towards the leading edge, interfering with the flow developing over the model itself [13]. This is a known shortcoming of

reflection plane models [40], and highly swept wings are particularly influenced by this interference effect due to the amount of cross-flow over them: root interaction effects are likely to propagate down the wing span due to the crossflow.

The full-span model will also have interference effects introduced by the presence of its support mechanism. It is possible to account for and remove the drag increment introduced by the wing support struts, but the effect the presence of those struts have on the flow field around them at their juncture with the wing is more difficult to quantify without complex methods like *tare and interference*. [40].

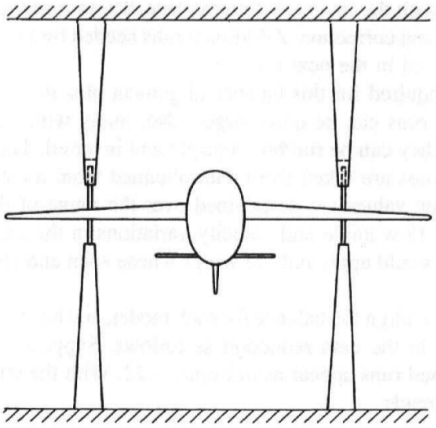

Figure 2.19: Tare and interference setup example [40]

In this method, data is often gathered using struts mounted from above and below, in addition to the normal data measured, as illustrated in Figure 2.19. The model is also often flipped upside-down. Using the multiple configurations, a linear combination of the deltas is used to extract the struts' effects on the flowfield (the interference effect) and the added drag (the tare effect) [40]. This method is complicated as the model needs to be specially designed to accomplish it. Furthermore, it requires extra time in the tunnel test to be set aside to quantify these effects. Without this quantification, the interference effects will remain in the data and contribute to the uncertainty introduced by this particular model support method and test environment.

It is anticipated that there will be noticeable differences between the full-span and semi-span models due to both the differences in geometry and the differences in model type and installation. Furthermore, the difference in wind tunnel test sections and the types of wind tunnel corrections needed will introduce different effects on the semi-span and full-span model results.

2.3. Modern Design of Experiments

Over the last two to three decades, a new approach to experiment design has been slowly adopted in the field of aerodynamics and aircraft testing. This new methodology and approach can be better thought of as a *new testing philosophy* as it runs counter to the core testing philosophy most wind tunnel engineers hold, despite its adoption over the past decades outside of the aerospace industry [45]. This is because this Modern Design of Experiments looks at experiments as a mean to generate adequate prediction models instead of only measuring large amounts of data points [43].

Standard wind tunnel practice is to gather as much data as possible from a test while going to great lengths to ensure the accuracy of each individual data point. This is done in a one-factor-at-a-time (OFAT) approach, where one variable is changed while all others are held constant when gathering data. The engineers at NASA Langley have been trying to bring their colleagues out of the past and to open their eyes to the great advantages of MDOE methods, and other institutes and test engineers are starting to catch on [43], [46]. In the literature, a distinction is sometimes made between Design of Experiments (DOE) and Modern Design of Experiments, where the latter sometimes refers to the design of deterministic numerical experiments [47]. In this report, the framework and nomenclature

used by the researchers at NASA Langley is adopted to refer to the Design of Experiments applied to wind tunnel testing and Response Surface Methodologies (RSM) as *MDOE*, as is done in this research.

In the following sections, Response Surface Methodologies is introduced in subsection 2.3.1, the benefits from using MDOE methods will be discussed in subsection 2.3.2, different MDOE techniques will be presented in subsection 2.3.3, some examples of MDOE methods being employed in experiments will be given in subsection 2.3.4, and some final challenges and considerations when using MDOE methods will be concluded with in subsection 2.3.5.

2.3.1. Response Surface Methodologies

An aircraft's performance can be predicted and assessed through wind tunnel testing. This is done by measuring the aircraft model configurations over "sweeps", setting the model at different angles to the flow and measuring data across a range of angles in discrete increments. Using these sweeps of measurements, the magnitude of data, such as the maximum lift coefficient or ratio of lift to drag coefficient at cruise angle of attack, can be directly measured. Additionally, derivatives of different forces or moments with respect to these angles can be calculated using the data. Differences between configurations can be calculated to observe control effectiveness or percent improvements by subtracting one configuration data set from another. This is the traditional approach to interpreting and using wind tunnel data.

A more comprehensive way to use the data measured in a wind tunnel experiment is to construct a response model using RSM. A response surface model is a mathematical model that is fitted with data points and approximates the relationship between the independent variables and the response behavior. This model can then be used to interpolate between the measured data points within the design space. RSM is a common numerical methods tool used in a variety of fields, and it has many applications in optimization, design, and interpretation usages [48].

RSM is especially useful in analyzing wind tunnel data, as more about the test model can be predicted and understood beyond what is directly measured [49]. Additionally, using RSM, the data gathered improves the uncertainty assessment of more than just the point at which it is measured, which is a limitation of traditional wind tunnel data analysis approaches. Each data point contributes to both the uncertainty assessment at that location and to the uncertainty in the response model's prediction [49]. Models fitted with wind tunnel data thus provide more information and more precision than a collection of individual measurements can.

Linear Models

A response surface model is often formulated as a multiple linear regression, where the response y is represented as a linear combination of k independent variables or regressors x_j, each scaled by a model coefficient θ_j [48]:

$$y = \theta_0 + \theta_1 x_1 + \theta_2 x_2 + \cdots + \theta_k x_k + \epsilon \tag{2.3}$$

For the i^{th} measurement or observation, this becomes:

$$\begin{aligned} y_i &= \theta_0 + \theta_1 x_{i1} + \theta_2 x_{i2} + \cdots + \theta_k x_{ik} + \epsilon_i \\ &= \theta_0 + \sum_{j=1}^{k} \theta_j x_{ij} + \epsilon_i, \quad i = 1, 2, \ldots, n \end{aligned} \tag{2.4}$$

This expression can be compactly written in matrix form, resulting in the Linear Model (LM) form:

$$\mathbf{y} = \mathbf{X}\boldsymbol{\theta} + \boldsymbol{\epsilon} \tag{2.5}$$

Here:

- $\mathbf{y}$ is an $n \times 1$ vector of responses,
- $\mathbf{X}$ is the $n \times p$ design matrix containing the predictor values,
- $\boldsymbol{\theta}$ is a $p \times 1$ vector of model coefficients,
- $\boldsymbol{\epsilon}$ is an $n \times 1$ vector of residual errors.

The ordinary least squares (OLS) method estimates the coefficients by minimizing the sum of squared residuals. The resulting estimate is:

$$\mathbf{b} = (\mathbf{X}^\top \mathbf{X})^{-1} \mathbf{X}^\top \mathbf{y} \tag{2.6}$$

Using this, the predicted responses are:

$$\hat{\mathbf{y}} = \mathbf{X}\mathbf{b} \tag{2.7}$$

With a properly fitted model, any input within the design space can be used with $\mathbf{b}$ to estimate the corresponding response.

The number of parameters p in a polynomial regression model depends on the number of variables k and the polynomial degree d. The minimum number of points required to estimate all coefficients is given by:

$$p = \frac{(d+k)!}{d!\,k!} \tag{2.8}$$

Any additional data beyond this minimum can be used to improve model precision and assess lack of fit. This is often referred to as *scaling* the experiment. For example, to protect against model inference errors at 95% confidence, a scale factor of approximately 1.625 may be recommended [50].

The residual sum of squares, or error sum of squares SS_E, quantifies the unexplained variation in the model:

$$SS_E = \sum_{i=1}^{n} (y_i - \hat{y}_i)^2 = \mathbf{y}^\top \mathbf{y} - \mathbf{b}^\top \mathbf{X}^\top \mathbf{y} \tag{2.9}$$

Given $n - p$ residual degrees of freedom, the model variance is estimated as:

$$\hat{\sigma}^2 = \frac{SS_E}{n-p} \tag{2.10}$$

This estimated variance is used for statistical inference and for assessing model adequacy. Further evaluation using hypothesis tests such as ANOVA is discussed in subsection 2.3.3.

Linear Mixed Models

For wind tunnel tests, data is typically measured in batches or blocks, resulting in multiple sources of error. Unlike linear models fit using OLS, which assumes identically and independently distributed errors, Linear Mixed Models (LMMs) explicitly account for both fixed effects and random effects [48], [51]. They are especially suitable when responses are correlated within groups, such as blocks or batches in a wind tunnel test.

A LMM takes the form:

$$\mathbf{y} = \mathbf{X}\boldsymbol{\theta} + \mathbf{Z}\mathbf{u} + \boldsymbol{\varepsilon} \tag{2.11}$$

where:

- $\mathbf{y}$ is the vector of responses,
- $\mathbf{X}\boldsymbol{\theta}$ models the fixed effects,
- $\mathbf{Z}\mathbf{u}$ represents the random effects,
- $\boldsymbol{\varepsilon}$ is the residual error.

The random effects $\mathbf{u}$ and residuals $\boldsymbol{\varepsilon}$ are assumed to follow multivariate normal distributions:

$$\mathbf{u} \sim \mathcal{N}(\mathbf{0}, \mathbf{G}), \quad \boldsymbol{\varepsilon} \sim \mathcal{N}(\mathbf{0}, \mathbf{R})$$

This leads to a marginal model:

$$\mathbf{y} \sim \mathcal{N}(\mathbf{X}\boldsymbol{\theta}, \mathbf{V}), \quad \text{where} \quad \mathbf{V} = \mathbf{Z}\mathbf{G}\mathbf{Z}^\top + \mathbf{R}$$

- $\mathbf{X}$ is the fixed effects design matrix (e.g., test conditions),
- $\mathbf{Z}$ is the random effects design matrix (e.g., block assignments),
- $\mathbf{V}$ is the overall covariance matrix of the response vector.

In an experiment modeled by a LMM, the random effects model the variability due to differences between blocks of measurements, allowing these effects to be estimated and removed before fitting the fixed effects. The variance components $\mathbf{G}$ and $\mathbf{R}$ are estimated using either Maximum Likelihood (ML) or Restricted (Residual) Maximum Likelihood (REML), with REML typically preferred for unbiased variance estimation. These methods are suggested as alternatives to needing balanced or orthogonal experiment designs such that OLS can be used [52].

ML and REML estimate the variance components by optimizing the marginal log-likelihood of $\mathbf{y}$. The marginal log-likelihood measures how well the model explains the observed data after accounting for uncertainty in the parameters. In ML, the matrix form of the marginal log-likelihood is formulated as so [51]:

$$\ell_{\text{ML}}(\boldsymbol{\theta}, \boldsymbol{\phi}|\mathbf{y}) = -\frac{1}{2}\left[n\log(2\pi) + n\log\sigma^2 + \log|\mathbf{V}| + \frac{1}{\sigma^2}(\mathbf{y} - \mathbf{X}\boldsymbol{\theta})^\top \mathbf{V}^{-1}(\mathbf{y} - \mathbf{X}\boldsymbol{\theta})\right] \tag{2.12}$$

- $\boldsymbol{\phi}$ is the vector of all variance parameters

In REML, the likelihood is formulated differently, estimating the likelihood of only the variance parameters given the data [51]:

$$\ell_{\text{REML}}(\boldsymbol{\phi}|\mathbf{y}) = -\frac{1}{2}\left[(n-p)\log\sigma^2 + \log|\mathbf{H}| + \log|\mathbf{X}^\top\mathbf{H}^{-1}\mathbf{X}| + \frac{1}{\sigma^2}\mathbf{y}^\top\mathbf{P}\mathbf{y}\right] \tag{2.13}$$

$$\mathbf{P} = \mathbf{K}(\mathbf{K}^\top\mathbf{V}^{-1}\mathbf{K})^{-1}\mathbf{K}^\top \tag{2.14}$$

$\mathbf{K}$ is the matrix that isolates the portion of the data $\mathbf{y}$ that only contains information about the variance components, such that the $\mathbf{K}^\top\mathbf{y}$ linear combinations are orthogonal to θ. By restricting the data available available for the likelihood optimization, the algorithm is said to be *restricted* and returns variance structure estimates that are independent of the model's fixed effect structure.

In both cases for ML and REML, the marginal log-likelihood is maximized using an iterative approach, using the partial derivatives of the likelihood to find solutions for the fixed effects and random effects parameters in ML and only the random effects parameters in REML. The algorithm substitutes each iteration's estimate for the parameters back into the equations until the solution converges.

Once the covariance structure $\mathbf{V}$ is known, either via ML or REML, the fixed effects can be estimated using the Generalized Least Squares (GLS) solution:

$$\hat{\boldsymbol{\theta}} = \left(\mathbf{X}^\top\mathbf{V}^{-1}\mathbf{X}\right)^{-1}\mathbf{X}^\top\mathbf{V}^{-1}\mathbf{y} \tag{2.15}$$

This formulation generalizes the OLS estimate from Equation 2.6 by incorporating the full error covariance structure via $\mathbf{V}$. The result is an unbiased, efficient estimate of the fixed effects even when the data exhibits grouping or correlation.

By explicitly modeling block-level variability, linear mixed models provide more accurate estimations of the significant relationships measured and better predictive performance in the context of wind tunnel experiments, where measured blocks are often grouped by configuration.

2.3.2. Benefits

Designing wind tunnel experiments using MDOE principles emphasizes informed, statistically-driven data point selection whereby the resulting dataset as a whole is much more accurate and significant in fitting RSM models than a collection of individually "clean" data points could be. NASA Langley's Richard DeLoach calls this MDOE's "integrated research quality and productivity" approach in contrast to OFAT's "conventional focus on individual data point quality" [43]. Additionally, MDOE better enables the research to accurately capture complex interaction effects between multiple variables, something that is easily and frequently overlooked in OFAT tests.

As in any experimental setup, statistical stability and repeatability are crucial for reliable wind tunnel testing. Wind tunnel tests often span several days or even weeks, making it essential that measurements taken on one day are within an acceptable margin of error when repeated on another. However,

this desired repeatability is more often assumed out of convenience rather than demonstrated [45]. Numerous factors can influence the stability of the data, introducing systematic errors into the experiment. In the aerodynamic context, variations in temperature, even over the course of a single day, can have unintended effects on measurements. Other sources of variability, such as changes in humidity, wind speed, or mechanical drift in the equipment, can also impact the accuracy of measurements. Even standard practices like frequent wind-off zeros or calibrations cannot entirely mitigate these sources, ”because Nature displays a relentless tendency to drift when it is least convenient for the purposes of experimental research” [45].

The failure to identify the presence of systematic variance in results can lead to a number of pitfalls and shortcomings, especially of the Type I and II inference errors [45]. A Type I inference error is a false positive, and a Type II error is a false negative. In the case of building a model from measured data, if systematic variance is present and unmitigated, the resulting variance estimate for a particular variable could be overinflated, resulting in its exclusion from a model if its effect is thought to be too small and a failure in the model to capture the physical relationship between the design variables [45].

What is left to the responsible test engineer, then, is to anticipate the presence of these systematic variances in the test and to design an experiment to account for them. This is called ”scaling” the experiment, where measurements are planned beyond that which is necessary to meet the objectives of the test to improve the entire test’s quality [45], [46]. Gains stand to be made in test quality because the magnitude of the systemic error, though small, can be larger than the random experimental error if present. It is advantageous to plan for this source of variance, almost like an insurance policy, to make the most out of an experiment [43], [45]. Using quality assurance techniques from MDOE methods disrupts the correlation between the systematic experimental errors and the response measured, improving the uncertainty levels of the results and protecting from bias [50].

Another major benefit of designing wind tunnel tests using MDOE methods is the more thorough exploration and characterization of the possible sample space for an experiment compared to what is available in an OFAT approach. For example, one study using the OFAT approach gathered data describing 5575 different data points over the course of their tests [50]. With just seven independent variables, such as angle of attack, canard settings, and wind speed, the possible number of combinations that could be tested was 736,250. The gathered data points make up a mere 0.76% of this sample space. When considering the realistic combinations of the variable levels, the number of reasonable combinations decreases to 29,450 from 736,250. The gathered OFAT data set still only covered around 19% of those combinations. The MDOE approach, by comparison, was able to cover that 19% of the design space with only 20% of the data points and in half the time. Given an equal test duration, it can be seen how the MDOE approach could be used to examine more of the design space using less data measurements.

2.3.3. Techniques

There are several techniques used to design an experiment and analyze its results using the MDOE framework. Several are highlighted in the following subsections.

Space Selection

When designing test matrices, the combinations of levels of the selected independent variables is determined by the goals of the experiment (i.e. the response being investigated) and the method of site selection (OFAT vs MDOE/RSM methods). A description of the different space selection methods will be discussed here.

The **OFAT** method is the approach of changing a single independent variable across its tested range while holding all others constant, usually at the baseline level. This is the traditional approach in wind tunnel testing, but it is insufficient for determining the interaction effects between different combinations of levels of multiple variables at once [50]. For example, unless motivated by past analysis or theory, it is inaccurate to measure a delta in lift coefficient due to a flap deflection and a delta due to a spoiler deflection separately and then linearly add those two deltas to approximate the combined effect.

When using a MDOE method to design an experiment to fit a RSM model, the experiment design is referred to as a *response surface design* [41]. Factorial Designs are one response surface design that test each independent variable in combinations with others, varying each of them to a high and low level

simultaneously. For a Full Factorial Design (**FFD**), all possible combinations of variables are tested, and it is most efficient when testing each variable at a high level and a low level as shown in Figure 2.20. In so doing, the relationship of the measured response to a change in an independent variable can be seen, but more interestingly, the measured response to a combination of different variables can also be assessed. In a wind tunnel example, an aircraft would be measured at an angle of attack with various control surfaces deflected at once. In an OFAT approach, a combination of flap deflections will be tested in an alpha sweep, or a range of spoiler deflections might be tested, but with a FFD combinations of spoiler and flap deflections are observed together for an alpha sweep. The number of

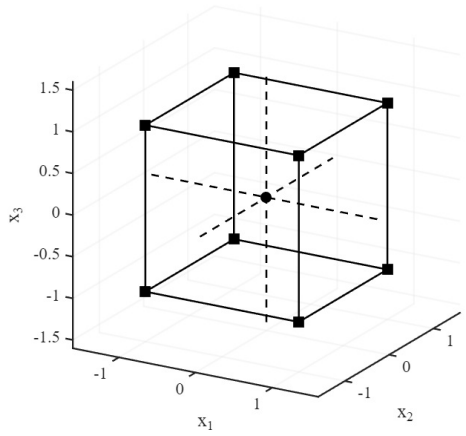

Figure 2.20: Full Factorial Design with three factors (k=2)

data points needed to capture all interaction effects between independent variables grows rapidly with increasing number of variables and levels. Because two levels need to be measured at a minimum to capture the effect of changing a single variable, the number of data points can be expressed as the following:

$$N = n^k = 2^k \tag{2.16}$$

where N is the number of points needed for a n-level design and k is the number of independent variables [46]. This means for just 3 variables tested at 2 levels, $N = 8$ points are needed. This can become quite costly quite fast, especially if more than just two levels are desired. A two-level FFD experiment can be used to screen the design space to see which variables and interactions are the most significant, thereby providing the test engineers info needed to refine the site selection for future experiments.

A less costly factorial design method is the Fractional Factorial Design, where, as the name suggests, a *fraction* or subset of the possible combinations is tested at the expense of some of the higher-order interactions. Less data points are required from this approach, but the burden lies on the test engineer to neglect certain interactions, whether based on previous knowledge or theoretical backing. This approach is also widely used in screening experiments as the accuracy of the response prediction is less important than identifying the significant factors. When only a fraction of the possible combinations are tested, the higher interactions are indistinguishable from other variables in the model created using this approach, and these interactions are said to be *aliased* to those variables [41], [48].

The Central Composite Design (**CCD**) is designed to best fit a quadratic response model by adding points to a two level FFD, and it is especially good for high-precision fits of second-order models [53]. An example of this site selection design is shown in Figure 2.21a, where the center point is often replicated and used to estimate the random error in the experiment [48]. Another good method for fitting second-order models is the Box Behnken Design (**BBD**), which uses less points than a CCD, as seen in Figure 2.21b [48]. Additionally, a BBD never tests the variables all at their highest or all at their lowest levels, which is helpful when doing so could result in an extreme or dangerous scenario (i.e. a high angle of attack at a high Mach number).

A popular response surface design is the **D-Optimal** design. This design uses a computer algorithm to randomly populate the sample space to ensure the smallest error in the model coefficients after

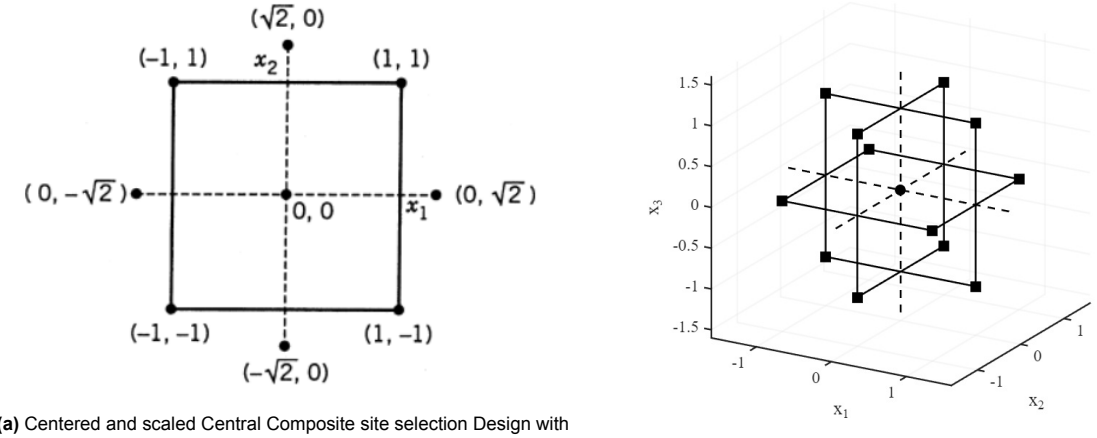

(a) Centered and scaled Central Composite site selection Design with two factors (k=2) [48]

(b) Box Behnken Design with three factors (k=3)

Figure 2.21: Central Composite and Box Behnken site selection designs

regression. The ”D” in ”D-Optimal” comes from the approach it uses to minimize the determinate of the design matrix, $\mathbf{X}$ from Equation 2.5 [50]. The result is minimal error in the regression coefficients. This is opposed to the **I-Optimal** (or IV-Optimal) approach, which minimizes the average prediction variance over the resulting model [50], [54]. The D-Optimal approach handles quality assurance by placing replicate points on the boundary of the test sample space to have the smallest error where the leverage is greatest.

The I-Optimal design is arguably as good if not better than the D-Optimal design, though the comparison in performance varies by test and modeling objective; it is often observed that when optimizing an experiment design for a low average variance across the model, the variance at the measured points performs on par with a D-Optimal approach [48]. Again, the selection between D-Optimal and I-Optimal depends on the experimenter's wish to increase precision in the model parameters or the in the model prediction [48]. There are other strategies and designs that optimize one aspect of the RSM over another that can be found in various resources on experiment design [48], [50].

For all of these designs, the design variables of interest are limited to some range of investigation. These ranges are then conventionally transformed and scaled to a range of ± 1. This is done with Equation 2.17, where x is the resulting factor level in scaled and centered units, ξ is the factor level in physical units, H is the physical value for $x = +1$, and L is the physical value for $x = -1$ [45].

$$x = \frac{\xi - \frac{1}{2}(H + L)}{\frac{1}{2}(H + L)} \tag{2.17}$$

One way to use these test designs is to divide the sample space into different sub-spaces. A single design could be used to sample from each of those sub-spaces, being appropriately scaled and located for each sub-range within each, or different designs could be used in different spaces depending on the expected response or any screening efforts previously made. For example, a simple FFD could be used in a linear region while a CCD is used in a region where the response is expected to be quadratic. This division of sub-spaces is not uncommon, and an example is discussed in Section 2.3.4.

Once space selection has been achieved using one of the above designs, measures can be taken to minimize the uncertainty with which the measurements will be measured. MDOE uses methods to help minimize the variance of a measured data set and to increase the precision in which results can be reported. Those methods include replication, randomization, and blocking.

Replication

Replication refers to the process of repeating measurements at ostensibly identical conditions and factor levels in order to assess the repeatability of an experiment, reveal any systematic variance in the data, and increase the precision in the repeated configuration. This is done by exploiting the $\frac{1}{n-1}$ factor in Equation 2.2; with an increasing number of points in a data set, the standard deviation of a normal

distributed number of points should decrease as that number increases and the mean value reported with greater precision. This is only true if the measured points are normally distributed without bias or systematic offsets and stable in time [40], [45]. If a repeated condition was measured at various intervals throughout a test but in the presence of some drift with time, the standard deviation of the repeated dataset would increase with each new data point. Both scenarios are demonstrated in Figure 2.22, where the replicate samples free from bias display much more precision and the replicates with bias have a larger deviation around the mean.

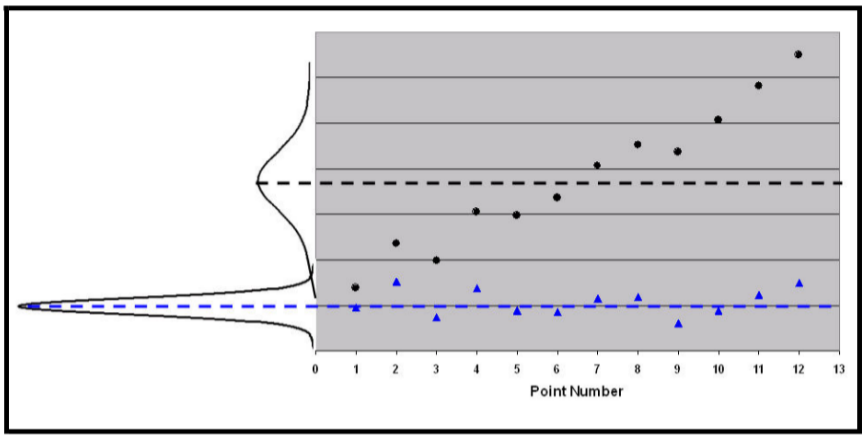

Figure 2.22: Replicate measurements with (black/square) and without (blue/triangle) unexplained systematic variation, which affects both mean and standard deviation [45]

This systematic bias can often be mitigated by the randomization techniques discussed below, and when the bias is accounted for, replication can generally be used to increase confidence in the measured data by decreasing the standard deviation and reducing the associated uncertainty to random error.

Randomization

Randomization serves as a way to uncorrelate the measured response from any systematic effects that may be present. Consider a wing being measured over a range of angles of attack. If the lift of the wing is measured as the wing is sequentially set at higher angles of attack, the resulting lift measurement is susceptible to be influenced by any other linear bias that might also be occurring. If a temperature drift with time corresponded in sync with the increase in lift, the temperature would become a covariant and result in the measured lift being measured as a function of angle of attack and time and not as an independent function of angle of attack alone. This is illustrated in Figure 2.23, where the left-hand plot demonstrates how the measured lift varies from the true response due to the temperature correlation.

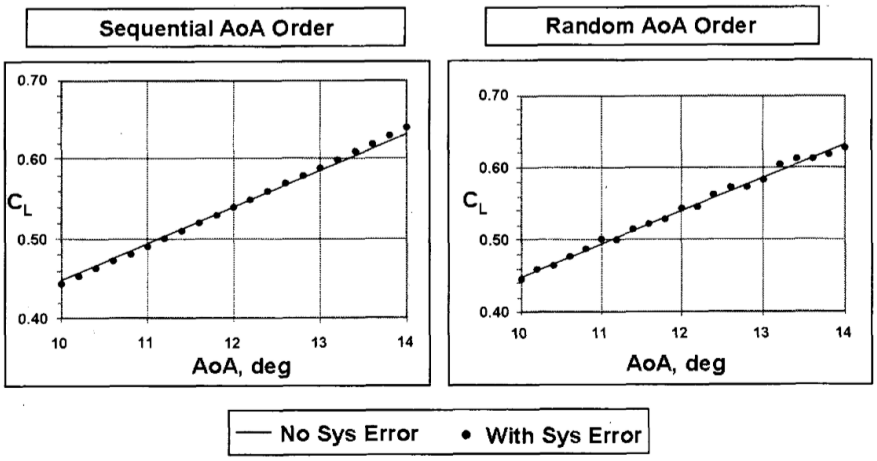

Figure 2.23: Lift coefficient measured as a function of angle of attack, where angle of attack levels are set sequentially and randomly [55]

By randomizing the order in which the angle of attack was measured, as shown on the right, the influence of the temperature drift is uncorrelated from the measured lift response, resulting in a better model fit for the true lift response. The systematic, unexplained variance from the left is reduced to random error on the right [55]. In a similar manner, the various independent variable levels that are changed in an experiment should not be sequentially changed but randomized instead. In so doing, much of the within-run systematic variance can be mitigated against and the experimental data can be made statistically independent.

Blocking

Blocking is yet another quality assurance tactic used to capture effects of systematic variance in an experiment before they are presented as the target response. Blocking refers to the approach of separating an experiment test matrix into blocks where a portion of similar configurations are tested together over the range of the independent variables, often with replicate runs or measurements taken where these blocks meet. For example, if a particular independent variable were to be tested at high levels and low levels, blocking would dictate that some of the high levels be tested soon after the low levels in a block, instead of all of the high levels being tested at once followed by the low levels. This blocking permits systematic variations between the two blocks to occur in a way that is not correlated to a design factor change, and when those systematic variations are large enough to be distinguishable in the presence of ordinary random error, a significant block effect can be identified [56].

An example of blocking is illustrated in Figure 2.24, detailing an experiment done in two blocks: one block in the morning and one block in the afternoon. The shift from the morning data set down to the afternoon data set is the systematic variance between the two blocks. Consider what would've happened without this blocking: all high levels might have been measured in the morning, and all low levels might have been measured in the afternoon, leading to an overall steeper slope and a lower y-intercept. Due to the blocked-off test matrix, the effect is variance is identified and automatically changed from impacting the slope and y-intercept to just the y-intercept. Though without correction the intercept would be affected, the relationship between the response and the factor change is correctly assessed in the face of the systematic error thanks to the blocking strategy.

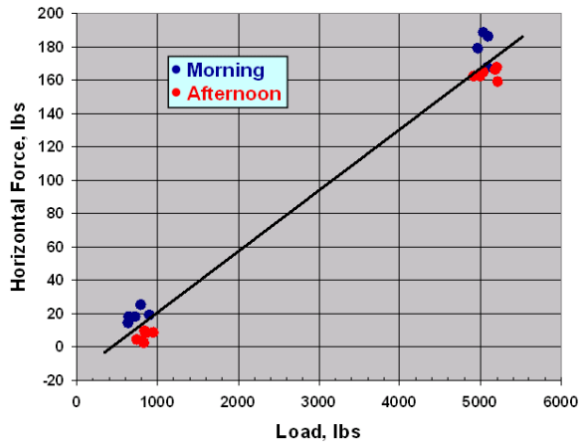

Figure 2.24: Unexplained systematic variation identified through blocking [45]

Including blocks in a test matrix can help guard against systematic variance introduced by changing wind tunnel staff over shifts, ambient conditions throughout a day or week, and major configuration changes made to the model. When blocking is used in RSM designs, the response model can explicitly include a term to account for the block effects, a block effect factor [56]. If this block effect is deemed significant, it can significantly improve the precision of the RSM model because a source of systematic variation in the measured response is now explained and resolved.

Analysis of Variance

The Analysis of Variance (ANOVA) is a statistical method used to partition the variability in a dataset into meaningful components, enabling the evaluation of the significance and adequacy of a model. In the context of RSM, ANOVA provides a way for understanding how much of the observed variation in the response is explained by the model and how much remains unexplained.

At its core, ANOVA decomposes the total sum of squares (SS_T) into components representing the variability explained by the model (regression sum of squares, SS_R) and the unexplained variability (error sum of squares, SS_E):

$$SS_T = SS_R + SS_E \tag{2.18}$$

This decomposition is key to various RSM model diagnostics, such as testing the significance of regression, assessing lack of fit, and quantifying random error [41], [44], [48].

The ANOVA method uses the F-statistic to compare variances associated with these components, facilitating hypothesis tests that guide model refinement. In this way, ANOVA helps engineers and researchers evaluate the significance of model factors, detect systematic inadequacies in the model, and ensure that the response surface appropriately describes the data.

ANOVA can be used to determine if a RSM model can explains a significant portion of the variability in the measured response, that is, if there is a substantial relationship between the model's factors and the measured observations. If there is such a relationship, then a change in a model factor can explain a change in the response. This comparison is formally constructed as a method to accept or reject a "null hypothesis", which is a general statement assumed to be true until further data proves otherwise [57]. The null hypothesis posed in the test of significance of regression is that no relationship exists between the model factors and the response, and the coefficients associated with each factor are equal to zero.

The F-statistic is used to test this null hypothesis and is calculated as the ratio of the variance explained by the model to the variance attributed to the residual error, and it is calculated using Equation 2.19 [41], [48].

$$F = \frac{\frac{SS_R}{p}}{\frac{SS_E}{n-p-1}} = \frac{MS_R}{MS_E} \tag{2.19}$$

In this equation, MS_R and MS_E refer to the Mean Square variance of regression and residual error, respectively, and SS_R is calculated using Equation 2.20 [41], [48].

$$SS_R = \mathbf{b}'\mathbf{X}'\mathbf{y} - \frac{\left(\sum_{i=1}^{n} y_i\right)^2}{n} \tag{2.20}$$

The resulting F-statistic from Equation 2.19 is then compared to the critical F-statistic for the null-hypothesis, which is found using a given α and corresponding confidence level $(1-\alpha) * 100\%$ and the degrees of freedom associated with SS_R and SS_E. The null hypothesis is then rejected if $F > F_{critical}$, and it is said that the RSM model explains the variability in the measured response with the confidence level used.

One application of calculating the SS_R is to use it to calculate a model's R^2 coefficient of determination, using the equation

$$R^2 = \frac{SS_R}{SS_T} = 1 - \frac{SS_E}{SS_T} \tag{2.21}$$

where R^2 indicates the percentage of the data's variability explained by the model [48]. To guard against overfitting a model, the adjusted R^2 or R^2_{adj} value is used, which is adjusted for the number of terms in the model [48]:

$$R^2_{adj} = 1 - \frac{n-1}{n-p}(1-R^2) \tag{2.22}$$

One application of ANOVA is testing the significance of an external factor in a constructed RSM model. If a blocking effect or drift in replicates are observed over the duration of an experiment, the test engineer could add a factor to the model to incorporate an uncontrolled factor, such as time or block number. Using ANOVA, the engineer would compare then the residuals of the model with and without the added systematic bias term, and if the change is significant, the engineer can say the added factor is significant in the model's predictive ability. Alternatively, if the change is not statistically significant, it is said the added factor's change to the model cannot be distinguished from the levels of residual error present in the model and data.

2.3.4. Examples

MDOE methods have been used with great success at NASA Langely for the past few decades, reducing the cost and length of their tests [43], [50]. An overview of 11 different Langley experiments using the MDOE approach showed that there was an overall improvement in efficiency when compared to OFAT; on average, 28% of the number of data points from OFAT were needed in the MDOE approach to reach the same results and only 42% of the time [46]. This analysis was done to justify the use of MDOE methods at the German Dutch Wind Tunnels (DNW), where an initial implementation of a D-Optimal test resulted in predictions for two times more than the OFAT case at 61% of the costs [46].

An X-31 model was investigated at the Langley Full-Scale Tunnel in partnership with Old Dominion University using RSM [58]. Using MDOE techniques - replication, randomization, and blocking - the test engineers characterized the aircraft's nonlinear performance over a section of the aircraft's flight envelope including various control surface actuation. In this study, a face-centered CCD (FCD) was used to adequately test the independent variables at five levels in each test matrix block. This allowed the engineers to evaluate the quality of fit of a model that included pure cubic terms in the response surface, a choice motivated by initial screening data that had been gathered to evaluate the testing limits. After regressing the most general form of the model using the measured data, the engineers used ANOVA to further refine the model and determine each term's significance. The final model was able to predict the baseline, test data with acceptable precision [58].

In another example, the design and testing of the F/A-18E/F Super Hornet's buffet attenuation device was conducted using MDOE techniques that reduced the needed configuration iterations from 70 iterations to 19 [59]. First, the MDOE approach was verified using the F/A-18C/D design data, which had

been gathered using 70 design iterations to find the optimal buffet attenuation device. Using the C/D data, a CCD was used to sample that data and create a quadratic regression model to identify both how the response varied with the design parameters and to predict the optimal design configuration. The optimal design found using the regression model of a sample of the past data agreed closely with the best results that were obtained with those original 70 configurations. The validated CCD test was used to gather the data needed to perform a similar analysis for the E/F buffet attenuation device design, needing only 19 iterations [59].

One other study employed MDOE/RSM techniques when investigating a cropped delta-wing in supersonic flow, and the model used is shown in Figure 2.25 [49]. This test divided the test design space into six different regions along the angle of attack and angle of sideslip ranges after having conducted a screening test to assess the expected response behavior. The motivation for splitting the design space into subspaces was to decrease the amount of data needed to adequately model the wing's response. For example, less data is needed to characterize a linear force response region than is needed to characterize a response in a quadratic or nonlinear region. The precision requirement for this study was set such that for any alpha-beta combination within the design space the predicted result by the resulting RSM and the physically measured data could not be distinguished from each other with at least 95% confidence. Selecting measurement points within the six subspaces using a CCD for each subspace, 72 total data points were gathered to fit second-order RSM models for each subspace. These models were then added piece-wise together to describe the response function over the entire design space. Through an analysis of the model quality and fit after the initial experiment, it was found that some of the subspaces required more data to fit higher, third-order terms to adequately model specific forces and moments. Careful analysis was done to reject and add different terms for the various subspaces for all force and moment responses until the models adequately fit the 26 validation data points that were measured but not used in the model creation [49].

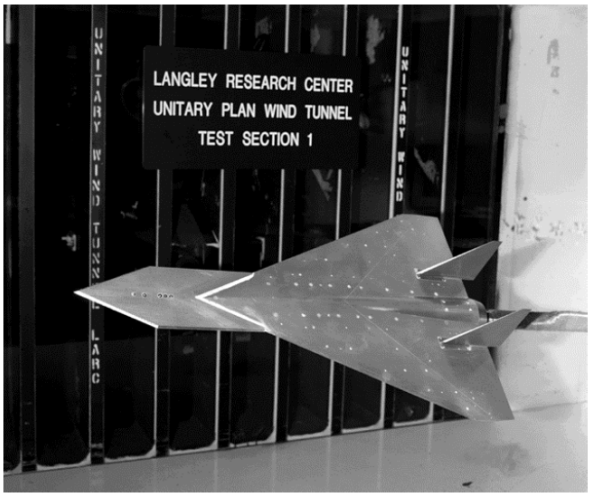

Figure 2.25: 65-degree cropped delta wing tested using MDOE/RSM techniques [49]

2.3.5. Challenges and Considerations

The way to make the most of a MDOE approach is in an iterative manner, and the initial setup of a modern experiment can be greatly aided by reference data if available [45], [46], [50]. As the purpose of a modern experiment is to fit a response model, knowledge of the general form of the model describing the physical behavior being tested will lend to an intelligent selection of the areas of investigation. Such an informed selection improves the accuracy of the resulting model, because areas that will have a strong leveraging effect on the rest of the model can be detected beforehand and mitigated against. One could theoretically use only one modern experiment to fit a very generic model, a model that had a high order with multiple interaction contributions, but fitting such a model with good accuracy requires a large volume of data. Doing a simple FFD or Fractional Factorial Design experiment can be a great tool for screening the design space to get an idea of the shape of the response if it is unknown and to identify interactions of interest between the design variables [42].

Though great advantages stand to be gained when using a MDOE methodology, the burden is no longer placed on gathering as much data as possible during the test and is instead placed on an intelligent formulation of the response model form before the test, an identification of the subspaces and the best site selection method for the anticipated response, and a careful analysis of the model's variance afterwards. To create a model that meets the stringent accuracy requirements most engineers desire, this process will often be repeated, with more than one experiment use to validate the model or improve it in areas where the prior analysis reveals unacceptable uncertainty.

For unconventional aircraft designs, this process can be difficult, especially if the design is shown to defy conventional or empirical prediction models. In such new territory, it is challenging to accurately identify the form of the response model without reference data or screening. With such reference data, however, one can start with a more informed model and use some techniques to optimize it.

For example, an algorithm using such techniques was developed by Ulbrich and implemented in Reichert's investigation [46], [60]. In the implementation, Reichert was able to reduce the terms in one part of the model from a 10-order polynomial to a simple polynomial shown in Equation 2.23, where the lift coefficient is expressed as a function of the regression coefficients (θ_i), angle of attack (α), and Mach number (M) [46]. The optimization passes the initial model through three steps: VIF test, P-Value Test, and R-Press test.

$$C_L = \theta_0 + \theta_1\alpha + \theta_2\alpha^2 + \theta_3 M\alpha + \theta_5\alpha^2 M \tag{2.23}$$

This optimization algorithm requires enough data to fit the highest-order model and evaluate the significance of different variables on the result of the response. Thus, given an unconventional, untested model, one could design a FFD test to screen the sample space and set up a generic model form [46], [60]. Using that form, they could perform a more in-depth investigation using a D-Optimal test matrix. After using the new data to fit their RSM, ANOVA could be used to assess the quality of the RSM and given the need for improvement, the RSM form could be optimized before informing a final investigation, using another test to fill in the gaps of the previous experiment [44], [53], [60]. At first glance, this might seem more complicated than running one investigative OFAT test, but the OFAT approach is inherently inhibited in its ability to comprehensively survey the design space and identify important interactions like the MDOE approach can.

3

Methodology

To meet the research objective and answer the research questions presented in chapter 1, a wind tunnel test was conducted and force and moment data was collected. Flap and spoiler parts were manufactured to study their effectiveness, and using the experiment data gathered, regression models were fit to provide insight and enable different analyses. This chapter documents the methodology used to design the wind tunnel experiment in sections 3.1 and 3.2 and the design of the flap and spoiler parts in section 3.3. Information on the facility, model, and test setup used is provided in section 3.4, and the chapter concludes with the methodology used to process the wind tunnel data and construct the response surface models in section 3.5.

3.1. Experiment Design Variables

For this experiment, different variables of interest were considered. The ones selected were the most relevant to answering the research questions and are discussed in this section. The variables pertaining to the configurations tested on the Flying V wind tunnel model are found in subsection 3.1.1, and the variables controlling the model orientation within the tunnel are discussed in subsection 3.1.2.

3.1.1. Configuration Variables

The different variable choices that control the model configuration are discussed in the next two subsections. These variables control the experimental factors that are the hardest to change during the experiment because they require the tunnel to be turned off to be changed and take significant time to vary relative to other variables.

Flaps (δ_f)

For the split flaps, it was decided to only vary the deflection angle, keeping the flap design parameters, such as chord, span, and aspect ratio, constant. This was done to keep the flap design as similar to the original flap designed by Eftekhar as possible, namely, the selected design Flap B in 0.8C R1 [4]. Varying just the flap deflection angle, measurements could be made that would reveal the relationship between flap effects and the model orientation.

The flap deflection angle, denoted by δ_f, had a range from 0° to 60° deflection, where the deflection angle was measured between the deflected flap's chord line and the flap chord line when flush with the surface at 0° or no deflection, as seen in Figure 3.1. This deflection angle was measured in the plane perpendicular to the flap's hinge line.

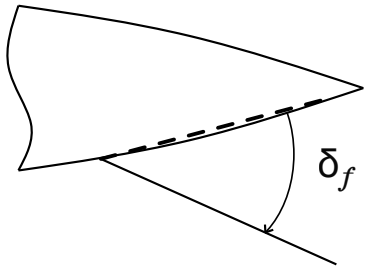

Figure 3.1: Positive flap deflection angle notation

It was decided to simultaneously vary both the left and right flaps, also referred to as the port and starboard flaps. This was done because it is unusual for the flaps to have different deflections from each other and because this choice reduces the number of independent variables in the experiment.

Spoilers (δ_{sp})

Like the split flaps, the experiment variable chosen for the spoiler was the deflection angle, keeping the spoiler design parameters constant in this experiment. The spoiler design was the same as indicated by Erdinçler, namely, the M AC 1 spoiler [5]. The spoiler deflection angle is generally notated by δ_{sp}. The four spoiler surfaces on the model, two on each wing, were split into three groups, with each group being described by a deflection angle variable.

The first group was controlled by the design variable $\delta_{sp,1}$, representing the simultaneous deflection of both the left and right inboard spoilers. The second group was controlled by the design variable $\delta_{sp,2\ell}$, representing the deflection of the left wing outboard spoiler. Last, the third group was controlled by the design variable $\delta_{sp,2r}$, representing the deflection of the right wind outboard spoiler. The subscript 1 denotes an inboard spoiler, and the subscript 2 denotes an outboard spoiler. When all three spoiler groups are deflected together to the same angle, the shorthand notation is δ_{sp}.

The spoiler surfaces were grouped as such for a few reasons. First, it was assumed that the inboard spoilers would not be asynchronously or asymmetrically deployed as these are closer to the wing root and primarily used together for lift dumping. Therefore, the two inboard spoilers were controlled by one variable. Second, the two outboard spoilers, while also contributing to lift dumping, could be used for roll control. By splitting the two outboard spoilers into variables that could be varied independently from each other, the model forces and moments could be described by symmetric and also differential outboard spoiler deflection. Third, by separating the inboard and outboard spoiler panels into different independent variables, any relationships or effects of an inboard spoiler on the outboard, or vice versa, could be measured and assessed.

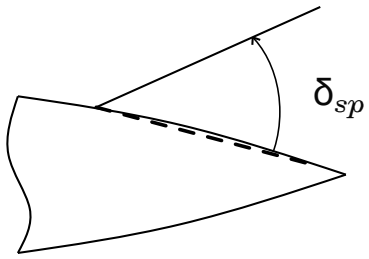

Figure 3.2: Positive spoiler deflection angle notation

Like the split flaps, the spoilers all vary from 0° to 60°, with the spoiler deflection angle being defined in the same way as the flaps, in the plane perpendicular to the spoilers' hinge lines. The spoiler deflection angle is measured positive when the spoiler is deflected upwards relative to the aircraft, as seen in Figure 3.2. Together, the one split flap and three spoiler variables make up the four hard-to-change configuration variables of this experiment. To aid in reader comprehension when referring to a given

configuration in this report, most plots are accompanied with a back view of the Flying V with the corresponding flap and/or spoiler deflections, like the one shown in Figure 3.3.

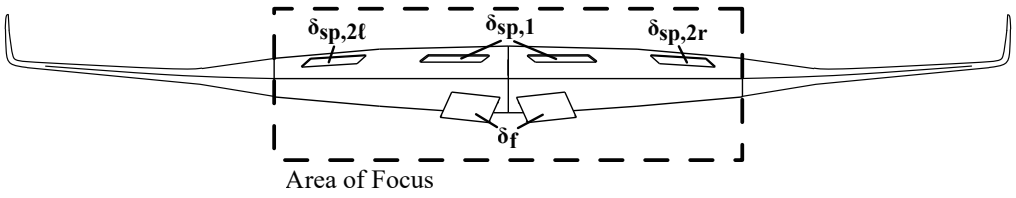

Figure 3.3: Full flap and spoiler deflection configuration on Flying V, back view

3.1.2. Model Orientation Variables

The Flying V model orientation within the tunnel is controlled by the pitching of the model and the yawing of a turn table. This provided the two orientation angles discussed below, which are treated as the model orientation variables.

Angle of Attack (α)

The first variable selected to describe the model orientation was the angle of attack, denoted by α, which describes the incidence the model has to the freestream velocity in the balance's x-z plane. The range for this independent variable was initially identified to be -3° to 25°, and it was divided into two subranges: -3° to 15°, and 15° to 25°. These ranges were selected to capture some important regions of interest:

- $\alpha = -2.5°$: The Flying V brake angle, or the angle of attack at which the Flying V's brakes are activated at landing [5]. This angle is influenced and informed by the spoiler effects, so having measurement data in this region is important for future analysis and predictions.
- $\alpha = 15°$: The earliest angle of attack at which the pitch break is observed when in sideslip. In order to adequately model the forces and moments, it was needed to split the measurement range at the point at which the behavior dramatically changes. For instance, it is easier to accurately model lift with a linear range before stall and a quadratic range around stall instead of using one function to describe the whole range [46], [49].
- $\alpha = 25°$: The highest expected angle of attack for the Flying V in normal flight conditions is around $\alpha = 20°$, but an upwards gust, especially at low speeds as in takeoff and approach conditions, could cause the angle of attack to increase past that. Thus, it would be helpful to have data up to a higher α, namely, 25°, in order to have data with the spoilers and flaps to predict different behaviors.

However, it was discovered that the model installation available could only pitch the model either from 0° to 30 ° or from -15° to 15° due to the limited range in the universal joint in the aft strut. Because there was no interest in the range below -2.5° angle of attack, the majority of the desired information lay in the first range. Thus, the model orientation variable α was limited to the range 0° to 25°.

Angle of Sideslip (β)

The second orientation variable was the angle of sideslip, denoted as β. Sideslip is defined as the freestream velocity's incidence with the model on the horizontal plane, defined as positive when the aircraft's nose is pointed to the left of the oncoming air. This was an important variable for this experiment as the research questions in chapter 1 ask how the model forces and moment change with the other five experiment variables and then how those relationships vary with changing angle of sideslip.

The range for this variable was from 0° to -15°. The motivation for this range comes from two considerations. The maximum sideslip angle is dictated by regulation as the maximum angle at which the aircraft must exhibit lateral-directional stability [39]. This angle is derived from the stall speed in

landing configuration, as shown in Equation 3.1. As spoilers and flaps are typically used for take off and landing, it was deemed important to gather data to evaluate the Flying V design against regulation requirements for these conditions. With the current landing predictions, the maximum sideslip angle needed is shown to be $\pm$13.5°, but to give margin in case of future improvements, the maximum angle tested during this experiment is -15°.

$$\beta_{max} = \arcsin(\frac{30}{1.13 \times V_{SR1}}) = \arcsin(\frac{30}{33.05}) = 13.5^\circ \tag{3.1}$$

Rather than vary the angle of sideslip from -15° to +15°, it was decided to make an assumption of symmetry in the model and only measure negative β. The negative sideslip was selected to enable comparisons to past tests where only the negative sideslip was measured. Choosing to measure only the negative sideslip was also done to ensure the research questions could be answered even if the experiment was not fully completed. A subset of the planned measurements allow for a simple factorial analysis, which show how a response changes when the experiment variables change from a low to a high value. If the low and high values of β correspond to $\pm$ 15 or $\pm\beta$, then little could be said about how the response changes with β because the conditions would be close to symmetric for a factorial analysis. If instead a range of 0° to -15° was chosen, the factorial analysis would be done with non-symmetric conditions and allow for the research questions to be answered if all planned measurements were not gathered.

Together, the angle of attack and angle of sideslip experiment variables describe the variation of the model orientation in the wind tunnel needed in order to answer the research questions. These experiment variables are much easier to change than the configuration variables because they can be changed in a matter of seconds while the tunnel is still on. The exact angle values selected for testing was indicated by the space selection design chosen in subsection 3.2.3, but the values were rounded to the nearest 0.5 value to guard against operator error and typos when setting the model orientation in the tunnel.

Other possible variables, such as the freestream velocity or dynamic pressure, trip strip locations, rudders, and model roll angle were not deemed necessary to answer the research questions, thus each of these values were fixed or not present in this experiment.

Notably, the freestream velocity was fixed and not used as an experimental variable. This was because the research questions do not consider the changes due to changing Reynolds number. This is also motivated by the fact that the Reynolds effect of the Flying V is not yet well understood, so little could be done with data gathered by changing the freestream velocity anyways. As a result, this value was fixed at a value previously tested, $V_\infty = 35$ m/s, $Re \approx 7.8 \times 10^5$.

3.2. Test Matrix

The test matrix designed for this experiment took considerable planning, analysis, and tradeoffs. In the following subsections, a discussion on the screening of past experimental data is given in subsection 3.2.1, followed by the test matrix design strategy and design constraints in subsection 3.2.2. The trade study done to determine the final test design is presented in subsection 3.2.3, followed by subsections on special considerations added to the test matrix, such as the static tares in subsection 3.2.4, flow angularity assessment in subsection 3.2.5, and the planned validation runs in subsection 3.2.6. The final test matrix overview is included in Appendix A.

3.2.1. Screening Data

Data from previous tests is incredibly useful in planning an experiment with MDOE techniques. Fortunately, data from a previous experiment with the same Flying V model conducted in the LTT was available for analysis and screening. This data, which was purely a function of angles of attack and sideslip, was used to screen the sample space and the measured responses to anticipate what form the responses take and what ranges and subranges would be best for the present experiment. An aircraft's forces and moments are largely functions of the orientation angles, and most control surfaces and high lift and lift dumping devices effectively shift these functions up or down, left or right. Screening data, then, can significantly improve the effectiveness of a test design when using MDOE techniques,

especially because the test design is determined by the maximum order of the polynomial describing a measured response.

From the screening data, it was seen that a change in response behavior was generally seen across the forces and moments as early as around angle of attack $\alpha = 15°$ when at the maximum sideslip, as seen in Figure 3.4. Though there was arguably a sharper change at the pitch break location at zero sideslip, it was important to take the smaller angle of attack as the boundary. This informed the decision to split the angle of attack variable range into two subranges as discussed in subsection 3.1.2, divided at $\alpha = 15°$. The existing data was also used to fit the forces and moments as functions of angles of attack and sideslip. This informed the minimum number of unique data angle combinations needed to best fit responses over each range.

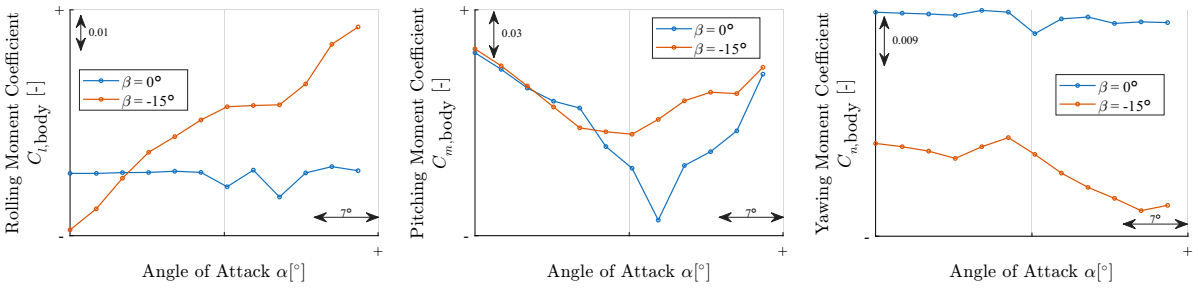

(a) Screening data for rolling moment coefficient

(b) Screening data for pitching moment coefficient

(c) Screening data for yawing moment coefficient

Figure 3.4: Screening data angle of attack sweeps for body-axis moments

For example, it was found that the maximum order of polynomial needed to fit the drag coefficient over the upper range of angle of attack was a fourth order polynomial. The reason for this higher order is likely due to the incorporation of sideslip angle and the vortex lift generated over the Flying V, whereas the classical drag equation only accounts for parasitic drag and drag due to lift and assumes symmetric and attached flow. Using the equation described in Equation 2.8, it was found the minimum number of points needed to fit this fourth-order polynomial was 15. This maximum polynomial order was shared with other models fit to the other forces and moments across both subranges, so this was taken as the minimum number of unique angle combinations for each α subrange. The process and results of fitting the screening data will be discussed further in chapter 4.

3.2.2. Split Plot Test Design

Using MDOE techniques, the order of the independent variable combinations to be tested during the experiment needs to be completely randomized. This is done to uncorrelate any source of systematic error from the measured response and reduce it to random noise, as discussed in subsection 2.3.3. However, this requirement poses difficulties in configuration testing, which is often done in wind tunnel testing. Such a complete randomization of the order of the experiment would result in the wind tunnel model configuration being changed with nearly every data point measured. This is only feasible with remotely actuated control surfaces, where the configuration variables could be changed while the tunnel remains on. Fortunately, there is a strategy within the MDOE framework to handle this randomization constraint when remote surface actuation is not available. This strategy groups together the measurements made with a common configuration into blocks and then randomly arranges the order of these distinct configuration blocks, as is illustrated in Table 3.1. This approach is called a “split plot” design [61].

A split plot design categorizes experimental variables into two types based on how easily they can be changed during an experiment: *hard-to-change* and *easy-to-change*. In this experiment, the flap and spoiler deflection angles were hard to change, while the model orientation angles were easy to change, as they could be adjusted without shutting down the wind tunnel.

In split plot terminology, each unique combination of hard-to-change factor levels belongs to a whole plot, and the corresponding variables are referred to as whole plot factors. Measurements taken under a given whole plot are called subplots, with the easy-to-change variables known as subplot factors.

Fully Randomized				Split Plot			
α	β	Config	Description	α	β	Config	Description
0°	-1°	1	flaps down	0°	-1°	1	flaps down
0°	-1°	0	clean	1°	1°	1	flaps down
1°	1°	2	spoilers up	-1°	0°	1	flaps down
0°	1°	3	flaps and spoilers	0°	1°	3	flaps and spoilers
0°	1°	0	clean	1°	0°	3	flaps and spoilers
0°	1°	2	spoilers up	0°	-1°	0	clean
1°	-1°	0	clean	0°	1°	0	clean
1°	1°	1	flaps down	1°	-1°	0	clean
-1°	0°	1	flaps down	1°	1°	2	spoilers up
1°	0°	3	flaps and spoilers	0°	1°	2	spoilers up
1°	0°	2	spoilers up	1°	0°	2	spoilers up

Table 3.1: Example fully randomized test design and split plot test design

Figure 3.5 illustrates this split plot structure using a CCD design with two whole plot and two subplot factors. Boxes represent different combinations of whole plot factor levels (Z_1, Z_2), while dots indicate the measurements taken at various subplot factor settings within each whole plot.

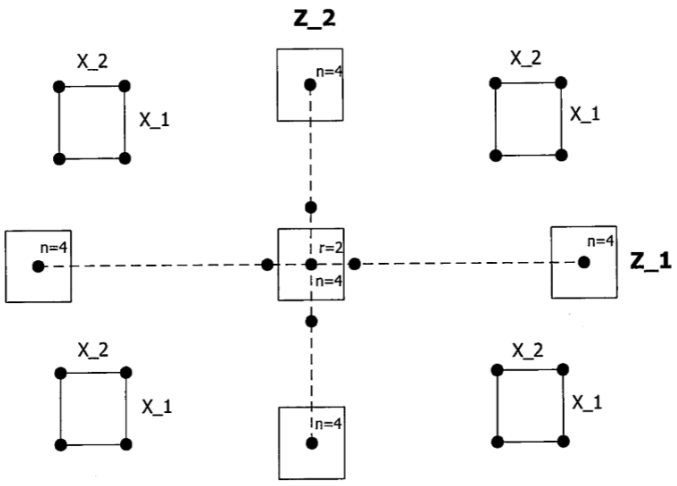

Figure 3.5: A Central Composite site selection Design used in a split plot experiment with two hard-to-change factors (Z_1, Z_2) and two easy-to-change factors (X_1, X_2). $n = 4$ indicates 4 measurements and $r = 2$ indicates 2 replicates of the whole plot [62]

While the split plot design respects the time constraints a configuration experiment presents, it does allow for block effects to be associated with each configuration grouping. These unwanted effects can be mitigated, though, by analyzing the measurements with a mixed effects model and Generalized Least Squares instead of using Ordinary Least Squares. The OLS regression assumes every point is measured with the same independently distributed experimental error, but introducing block effects invalidates this assumption and thus requires another analysis approach, as discussed in subsection 2.3.1.

Following MDOE techniques, the test matrix designs considered were all randomized in their whole plot and sub plot run orders. In this way, precautions were made against the presence of systematic errors and biases in the experiment, whether or not those errors would be present or significant. It was clearly seen that randomizing the run order increased the experiment execution time, often adding around 10 hours to the time estimate, but this was deemed necessary to improve the accuracy of the results. The constrained randomization of the test design can be seen in Table A.2, where the order of the whole

plot index groups in the 'WP' column is randomized and the order of the AoA and AoS columns are randomized within each WP group.

Balanced Split Plot Design

A split plot design can further be improved if it is balanced. This is demonstrated by Vining, Kowalsky, and Montgomery where they show that the result of a balanced split plot analysis using generalized least squares is equivalent to when that same design is analyzed with ordinary least squares [62]. This enables a split plot test design to be analyzed with simpler methods, so balanced designs were considered in this experiment.

The requirements for a balanced split plot are as follows.

1. Every whole plot has an identical number of sub plot runs
2. The subplots in a whole plot are orthogonal to each other
3. The axial whole plot blocks have only subplot center runs
4. The center whole plot blocks have either only subplot axial runs or only subplot center runs

Taking a normal quadratic MDOE test design and organizing it into whole plot and sub plot factors, a split plot design can be created. Then, by adding runs or measurements to each whole plot, the target number of sub plot runs can be met while also ensuring the resulting whole plot is orthogonal. To this end, MATLAB's `cordexch` and `doptimal` functions were used to generate the new sub plot runs for each whole plot lacking the target number of measurements. Balanced split plot test designs were considered next to traditional designs in the trade study discussed below.

3.2.3. Trade Study

Using a collection of MATLAB scripts developed during the duration of this project, a variety of different MDOE test designs were compared and considered. Given quadratic behavior of the expected responses, CCD and Faced CCD designs were considered, along with different variations. The different variations included the default design, balanced designs, composite designs with an extra FFD superimposed to add more data points, and designs with different variable ranges.

Each split plot design was randomized such that the order of the whole plots was random and the order of measurements within each whole plot was randomized. This randomized design was then fed into a time estimator script. This randomization is in keeping with MDOE techniques and was important in accurately estimating the time required for each experiment design.

Using a script, the time needed to execute each design was estimated using inputs like sample duration time, time needed to turn the tunnel on and off, time needed to orient the model, time needed to change configurations, and more. The parameters used can be seen in Table 3.2. The designs that would take longer than the allotted time slot were disqualified, and the designs that could be executed in the given time were considered.

Parameter	**Value**	**Units**	**Parameter**	**Value**	**Units**
Dwell Duration	10	sec	Time to Turn On Tunnel	5	min
Wind-Off Dwell Duration	3	sec	Time to Turn Off Tunnel	2	min
Sample Duration	10	sec	Time to Change One Surface	10	min
Pitch motor speed	0.5	$\frac{\text{deg}}{\text{sec}}$	Start-of-Day Margin	15	min
Turntable motor speed	0.25	$\frac{\text{deg}}{\text{sec}}$			

Table 3.2: Time estimate parameters

A trade study was done comparing the advantages and disadvantages to the different designs, beyond considering the time estimate alone. Table 3.4 highlights the primary parameters considered and pro-

vides the motivation for the selected design. Using the time estimating script, it was easy to see that having more than two subranges in the model orientation variables greatly extended the test duration past the allotted 4.5 days and were thus not considered in the trade study results below. The ”inscribed” CCD style denoted in Table 3.3 and Table 3.4 refer to a CCD design entirely constrained by the factor bounds with its axial points lying on the ± 1 factor levels. The unit square in the inscribed CCD is then scaled down, by $1/\sqrt{2}$ in the case of Figure 3.7.

CCD Style	Extra Pts	WP Factor Levels	SP Factor Levels	Unique SP Pts
Faced	No	3	3	9
Faced	Yes	3	5	13
Inscribed	No	5	5	9
Inscribed	Yes	5	5	13

Table 3.3: First trade study: faced and inscribed Central Composite Design (CCD) test design types for a variety of Whole Plot (WP) and Sub Plot (SP) factors

Design	Extra Points	Balanced	Number of Measurements			Time
			Unique Combos	Unique SP Combos	Total	
1	No	No	49	9	98	32.3 hr
2	Yes	No	109	13	222	35.5 hr
3	No	Yes	112	9	224	37.5 hr
4	Yes	Yes	168	13	336	40.1 hr

Table 3.4: Final trade study: comparison for inscribed Central Composite Design (CCD) test design types for a variety of different added Sub Plot (SP) and Whole Plot combinations

Selected Design

It was found that Design 2, the inscribed CCD design with the superimposed extra FFD points added, was the most promising design due to the following reasons.

First, the CCD design included five levels for every design variable compared to the plain FCD design. This can be seen in Table 3.3. Extra levels could be easily added to the subplot factor levels in the FCD design, but adding extra levels to the FCD whole plot levels dramatically increased the test design size. The CCD design explores the design space more efficiently in comparison. It was seen in the screening data that five levels in the whole plot factors were needed to best fit and describe the flap and spoiler effects. When contrasted to the three levels offered by the Faced CCD, the regular CCD design would provide more accuracy and detail in the measured response over the configuration design space.

Second, when looking at Table 3.4, the number of unique data points available in Design 2 allows the design to fit a maximum order polynomial of three degrees exactly. This can be seen by observing Table 3.5, where the ”Points needed”, p, indicates the minimum number of points needed to fit a polynomial of k different factors with all terms up to the d^{th} order, as calculated by Equation 2.8. In the MDOE context, this is not the minimum number of unique data points needed to be collected in an experiment, however. In order to meet uncertainty levels set in the design, a specific number of points greater than the minimum p is needed to increase the model’s precision. This is referred to as the ”scaled” number of points needed n, as mentioned in subsection 2.3.1, and it is also shown in Table 3.5. These additional points can be replicate points. Finally, the table indicates the number of points needed for each subspace. For this experiment then, which features two subranges, the total number of points is doubled, resulting in the final row of Table 3.5.

It can be seen, then, that Design 2 has sufficient unique points to fit a 2nd and 3rd order polynomial and enough total points to meet the scaled 2nd order requirement but not enough total points for the scaled 3rd order requirement. In contrast, Design 4 does have enough total points to meet the scaled criteria for a full 3rd-order polynomial in six factors over two subranges. However, Design 4 takes too long to execute and is not a feasible design.

From the screening data, it was seen that a maximum of a 4th-order polynomial fitted the data with reasonable success. The minimum number of points needed for this 4th-order polynomial with just two factors, angle of attack and angle of sideslip, can be seen from Table 3.5 as 15 unique points for each subspace. From Table 3.7, it can be seen that Design 2 has 13 unique points in its sub plot factors in each subspace. This indicates that Design 2 could fit almost up to a full 4th-order in the subspace factors, better than Designs 1 and 3 can. As it is not expected that the flap, spoiler, and their interaction effects will feature high quadratic terms past the 2nd-order, it is a satisfactory trade off that Design 2 includes enough data points to fit more than a full 2nd-order polynomial across all six experiment factor and enough extra points to provide more resolution in the subplot factors, where higher polynomial terms are expected.

Polynomial Order (d)	2	3	4	4
Factors (k)	6	6	6	2
Points Needed (p)	28	84	210	15
Points Needed Scaled (n)	46	137	342	25
Total Points (n)	92	274	684	50

Table 3.5: Data points needed to fit different polynomials

Third and last, Design 2 comes closest to the 36 hour test duration budget allotted to this experiment. Design 3 is slightly longer, has slightly more data points, and has the advantage of being balanced and analyzable with OLS, but it has the significant disadvantage of having less resolution in the subplot factors. Design 1 has a lower test time as it features less total data points than Design 2. Design 2 can be seen to be much more time efficient than Design 1 by fitting in more data points. Looking at the following time estimate chart in Figure 3.6, it was seen that the same number of time-intensive configuration changes were planned in Designs 1 and 2, but more wind-on time was allocated in Design 2, resulting in its better efficiency and final selection.

In the end, Design 2 was modified slightly: it was found that modifying the core CCD points such that the corner points composed a 2^{6-1} Fractional Factorial Design improved the time estimate and provided more margin. The Resolution V 2^{6-1} design contains a subset of the points normally in a FFD, but with this subset, the main and two-way interaction effects are unconfounded and can be accurately identified.

The time estimate chart and the data site selections associated with the selected design can be seen in Figure 3.6 and Figure 3.7. Using these diagrams, the test design could be double checked, the sensitivity to different parameters such as the sampling time could be assessed, and the number of factor level combinations could be seen. Figure 3.6 was transformed into a checklist to assess test progression, allowing the wind tunnel operators to check if the test was ahead or behind of schedule during the test execution. Figure 3.7 shows the each of the six experimental design factors plotted against each other, where X1 through X4 represent the flap, inboard spoiler, left outboard spoiler, and right outboard spoiler deflections respectively and X5 and X6 represent the angle of attack and angle of sideslip respectively.

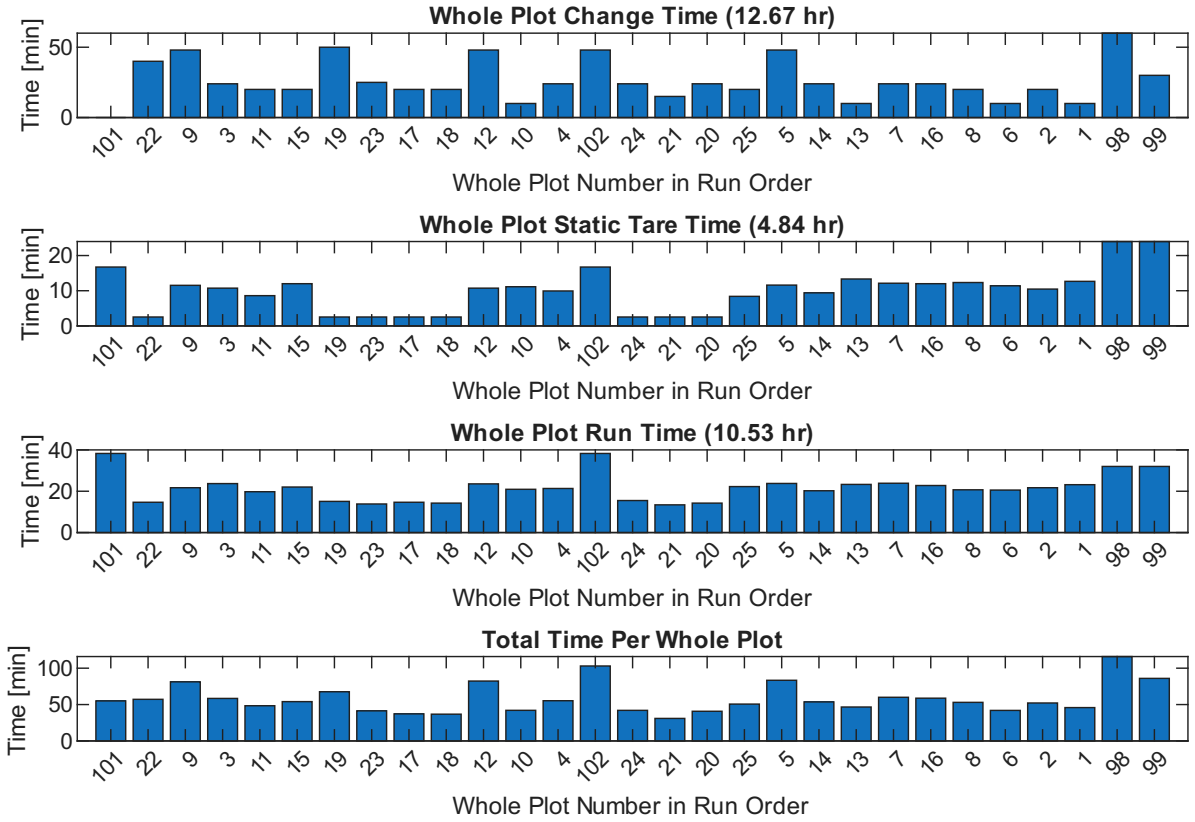

Figure 3.6: Time estimate chart for Design 2 with randomized whole plot order. A whole plot is a single configuration of hard-to-change variables

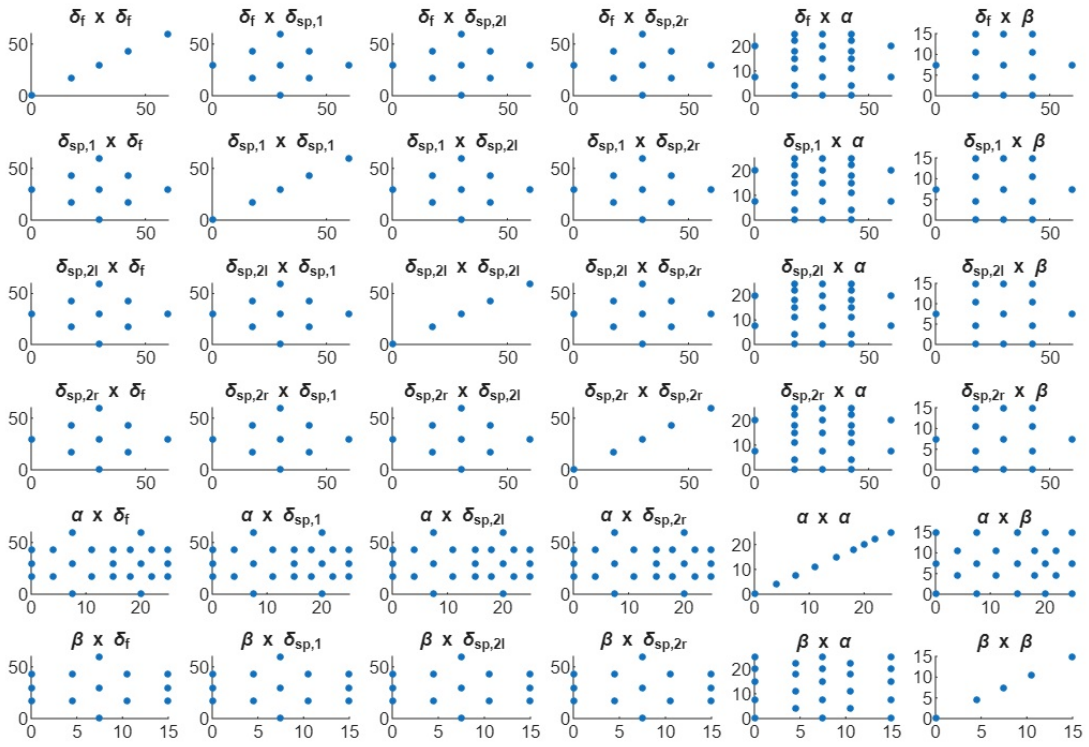

Figure 3.7: Experiment design factor level combinations for Design 2

3.2.4. Static Tares

In addition to the primary measurements planned for the fitting of the response surface models, extra measurements were planned for the experiment to support the data analysis. Importantly, 'static tares' or sweeps of tare data were measured with the model installed and the wind off. They are so called due to being measured in wind-off or 'static' conditions. These wind-off measurements were planned for each unique (α, β) combination and served as measurements for the model weights and moments at each orientation. When a measurement was later taken at each unique orientation with the wind on, that measurement would essentially be a sum of the forces and moments acting on the model by the wind and the forces and moments acting on the model due to its weight. As only the forces and moments due to aerodynamics are of interest, it was needed to measure the model weight forces and moments alone to allow this tare to be done in postprocessing.

These static tares were planned not only for every unique orientation but also every unique model configuration. Adding surfaces to the model changes the weight and the weight distribution of the model, so a static tare measured for one configuration doesn't necessarily apply to a second configuration. Fresh static tares were also planned for the start of each major block of testing, whether at the start of day or after the lunch break. This was to tare the effects of the balance settling or shifting whether due to temperature, time, or some other unknown and uncontrollable variable. These static tares were incorporated in the above test designs and their time estimates.

3.2.5. Flow Angularity

Some of the data planned to be measured with the wind on was not intended to be used for the response surface model fitting. A subset of this data belonged to the flow angularity runs. Every tunnel has some characteristic flow angularity in its test section. This is because every tunnel is manmade and susceptible to slight error in the manufacturing or even damages or strain due to operations that slightly shifts the direction of the test section flow slightly from the test section centerline. This offset or angularity of the test section flow means that a model measured at mechanical 0° might actually experience wind at some incidence and side slip. Furthermore, wind tunnel models themselves are susceptible to asymmetry and manufacturing imperfections. Combined, these imperfections require flow angularity corrections if deemed significant.

Barlow, Rae, and Pope suggest that in most cases, the upflow component of the tunnel flow angularity is the most critical to assess because it will affect the accuracy of the drag and lift measurements [40]. The way to assess this upflow is to simply run from zero lift to stall both upright and inverted. However, inverting the model was not possible in this experiment, so the upflow component was neglected.

As this experiment seeks to assess side-slip effects, the sideslip angularity was important to know. To ensure repeatability and cross-test comparisons, the flow angularity in sideslip was assessed at the start of the experiment and used to correct the reported orientation angles. This was done by finely sweeping the model in sideslip and in deltas of 0.1° from β =-1° to β =+1°. In so doing, the sideslip angle at which zero sideforce was measured could be identified. The difference from mechanical zero to this identified angle is the flow angularity correction, and this correction can be applied to the angles associated with each measurement in the post-processing.

3.2.6. Validation Runs

As a final component of the test matrix design and planning, validation runs were incorporated throughout the test design. These validation runs would gather data to be exclusively used to test the regression model results fitted by the main wind tunnel test data. The validation runs themselves were not to be used in the model fitting. It was important to chose validation sweeps that would include points beyond that which was directly tested. This allows the model's interpolative ability and accuracy to be tested and validated. Two validation configurations were initially chosen, and two alpha sweeps and one beta sweep per subspace were planned per configuration. In this way, the validation runs would be compared to the model predictions at some angles not tested and some configurations not tested.

These two validation blocks were placed one at the beginning of the test and the other halfway through the test. The order of points within the validation sweeps were randomized, and the time needed to complete each validation block was included in the above test design time estimates. In the end, four more validation configurations were tested during the experiment due to the extra time gained. The

configurations tested and the results of the validation runs are discussed in chapter 4.

3.3. Part Design and Manufacturing

To test the flap and spoiler effects, flap and spoiler surfaces needed to be manufactured. Using the relative dimensions and locations designed and selected in past research, the surfaces were scaled and designed to interface with the 1.84% full-span FTT Flying V model. The design was done using the 3DEXPERIENCE suite. The design and manufacturing process for the flaps and the spoilers are discussed below in subsection 3.3.1 and subsection 3.3.2. The design of alignment blocks used to aid in the surface positioning on the model is also discussed in subsection 3.3.3.

3.3.1. Flap Design

The previous split flap design consisted of a flat aluminum parallelogram plate supported by 3D printed offset blocks. The plate was taped to the blocks, and the assembly was taped to the old 4.8% half-span Flying V model. Due to the difference in Flying V model geometry, adjustments needed to be made to the flap design.

Most notably, the LTT model surface where the flap needed to be placed was not the same shape as the OJF model. A piece was designed to interface with the concave LTT model surface and serve as an offset block to support the flap surface. Due to the treatment applied to the LTT Flying V model's surface, special care was taken to prevent the aluminum flap surface from touching or scratching the model surface. Material was removed from the printed support block to account for the thickness of the tape that would be used to secure the flap to the model surface.

The flap surface itself was simplified to a flat plate that was cut from aluminum. This improved the strength and stiffness of the flap, provided a smoother surface finish, and minimized the amount of finishing work needed. Stiffeners were incorporated in the flap support design to better support this aluminum flap surface and prevent vibration at the thin trailing edge corner.

In keeping with the design from Eftekhar, the flap length was 20% of the chord, and the flap leading edge was positioned at the 80% chord line of the inboard trunk [4]. The flap trailing edge approximately extended to the wing trailing edge, though the simplified flat plate extended slightly beyond that. The flat plate cut for the 60° deflection was 2 mm thick, while the flat plates for the other deflections were cut from 1.5 mm thick aluminum. This difference in thickness was due to the limited availability of the 2 mm aluminum.

The 3D printed flap support design and the aluminum plate can be seen in Figure 3.8 and Figure 3.9. The design was made parametrically, allowing for the deflection angle to be changed with ease to make the different deflection blocks.

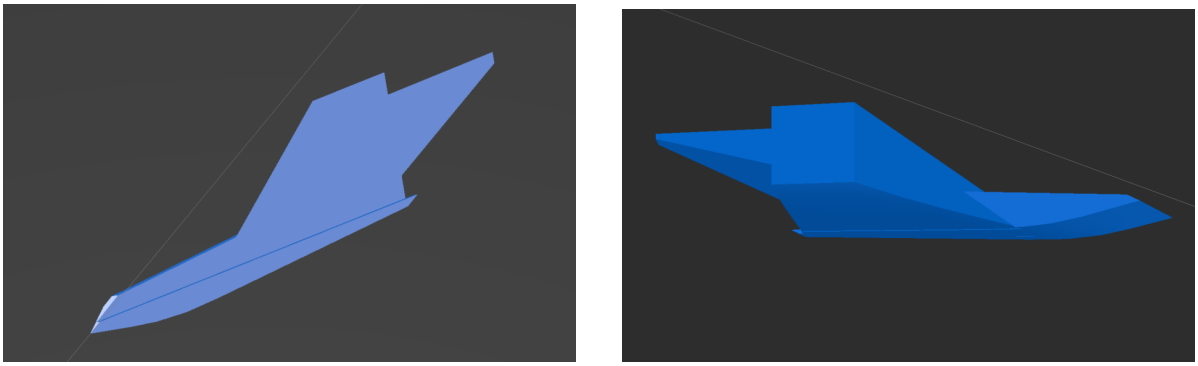

(a) 60° RHS flap deflection support - front view

(b) 60° RHS flap deflection support - back view

Figure 3.8: 60° RHS flap support design

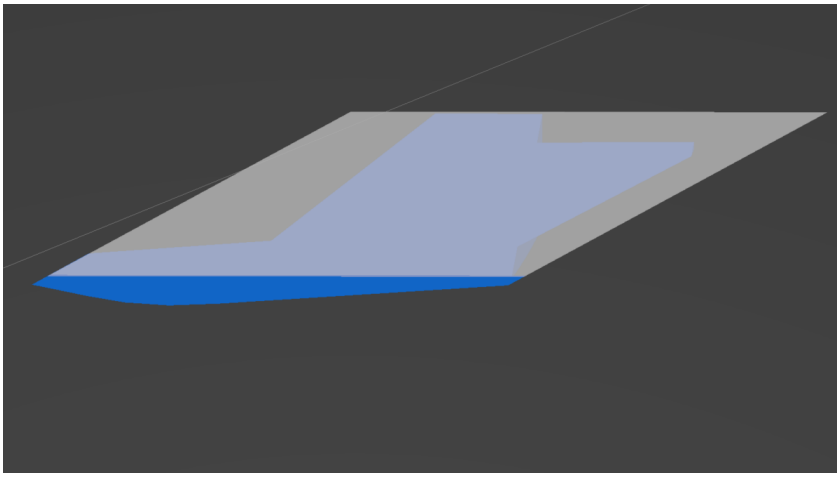

Figure 3.9: 60° RHS flap with flat plate, aluminum shown as transparent

3.3.2. Spoiler Designs

The final spoiler design decided upon in previous research consisted of two spoilers, one on either side of the engine, with their leading edge on the local 80% chord line [5]. The spoiler trailing edge stops at the local 90% chord line. Due to the resulting size when scaled to the smaller LTT model, the spoiler surface curvature was quite small and easily represented with a flat plate. Both inboard and outboard spoiler surfaces were thus simplified to a flat, rectangular aluminum plate with a 3D printed support for deflections. As with the flaps, the spoiler supports had material removed to account for the thickness of the tape between the support and the model surface and between the support and the spoiler plate.

Like the flap geometry, the 3D printed support served to protect the model surface from scratches and to also provide a snug fit between the spoiler and the curved model surface. In order to avoid interfering with the crossflow across the wing span, the area behind the spoiler was removed, leaving a few supporting arms onto which the aluminum plate was taped. This was done for all but the lowest deflection angle spoiler where, due to the shallow deflection angle, the supporting plastic block was so thin and small that it was infeasible to reliably manufacture with the available tools. In the case of the outboard spoiler, the aluminum surface of the spoiler was so small on the smallest deflection that it was more accurate to forgo the aluminum altogether and model the whole spoiler deflection out of PLA.

The chord of the inboard spoiler was 19.9 mm and the span perpendicular to the local chord was 152.2 mm. The chord of the outboard spoiler was 18.1 mm and the span perpendicular to the local chord was 110.6 mm. These dimensions were rounded to the nearest 10th of a millimeter after scaling from the original design to accommodate the machining precision available for the aluminum plates. Both inboard and outboard spoiler plates were cut from 1 mm aluminum.

The 3D printed spoiler support designs can be seen in Figure 3.10 and Figure 3.11. The designs were made parametrically, allowing for the deflection angles and other necessary parameters to be changed with ease.

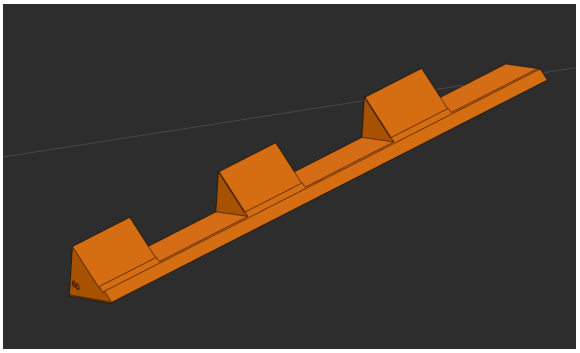

(a) 60° RHS inboard spoiler deflection support - front view

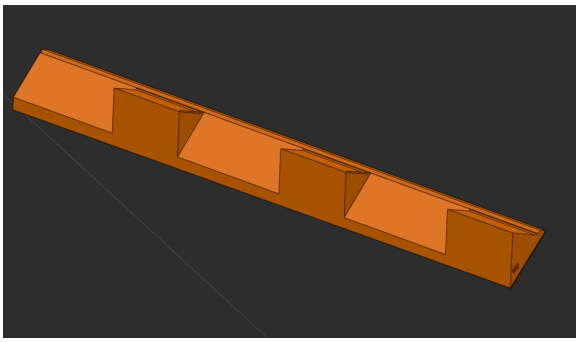

(b) 60° RHS inboard spoiler deflection support - back view

Figure 3.10: 60° RHS inboard spoiler support design

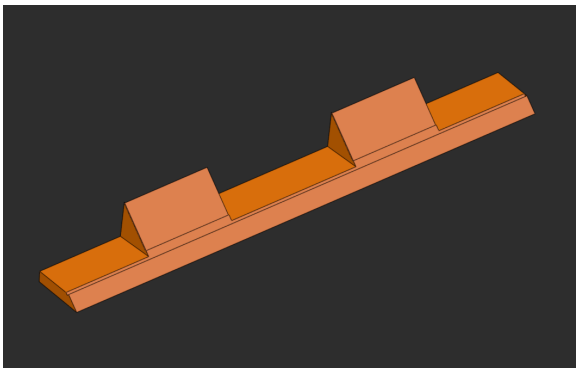

(a) 60° RHS outboard spoiler deflection support - front view

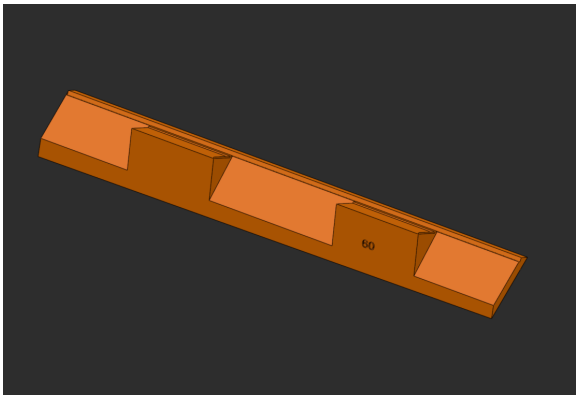

(b) 60° RHS outboard spoiler deflection support - back view

Figure 3.11: 60° RHS outboard spoiler support design

3.3.3. Alignment Block Designs

To quickly and reliably exchange the different deflection assemblies on the wind tunnel model between whole plot run blocks, different blocks were created to act as installation guides. By fitting the blocks along the model trailing edge, the blocks would have a specific and repeatable fit, aided also by aligning with different features on the model. Once positioned, the alignment blocks could be used to position and apply the flaps and spoilers to the model using double sided sticky tape.

3.3.4. Manufacturing and Assembly

The manufacturing of all 3D printed parts was done using the Prusa Original Mk3 and Mk4 printers in the TU Delft Shaping Matters Lab using 1.75 mm PLA filament and a 0.4 mm nozzle. For the aluminum flat plates, spare aluminum was cut to size using a variety of machines including a metal hand press and a plate shear machine. All parts, plastic and metal, were carefully finished and their edges sanded to ensure the model surface wouldn't be scratched. The flap and spoiler parts were finally assembled using strong double-sided sticky tape and dabs of superglue as needed. The finished parts can be seen in Figure 3.12.

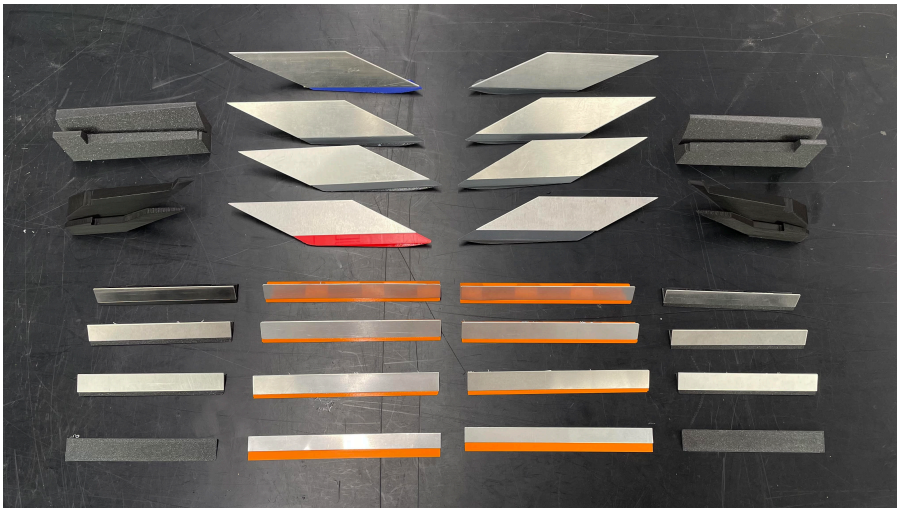

Figure 3.12: Assembled flap, spoiler, and alignment block parts for the 1.84% scale Flying V LTT model

3.4. Test Setup

The Delft University of Technology boasts a large number of wind tunnels that can test a wide range of conditions, from subsonic to hypersonic flow. For this experiment, the subsonic Low Turbulence Tunnel was used to gather the needed data. A description of the tunnel is given in subsection 3.4.1, the Flying V wind tunnel model is presented in subsection 3.4.2, and the installation and model set up is discussed in subsection 3.4.3.

3.4.1. Low Turbulence Tunnel

The TU Delft Low Turbulence Tunnel (LTT) has one of the world's lowest turbulence intensity levels of less than 0.07% at maximum speed. A wind tunnel's turbulence intensity is a measure of the smoothness and uniformity of the flow through a tunnel, and a low intensity level means that little experimental error is introduced by the quality of the tunnel's flow [40]. The LTT has an octagonal test section that is 1.8 meters wide and 1.25 meters high. The tunnel has 10 of these test sections that can be interchanged with each other, allowing a model to be prepared outside of the tunnel to improve efficiency. The maximum test velocity in the tunnel is about 120 m/s. The LTT is also a closed return wind tunnel and is also equipped with a cooling system to aid in temperature stability. The tunnel is equipped with a 6-component mechanical balance in addition to an array of other testing equipment for pressure readings, PIV, and hot wire anemometry [63]. A schematic of the LTT can be seen in Figure 3.13.

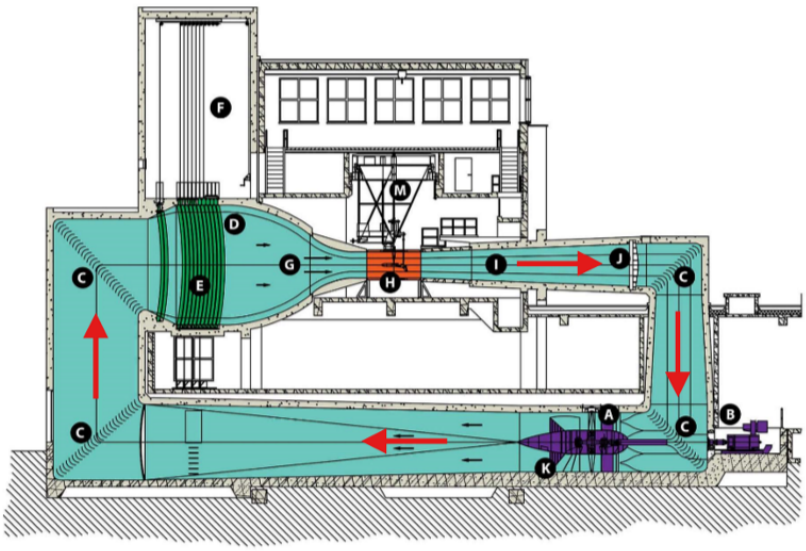

Figure 3.13: Schematic of the TU Delft Low Turbulence Tunnel. Image credit: Momchil Dimchev

3.4.2. The Full-Span Model

The full-span Flying V model was designed and manufactured for the LTT. It can be tested with either Küchemann wingtips or winglets, and its smooth and treated surface makes it suitable for flow visualization studies, like PIV and fluorescent oil flow. Additionally, different sections, such as the model nose, leading edges, and junctions can be removed and exchanged for different designs. The scaled locations and dimensions of the spoiler and flap parts are shown in Table 3.6. In the table, (x/c) represents the constant chord line with respect to the streamwise chord, $(x/c)_{loc}$ represents the constant chord line with respect to the local chord–which is perpendicular to the constant $c_{1/4}$ chord line, and $(y/b_{0.5})\%$ is the percent spanwise location with relative to the semi-span length. The flap chord is provided in terms of the streamwise chord, and the spoiler chords provided are perpendicular to their hinge line. The Inboard (IB) and Outboard (OB) Span Locations listed in Table 3.6 refer to the relative spanwise location of the most inboard or outboard point on the surface hinge line.

	Flap		Sp1		Sp2	
Parameter	**Value**	**Unit**	**Value**	**Unit**	**Value**	**Unit**
LE Length	112.3	mm	152.2	mm	115.4	mm
Chord	86	mm	19.8	mm	18.8	mm
LE Chord Line	0.8	(x/c)	0.8	$(x/c)_{loc}$	0.8	$(x/c)_{loc}$
TE Chord Line	1.0	(x/c)	0.9	$(x/c)_{loc}$	0.9	$(x/c)_{loc}$
Hinge Line Sweep Angle	62.2	deg	64.3	deg	58.8	deg
IB Span Location	1.65	$(y/b_{0.5})\%$	6	$(y/b_{0.5})\%$	28	$(y/b_{0.5})\%$
OB Span Location	10.4	$(y/b_{0.5})\%$	17	$(y/b_{0.5})\%$	38	$(y/b_{0.5})\%$

Table 3.6: LTT spoiler and flap dimensions and positions

A planform view of the model and the relative flap and spoiler locations on the model in Figure 3.14. The model geometry details are provided Table 3.7. The reference areas and lengths and the moment reference point specified in Table 3.7 are the ones used in the data processing, which is described in subsection 3.5.1.

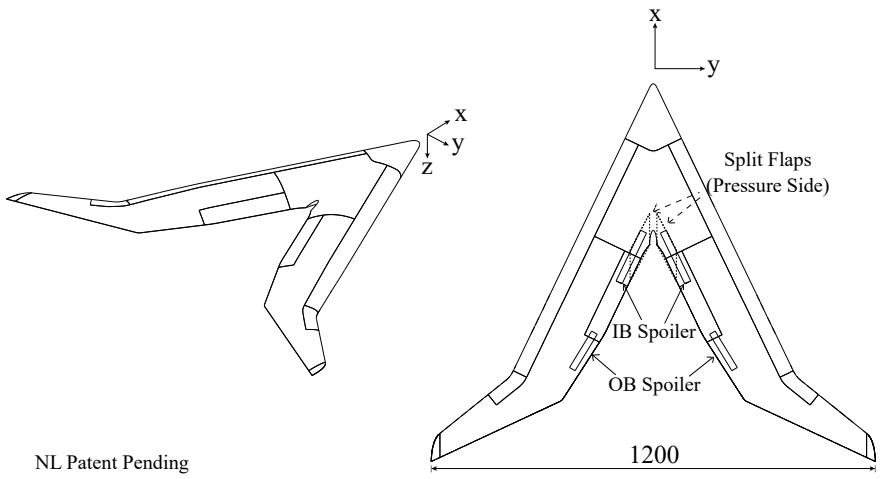

Figure 3.14: Split flap and spoiler locations on 1.84% Flying V LTT model with wingtips installed

Parameter	Value	Unit
Span (b)	1200	mm
Reference Area (S)	0.307	m^2
Reference point (x_{ref})	519	mm
MAC ($\bar{c}$)	338	mm
Scale	1.84	%

Table 3.7: Wind tunnel model specifications, based on the Flying V design by Laar [9][64]

3.4.3. Model and Surface Installation

The Flying V model was suspended from the LTT test section roof and connected to the LTT mechanical balance, which is located above the test section as seen in Figure 3.13. The model hinges on the two wing struts it hangs from, and the model pitch is controlled by the aft strut, as seen in Figure 3.15b and Figure 3.16.

Once installed, the model was mechanically aligned within the tunnel using a combination of a laser system and an inclinometer. Using a 3D printed piece that fit over the model nose, the model was aligned to the turntable with reference to a laser aligned with the tunnel centerline. The 3D printed nose block had an alignment guide line that was lined up with the laser. For the model pitch attitude, zero angle of attack was set using an inclinometer on the model, using again the 3D printed nose piece as a flat surface. In this way, the model was reliably aligned with the tunnel centerline at zero angle of attack and zero turntable yaw angle.

Important to note is that a horizontal fairing was installed in the wind tunnel downstream of the test section to allow for a traverse system for pressure measurements and PIV readings. Past results suggest that the fairing is far enough downstream to not interact with the flow over the Flying V in the test section. As a result, the presence of the fairing is assumed to be negligible in this experiment.

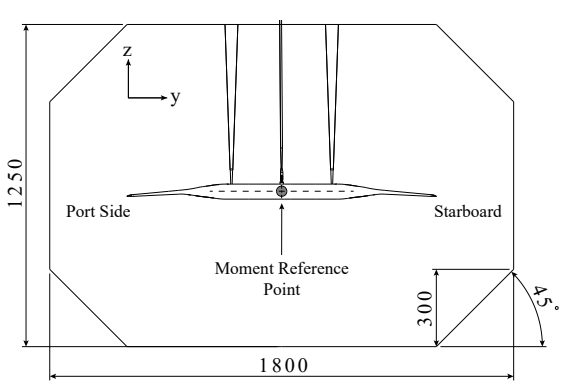

(a) Schematic of the LTT cross-section viewed downstream at $\alpha = 0^\circ$. Dimensions are given in mm. [65]

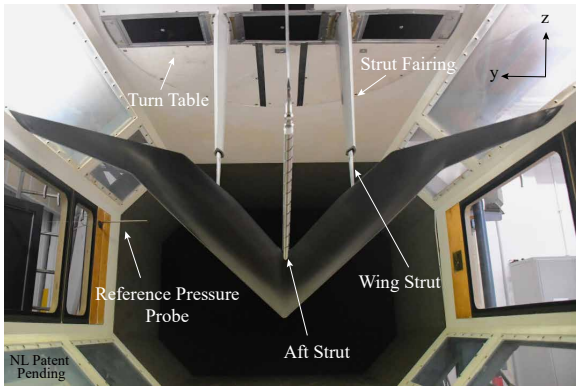

(b) Model setup in the test section, viewed from below and looking upstream at $\alpha = 10^\circ$ [65]

Figure 3.15: Overview of the model setup in the LTT with an inverted model setup

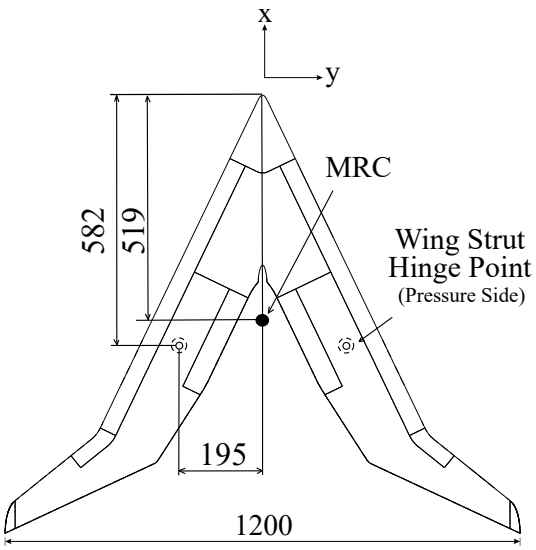

Figure 3.16: Moment reference point and wing strut installation point locations. Dimensions are given in mm [65]

Double-sided sticky tape and cellophane tape was used to secure the flap and spoiler parts to the model. At the locations where the flaps and spoilers were installed, a thin layer of scotch tape was placed on the model to aid in the removal of the surfaces using the superstrong double-sided sticky tape. In total, one layer of double-sided tape (and sometimes an added layer of scotch tape) was between each deflection surface and the model surface. To seal the leading edge of the deflection surface where it met the model surface, a piece of cellophane tape was used.

To ensure a repeatable installation of the deflections, the surface alignment blocks were used to tape down each surface deflection. These blocks were a negative of the model's trailing edge, so they had a snug fit. Additionally, their alignment could be double checked by comparing their position with different model geometry seams. In this way, the deflection surfaces were reliably positioned without any fasteners or inscriptions made on the model surface, keeping the model in good condition for future research.

3.5. Data Analysis Procedure

In this section, the methodologies used to process the data and then fit and analyze the output response surfaces is discussed. This approach highly influenced the experiment design and structure. The data process flow from raw data to usable response surfaces and equations will be discussed in the following subsections, starting with the general data processing in subsection 3.5.1 and the reference

frame rotations in subsection 3.5.2. The specific methods using in the RSM analysis are discussed in subsection 3.5.3

3.5.1. Data Processing

Once the raw balance data was collected and stored in the form of .txt files, it was then processed for interpretation and further use. This processing procedure took place using a set of MATLAB scripts developed by the TU Delft Aerospace Engineering faculty for the LTT facility. These scripts turned the .txt file data tables into data structures that were neatly organized, enabling different operations, like plotting the results or calculating derivatives. The basic processing flow is as follows.

First, the specified data files are read by the script, which organize and tabulate the data. Second, the tunnel conditions are extracted from the pressure data and organized with the balance data. Third, the wind-off zero measurements are removed from the raw balance data, effectively taring the balance data. After this wind-off tare is calculated, the balance data is then transformed from its left-handed reference system to the traditional right-handed reference system, indicated by reference system `(a)` in Figure 3.17. Fourth, the balance data is then transformed and nondimensionalized into coefficients using the reference lengths and the recorded tunnel pressure measurements. The equations for the nondimensionalization of the balance forces and moment are shown here:

$$C_{FX} = \frac{F_X}{q_\infty S} \qquad C_{FY} = \frac{F_Y}{q_\infty S} \qquad C_{FZ} = \frac{F_Z}{q_\infty S} \tag{3.2}$$

$$C_{MX} = \frac{M_X}{q_\infty S b} \qquad C_{MY} = \frac{M_Y}{q_\infty S c} \qquad C_{MZ} = \frac{M_Z}{q_\infty S b} \tag{3.3}$$

Fifth, the coefficients are rotated between the different axis systems and saved in each system, allowing for different types of analyses to be done in the different axes. If tunnel corrections are to be applied, they are done before the final save in each reference system. The rotations are discussed in subsection 3.5.2. The final data structure holding the processed data, tunnel conditions, and model reference lengths is saved for future use and analysis, whether plotting or for the fitting of regression models.

In this experiment, no wind tunnel corrections were performed, thus, they are not seen in the above data postprocessing procedure. As mentioned in section 2.1, the flow physics over the Flying V invalidate some of the underlying assumption in the classical wind tunnel corrections. As of this experiment, there are no accurate wind tunnel corrections available for the Flying V, thus the measured responses should be as uncorrected wind tunnel data, not corrected for the wind tunnel wall effects, support effects, Mach effects, or Reynolds effects.

The only modifications made to the raw balance data are that the weight of the model is removed from the balance forces and moments, the forces and moments are normalized into aerodynamic coefficients, the angles are corrected due to the aft strut bending, and the coefficient data are finally rotated into the output wind and body axis system using the above equations. The angle of attack correction due to aft strut bending was calculated in a previous test by van Luijk using the same model setup and was thus also used in this experiment [65]. Other corrections or data manipulation like removing the effects of the model supports are not included in this experiment due to the complexity of such methods, as mentioned in subsection 2.2.4.

3.5.2. Data Transformations

Before the wind and body axis coefficients are output, the moments are transferred to the model's moment reference center. This is done in the balance axis system by translating the moments. This is done in Equations 3.4–3.6.

$$C_{MX,\,\text{bal}} = C_{MX} - y_{\,\text{bal}} \cdot C_{FZ} + z_{\,\text{bal}} \cdot C_{FY} \tag{3.4}$$

$$C_{MY,\,\text{bal}} = C_{MY} - z_{\,\text{bal}} \cdot C_{FX} + x_{\,\text{bal}} \cdot C_{FZ} \tag{3.5}$$

$$C_{MZ,\,\text{bal}} = C_{MZ} - y_{\,\text{bal}} \cdot C_{FX} + x_{\,\text{bal}} \cdot C_{FY} \tag{3.6}$$

One moment reference center was used in this experiment. The reference center corresponded to the (x,z) coordinate of the leading edge of the MAC on the wind tunnel model, located $x_{ref} = 519$ mm from the nose of the model, as indicated by Table 3.7 and Figure 3.16 and consistent with the analysis done by van Luijk [65]. When used in the moment transfers, the moment reference center is expressed in the balance reference frame, which is centered in the test section. Thus, the moment reference center in the balance reference frame is expressed as $X_{MRC} = [-0.1875, 0, 0.0651]$, where the $x-$ and $z-$components are normalized by the Flying V model MAC and the $y-$component is normalized by the Flying V model span. In the tunnel's balance axis, positive X points downstream, Z points towards gravity, and Y follows from the left hand rule. Physically, the reference point lies below and upstream the test section center. All moments presented in this report are with respect to this moment reference center.

After translating the moments to the moment reference center, the moments and forces are rotated to the body axis to be available for wind tunnel corrections. This requires the force and moments be rotated from the balance axis to the body axis using an Euler rotation. The difference between the body axis, wind axis, and aerodynamic (also called "stability") axis systems can be seen in Figure 3.17. Positive lift and normal forces are defined as opposite the positive z-axis in the wind and body reference frames, respectively; the positive drag and tangential forces are defined as opposite the positive x-axis in the wind and body reference frames, respectively. After moving to the RHS aerodynamic reference frame, all moments are defined as positive around their corresponding axes using the right hand rule. The equations used in the balance-to-body transformation are found in Equation 3.7 - 3.12.

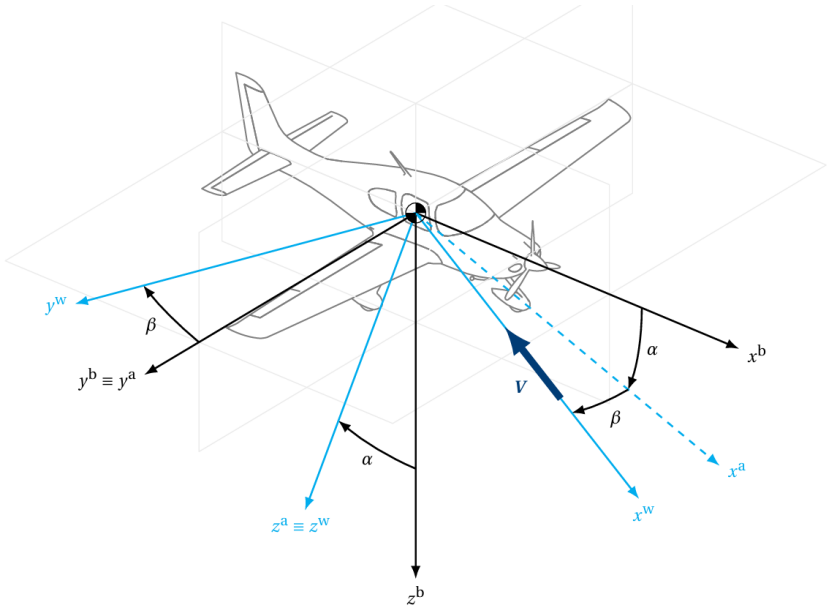

Figure 3.17: Body (b), wind (w) and aerodynamic/stability (a) reference frames [66]

$$C_{Fn} = C_{FZ} \cdot cos\alpha + C_{FX} \cdot sin\alpha \tag{3.7}$$

$$C_{Ft} = -C_{FY} \tag{3.8}$$

$$C_{Fs} = C_{FZ} \cdot \cos\alpha + C_{FX} \cdot \sin\alpha \tag{3.9}$$

$$C_{RM,\,\text{body}} = C_{MX,\,\text{bal}} \cdot \cos\alpha - C_{MZ,\,\text{bal}} \cdot \sin\alpha \tag{3.10}$$

$$C_{YM,\,\text{body}} = C_{MY,\,\text{bal}} \tag{3.11}$$

$$C_{PM,\,\text{body}} = C_{MZ,\,\text{bal}} \cdot \cos\alpha + C_{MX,\,\text{bal}} \cdot \sin\alpha \tag{3.12}$$

To output the coefficients in the wind axis, the forces and moment coefficients from the body axis were rotated into the wind axis using an Euler rotation, rotating around the body-fixed y-axis by α and then

around the aerodynamic frame's z-axis by β. The equations used in this transformation are found below are simplified to use the conventional C_{Fn} normal force coefficient, C_{Ft} tangential force coefficient, C_{Fs} side force coefficient and corresponding body moment coefficient notations from the body axis as inputs. This switches the signs on some of the standard Euler rotation equations.

$$C_L = C_{Fn} \cdot \cos\alpha - C_{Ft} \cdot \sin\alpha \tag{3.13}$$

$$C_D = (C_{Fn} \cdot \sin\alpha + C_{Ft} \cdot \cos\alpha) \cdot \cos\beta + C_{Fs} \cdot \sin\beta \tag{3.14}$$

$$C_Y = C_{Fs} \cdot \cos\beta - (C_{Fn} \cdot \sin\alpha + C_{Ft} \cdot \cos\alpha) \cdot \sin\beta \tag{3.15}$$

$$C_{RM,\,\text{wind}} = C_{RM,\,\text{body}} \cdot (\cos\alpha\cos\beta + \cos\alpha\sin\beta) - C_{YM,\,\text{body}} \cdot (\sin\alpha\cos\beta + \sin\alpha\cos\beta) \tag{3.16}$$

$$C_{PM,\,\text{wind}} = C_{PM,\,\text{body}} \cdot \cos\beta - C_{RM,\,\text{body}} \cdot \cos\alpha\sin\beta + C_{YM,\,\text{body}} \cdot \sin\alpha\sin\beta \tag{3.17}$$

$$C_{YM,\,\text{wind}} = C_{RM,\,\text{body}} \cdot \sin\alpha + C_{YM,\,\text{body}} \cdot \cos\alpha \tag{3.18}$$

Codifying Design Variables

To best fit the gathered data to polynomial models, MDOE techniques dictate that the factor levels tested should be codified and centered around 0. Thus, after processing the data, the flap and spoiler surface deflection angles can be transformed from the range [0, 60] to [-1, 1]. In the same way, the angles of sideslip can be transformed from [0, 15] to [-1, 1]. For each of the angle of attack ranges, the ranges can likewise be transformed to the range [-1, 1]. These transformation results in an orthogonal design matrix, which improves the numerical precision of the model fitting tools discussed in subsection 3.5.3. After the models are fitted with the codified factor levels, the resulting equations can then be scaled back to the physical units.

3.5.3. MATLAB Response Surface Methodologies

As the data processing scripts used above were available in the MATLAB environment, the model regression using RSM was also performed in MATLAB. Using the Statistics and Machine Learning Toolbox, several tools were available for the different aspects of RSM, from test design to model fitting and analysis. This section highlights some of the specific MATLAB tools used to employ RSM in the analysis of this experiment.

For the verification process, the Ordinary Least Squares regression function, `fitlm`, was used to fit the available data to a Linear Model. `fitlm` takes in a table or matrix of the tested factors, one column for each factor, and the response measured. Then, depending on the optional inputs, the function will fit a model that is a function of the measured response in terms of each column inputted or with an indicated model form, such as '$C_L \sim 1 + aoa + aos$', where each function term is multiplied by a coefficient found through regression. The outputted linear model object contains useful properties such as model statistics, which indicate the model's quality of fit or accuracy. These statistics are calculated through the ANOVA automatically, though an `anova` function also exists in MATLAB to perform this analysis explicitly.

Other important functions used in the RSM was `predict`, which uses a regression model object and predicts the model response over a specified range. This function also outputs the model's confidence intervals (CIs), which are essential for validating a regression model and assessing the its uncertainty. When the best model form is not known *a priori* then it is helpful to use the `stepwiselm` function, which performs the same linear regression on a dataset but in a stepwise manner, adding or removing terms from the model up to a limit while being guided by the ANOVA results and the p-value calculated for each model term. The ANOVA results are calculated using the fundamentals discussed in subsection 2.2.3 and subsection 2.3.3. This `stepwiselm` function is especially useful for determining the best model fit for a function with many independent factors.

For more complex analyses, like GLS, the Statistics and Machine Learning toolbox also contains `fitlme`, which returns a LMM object [67]. This is used in place of the above `fitlm` tool when needed, such as in split plot experiment analyses or in cases where the response can better be modeled as a function of fixed effects and random effects. Using these functions, one can assess if a correlation exists between a block's results and when that block was conducted, as discussed in subsection 2.3.3.

As a stepwise regression algorithm does not yet exist in the Statistics and Machine Learning toolbox for LMMs, a custom function was made to identify a LMM to best fit the data when the structure was not known *a priori*. This function iteratively adds fixed effects terms to the LMM and compares the p-value of each added term to determine the likelihood of its presence in the true model structure. In order to compare different LMM iterations, REML should not be used for the significance testing because the REML likelihood function is independent of the changing model fixed effects structure [51]. As such, ML is used to fit and compare the LMMs as fixed effects terms are added to them. Once the candidate terms have been looped through and the most significant ones identified, the final model structure is refit using REML to obtain an unbiased estimate of the random effects.

4

Verification and Validation

This chapter details the work done to verify the usage of the methodology described in chapter 3 in this research, and the approach used to validate the results and assumptions made is also highlighted. The verification work is presented in section 4.1, and the validation method is discussed in section 4.2

4.1. Verification

To verify the RSM and MDOE techniques were appropriate methodologies to design and analyze the Flying V wind tunnel test and results, previous wind tunnel data was examined. Specifically, Flying V data that was gathered in the LTT a year prior was used to test the methods. Several sweeps of data were available in both angles of attack and sideslip. As MDOE techniques use a subset of the possible samples to construct RSM models, the data available was sampled from as if the test had been designed with MDOE techniques. One benefit from this approach was that the rest of the data available could be used to validate the constructed models. The process of taking datasets gathered using OFAT techniques and sampling from a subset to describe the whole using MDOE techniques is a common practice in literature that highlights the advantages of the MDOE framework. The process done in this research is described in subsection 4.1.1. Next, the verification of the underlying regression analysis assumptions are checked in subsection 4.1.2, and the short-term and long-term repeatability are checked in subsection 4.1.3. Finally, a discussion on the flow angularity results is presented in subsection 4.1.4.

4.1.1. Sampling Past Data

As mentioned, many sweeps of data from a previous test were available for use. Not only were multiple sweeps available, but all sweeps were repeated three different times. These sets of repeats are referred to as Sets 1 - 3. Data from Set 1 was used for the model construction, and additional data from Set 3 was used as repeats, providing the scaled number of points needed using the scaling factor 1.625. First, the sweep data from Set 1 was truncated at the maximum values of the sweep ranges used in this research: $\alpha = 25°, \beta = -15°$. The data beyond this range wasn't of interest in this research. This data was then divided into two subranges at the same angle of attack as the test design from section 3.2. The ranges of the data used are shown in Table 4.1. To sample this available truncated

Variable	Range 1		Range 2	
	Min	Max	Min	Max
α	0	15	15	25
β	0	-15	0	-15

Table 4.1: Verification data ranges

data, a traditional CCD design was used to selected which data points to use. This CCD test design was inscribed in the range of the data available such that axial points lay on the maximum and minimum

values of the range, using one CCD site selection for each range. In each range, the four corner points, corresponding to all combinations of max and min α and β for that range, were also used, as this was the composite design selected in the trade study.

Because not all of the data gathered fell exactly on the sites prescribed by the CCD, the points that were closest to the ideal locations were selected as needed. The modified site selections versus the standard CCD selections can be seen in Figure 4.1.

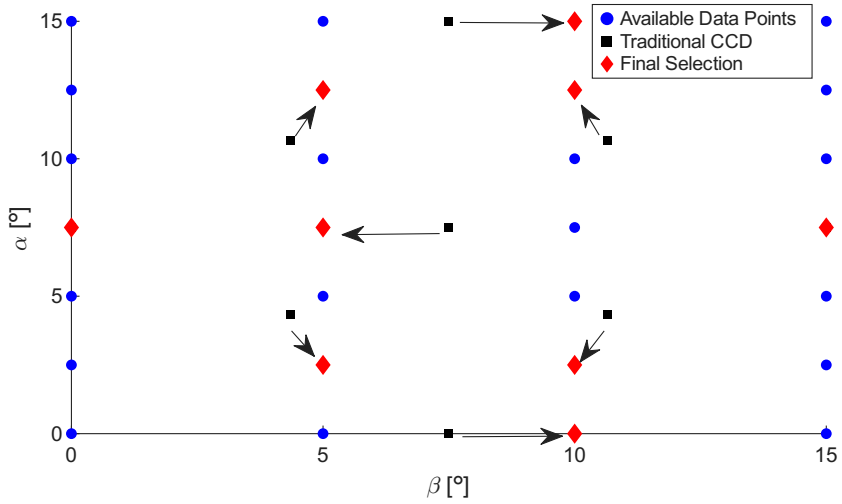

Figure 4.1: Modified site selection for sampling from screening data vs standard CCD

4.1.2. Linear Model Construction and Diagnostics

Having sampled data from Set 1 in both the lower and upper ranges of angle of attack, the angle of attack and sideslip combinations and the resulting forces and moments measured there were fed into a stepwise linear regression function. The output was a single RSM model for each force and moment in each range; the output was a function of a force or moment in terms of α, β. These models were assessed for accuracy in several ways.

First, the ANOVA results were examined to see the confidence with which each model parameter was determined. The models were adjusted until each term was determined with 95% confidence, corresponding to a p-value of less than 0.05. Second, the model predictions were plotted across the whole sample space that the fitted data came from. From this surface plot, it was quickly seen whether or not the regression polynomial model was overfit and oscillating in a nonphysical way between the fitted points. If the model looked physical and reasonable, the model was then third tested for validity by plotting the model's predictions vs the data available in Set 2. The surface plot for Range 1 of the C_D model is shown in Figure 4.2. This model had nine significant terms, as indicated in Equation 4.1, where $C_{D,i}$ is the i^{th} regression coefficient found.

$$C_D = C_{D,0} + C_{D,1}\alpha + C_{D,2}\beta + C_{D,3}\alpha\beta + C_{D,4}\alpha^2 + C_{D,5}\beta^3 + C_{D,6}\alpha^2\beta + C_{D,7}\alpha\beta^2 + C_{D,8}\alpha^3 \quad (4.1)$$

The model was deemed valid and accurate if the predicted model values overlapped with the Set 2 data, including the confidence intervals of both. Because the true uncertainty/variance values for the sampled data wasn't available, the uncertainty was estimated by calculating the sample standard deviation from the repeats using Equation 2.2. The Set 2 data was then plotted with $\pm 2\sigma$ where each point had its own σ estimated by this calculation. If the model predictions and its confidence intervals overlapped with the Set 2 data and estimated intervals, and if the general trend of the curves matched, then the model was found to be valid. An example of one of these plots for the drag coefficient in Range 1 can be seen in Figure 4.3.

Using only 21 data points of the 56 available in Range 1 from Sets 1 and 3, for example, the model fitted was able to describe the responses reasonably well, performing with the expectations given by MDOE methodologies. However, for some of the other forces and moments, especially in the upper range, the

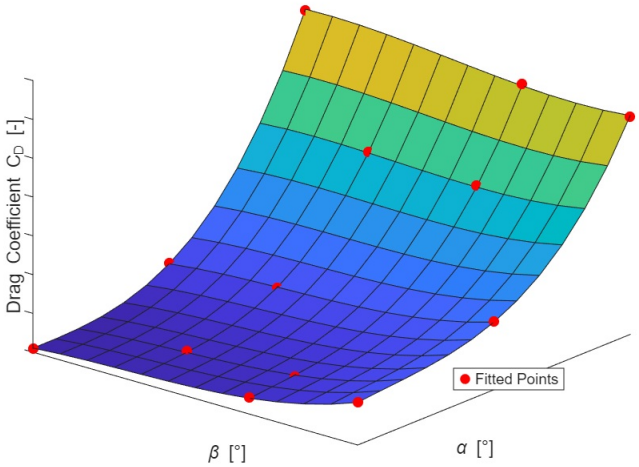

Figure 4.2: C_D model prediction for Range 1

corners of the sample space was poorly predicted by the regression models. This is not very surprising considering the CCD design contains no ”corner points” or those points where all combinations of the variables’ maximum and minimum values are tested. It was found that adding these corner points from the available data when fitting the models improved the predictive ability of the regression models.

To verify the assumptions behind the regression used to construct the regression models, the residuals of the model were examined. One plot was made where the difference between the fitted data points and the model prediction at those points, known as the model ”residuals”, was plotted against the full value predicted by the model at those points. This plot helps identify areas of the model that don’t fit the data well; any clear pattern in this scatter plot reveals that there is a component of the data that is not captured or fitted by the model. A plot that has no distinguishable pattern reveals that the residual error of the model has roughly the same accuracy at all parts of the model at which it was fit.

A second plot was made where the model residuals were plotted in a probability plot or a ’Q-Q’ plot. Taking the collection of residuals, the average residual and the group standard deviation is calculated. The probability distribution of the residuals is then plotted against each residual value. Normally distributed residuals all should fall on a straight line on this plot. Residuals that fall away from this line reveal that the fitted value is an outlier, either erroneous or representative of an unmodeled effect. The two plots for the C_D model fitted over the Range 1 can be seen in Figure 4.4.

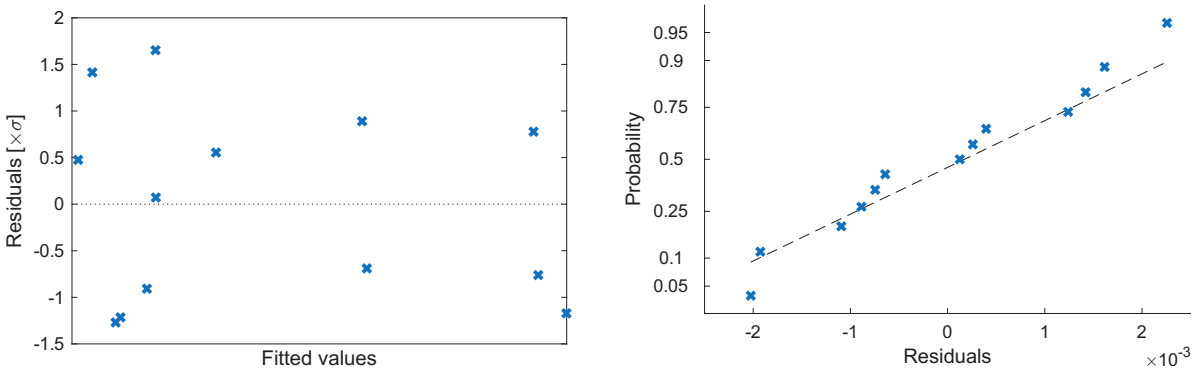

(a) C_D model residuals for each fitted point

(b) Q-Q probability distribution of the C_D model residuals

Figure 4.4: C_D Range 1 residual analysis plots

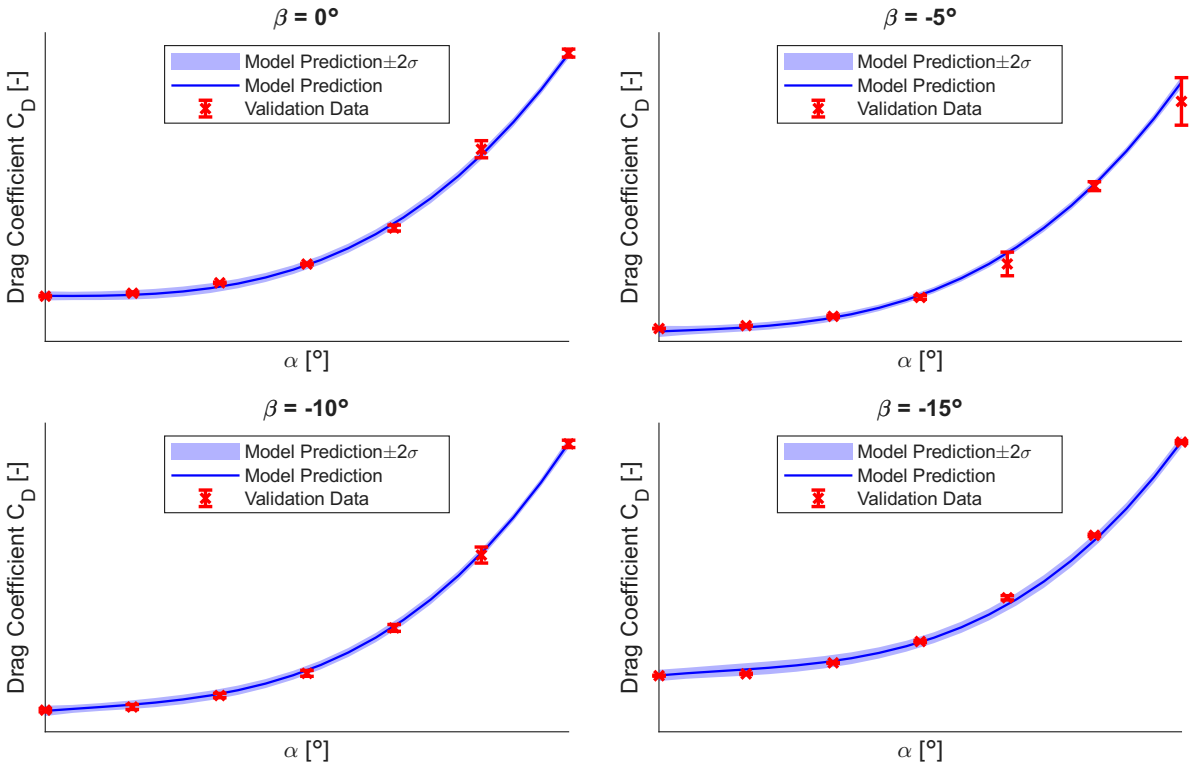

Figure 4.3: C_D verification regression model predictions and validation data for various angles of sideslip and attack

Because the two plots show nominal residuals, it can be said that the model fits the sampled data points with proper precision, with 95% confidence. This endeavor verified that the MDOE framework is suitable for collecting, analyzing, and representing Flying V wind tunnel data measured in the LTT.

4.1.3. Repeatability

To establish the repeatability of the wind tunnel model, installation, and measurement methodology, repeat data sweeps were measured under ostensibly identical conditions and orientations and at various times within the test. To establish the time-independence of the measurements over a short term, the within-test repeat sweeps were performed at the start of the test and at the end of the test. To establish the repeatability of the model installation, a cross-test repeat of two sweeps measured in 2024 with the same model and setup was conducted. The results from both repeatability analyses are shown in the next two subsections.

Short-Term Repeatability

Repeat alpha sweeps were measured for the Flying V model with the winglets installed at the start and end of the experiment to assess the within-test repeatability. Cubic interpolation was used to account for the slight setpoint angle mismatch between the sweeps. The difference between the sweeps at fixed sideslips of $\beta = 0°$ and $\beta = -15°$ are displayed versus the estimated experimental uncertainty due to block effects in Figure 4.5. The repeatability of the body axis forces and moments are essentially the same as the wind axis forces and moments shown here, just in a different reference system. As such, only the wind axis values are shown.

Looking at the C_L repeatability in Figure 4.5a, it can be seen that there is generally good agreement between the repeats at both sideslip angles, with the exception of the highest angle of attack at zero sideslip. This difference between C_L manifests also as outlier differences in C_D in Figure 4.5b, likely due to the difference in drag due to lift.

In Figure 4.5c, the $\beta = -15°$ C_Y repeats show better repeatability than the $\beta = 0°$ C_Y repeats. This is likely due to unrepeatable asymmetries in the vortical flow over the model at the zero sideslip orientation. This is discussed by van Luijk, who observed asymmetries in vortex development at ostensibly

symmetrical conditions [65]. This might explain the worse repeatability at $\beta = 0°$.

The lack of repeatability in C_Y manifests itself in the $C_{n,\text{ wind}}$ moment especially in Figure 4.5f and the $C_{l,\text{ wind}}$ as well in Figure 4.5d, as these are primarily functions of C_Y. The $C_{m,\text{wind}}$ moment shows acceptable repeatability within test in Figure 4.5e, though, and the $C_{l,\text{ wind}}$ is acceptable too, considering the estimated $\pm 2\sigma$ uncertainty is the lower bound of the true uncertainty.

Long-Term Repeatability

Repeat alpha sweeps were also measured for the Flying V model with the wingtips installed to assess the test-to-test repeatability. To this end, two alpha sweeps from the May 2024 wind tunnel campaign were repeated and compared with. Cubic interpolation was again used to account for the slight setpoint angle mismatch between the sweeps. The difference between the sweeps at fixed sideslips of $\beta = 0°$ and $\beta = -15°$ are displayed versus the estimated experimental uncertainty due to block effects in Figure 4.6. The repeatability of the body axis forces and moments are essentially the same as the wind axis forces and moments shown here, just in a different reference system. As such, only the wind axis values are shown.

The C_L and C_D repeatability are generally fine when looking at the $\beta = -15°$ data in Figure 4.6a and Figure 4.6b. However, the data measured at $\beta = 0°$ shows discrepancies after angle of attack $\alpha = 15°$. This is due to a difference in the vortex formation and breakdown, as apparent in the $\beta = 0°$ $C_{m,\text{ wind}}$ repeatability shown in Figure 4.6e. The exact angle of attack at which the pitch break occurs seems to differ between tests, explaining the discrepancies in the three force and moment plots.

Why this difference occurs could be due to slight differences in the test setup and model installation, such as slight variations in the trip strip locations. It is unlikely that this difference across tests is due to different testing conditions, like a Reynolds number or temperature difference, as the pitch break location due to vortex breakdown remains repeatable within a week where the temperature varied from test start to end, as shown in Figure 4.5e.

Supporting the hypothesis that test-to-test differences are due to model installation is the plot of differences in the C_Y graph in Figure 4.6c. The $\beta = 0°$ repeat deltas are very noisy, reflecting the differing trends in C_Y with angle of attack from one test to the next, though the deltas are still centered around zero. Though no oil flow is available to confirm this for the 2025 data, the oil flow for the 2024 test showed asymmetric flow conditions at zero sideslip for a range of angles of attack. Since the flow symmetry is sensitive to the model installation, it would follow that slight model installation error would also lead to different asymmetries across tests and thus to different trends in C_Y and the associated $C_{l,\text{ wind}}$ and $C_{n,\text{ wind}}$ moments.

The $\beta = -15°$ repeat deltas for C_Y are more difficult to explain. Figure 4.6c shows that there is a constant offset at the lower angles of attack and then the difference between tests switches signs from $\alpha = [10°, 25°]$. The fact that there is still a difference in trend in C_Y (and thus $C_{l,\text{ wind}}$ and $C_{n,\text{ wind}}$) at nonzero sideslip indicates that the difference in model installation might be sourced in the trip strip installation.

While the lack of reproducibility with some force and moment trends across tests is of some concern, it is comforting to note the within-test repeatability is mostly within the estimated experimental uncertainty. Thanks to the within-test repeatability, a test campaign could be compared with another campaign analytically, keeping the identified cross-test discrepancies in mind and presenting test-to-test comparisons with the appropriate qualifications. Ideally, the source of cross-test discrepancy is identified and removed altogether.

4.1.4. Flow Angularity

To verify that the tunnel centerline corresponded to the aerodynamic sideslip angle of zero, flow angularity sweeps were measured. The results were confusing. To begin with, the sideforce coefficient measured with the clean model and winglets installed is shown in Figure 4.7. The ”Run 1” data indicated was measured at the start of the test. The ”Run 2” and ”Run 3” data were both run back to back at the end of the test but in different sweep direction. The string ”l-r” indicates a sweep from left to right, and ”r-l” indicates right to left. Both sweep directions and all three runs indicate a $C_Y = 0$ at nonzero sideslip, roughly $\beta = -0.35°$.

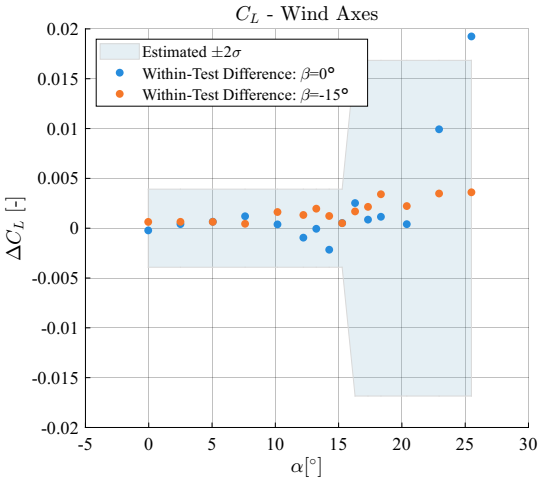

(a) Lift coefficient (C_L)

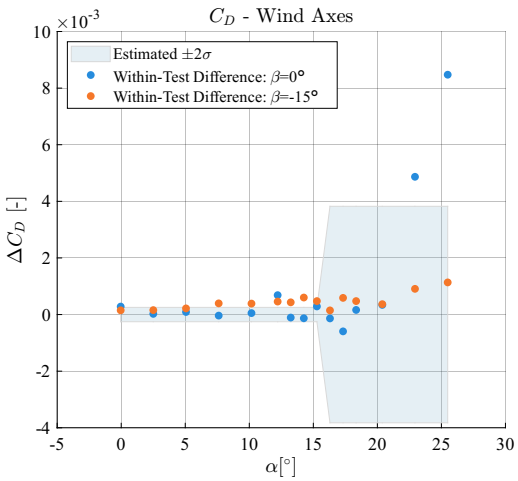

(b) Drag coefficient (C_D)

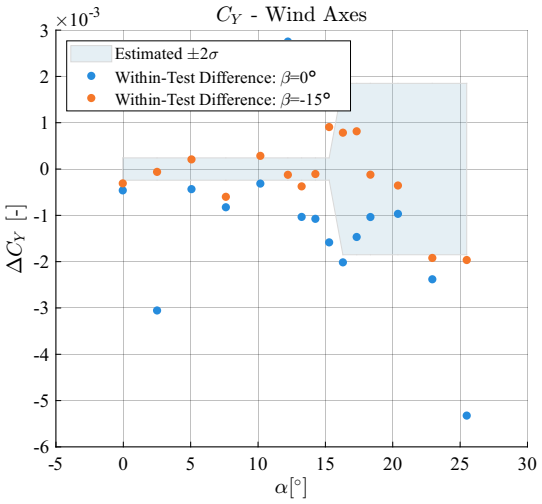

(c) Side force coefficient (C_Y)

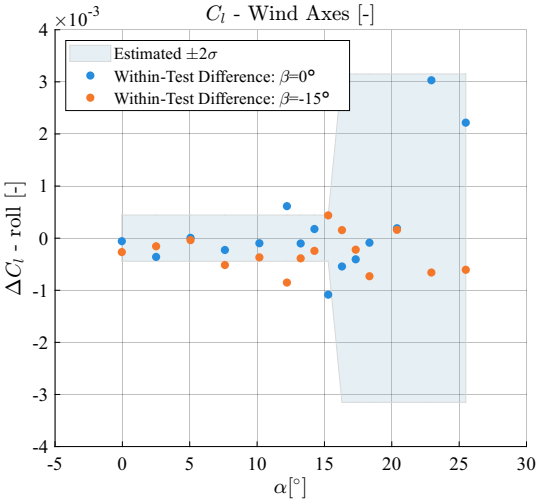

(d) Rolling moment coefficient (C_l)

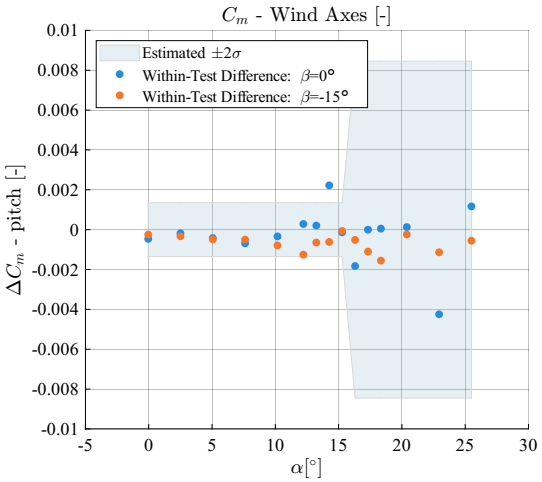

(e) Pitching moment coefficient (C_m)

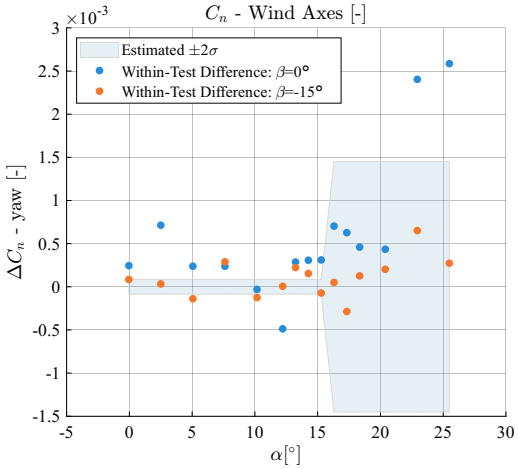

(f) Yawing moment coefficient (C_n)

Figure 4.5: Within-test deltas for wind axis force and moment coefficients

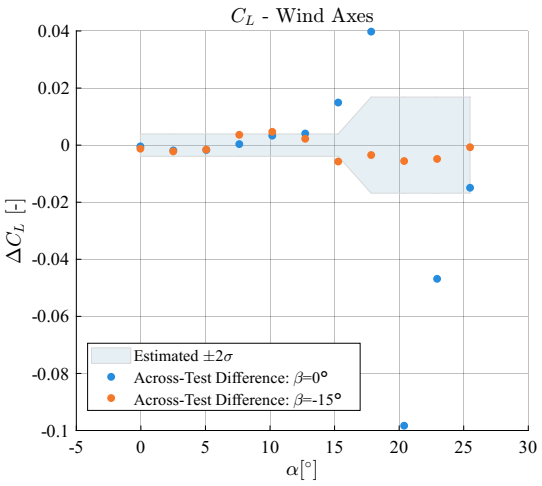

(a) Lift coefficient (C_L)

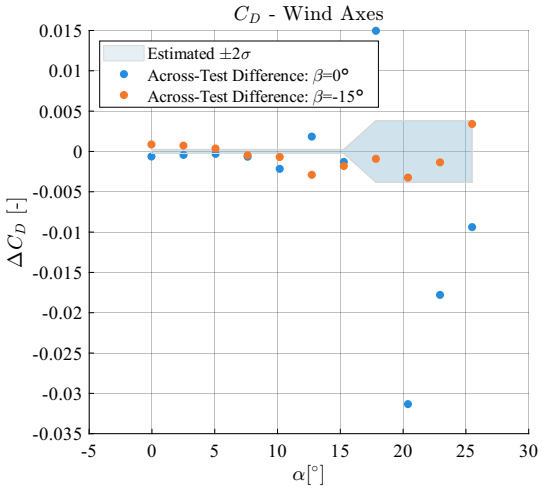

(b) Drag coefficient (C_D)

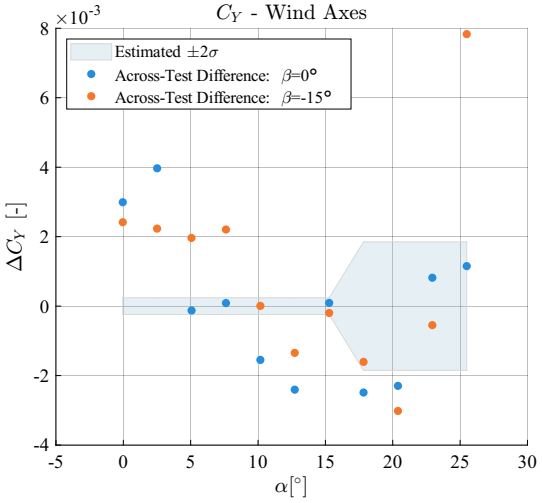

(c) Side force coefficient (C_Y)

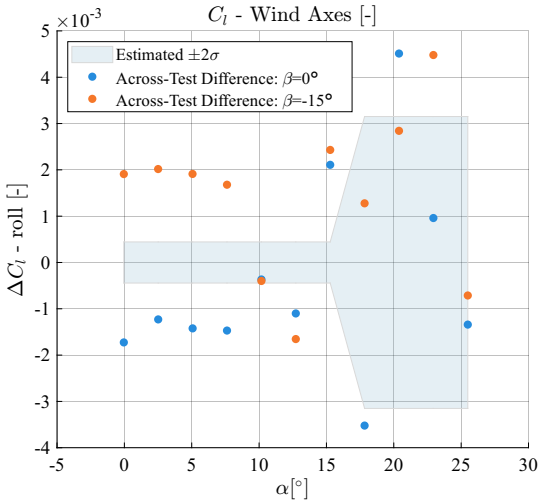

(d) Rolling moment coefficient (C_l)

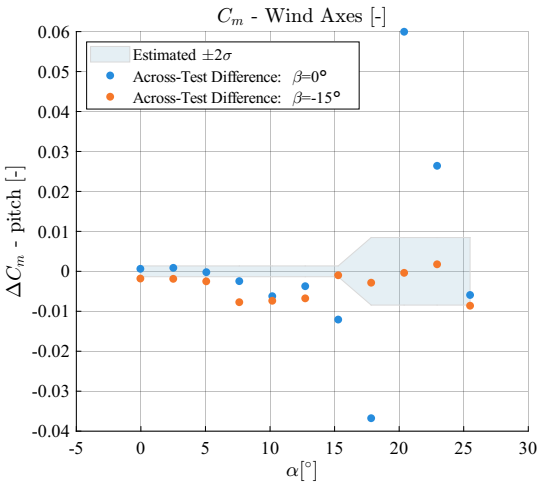

(e) Pitching moment coefficient (C_m)

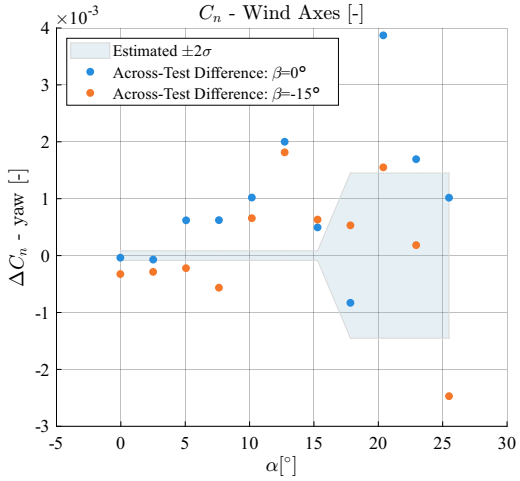

(f) Yawing moment coefficient (C_n)

Figure 4.6: Cross-test deltas for wind axis force and moment coefficients

If this were truly the symmetric flow condition associated with true zero sideslip angle, then there should be a corresponding minimum drag measured at that point. Looking at Figure 4.8, the minimum drag measured is measured at a small positive sideslip angle for all three runs. The drag plot looks messy due to a measurement taken twice at $\beta = 0°$ in each sweep, once as the sweep passes it and once at the start or end of the sweep. Interestingly, "Run 1" displays a peculiar drop in drag coefficient from $\beta = 0°$ to the next positive sideslip angle. Additionally, the drag measured at $\beta = 0°$ switches between the continuous trend in "Run 2" and "Run 3" and the trend displayed in "Run 1". It is not known what causes these behaviors.

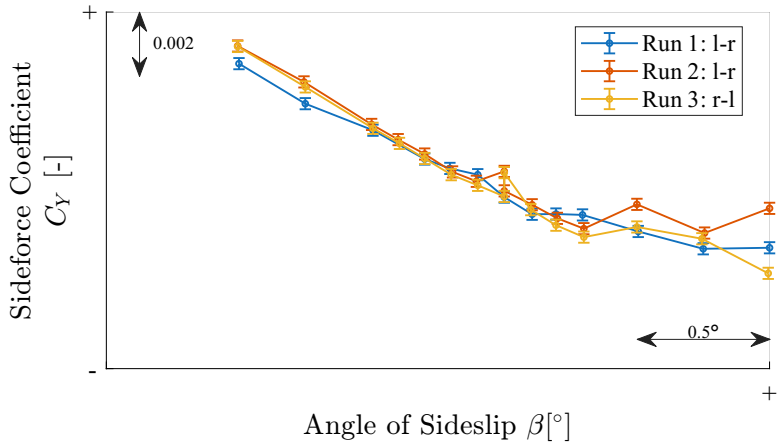

Figure 4.7: C_Y flow angularity sweep at $\alpha = 0°$, error bars indicate $\pm 2\sigma_{balance}$

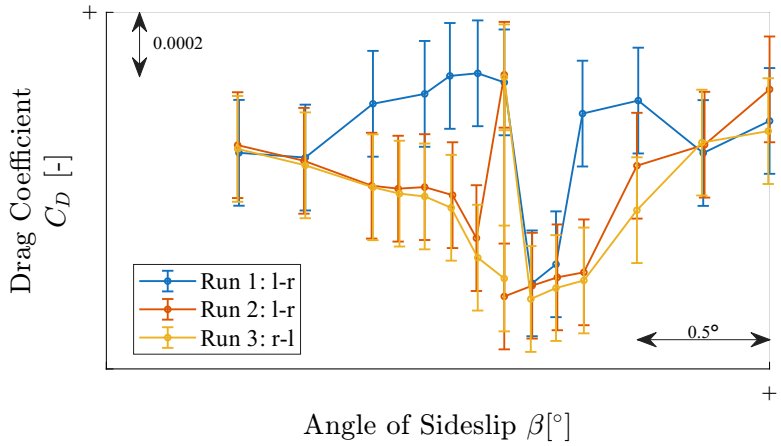

Figure 4.8: C_D flow angularity sweep at $\alpha = 0°$, error bars indicate $\pm 2\sigma_{balance}$

Looking at Figure 4.7 and Figure 4.8, it is inconclusive if $\beta = -0.35°$ is the true zero sideslip angle or if a small, positive sideslip offset is needed to account for flow angularity. Both observations made in the figures could have their causes due to strut misalignments or differences in the installed winglet geometries. To double check if the $\beta = -0.35°$ could be the true offset needed, an alpha sweep was conducted at that angle to see if the sideforce measured at $\alpha = 0°$ would be equal to zero and the sideforce-dependent moments have a lower slope. The results are shown in Figure 4.9, Figure 4.10, and Figure 4.11.

In Figure 4.9, the measured sideforce coefficient surprisingly does not coincide with $C_Y = 0$ for the $\beta = \beta_{fa}$ sweep at $\alpha = 0°$, though it does move closer to zero from the $\beta = 0°$ data point. Furthermore, the trend of C_Y with α does not flatten out but increases in slope instead. The same is seen for the lower angles of attack in the rolling moment in Figure 4.10. In Figure 4.11, the yawing moment trend with α also doesn't flatten out. The only change is a downward offset from $C_n = 0$ at $\alpha = 0°$ that is

constant in direction but changing in magnitude for the alpha sweep. These trends suggest that the identified β_{fa} is not truly the flow sideslip angularity.

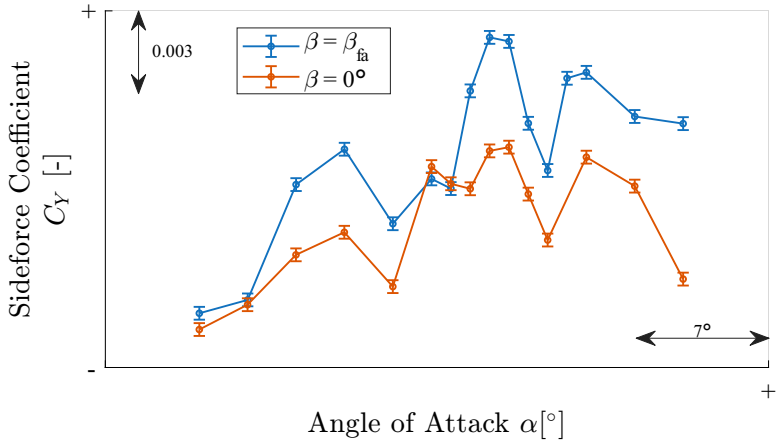

Figure 4.9: C_Y flow angularity sweep at $\alpha = 0°$, error bars indicate $\pm 2\sigma_{balance}$

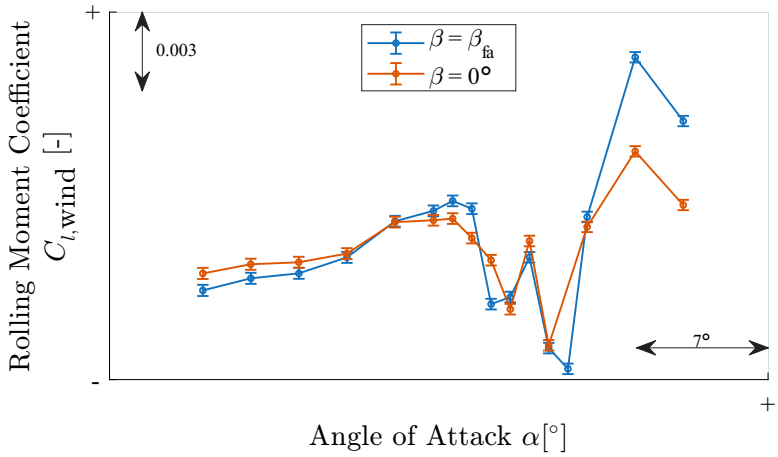

Figure 4.10: $C_{l,\text{wind}}$ flow angularity sweep at $\alpha = 0°$, error bars indicate $\pm 2\sigma_{balance}$

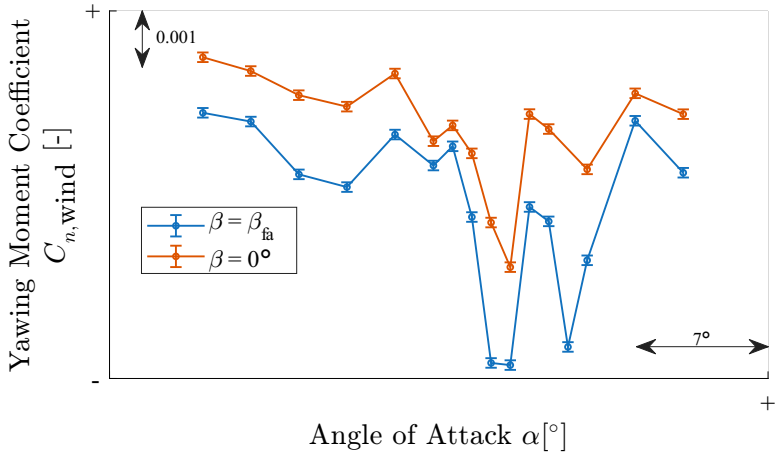

Figure 4.11: $C_{n,\text{wind}}$ flow angularity sweep at $\alpha = 0°$, error bars indicate $\pm 2\sigma_{balance}$

From this investigation, it is difficult to say if there is significant sideslip flow angularity over the Flying

V in the LTT due to tunnel quality, model surface finish, or strut affects. The nonzero sideforce and lateral-directional moments measured at the tunnel's zero pitch and yaw angles indicate that there are not symmetric flow conditions over the Flying V at what is currently described as $\beta = 0°$. Since it is not known what is causing these nonzero forces and moments, the offsets are not corrected in the data presented in this report. Any true angle offsets are also not conclusively identified or corrected for, so the sideslip angles reported in this report are as measured.

4.2. Validation

It was necessary to validate the hypothesis that there would be little to no hysteresis effects in this experiment. The analysis done to check for hysteresis and validate that decision is shown in subsection 4.2.1. Also included in this section is a discussion in subsection 4.2.2 on the validation approach taken to validate the regression model results, though the validation results for the models themselves are shown in section 5.3 and more extensively in Appendix C.

4.2.1. Hysteresis

When assessing the data gathered in previous research, it was assumed that the hysteresis effects on the 1.8% scaled Flying V model tested in the LTT were negligible. It was hypothesized that there would likewise be no hysteresis effects introduced by winglets or by flap and spoiler deflections on the same model, but measurement data was taken at two specific configurations to validate that hypothesis. Hysteresis here is defined as the time and direction-dependent nature of a measured response, typically due to a change in measured response when sweeping back down in angle of attack after the airflow has stalled over the wing.

First, an angle of attack sweep at zero sideslip was taken from low angle of attack to high angle of attack and back down to the start again. The difference between the measurements going up and then going back down can be seen in Figure 4.12. The data shown was measured with no flap or spoiler deflections and only with the winglets installed. The deltas for the C_L measurements fit within the estimated confidence interval from the block effect, but only the differences at the maximum and minimum angles of attack fit within the balance uncertainty. However, the deltas indicate that the measured lift is higher going down than it is going upwards, which is the opposite of the behavior expected if true hysteresis was occurring. The difference in C_D going up and then down shown in Figure 4.12b follows the trend in C_L, where an increase in lift corresponds to an increase in drag due to lift.

It seems the error in measurements due to sweep direction, either approaching the orientation from below or from above, is not within balance uncertainty, but it is close to the same error as if one run were to be repeated within the same experiment. As such, the introduced error due to guarding against systematic error while ignoring approach-direction error is not critical, and the assumption to neglect it is validated.

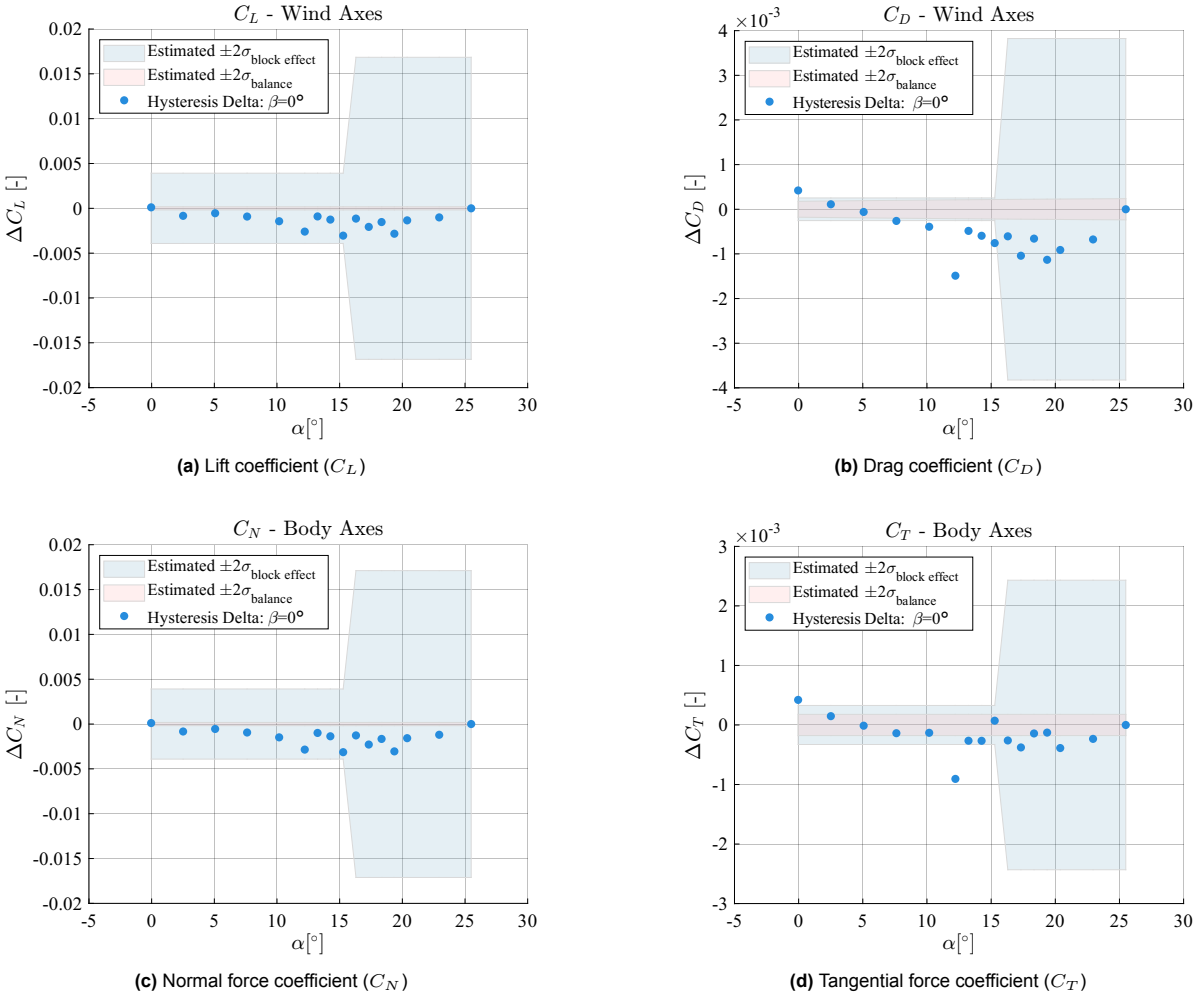

(a) Lift coefficient (C_L)

(b) Drag coefficient (C_D)

(c) Normal force coefficient (C_N)

(d) Tangential force coefficient (C_T)

Figure 4.12: Hysteresis deltas for clean model at $\beta = 0°$ sideslip

To assess if hysteresis is introduced when flaps and spoilers are deployed, measurements were taken within one run where the model was measured from angles of attack $\alpha = 20°$ to $\alpha = 25°$ and down to $\alpha = 20°$ again. This was done at a sideslip of $\beta = -7.5°$ and with all flaps and spoilers deflected to $17.5°$. The results are shown in Figure 4.13.

For all of the deltas between the up and down data, the differences lie reasonably close to the balance uncertainty and completely within the block effect uncertainty. As in Figure 4.12, the deltas bias downwards in Figure 4.13, indicating an increase in lift and drag as the model is moved from high to low angles of attack. This is again the opposite of regular hysteresis behavior, so the trend can be attributed to experimental error. The magnitude of the error is small in comparison to the two estimated confidence intervals, and the assumption to neglect preventing any potential hysteresis affects when the flaps and spoilers are deployed is validated.

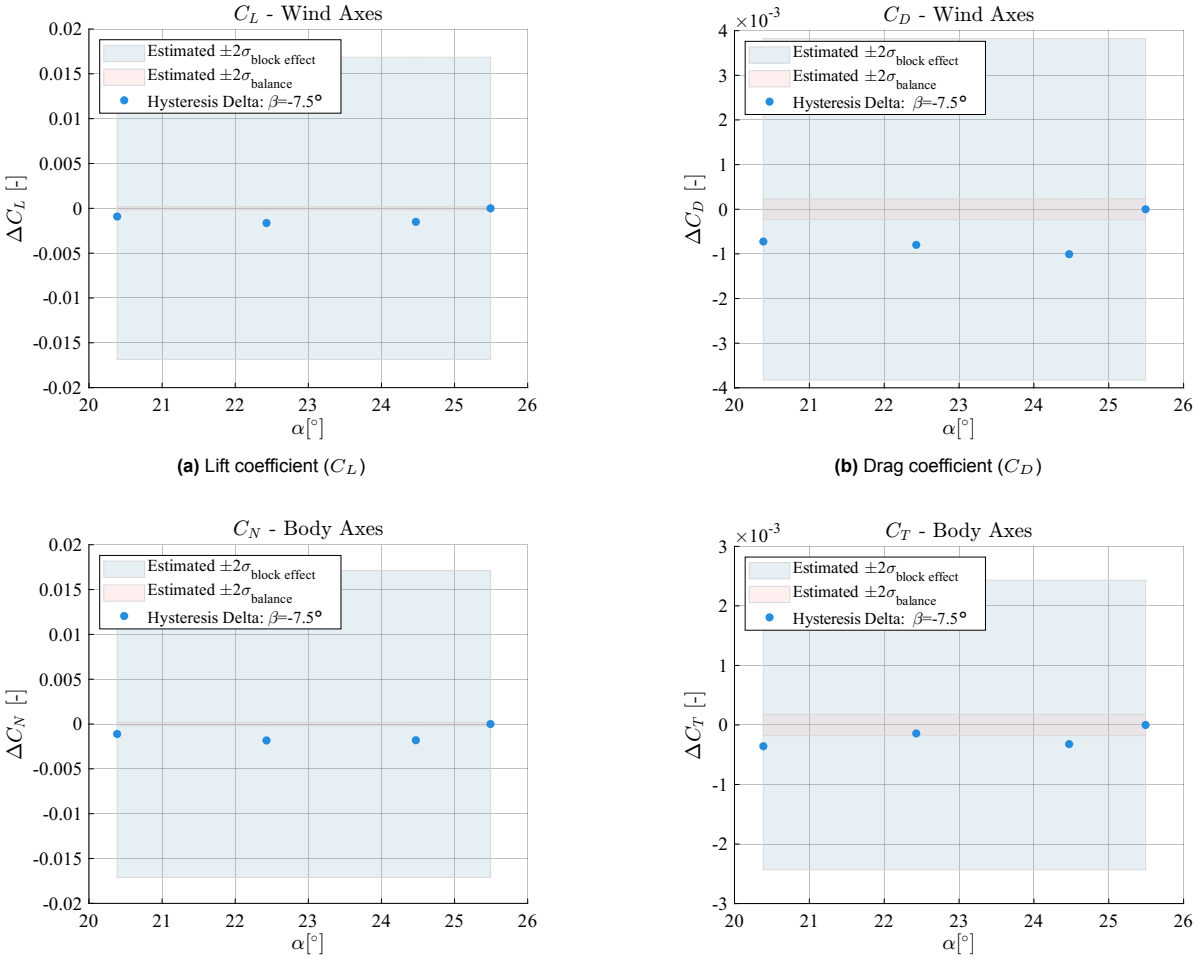

(a) Lift coefficient (C_L)

(b) Drag coefficient (C_D)

(c) Normal force coefficient (C_N)

(d) Tangential force coefficient (C_T)

Figure 4.13: Hysteresis deltas for model with all flap and spoiler deflections at $17.5°$ deflection at $\beta = -7.5°$ sideslip

4.2.2. Model Validation

To validate the models fitted from the wind tunnel data gathered in this research, a procedure similar to the one used to validate the verification models in section 4.1 was used. Once the models were constructed, the model predictions were plotted against validation data, data that had not been used in the model fitting but had been reserved for validation. This validation data was gathered during the wind tunnel test. These validation measurements were also used to numerically assess the model's predictive capabilities, using them to calculate the residual RMSE of each model with respect to the validation data. The results for the models' RMSE values can be found in Table 5.10.

As the models' predictive capabilities needed validating, a configuration that wasn't explicitly tested was used to collect the validation data. Other configurations represented configurations of interest; measuring validation data with these configurations would allow the models to be validated for key predictions of interest. The specific configurations can be seen in Table 4.2.

Config	Flap	Sp1	Sp2l	Sp2r	Use Case
Config 1	60	60	60	60	Touchdown
Config 2	42.5	30	30	17.5	None
Config 3	0	30	30	30	Rapid Descent
Config 4	30	30	30	30	None
Config 5	30	0	0	0	Approach
Config 6	60	0	0	0	Landing

Table 4.2: Validation configuration variable levels

The angle of attack and sideslip sweeps chosen for these validation configurations were chosen to overlap with some of the fitted combinations and to test the models' interpolative and predictive capabilities in the subplot variables too. One angle of attack sweep was thus collected at $\beta = 0°$ in both the lower and upper range, one angle of attack sweep was thus collected at $\beta = -13°$ in both the lower and upper range, and two sideslip sweeps were collected, one in the lower and one in the upper range. The lower beta sweep was collected at a constant $\alpha = 12.5°$ and the upper beta sweep was at constant $\alpha = 17.5°$. These sweeps can be seen in Figure 4.14 along with the 2D projection of the entire experiment sample space in the α and β plane. Some results of the validation sweeps plotted against the fitted models are shown in subsection 5.3.2, and the validation sweeps for all flap and spoiler effects models for the wind axis forces and body axis moments can be found in Appendix C.

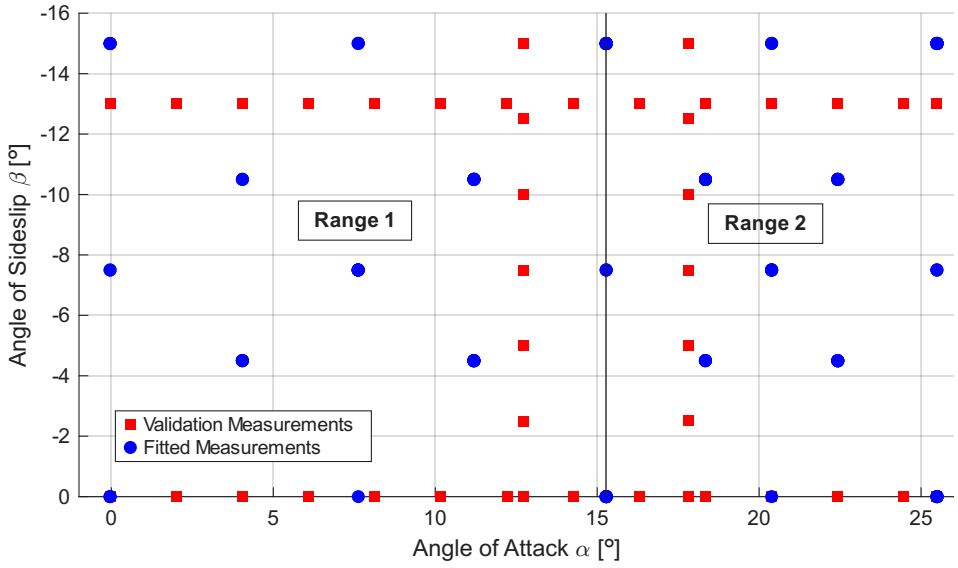

Figure 4.14: Locations of validation measurements and fitted measurements projected to 2D α and β plane for sample Ranges 1 and 2

5

Results and Discussion

This chapter summarizes the results of the wind tunnel experiment conducted in May 2025 for the research presented in this report. Section 5.1 covers the Analysis of Variance done on repeat runs measured during the experiment, showing the justification for modeling the data with Linear Mixed Models and for the selection of the sample duration used. The data was fit with both Linear and Linear Mixed Models, and some comparisons and differences are highlighted in section 5.2. Next, the LMM validation results are presented in section 5.3, where some of the limitations and shortcomings of the fitted models are shown. The models and collected data are then used to investigate the flap and spoiler effects in section 5.4 and section 5.5. Lastly, a synthesis of the results and findings is given in section 5.6.

Due to confidentiality constraints, the tick marks have been removed from all plots. Reference lengths have been provided in graphs to give a sense of scale. The final regression model coefficients are likewise not disclosed, and only the significant model terms are presented.

5.1. Analysis of Data Variance

Using the C_L data available from Run 9a and its two repeats, Run 9b and 9c, an analysis of variance was conducted to determine if the differences in the repeated measurements within and between the repeated runs were statistically significant and if the mean C_L could be said to be the same across each repeat run. As an example, the ANOVA process results for the Range 2 C_L data is shown step-by-step in subsection 5.1.1. The results from such an analysis indicate whether or not a Linear Model or Linear Mixed Effects Model is more suitable to describe the data with. Using the ANOVA results, subsection 5.1.2 covers the estimated experimental error for the data measured in this experiment. Lastly, subsection 5.1.3 discusses the effect of different sample durations that were used to gather the wind tunnel measurements.

5.1.1. Run 9 Analysis of Variance

Using the principles discussed in subsection 2.3.3 and detailed in [44], the Sum of Squares (SS) for each group of C_L samples was calculated. Six repeat measurements were made in each repeat of Run 9, resulting in five degrees of freedom for each run. The results for the SS are shown in Table 5.1. Taking the square root of the total SS divided by the total df results in the pooled C_L standard error across all three repeat runs.

Variable	Run			Total
	9a	9b	9c	
SS	2.0562×10^{-7}	2.7853×10^{-7}	1.2686×10^{-6}	1.7528×10^{-6}
df	5	5	5	15

Table 5.1: Range 2 C_L Sum of Squares (SS) and degrees of freedom (df) for Runs 9a, 9b, and 9c

Next, looking at the variance between runs, that is, the variance between each run's mean C_L, the variance *due* to block effect can later be assessed for significance. Taking the difference between each run's average C_L value, indicated by μ_i, and the pooled average $\bar{C_L}$ results in the column labeled '$\bar{C_L} - \mu_i$' in Table 5.2. The true C_L average is proprietary and not shown. The column 'Weighted' is the weighted Sum of Squares, found by multiplying the number of observations by the 'Squared' column.

Run	Rows	Average $\mathbf{C_L}$	$\mathbf{\bar{C_L} - \mu_i}$	Squared	Weighted
9a	6	μ_1	-0.0037617	1.4151×10^{-5}	8.4904×10^{-5}
9b	6	μ_2	0.00078078	6.0962×10^{-7}	3.6577×10^{-6}
9c	6	μ_3	0.002981	8.8862×10^{-6}	5.3317×10^{-5}

Table 5.2: Range 2 C_L between runs statistics by repeat

Taking the weighted SS from Table 5.2, the resulting SS due to between-run variance is found by dividing the weighted SS by the degrees of freedom available, in this case 2. This is summarized in Table 5.3 where the variance within runs and between runs is shown.

Variable	Within Runs	Between Runs	Total
df	15	2	17
SS	1.7528×10^{-6}	1.4188×10^{-4}	1.4363×10^{-4}

Table 5.3: Range 2 C_L summary of degrees of freedom (df) and Sum of Squares (SS)

With the two sources of variance in hand, the ANOVA is done. The samples' F-value is found comparing the degrees of freedom and the Mean Squares values and using Equation 2.19. As shown in Table 5.4, it is apparent that the F-value calculated is two orders of magnitude greater than the critical F-value. This indicates that, compared to the variance within each run, the variance that occurs between the repeat runs is so large that it can be said with 95% confidence that it is not explained by random variance alone. The p-value shows that there is a minuscule chance that the calculated F-value could be generated by chance. From these results, the null hypothesis that the three group C_L means are identical is rejected.

Source	SS	df	MS	F	p-value	F_{crit}
Between Columns	1.4188×10^{-4}	2	7.094×10^{-5}	607.0881	4.4522×10^{-15}	3.6823
Within Columns	1.7528×10^{-6}	15	1.1685×10^{-7}			

Table 5.4: Range 2 C_L ANOVA results for between- and within- column variation

Performing Fisher's Least Significant Difference test, it is seen that all three repeat runs differ significantly from each other. The specified significance level from Fisher is shown in Equation 5.1, and the

difference between each group mean was greater than this significance level.

$$LSD = t_{a/2,c(r-1)}\sqrt{\frac{2MS_E}{r}} = t_{0.025,15}\sqrt{\frac{2 \times (1.1685 \times 10^{-7})}{6}} = 2.1314 \times 1.9736 \times 10^{-4} = 0.421 \times 10^{-3} \tag{5.1}$$

This is visualized and verified in Figure 5.1, which shows each run's normal probability density as a function of the run's C_L mean and the pooled standard deviation for both Range 1 and 2.

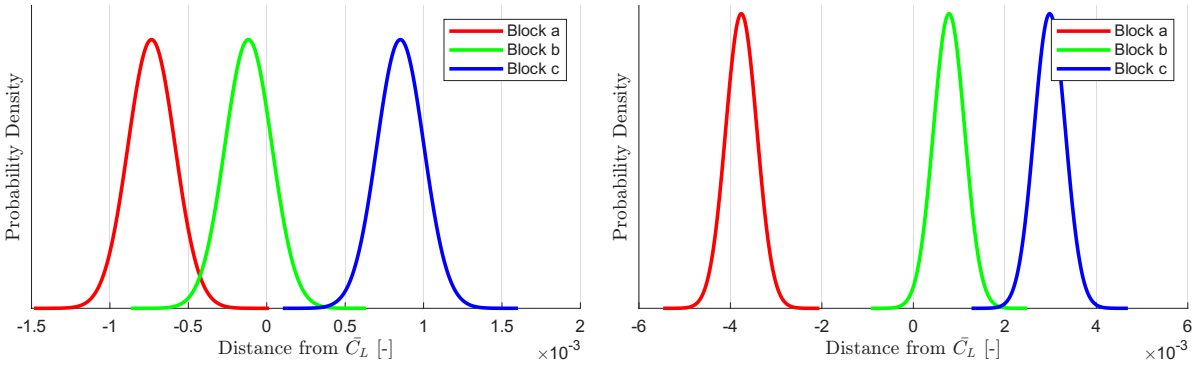

(a) Range 1 **(b)** Range 2

Figure 5.1: Repeat run sample distributions of C_L measurements from both ranges using ANOVA results

This analysis on the repeat runs Run 9a, 9b, and 9c was done for every force and moment coefficient in both ranges. All results illustrate the statistically significant block effect that is introduced when measuring data at different times during an experiment in a non-stable testing environment. Run 9a was measured on the second day of the test, Run 9b in the evening of the fourth day, and Run 9c in the morning of the fifth day. There was a model change between Run 9a and 9b, but not between 9b and 9c. It is interesting to note no consistent bias between group means is apparent as a result of the model change.

5.1.2. Experimental Error Estimation

Run 9 had a configuration with deflected flaps and spoilers, and the data was measured in the center of Range 1 and Range 2. Therefore, the ANOVA results from the Run 9 repeats were used to estimate the experimental uncertainty in each range for every force and moment response measured. Between the first and second execution of Run 9, the configuration was changed and two days separated the repeat from the initial run. The second and third execution of Run 9 were run back-to-back, but the second at the end of one day and the third at the start of the next. As such, the Run 9 repeat measurements contained both within run variability and also block effects due to configuration change, due to execution within the test, and due to time of day.

As ANOVA was used to quantify and separate the within-run and between-run variability, the between-run variability could be extracted from the Run 9 repeats and used to estimate the error introduced by configuration changes and systematic errors throughout the test. Taking only this between-run variability value for each range and response type, the variability was used as an estimate for the experimental variability for every run within the experiment. Though this was not directly fed into the fitted regression models, the estimated experimental variability was used to present the validation data, seen in section 5.2 and section 5.4. The values used can be seen in Table 5.5.

This value is considered the *estimated* experimental error because the true measurement variability is a function of all of the test variables. For example, significant model vibrations were observed at $(\alpha, \beta) = (15°, 0°)$, though the severity changed with flap and spoiler configuration. At other combinations of (α, β), less model vibration was observed. For orientations like $(\alpha, \beta) = (15°, 0°)$, the estimated experimental variability is likely lower than in reality because the onset of the model vibration might occur at slightly different conditions depending on the block effect. As a result, the estimated experimental error serves as a lower bound for the true experimental error.

$\sigma_{\mathbf{exp}}$	Range 1	Range 2
C_L	0.00200	0.00840
C_D	0.00013	0.00190
C_Y	0.00012	0.00093
$C_{l,\text{wind}}$	0.00022	0.00160
$C_{m,\text{wind}}$	0.00068	0.00420
$C_{n,\text{wind}}$	0.00004	0.00073
C_N	0.00200	0.00860
C_T	0.00016	0.00120
C_S	0.00012	0.00087
$C_{l,\text{body}}$	0.00027	0.00110
$C_{m,\text{body}}$	0.00066	0.00440
$C_{n,\text{body}}$	0.00002	0.00048

Table 5.5: Within-test standard error of aerodynamic coefficients for Range 1 and Range 2

5.1.3. Sample Duration Analysis of Variance

The ANOVA procedure was also used to analyze the effect of different sample durations. During the test, three sample groups were collected at different angles of attack and sideslip while the flaps and spoilers were deflected and while changing the duration over which a measurement was sampled. This was to assess the effect a shorter or longer sample time might have when testing with the flaps and spoilers deflected. A table of the specific conditions and durations tested can be seen in Table 5.6. The flap and all spoilers were deflected to 17.5° deflection, corresponding to configuration or whole plot 1.

Case	α	β	Sample Times	Number of Data Points Sampled
Range 1	7.5°	-7.5°	10, 15, 20 sec	3, 3, 3
Range 2	20°	-7.5°	10, 15, 20 sec	3, 3, 3
Extra	15°	0°	10, 15, 20 sec	3, 3, 3

Table 5.6: Sample durations used for repeat measurements at three unique angle of attack and sideslip conditions

By performing ANOVA on the three sets of repeat measurements taken, one set for each orientation combination, any potential differences due to the longer or shorter sample times could be assessed. The first orientation, $(\alpha, \beta) = (7.5^\circ, -7.5^\circ)$, corresponded to the center of Range 1; the second orientation $(\alpha, \beta) = (20^\circ, -7.5^\circ)$, corresponded to the center of Range 2. The third orientation, $(\alpha, \beta) = (15^\circ, 0^\circ)$, was added because it was the orientation at which the most model vibration during the test was observed. As such, the third orientation was the most likely location for there to be a significant effect due to sample duration.

Figure 5.2a, Figure 5.2b, and Figure 5.2c all show that the group means are not significantly different from each other when looking at the repeat C_L measurements. Indeed, at each orientation, the calculated F-values were less than the critical F-value, as much as by one order of magnitude for the first two cases. This was done for all force and moment data at each three orientations, and ANOVA revealed that no significant differences existed. This shows that no significant information is gained by sampling for more than 10 seconds with the flaps and spoilers deployed on the Flying V LTT model.

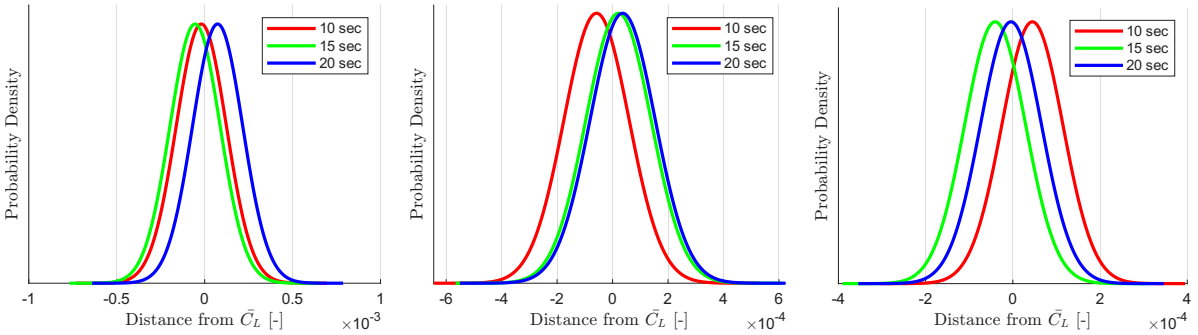

(a) Range 1 **(b)** Range 2 **(c)** Extra

Figure 5.2: Sample duration effect on C_L measurements for 10, 15, and 20 second sampling durations

5.2. Linear and Linear Mixed Models

From the results of the repeat whole plot run analysis in section 5.1, there is a justification to use Generalized Least Squares and ML/REML to model the two random error components in the experiment: one random experimental error source and one random error associated with group or block effects, i.e. due to turning the tunnel off between runs. Fitting the measurement data using OLS is no longer valid as OLS assumes each measurement point has single normally distributed source of random error, but the measurement data here has both a random error and also a block effect. Fitting OLS to this data would ignore the block effect, which would influence its ability to identify the significant effects in the model.

In this section, the differences between the fitted Linear Model and Linear Mixed Model regression results are highlighted, with a presentation of the residual diagnostics and the models' RMSE.

5.2.1. Residual Diagnostics

Comparing the C_L models for Range 1, it is seen in Figure 5.3 and Figure 5.4 how the Linear Mixed Model fitted with GLS has a slightly more normally distributed residual plot than the Linear Model fitted with OLS. Moreover, the LMM has less outliers and its residuals fall more along the normal probability line than the OLS model and its residuals do. This indicates the LMM residuals are more independently distributed when the random group effect is estimated and accounted for.

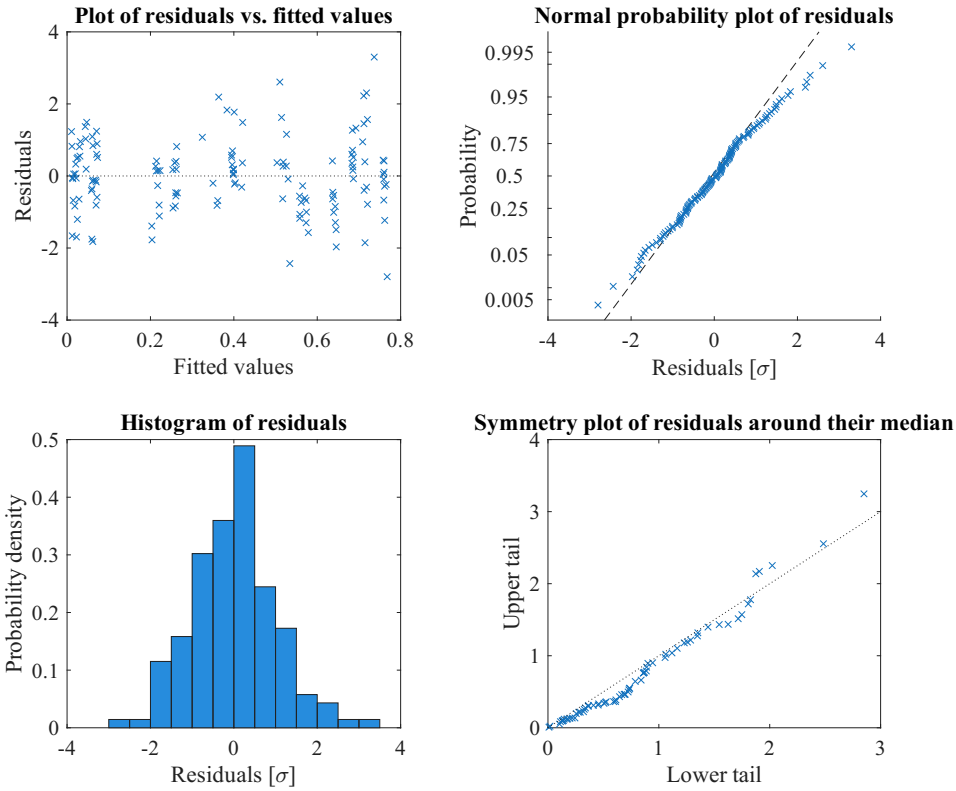

Figure 5.3: $C_{L,1}$ Linear Model residual plots

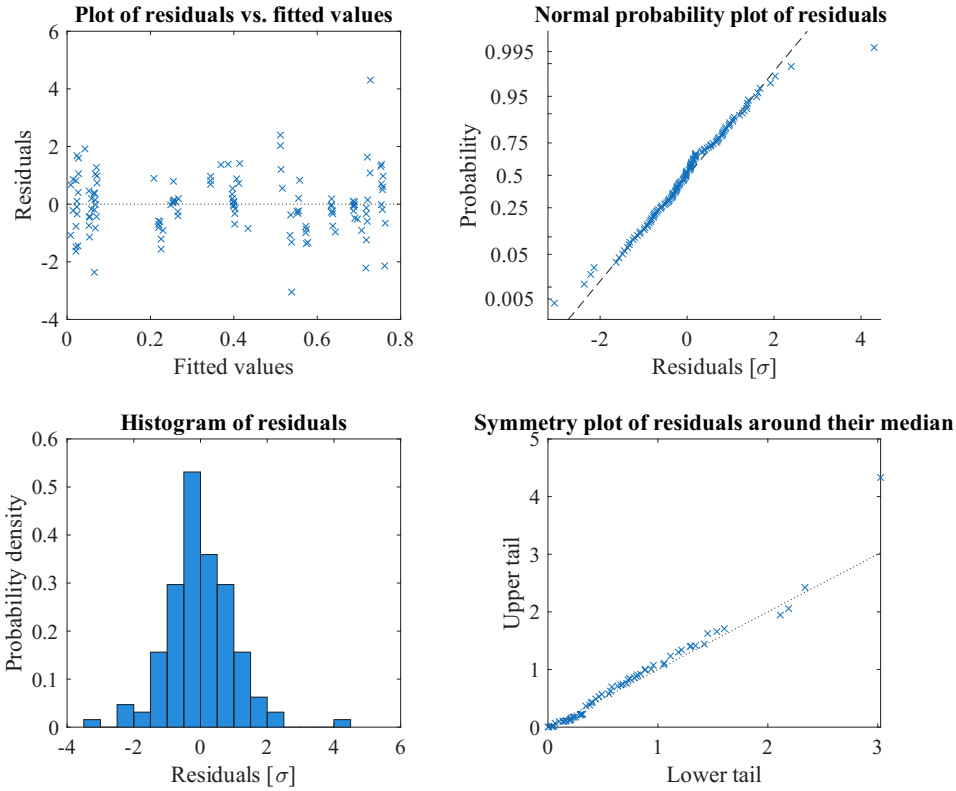

Figure 5.4: $C_{L,1}$ Linear Mixed Model residual plots

Looking at Table 5.7, it is seen how the RMSE of both models are about the same, but the real benefit from the LMM is its ability to better identify the significant model effects by estimating and separating the random error introduced by the whole plot block effect. For this LMM, the RMSE when predicted the validation data is slightly lower than for that of the LM model, which is remarkable when considering the LMM has fewer terms. For some models, including the one highlighted in Table 5.7, REML is unable to estimate the group effect, and the model residual error approaches the OLS model's RMSE.

Fit Method	RMSE	Validation RMSE	Whole Plot Block Error	Number of Terms
OLS	0.0071	0.0146	NA	19
GLS	0.0069	0.0143	0	12

Table 5.7: Range 1 C_L residual error components for OLS and GLS models

In other cases, however, REML is able to estimate the grouping random error source, as shown in Table 5.8 or in Table 5.9. For the $C_{T,1}$ model, the random effect due to configuration changes is estimated to be $\sigma_{\text{block}} = 3.0 \times 10^{-4}$, which is the same order of magnitude of the standard error between repeat runs given by the ANOVA of the repeat run measurements of C_T of $\sigma_{\text{block}} = 1.6 \times 10^{-4}$. As expected, though, the REML-identified group error estimate is larger than the ANOVA estimate because the REML estimate considered the variability in the entire test whereas the ANOVA estimate only looked at three runs.

Fit Method	RMSE	Whole Plot Block Error	Number of Terms
OLS	0.0011	NA	31
GLS	0.0011	3.0×10^{-4}	17

Table 5.8: Range 1 C_T residual error components for OLS and GLS models

For the $\Delta C_{L,1}$ model, the random effect due to configuration changes is estimated to be $\sigma = 0.0037$, which is close to the standard error between repeat runs given by the ANOVA of the repeat run measurements of $C_{L,1}$ of $\sigma_{exp} = 0.0020$. Again, the REML estimate is larger than the ANOVA estimate as exepected.

Fit Method	RMSE	Whole Plot Block Error	Number of Terms
OLS	0.0107	NA	21
GLS	0.0068	0.0037	12

Table 5.9: Range 1 ΔC_L residual error components for OLS and GLS effects models

5.2.2. Synthesis

The results highlighted in this section and in section 5.1 demonstrate how using ML/REML and GLS to analyze and model the measured wind tunnel data is necessitated. This is because the test design is unreplicated and not balanced and because the data contains at least two sources of variance. If the test design was balanced or completely replicated, then simpler methods like OLS could be used to analyze the data [52]. However, the time needed to measure the amount of replicated points and blocks needed to achieve such a test design ought to be compared with the value of *different*, unreplicated, unique data points being measured in that same time, especially when suitable, alternative methodologies exist to analyze such data. ML/REML and GLS are used to fit the regression models used to predict the responses shown in the remainder of this chapter. The methodology used is the same as that described in subsection 2.3.1 and subsection 3.5.3.

For several of the LMMs fit to both the full and effects coefficients, REML was unable to provide an estimate for the grouping random error effect that was nonzero, though the reason why is not entirely

clear. It is suspected the data set is likely too small for those models, and not enough variation within each subplot existed to accurately estimate the whole plot offsets. For example, nearly half of the whole plots contained only a single subplot data point per subrange that was repeated within the whole plot, as described by the CCD space selection design.

5.3. Fitted Model Validation

After fitting the regression models to the gathered measurements, the models performance were validated using validation data held apart during the model regression. The RMSE of the predictions and the visual plotting of the model predictions versus the validation data were used to assess the models' validity. Both efforts are highlighted in the following subsections.

5.3.1. Validation Residual Error

The RMSE calculated from the validation data points and the models' predictions of those data points was generally around twice the RMSE of the models themselves. This indicates that the validation data is not well predicted by the models within the models' error. A table highlighting the model RMSE and the RMSE when compared to the validation data can be seen below in Table 5.10.

Coefficient	Full Models			Effects Models		
	$RMSE_{Validation}$	$RMSE_{Model}$	Val/Model	$RMSE_{Validation}$	$RMSE_{Model}$	Val/Model
$C_{N,1}$	0.0120	0.0065	1.85	0.0108	0.0065	1.66
$C_{N,2}$	0.0313	0.0127	2.46	0.0207	0.0134	1.55
$C_{T,1}$	0.0032	0.0011	2.91	0.0029	0.0010	2.90
$C_{T,2}$	0.0046	0.0016	2.88	0.0030	0.0019	1.58
$C_{S,1}$	0.0043	0.0016	2.69	0.0030	0.0019	1.58
$C_{S,2}$	0.0062	0.0036	1.72	0.0056	0.0054	1.04
$C_{l,\text{body},1}$	0.0022	0.0012	1.83	0.0023	0.0013	1.77
$C_{l,\text{body},2}$	0.0051	0.0022	2.32	0.0049	0.0029	1.69
$C_{m,\text{body},1}$	0.0084	0.0045	1.87	0.0071	0.0036	1.97
$C_{m,\text{body},2}$	0.0183	0.0141	1.30	0.0139	0.0088	1.58
$C_{n,\text{body},1}$	0.0022	0.0006	3.67	0.0013	0.0007	1.86
$C_{n,\text{body},2}$	0.0026	0.0009	2.89	0.0022	0.0020	1.10
$C_{L,1}$	0.0143	0.0069	2.07	0.0115	0.0068	1.69
$C_{L,2}$	0.0369	0.0192	1.92	0.0202	0.0131	1.54
$C_{D,1}$	0.0041	0.0015	2.73	0.0025	0.0011	2.27
$C_{D,2}$	0.0078	0.0039	2.00	0.0068	0.0044	1.55
$C_{Y,1}$	0.0046	0.0018	2.56	0.0034	0.0021	1.62
$C_{Y,2}$	0.0044	0.0028	1.57	0.0056	0.0052	1.08
$C_{l,\text{wind},1}$	0.0022	0.0014	1.57	0.0018	0.0015	1.20
$C_{l,\text{wind},2}$	0.0031	0.0019	1.63	0.0031	0.0022	1.41
$C_{m,\text{wind},1}$	0.0093	0.0039	2.38	0.0079	0.0036	2.19
$C_{m,\text{wind},2}$	0.0205	0.0100	2.05	0.0164	0.0089	1.84
$C_{n,\text{wind},1}$	0.0023	0.0006	3.83	0.0014	0.0008	1.75
$C_{n,\text{wind},2}$	0.0033	0.0011	3.00	0.0023	0.0010	2.30

Table 5.10: Validation and model RMSE values and their ratios (rounded to 2 decimal places) for each aerodynamic model and effects model

Looking at Table 5.10, a few generalizations can be made. First, the Range 1 models have less residual error than the Range 2 models. This is expected, as the Range 2 response behavior is harder to model with low-order polynomials due to the increased amount of vortex breakdown at the higher angles of attack and sideslip, leading to more dramatic changes in the response trends. Second, the full models and effects models both have similar residual error, though the effects models tend to have higher RMSE values for Range 2. This is likely an artifact of the number of terms in the full models versus the effects models. As Figure 5.5 shows, the full models have more terms than the corresponding effects

models for any range or coefficient.

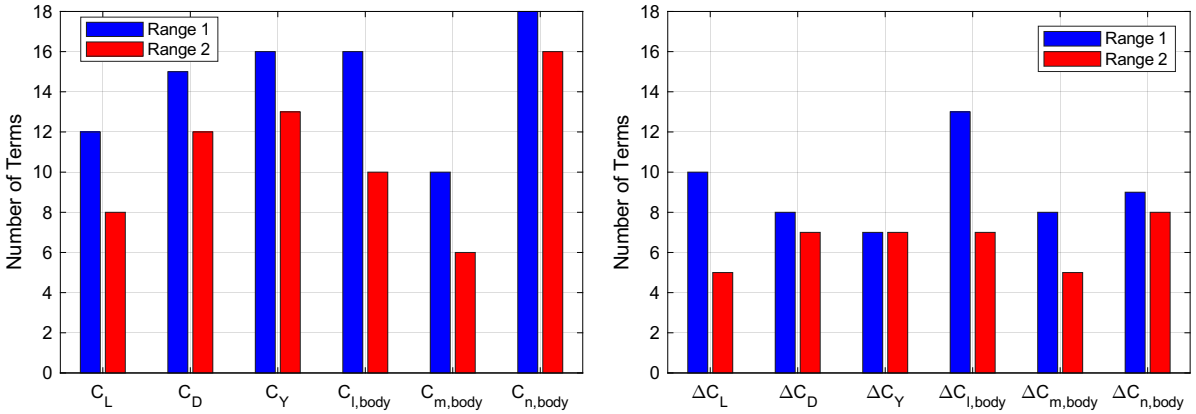

(a) Full models **(b)** Effects models

Figure 5.5: Number of terms in Linear Mixed Models for wind axes forces and body axes moments

The third generalization and observation made is that no model interprets the validation data within its own RMSE; all ratios of validation RMSE to model RMSE are greater than 1. However, this is to be expected, as the models are optimized for the data they are fitting and not for unknown predictions. Comparing the relative size of the validation RMSE to fitted RMSE, it can be seen if the model provides useful predictions by noting how much error the models have predicting the validation data relative to their inherit error. Table 5.10 shows that the ratios of validation to model RMSE is quite high for most models, with only a few ratios below 1.5, but the effects models tend to have lower ratios than the full models, suggesting better predictive performance.

Table 5.11 shows the coefficient of determination for each model, which highlights the amount of variability in the fitted data the models are able to explain. The table shows most of the full models explain the variability in the wind tunnel data quite well, 98-99% for almost every model. The effects models, however, aren't as accurate, especially for the Range 2 models. This reflects the higher variance observed in the data in that range, as indicated by the higher values in Table 5.5.

Model	Full Models	Effects Models
	$\mathbf{R^2_{adj}}$	$\mathbf{R^2_{adj}}$
$C_{N,1}$	0.99	0.94
$C_{N,2}$	0.99	0.68
$C_{T,1}$	0.99	0.97
$C_{T,2}$	0.99	0.87
$C_{S,1}$	0.99	0.84
$C_{S,2}$	0.99	0.83
$C_{l,\text{ body},1}$	0.99	0.73
$C_{l,\text{ body},2}$	0.98	0.49
$C_{m,\text{ body},1}$	0.97	0.67
$C_{m,\text{ body},2}$	0.82	0.46
$C_{n,\text{ body},1}$	0.99	0.80
$C_{n,\text{ body},2}$	0.99	0.72
$C_{L,1}$	0.99	0.93
$C_{L,2}$	0.98	0.68
$C_{D,1}$	0.99	0.97
$C_{D,2}$	0.99	0.66
$C_{Y,1}$	0.99	0.82
$C_{Y,2}$	0.97	0.84
$C_{l,\text{ wind},1}$	0.98	0.58
$C_{l,\text{ wind},2}$	0.99	0.58
$C_{m,\text{ wind},1}$	0.98	0.66
$C_{m,\text{ wind},2}$	0.89	0.47
$C_{n,\text{ wind},1}$	0.99	0.81
$C_{n,\text{ wind},2}$	0.99	0.93

Table 5.11: R^2_{adj} values (2 significant digits) for each aerodynamic model and effects model

5.3.2. Validation Plotting

The last way to validate the fitted models is to plot the models' predictions against the measured and reserved validation data. This quickly identifies model overfitting, incorrect model structures, and local areas that could use more data and improvement. Some example validation plots are given for a few models below. More validation plots are provided for the ΔC_L, ΔC_D, ΔC_Y, $\Delta C_{l,\text{body}}$, $\Delta C_{m,\text{body}}$, and $\Delta C_{n,\text{body}}$ models in Appendix C.

$\Delta C_{n,\text{ body},2}$ Effects Model

As Figure 5.6 shows, the validation data for the alpha sweep at zero sideslip are scattered around a constant value, which makes sense: there shouldn't be a change in yawing moment at symmetric flow conditions with symmetric flap and spoiler deflections. The model predictions encompass most of the validation data with its confidence intervals, though the slope of the zero sideslip predictions might be incorrect.

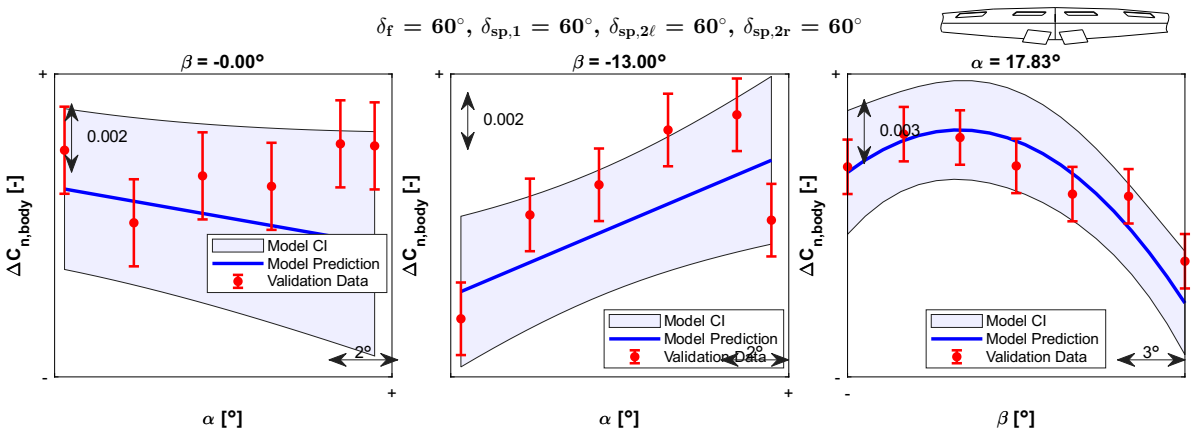

Figure 5.6: $\Delta C_{n,\text{ body},2}$ effects model validation: full deflections

The interpolation configuration case shown in Figure 5.7 shows great model predictions for the symmetric alpha sweep on the left, and the model does a decent job of encompassing the rest of the data. Looking at the plots, it is apparent that the model predicts most, but not all, of the variability of the data, leading to a moderate R^2_{adj} value of $R^2_{\text{adj}} = 0.72$.

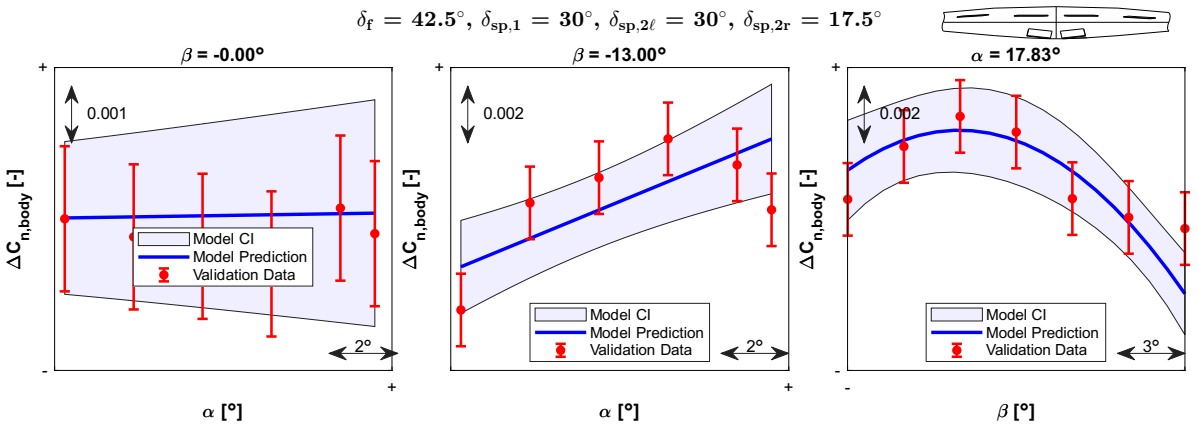

Figure 5.7: $\Delta C_{n,\text{ body},2}$ effects model validation: interpolation configuration

$\Delta C_{L,1}$ Effects Model

The $\Delta C_{L,1}$ effects model shows some better accuracy when looking at Figure 5.8 and Figure 5.9. Figure 5.8 pretty well captures the overall data trends and predicts the validation data within its CI. In Figure 5.9, The model underpredicts the interpolation alpha sweep for zero sideslip. Also, the validation data for the change in lift with sideslip seems scattered with a sharp change halfway through the sweep. It's not a surprise that the $\Delta C_{L,1}$ model predicts a simpler trend for this sideslip sweep since the model fits average trends and doesn't well capture sharp discontinuities.

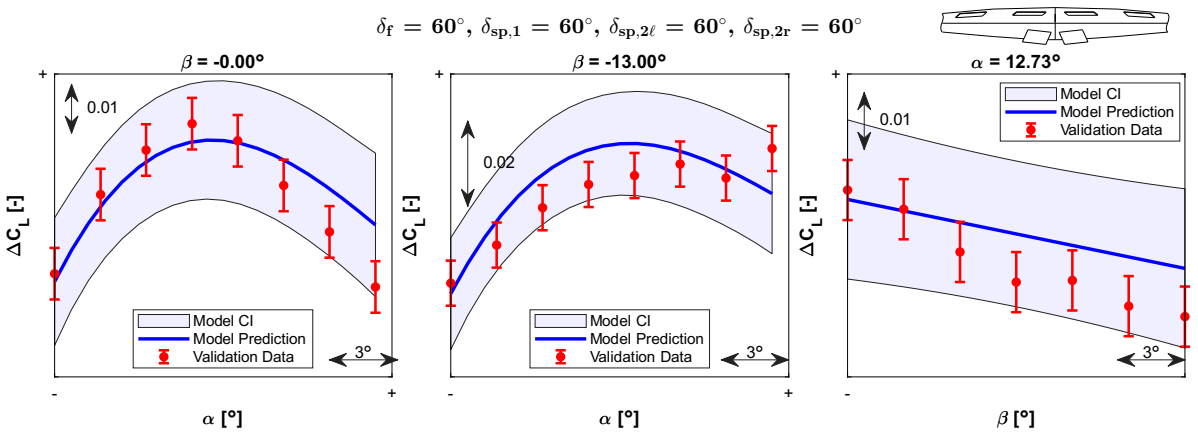

Figure 5.8: $\Delta C_{L,1}$ effects model validation: full deflections

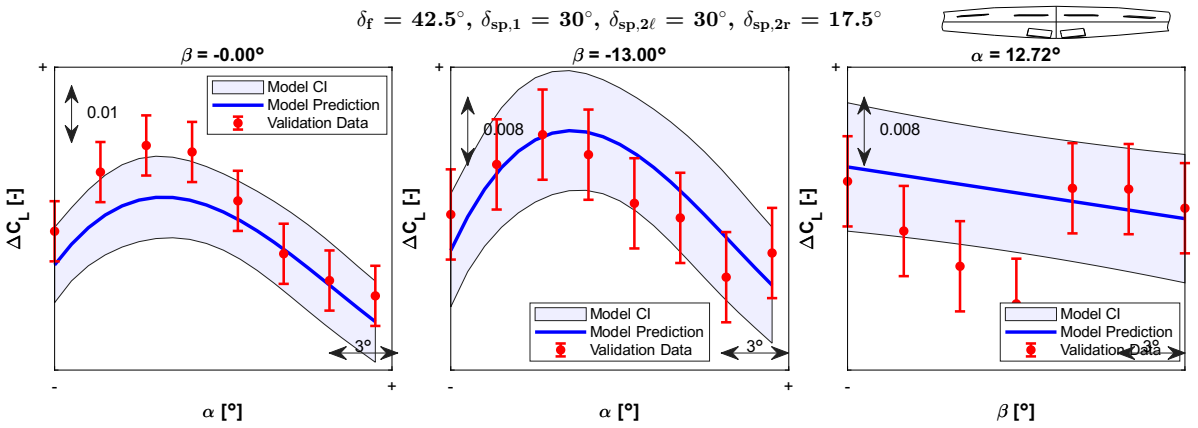

Figure 5.9: $\Delta C_{L,1}$ effects model validation: interpolation configuration

5.4. Flap and Spoiler Effects

Once the wind tunnel measurement data was processed, formatted, and fit, the fitted regression models and the measured configuration data were used to analyze the split flap, spoiler, and sideslip effects on the Flying V and assess the interactions between them. This section highlights the identified significant interaction effects using the models only, both by looking at the model information and by using the models to predict different trends of interest.

In subsection 5.4.1, the data measured for the flaps alone and spoilers alone configurations in the LTT is compared against the corresponding data measured in the OJF. The fitted effect models' structures are presented in subsection 5.4.2 for the body axis forces and moments. The significant interaction effects between the flap and spoiler devices, as indicated by the model terms, are discussed in subsection 5.4.3. In subsection 5.4.4, these interaction effects are plotted and visualized. Next, in subsection 5.4.5, the changing spoiler effects in sideslip are examined using the model predictions. The same is done for the flap effects in subsection 5.4.6. Lastly, subsection 5.4.7 covers the combined flap and spoiler effects and how the predictions change with sideslip.

5.4.1. Cross-Tunnel Comparisons

The change in C_L for flap and spoiler deflections measured in this experiment compared to the results measured in the OJF experiments is shown in Figure 5.10. Interesting to note is the difference in magnitudes between the trends: for both the flap and the spoiler deflections, the LTT data shows less effectiveness than the OJF data. For the flap effectiveness shown in Figure 5.10a, the maximum ΔC_L

achieved is about 20% lower in the LTT than in the OJF. The half deflection flap performs almost half as well in the LTT as it does in the OJF for almost all angles of attack.

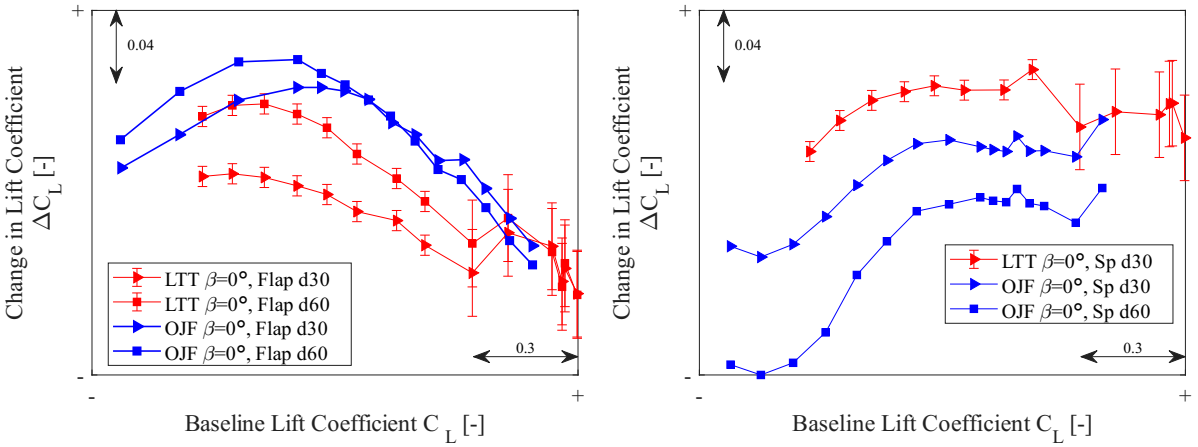

(a) LTT and OJF flap ΔC_L effects comparison [4]

(b) LTT and OJF spoiler ΔC_L effects comparison [5]

Figure 5.10: LTT vs OJF flap and spoiler effects comparison at zero sideslip

For the spoiler lift dumping effect shown in Figure 5.10b, only the half deflection configuration was directly measured in the LTT. The lift dumping trend looks quite similar to the OJF data with an almost constant intercept offset. The discrepancy between the OJF and LTT spoiler results most likely come down to differences in the underlying Flying V geometry and the resulting flowfield. For example, the spoiler designs on the OJF were installed at a 61° sweep angle, but the LTT inboard spoiler is swept back further to a 64.3° angle and the outboard spoilers to a 58.8° angle. This alone likely explains most of the difference seen in Figure 5.10b.

At $\delta_{sp} = 30°$ it appears the half deflection spoilers in the LTT actually generate a small amount of lift at the mid range of angles of attack. This was actually observed by Erdinçler in his research for this spoiler design in a slightly more aft location, as shown in Figure 2.14. It is possible this indicates the current spoiler design on the newly-optimized Flying V geometry might be too far aft. Alternatively, Erdinçler notes that these adverse spoiler effects can occur from a flow separation bubble caused by separation over the spoiler and reattachment behind the spoiler and before the aircraft wing trailing edge. This separation bubble would create a region of low pressure on the suction side of the wing, lessening the lift dumping effects of the spoilers. If this is the culprit phenomenon, these adverse effects at low spoiler deflections might be avoided by increasing the spoiler panel chord length. These possibilities and more are discussed in more detail in subsection 5.5.5.

Because the $\delta_{sp} = 60°$ configuration was not directly measured in this LTT test campaign, the fitted models are used to predict the maximum lift dumping achieved by the max spoiler deflections with some uncertainty in Figure 5.16. The comparison of the predicted maximum lift dumped by the spoilers in the LTT is compared with the OJF results in subsection 5.4.5.

It is important to remember that the data presented in Figure 5.10 is entirely uncorrected for the different test environments used to gather both batches of data. The OJF-specific open-jet wind tunnel corrections are different from the LTT-specific closed test section wind tunnel corrections. Additionally, the model geometries used in the OJF and the LTT are both different after accounting for the scale difference. Lastly, the presence of the aft strut rod near the flaps in the LTT and the presence of the splitter plate the OJF semi-span model is mounted to both have different effects on the flow close to the root of the model, further obscuring the significance of the comparisons made here.

5.4.2. Body Force and Moment Effects Models

The identified model structures for the flap and spoiler effects models in the body axis forces and moments are displayed in this section. Due to confidentiality constraints, the coefficient estimates found for each term are not presented in this report. In practice, each term presented in the model structure

is multiplied by some coefficient to scale that term. The rest of the effects models for the wind axis forces and moments are displayed in Appendix B, along with the identified model structures for the full force and moment models. As there is no change in a force or moment due to no surface deflection–all variables set to zero–there is no intercept for these effects models.

$$\begin{aligned}\Delta C_{N,1} = {} & \alpha + \delta_f + \delta_{sp,2r} \\ & + \alpha \cdot \delta_{sp,1} + \delta_{sp,1} \cdot \delta_{sp,2\ell} + \beta \cdot \delta_{sp,2r} \\ & + \alpha^2 + \delta_f^2 + \alpha \cdot \beta \cdot \delta_{sp,1} \\ & + \alpha \cdot \delta_{sp,1} \cdot \delta_{sp,2\ell} + (\alpha^2) \cdot \delta_{sp,1} + (\beta^2) \cdot \delta_{sp,2\ell} \\ & + \alpha^3 + \delta_f^3\end{aligned}$$

$$\begin{aligned}\Delta C_{N,2} = {} & \beta + \delta_f + \delta_{sp,2r} \\ & + \alpha \cdot (\beta^2) + (\alpha^2) \cdot \delta_f + \beta \cdot (\delta_f^2) \\ & + \alpha \cdot (\delta_{sp,1}^2) + (\beta^2) \cdot \delta_{sp,2r}\end{aligned}$$

$$\begin{aligned}\Delta C_{T,1} = {} & \delta_f + \alpha \cdot \delta_f + \delta_f \cdot \delta_{sp,1} \\ & + \delta_{sp,1}^2 + \alpha \cdot \beta \cdot \delta_{sp,2\ell} + \delta_f \cdot \delta_{sp,1} \cdot \delta_{sp,2\ell} \\ & + (\alpha^2) \cdot \delta_f + \beta \cdot (\delta_f^2) + (\alpha^2) \cdot \delta_{sp,2\ell} \\ & + \delta_f^3\end{aligned}$$

$$\begin{aligned}\Delta C_{T,2} = {} & \delta_f + \beta \cdot \delta_{sp,1} + \delta_f \cdot \delta_{sp,1} \\ & + \alpha \cdot \beta \cdot \delta_f + \alpha \cdot \beta \cdot \delta_{sp,1} + \alpha \cdot \delta_f \cdot \delta_{sp,1} \\ & + (\beta^2) \cdot \delta_f + (\alpha^2) \cdot \delta_{sp,1} + \delta_f \cdot (\delta_{sp,1}^2) \\ & + (\delta_{sp,2\ell}^2) \cdot \delta_{sp,2r} + \delta_f^3\end{aligned}$$

$$\begin{aligned}\Delta C_{S,1} = {} & \alpha \cdot \beta + \alpha \cdot \beta \cdot \delta_f + \alpha \cdot \beta \cdot \delta_{sp,1} \\ & + \beta \cdot \delta_f \cdot \delta_{sp,1} + \alpha \cdot (\beta^2) + (\alpha^2) \cdot \delta_{sp,2\ell} \\ & + (\delta_f^2) \cdot \delta_{sp,2\ell} + (\alpha^2) \cdot \delta_{sp,2r} + \delta_f \cdot (\delta_{sp,2r}^2)\end{aligned}$$

$$\begin{aligned}\Delta C_{S,2} = {} & \alpha \cdot \beta + \alpha \cdot \delta_{sp,1} + \delta_{sp,2\ell}^2 \\ & + \alpha \cdot \beta \cdot \delta_f + \alpha \cdot \delta_f \cdot \delta_{sp,2r} + \beta \cdot (\delta_f^2) \\ & + \beta^3\end{aligned}$$

$$\begin{aligned}\Delta C_{l,\text{body},1} = {} & \delta_f + \beta \cdot \delta_{sp,2\ell} + \delta_f \cdot \delta_{sp,2\ell} \\ & + \alpha \cdot \delta_{sp,2r} + \delta_{sp,2r}^2 + \alpha \cdot \beta \cdot \delta_f \\ & + (\alpha^2) \cdot \beta + \alpha \cdot (\beta^2) + (\beta^2) \cdot \delta_f \\ & + (\beta^2) \cdot \delta_{sp,2\ell} + \alpha \cdot (\delta_{sp,2\ell}^2) + \alpha^3 \\ & + \delta_{sp,2\ell}^3\end{aligned}$$

$$\begin{aligned}\Delta C_{l,\text{body},2} = {} & \delta_f + \alpha \cdot \delta_f + \beta \cdot \delta_{sp,1} \\ & + \alpha \cdot \beta \cdot \delta_{sp,1} + \beta \cdot \delta_f \cdot \delta_{sp,1} + (\beta^2) \cdot \delta_{sp,1} \\ & + \delta_{sp,1}^3\end{aligned}$$

$$\begin{aligned}\Delta C_{m,\text{body},1} = {} & \alpha \cdot \delta_{sp,2\ell} + \delta_{sp,2\ell} \cdot \delta_{sp,2r} + \delta_{sp,1}^2 \\ & + \delta_{sp,2\ell}^2 + \alpha \cdot \beta \cdot \delta_{sp,2\ell} + (\alpha^2) \cdot \beta \\ & + (\alpha^2) \cdot \delta_{sp,2\ell} + \alpha \cdot (\delta_{sp,2\ell}^2)\end{aligned}$$

$$\begin{aligned}\Delta C_{m,\text{body},2} = {} & \alpha \cdot \beta + \delta_{sp,1}^2 + \alpha \cdot \beta \cdot \delta_f \\ & + \alpha \cdot (\beta^2) + (\alpha^2) \cdot \delta_{sp,1}\end{aligned}$$

$$\begin{aligned}\Delta C_{n,\text{body},1} = {} & \alpha \cdot \beta + \alpha \cdot \delta_{sp,1} + \delta_f^2 \\ & + \alpha \cdot \beta \cdot \delta_f + \beta \cdot \delta_f \cdot \delta_{sp,2\ell} + \alpha \cdot (\beta^2) \\ & + (\alpha^2) \cdot \delta_{sp,2\ell} + (\alpha^2) \cdot \delta_{sp,2r} + \beta \cdot (\delta_{sp,2r}^2)\end{aligned}$$

$$\begin{aligned}\Delta C_{n,\text{body},2} = {} & \beta \cdot \delta_f + \alpha \cdot \delta_{sp,1} + \delta_{sp,2\ell}^2 \\ & + \alpha \cdot \beta \cdot \delta_f + \alpha \cdot \delta_{sp,2\ell} \cdot \delta_{sp,2r} + (\beta^2) \cdot \delta_f \\ & + \alpha \cdot (\delta_f^2) + \alpha \cdot (\delta_{sp,1}^2)\end{aligned}$$

5.4.3. Significant Interactions

Looking at the fitted models in subsection 5.4.2 and in Appendix B, the significant interaction effects can be identified from the models' formulae. Table 5.12 shows the flap and spoiler interaction groups for the full coefficient models, and Table 5.13 shows the interaction groups for the effects models. For simplicity, the significant interaction effects shown in Table 5.12 and Table 5.13 only contain the significant interactions between the flap and spoiler variables: no interactions with angle of attack or sideslip

are shown. For example, if the term $(\beta \cdot \delta_f \cdot \delta_{sp,1})$ exists in a model, it is displayed in the table as $(\delta_f \cdot \delta_{sp,1})$, with a shared group id in the 'δ_f' column and in the 'δ_{sp1}' column, to highlight which surfaces have any manner of interaction. This is done to make it more clear to identify which surfaces interact. The sideslip-dependent interactions will be discussed later.

Response	$\delta_{\mathbf{f}}$	$\delta_{\mathbf{sp,1}}$	$\delta_{\mathbf{sp,2\ell}}$	$\delta_{\mathbf{sp,2r}}$	$\delta^{\mathbf{2}}_{\mathbf{f}}$	$\delta^{\mathbf{2}}_{\mathbf{sp,1}}$	$\delta^{\mathbf{2}}_{\mathbf{sp,2\ell}}$	$\delta^{\mathbf{2}}_{\mathbf{sp,2r}}$
$C_{L,1}$		2	1,2	1,2				
$C_{L,2}$								
$C_{D,1}$			1	1				
$C_{D,2}$								
$C_{Y,1}$	2	1	2	1				
$C_{Y,2}$	1	2	1	2				
$C_{l,\text{ wind},1}$								
$C_{l,\text{ wind},2}$								
$C_{m,\text{ wind},1}$								
$C_{m,\text{ wind},2}$								
$C_{n,\text{ wind},1}$	1,2	2	1	3			3	
$C_{n,\text{ wind},2}$	1	1						
$C_{N,1}$		1	1	1				
$C_{N,2}$	1	1						
$C_{T,1}$								
$C_{T,2}$		1	1					
$C_{S,1}$	1,2	1,2	3	2	3			
$C_{S,2}$		1						1
$C_{l,\text{ body},1}$	2		1,2	1				
$C_{l,\text{ body},2}$	1	1						
$C_{m,\text{ body},1}$								
$C_{m,\text{ body},2}$								
$C_{n,\text{ body},1}$	1		1,2	2				
$C_{n,\text{ body},2}$								

Table 5.12: Full Linear Mixed Models significant interactions.
A common number indicates an interaction term

An interesting observation when comparing Table 5.12 and Table 5.13 is that the effects models in Table 5.13 generally contain more interaction terms. This result is obscured by the findings in section 5.3, where it was seen that the effects models generally had lower descriptive power as indicated in their R^2_{adj} value. In other words, the effects models have more interaction terms than the full models do yet describe the measurement data less well. Additionally, not all interactions identified in Table 5.12 are present in Table 5.13.

One reason the full models may contain fewer interaction terms between flaps and spoilers is that a larger portion of the variability in the measured data can be attributed to angle of attack and sideslip alone. Even in the absence of flap and spoiler deflections, the Flying V generates aerodynamic forces and moments as a function of flow conditions and model orientation. When fitting models to the full coefficients, these baseline effects dominate the response, reducing the *relative* influence, and thus the statistical visibility, of configuration-specific interactions. This means different flap or spoiler effects might be missed by the full models. In contrast, the effects models are built from the difference between each configuration and the clean case. Since the clean aircraft contribution has been subtracted, all remaining variability must be explained entirely by the configuration changes and their interactions with angle of attack and sideslip. This makes flap and spoiler interaction effects more prominent in the fitted models.

This might also explain why some terms in the full models are not present in the effects models: once the clean aircraft contribution is removed, the variability associated to a given interaction can be more accurately decomposed into different effects. For example, the $C_{L,1}$ model identified a $(\delta_{sp,1} \cdot \delta_{sp,2\ell} \cdot$

Response	$\delta_{\mathbf{f}}$	$\delta_{\mathbf{sp,1}}$	$\delta_{\mathbf{sp,2\ell}}$	$\delta_{\mathbf{sp,2r}}$	$\delta^{\mathbf{2}}_{\mathbf{f}}$	$\delta^{\mathbf{2}}_{\mathbf{sp,1}}$	$\delta^{\mathbf{2}}_{\mathbf{sp,2\ell}}$	$\delta^{\mathbf{2}}_{\mathbf{sp,2r}}$
$\Delta C_{L,1}$		1	1,2	2				
$\Delta C_{L,2}$								
$\Delta C_{D,1}$	2	2	1	1				
$\Delta C_{D,2}$								
$\Delta C_{Y,1}$	1		1					
$\Delta C_{Y,2}$	1			1				
$\Delta C_{l,\text{ wind},1}$								
$\Delta C_{l,\text{ wind},2}$	1	1		2	2			
$\Delta C_{m,\text{ wind},1}$								
$\Delta C_{m,\text{ wind},2}$	1	1						
$\Delta C_{n,\text{ wind},1}$	1		1,2	2				
$\Delta C_{n,\text{ wind},2}$	1,2	1,3	2					3
$\Delta C_{N,1}$		1	1					
$\Delta C_{N,2}$								
$\Delta C_{T,1}$	1	1	1					
$\Delta C_{T,2}$	1	1		2			2	
$\Delta C_{S,1}$	1,3	1	2		2			3
$\Delta C_{S,2}$	1			1				
$\Delta C_{l,\text{ body},1}$	1		1					
$\Delta C_{l,\text{ body},2}$	1	1						
$\Delta C_{m,\text{ body},1}$			1	1				
$\Delta C_{m,\text{ body},2}$								
$\Delta C_{n,\text{ body},1}$	1		1					
$\Delta C_{n,\text{ body},2}$			1	1				

Table 5.13: Effects Linear Mixed Models significant interactions.
A common number indicates an interaction term

$\delta_{sp,2r}$), effect, but the $\Delta C_{L,1}$ model split it into two terms: $(\delta_{sp,1} \cdot \delta_{sp,2\ell})$ and $(\delta_{sp,2\ell} \cdot \delta_{sp,2r})$. Alternatively, it is possible the full models misattributed effects to the flaps and spoilers that were in reality effects due to the Flying V orientation.

It is also noteworthy that the body-axis moment effects models generally contain fewer interaction terms than the wind-axis moment models. This may be because body-axis moments are more directly driven by the aerodynamic forces resulting from surface deflections, making them simpler functions of those inputs. In contrast, wind-axis moments are more complex, as they are derived from a combination of body-axis components and influenced by changes in orientation, introducing compounded dependencies. The opposite case is seen for the full moment models, with the exception of $C_{n,\text{ wind},1}$ and $C_{n,\text{ wind},2}$, where the body-axis moments have more terms than the wind-axis moments.

Interestingly, the body axis side-force full model and effects model, $C_{S,1}$ and $\Delta C_{S,1}$, exhibit the highest number of interactions between flap and spoiler deflections. This could be due to the sensitivity of the flow symmetry at zero sideslip. Under ostensibly symmetric conditions, even slight misalignments in yaw or small asymmetries in flap or spoiler deployment can disturb the vortex structures on either side of the Flying V, as shown in previous Flying V experiments and in other research [65], [68]. Taking just the example of the model yaw, the turntable required alignment in yaw each morning using a laser system. The repeatability of the alignment is within $\psi = \pm 0.2°$, the turntable accuracy is $\psi = \pm 0.001°$, and the alignment is ultimately made by eye and prone to human error. Even a small offset of $\beta = +0.1°$ could disrupt symmetry and cause asymmetric vortex development over the wings. Any potential disturbances are likely amplified by surface deflections, particularly flaps, leading to pronounced interactions between flap and spoiler effects in the side-force response.

A somewhat surprising result is the significant interaction between the outboard port and starboard spoilers for both the $C_{D,1}$ and $\Delta C_{D,1}$ models. The term $\delta_{sp,2\ell} \cdot \delta_{sp,2r}$ indicates that the increase in drag due to the outboard port and starboard spoilers is not simply a superposition of their individual effects

but that $\Delta C_{D,1}|(\delta_{sp,2\ell} \cdot \delta_{sp,2r}) \neq \Delta C_{D,1}|\delta_{sp,2\ell} + \Delta C_{D,1}|\delta_{sp,2r}$, where "|" indicates "due to a deflection of". This suggests that a deflection of one outboard spoiler does more than just locally spoil the lift over that portion of the wing or introduce localized flow separation but may even induce a change in the flow over the other wing and thus over the other spoiler. When plotting the model predictions, it appears the effect of this interaction is a slight reduction This is likely due to the Flying V's vortical flow, as discussed above and indicated by [68].

If a deflection of the outboard port spoiler introduces an increase of pressure halfway down the wing, the primary vortex structure upstream of the deflected spoiler will likely change, which in turn, will likely affect the complimentary vortex structure on the other half of the aircraft. In this way, an interaction between the outboard spoiler surfaces might exist. This might also explain the similar $\delta_{sp,2\ell} \cdot \delta_{sp,2r}$ interactions on the $\Delta C_{m,\text{ body},1}$ model, though, without flow visualization or pressure measurements, these descriptions are merely speculative.

In summary, for all forces and moments in the wind-axis effects models, at least one range has a significant interaction between the flap and a spoiler group. The only exception is ΔC_L, which is reflected in a similar lack in interactions in ΔC_N, C_L, and $C_{N,1}$. Additionally, the $\Delta C_{m,\text{ body}}$ effects models show no flap and spoiler interactions. However, the $\Delta C_{m,\text{ body}}$ effects models have relatively low R^2_{adj} values of 0.67 and 0.46 for Ranges 1 and 2, respectively, indicating that, if there was a true a flap-spoiler interaction, it is possible the model didn't capture it.

5.4.4. Change in Spoiler Effects Due to Flap Deflection

When deflected together, the flap and spoiler effects on the Flying V forces and moments interact and change, as indicated by the first column in the interactions tables Table 5.12 and Table 5.13. In some cases, the combined flap and spoiler effect on changing lift coefficient is simply the sum of the flap alone and the spoiler alone effects, such as at the 30° deflection case at zero sideslip. This is illustrated in Figure 5.11, where the measured data points are the statistically the same for the lift dumped by the spoilers relative to the clean model and also relative to the $\delta_f = 30°$ configuration. This is notated by the following:

$$\Delta C_L|_{\delta_{sp=30}} = C_L(\delta_{sp=30}) - C_{L,\text{clean}}$$
$$(\Delta C_L|_{\delta_{sp=30}})_{\text{wrt } \delta_f} = C_L(\delta_{f=30}, \delta_{sp=30}) - C_L(\delta_{f=30})$$

The sharp step change in the model predictions from the left side of the figure to the right seen in Figure 5.11 and the other figures in this subsection is an artifact of splitting the sample space into two subranges and fitting two separate models. The two models are not forced to meet at the subspace border, resulting in a step-wise discontinuity. There are techniques for resolving this if desired, but it was not done during this research [53].

The spoiler lift dumping effectiveness at 30 degrees deflection is virtually unchanged in the presence of mid flap deflections at zero sideslip. This is a little bit surprising as the pressure increase introduced on the suction side by the spoilers can sometimes impact the lift generated by the flaps on the pressure side, appearing to increase the spoilers' effectiveness [31]. This is especially true in slotted spoilers or spoilers paired with Fowler flaps. For the split flaps installed on the Flying V, however, combined deflection of both the split flaps and spoilers does not change the amount of lift dumping achieved by the spoilers within repeatability uncertainty. The one exception being the measurement taken around $\alpha \approx 16°$ in Figure 5.11.

The model predictions shown in Figure 5.11 are erroneous for both configurations for the lower range, as also highlighted in Figure 5.14 where the models are plotted against the validation data. The mean of the model prediction drops down from the true measurements after $\alpha = 5°$ for the Range 1 α-sweeps. The model predictions for both configurations are within each other's confidence intervals, indicating no flap-spoiler interaction terms and confirming the conclusion from the previous subsection.

Looking at Figure 5.12, it is seen that the drag added by the spoilers at $\delta_{sp} = 30°$ changes from $\delta_f = 0°$ to $\delta_f = 30°$. The difference between the measured data lies outside of repeatability error from the range $\alpha = [0°, 7.5°]$, $\alpha = [10°, 15°]$, and $\alpha = 25°$, represented by the error bars, so the differences are said to be statistically significant. For the lower range of angles of attack at zero sideslip, the spoilers

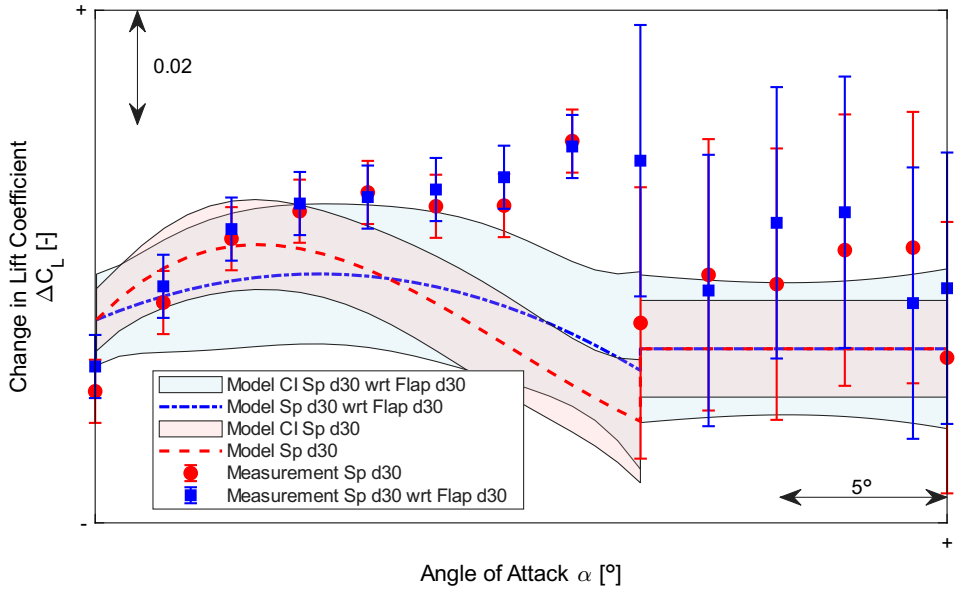

Figure 5.11: Change in $\Delta C_{L,\delta_{sp}}$ when combined with flap deflections.
All confidence intervals shown as $\pm 2\sigma$

add slightly more drag when the flaps are deflected than when they are not. This suggests the amount of separation behind the spoilers and the flaps is larger than the sum of separation introduced by the spoilers and flaps individually. On normal gapped spoilers, their effectiveness at adding drag increases when flaps are deployed because they spoil the flow over the flap, spoiling more than they would if the flap was not deflected [31]. Because the split flap does not extend from the wing trailing edge, the same effect would not be expected on a split-flap and split-spoiler configuration, but a similar result is seen in Figure 5.12, suggesting an interaction nonetheless.

Looking at how well the model predictions capture this phenomenon, the model predicts the spoiler effects for these two configurations are distinguishable from each other on the range $\alpha \approx [5°, 15°]$, where the lack of overlapping of a model's CI range and the other prediction is considered statistically distinguishable. The combined measured data and model predictions in Figure 5.12 highlight and confirm the flap-spoiler interaction that was observed in the model structure for the $\Delta C_{D,\delta_{sp}}$ models in the previous section.

Though the significant interactions table shown in Table 5.13 has no significant interaction effects between the flap and spoiler variables for the $\Delta C_{m,\text{ body}}$ model, when plotting the measured validation data versus the model predictions for how the spoiler effects on pitching moment change with and without flap deflection, the data indicates that there is some interaction effect. This can be seen in Figure 5.13, where the red and blue measurement data do not always overlap, particularly at angles of attack less than $\alpha \approx 17.5°$. Additionally, it is seen that the models poorly predict these configurations at these conditions, potentially indicating why there were no significant interaction terms identified. As mentioned before, it is possible the models fail to identify the flap-spoiler interaction seen in the data because of their relatively low R^2_{adj} values of 0.67 and 0.46 for Ranges 1 and 2, respectively.

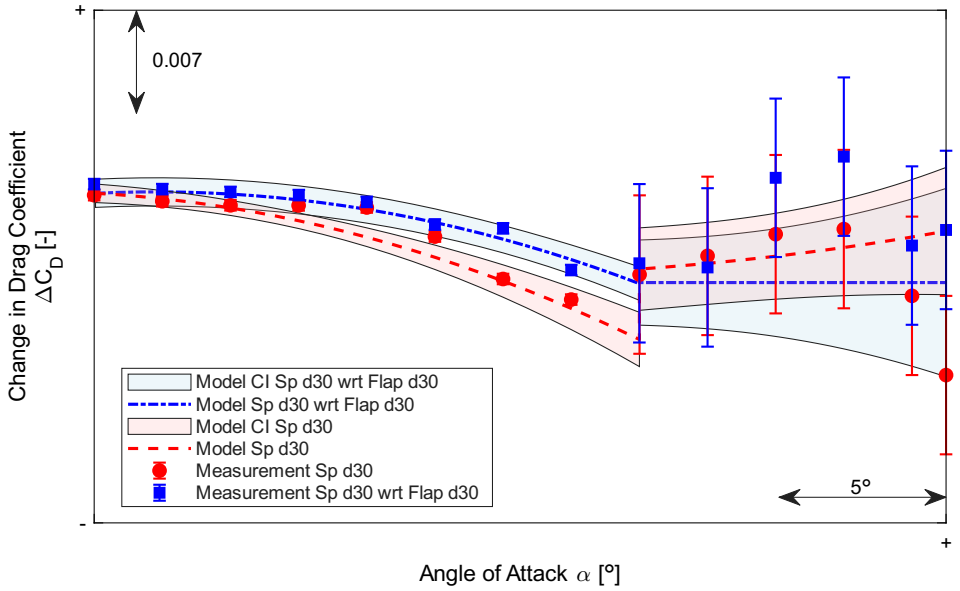

Figure 5.12: Change in $\Delta C_{D,\delta_{sp}}$ when combined with flap deflections.
All confidence intervals shown as $\pm 2\sigma$

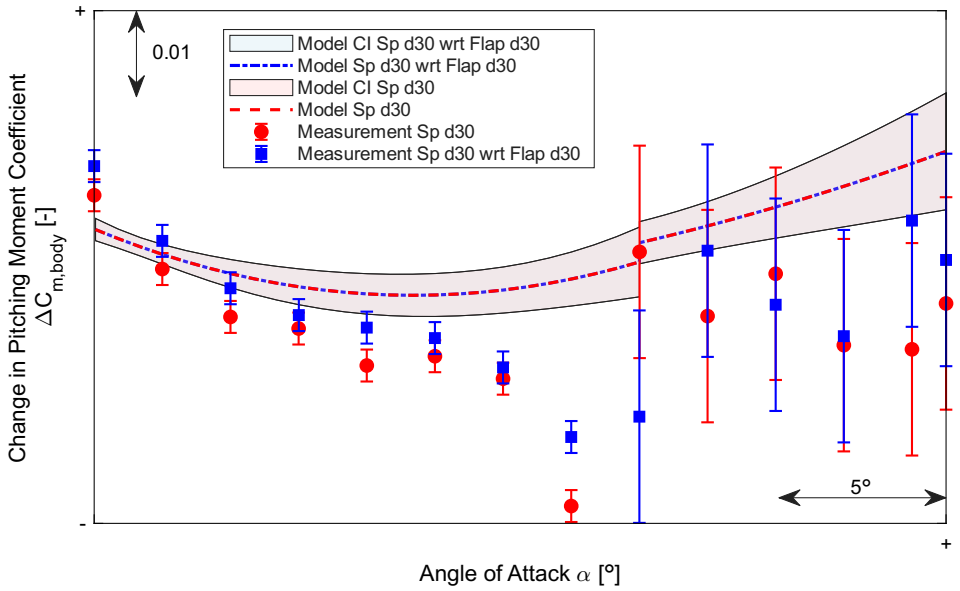

Figure 5.13: Change in $\Delta C_{m,\delta_{sp}}$ when combined with flap deflections.
All confidence intervals shown as $\pm 2\sigma$

5.4.5. Change in Spoiler Effects with Sideslip

As seen from the validation data shown in Figure 5.14 and Figure 5.15, the spoilers at 30 degree deflection are most effective at low angles of attack. At zero sideslip at angle of attack $\alpha = 12.73°$ it appears that a positive change in lift is induced by the 30 degree spoiler deflection but provides a negative change in lift at at angle of attack $\alpha = 17.83°$. At higher sideslip angles for both ranges, it looks like the lift dumped by the $\delta_{sp} = 30°$ spoilers remains statistically unchanged.

The failure of the model to predict the ΔC_L behavior due to the $\delta_{sp} = 30°$ spoiler deflection at zero sideslip in Figure 5.14 is simply a matter of lack of information. When the validation data is added to the model for fitting, the model was seen to have no problem accurately fitting the data without compromising the model accuracy or structure elsewhere. Validation data like the data shown in Figure 5.14 and Figure 5.15 show areas where more data is needed to improve a model's validity.

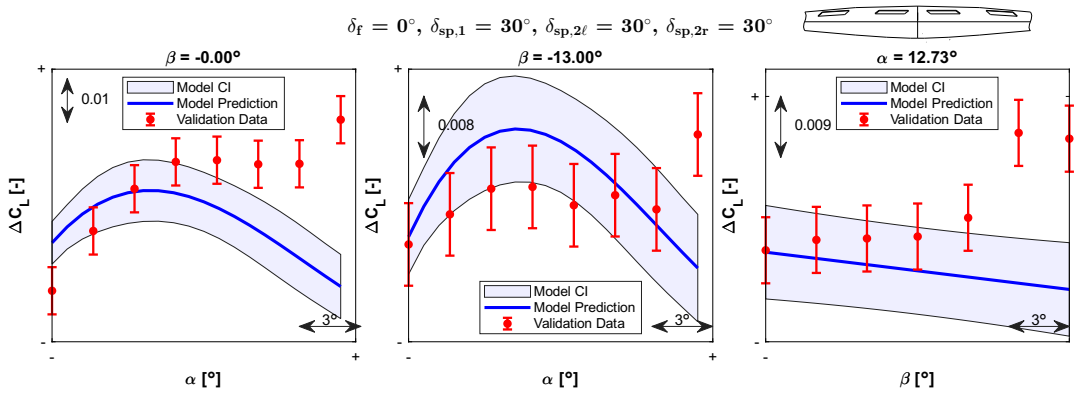

Figure 5.14: Range 1 ΔC_L model prediction and validation with spoiler deflections at $30°$

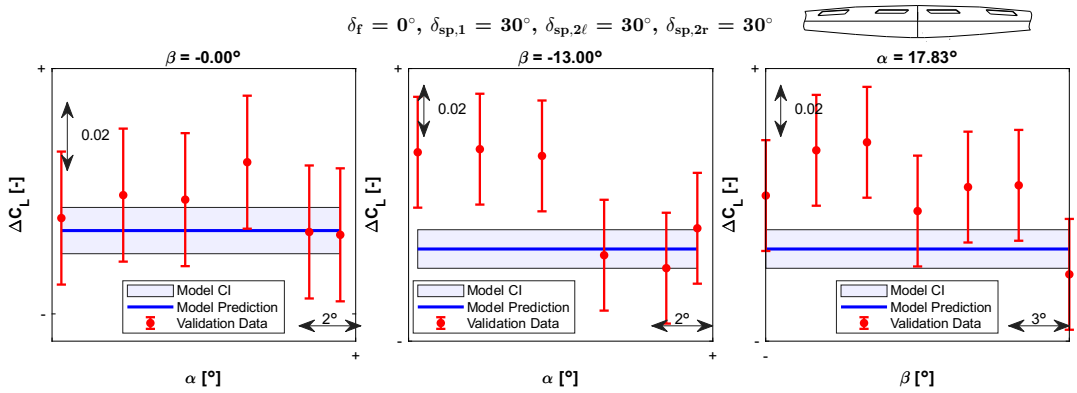

Figure 5.15: Range 2 ΔC_L model prediction and validation with spoiler deflections at $30°$

The validation data shown in Figure 5.15 is indistinguishable from 0 given the estimated repeatability confidence intervals. The spoiler surfaces are likely ineffective at these higher angles of attack, likely being engulfed in the trailing edge separation. For this configuration, only the center point of both ranges was measured and provided for fitting. The single center point likely set the intercept for the constant value predicted by the model in Figure 5.15. It could be seen how a measurement of $\Delta C_L \approx -0.04$ would offset the model from the rest of the validation data. The Range 2 ΔC_L needs more data for this configuration to predict the validation data accurately.

Moving beyond the validation data, the models were use to predict the orientation and configuration with maximum lift dumping due to spoilers deflection alone. The resulting max change in lift coefficient was predicted to be about 55% of the change measured in the OJF at orientation $(\alpha, \beta) = (0°, 0°)$. The plot used to retrieve this estimate can be seen in Figure 5.16.

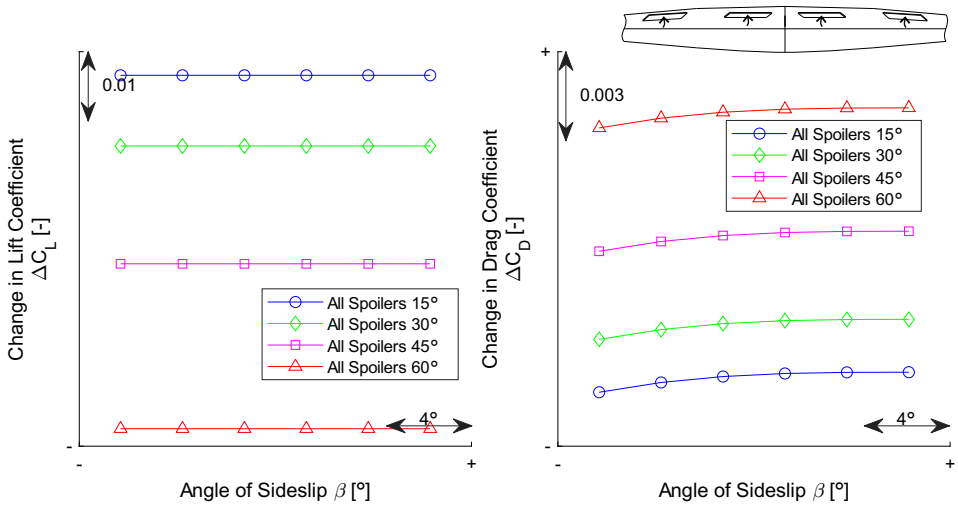

Figure 5.16: Predicted spoiler effects (ΔC_L and ΔC_D) at $\alpha = 0°$ for varying spoiler deflection and varying sideslip

As the spoilers are deflected alone at varying sideslip, it is seen in Figure 5.16 that the lift dumping effectiveness does not change with increasing sideslip. This is somewhat surprising. The literature discussed in subsection 2.1.2 suggest that spoilers on swept wings increase in effectiveness with sideslip. It is likely that indeed the windward spoilers dump more lift while at the same time the leeward spoilers dump less lift. The amount of lift that is dumped increases quadratically with spoiler deflection for all sideslips at angle of attack $\alpha = 0°$. Figure 5.16 also shows that the amount of drag produced by different spoiler deflections at $\alpha = 0°$ decreases very slightly as sideslip is increased. The predicted drag increase due to spoiler deflection is predicted to also increase quadratically, reaching a maximum value at $(\alpha, \beta) = (0°, 0°)$ for the maximum spoiler deflection.

5.4.6. Change in Flap Effects with Sideslip

Figure 5.17 shows the predicted change in ΔC_L and ΔC_D with increasing flap deflections at varying sideslip. Interestingly, the lift generated by the flaps is not predicted to change with sideslip at either $\alpha = 12°$ or $\alpha = 0°$ in Figure 5.18. The reasoning might be parallel to why the lift dumped by the spoilers also doesn't change with sideslip: due to the high sweep angle, the windward flap gets more effective as it becomes more perpendicular to the freestream velocity vector while the leeward flap becomes equally less effective. Interestingly, the model predicts that the lift generated increases linearly with flap deflection, which is validated by the data seen in Figure 5.10a but different from the OJF results [4].

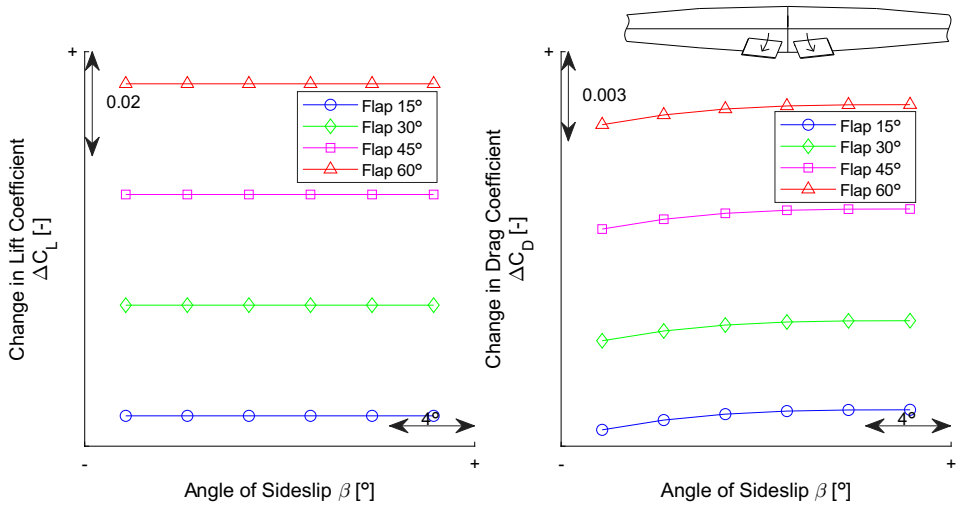

Figure 5.17: Predicted flap effects (ΔC_L, ΔC_D) at $\alpha = 12°$ for varying flap deflection and varying sideslip

For both Figure 5.17 and Figure 5.18, the ΔC_D added by flap deflections decreases slightly with increasing sideslip. This appears to be validated by the data presented later in section 5.5. The drag introduced by the flap deflection increases quadratically with increasing flap deflection. It is possible the decrease in drag with sideslip is due to the amount of separation behind the leeward flap decreasing more than the separation behind the windward flap increases.

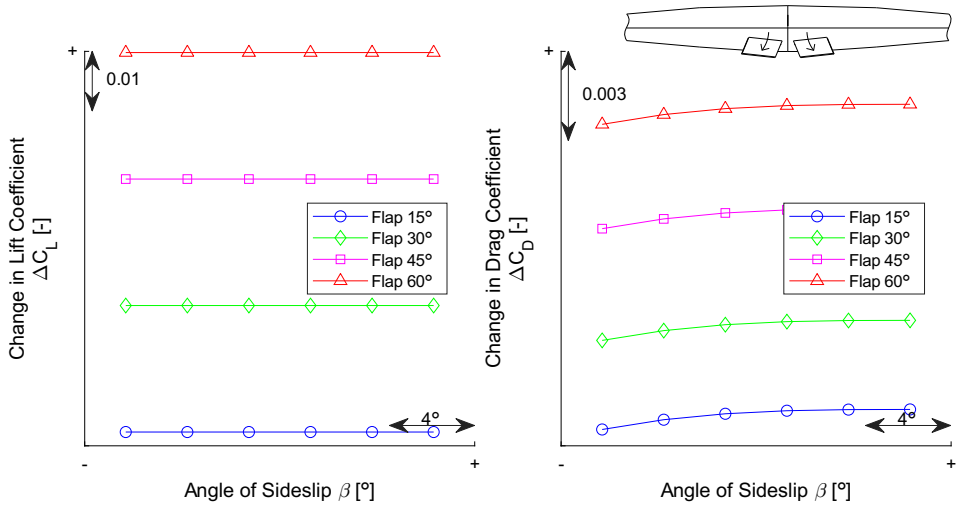

Figure 5.18: Predicted flap effects (ΔC_L, ΔC_D) at $\alpha = 0°$ for varying flap deflection and varying sideslip

For the change in drag at $\alpha = 0°$, the increase in drag due to maximum flap deflection is larger than that added by the maximum spoiler deflections predicted in Figure 5.16 by almost 50%. This is likely due to the flaps larger chord length compared to the spoilers, which would introduce a larger relative area of low pressure behind the flaps. The fact that the flaps produce more drag than the spoilers highlights one of the downsides of a split-flap design: they produce a lot of drag [29].

5.4.7. Change in Combined Effects with Sideslip

When the flaps are already deflected at the maximum $\delta_f = 60°$, deploying the spoilers does not drastically change the combined ΔC_L or ΔC_D relationship with sideslip, as seen in Figure 5.19. As the spoilers are deflected, there is no change in ΔC_L with sideslip, illustrating what it means for there to

be no flap-spoiler interaction in the ΔC_L model. Deflecting the spoilers at $\alpha = 0°$ increases the drag about the same for all sideslip angles until the maximum ΔC_D is more than double the value of ΔC_D due to spoiler deflection alone.

Figure 5.20 shows the change in moment effects for the same configuration. Deflecting the spoilers when the flaps are already fully deployed lessens how much ΔC_l changes with sideslip. When the flaps and spoilers are fully deployed, ΔC_l stops changing with sideslip at around $\beta \approx -7.5°$.Increasing the spoiler deflection serves to move the ΔC_l trend down, adding a $-\Delta C_l$ increment at angle of attack $\alpha = 0°$.

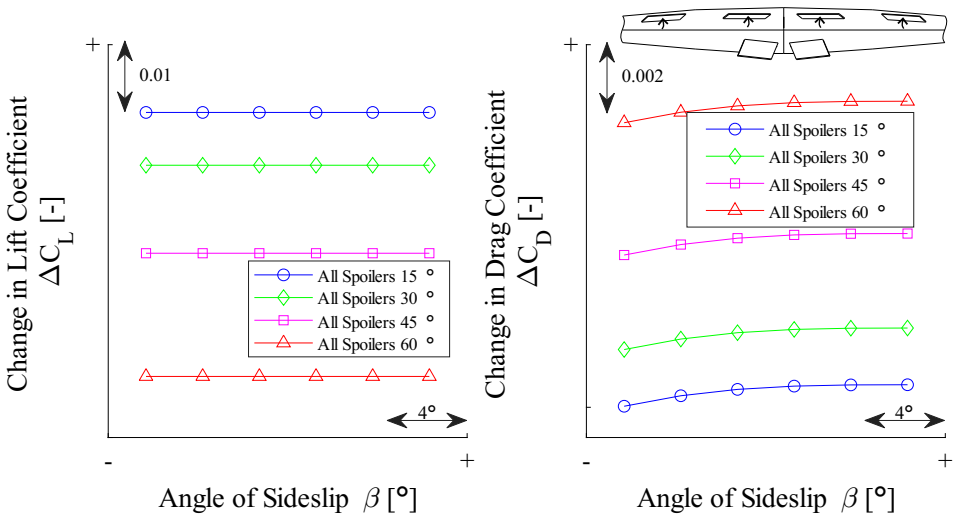

Figure 5.19: Predicted combined ΔC_L and ΔC_D at $\alpha = 0°$ for fixed $\delta_f = 60°$, varying spoiler deflection, and varying sideslip

ΔC_m increases with spoiler deflections, but it doesn't change with sideslip at $\alpha = 0°$. Like the ΔC_L models, the ΔC_m models had no flap-spoiler interactions, which is why there is no change in ΔC_m for combined flap and spoiler deflections in the lower range. The final predicted ΔC_m for zero sideslip is overestimated, as indicated by the validation data in Figure 5.21. The validation data shows that the model fails to predict measured negative change in pitching moment at zero sideslip and zero angle of attack. This incorrect offset could be mitigated by measuring more data with the flaps alone deflected. Adding the spoiler deflections does increase the pitching moment offset to be a net positive ΔC_m, which is confirmed by the measurements presented later in Figure 5.37.

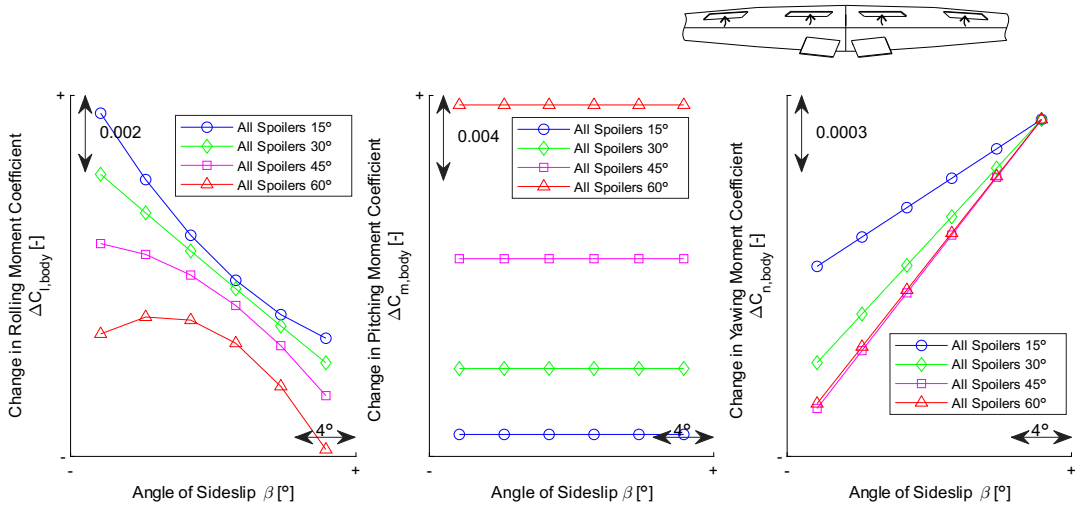

Figure 5.20: Predicted $\Delta C_l, \Delta C_n$ and ΔC_m at $\alpha = 0°$ for fixed $\delta_f = 60°$, varying spoiler deflection, and varying sideslip

The deflection of the spoilers at $\alpha = 0°$ changes the yawing moment from when the flaps are deflected alone by making the change in ΔC_n with sideslip more steep. This could increase the $\Delta C_{n,\beta}$ with increasing spoiler deflection, depending on the clean aircraft $C_{n,\beta}$ trend.

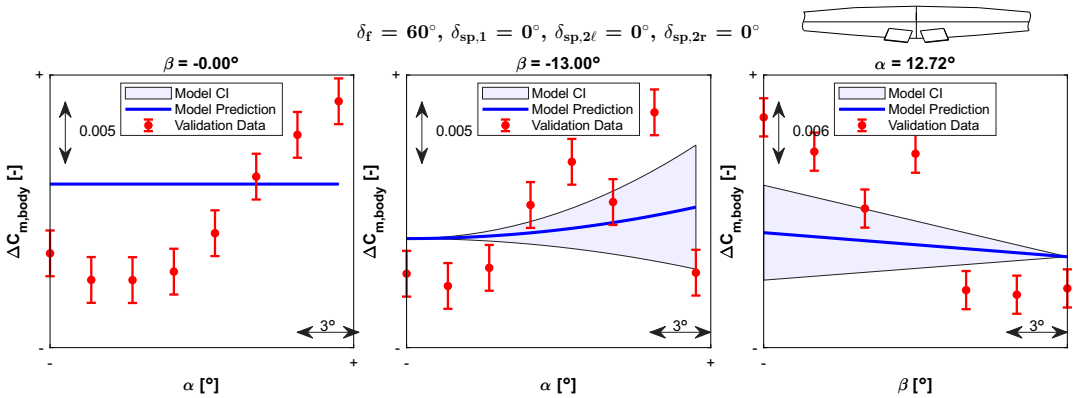

Figure 5.21: Predicted ΔC_m for fixed $\delta_f = 60°$ vs validation data

The increase in positive ΔC_m seen in Figure 5.20 due to spoiler deflections at $\alpha = 0°$ was also measured in the initial spoiler design study [5]. Deflecting the spoilers at $\alpha = 17°$ produces the opposite effect, a negative change in pitching moment, which is shown in Figure 5.22. This was also predicted in the previous spoiler design study [5].

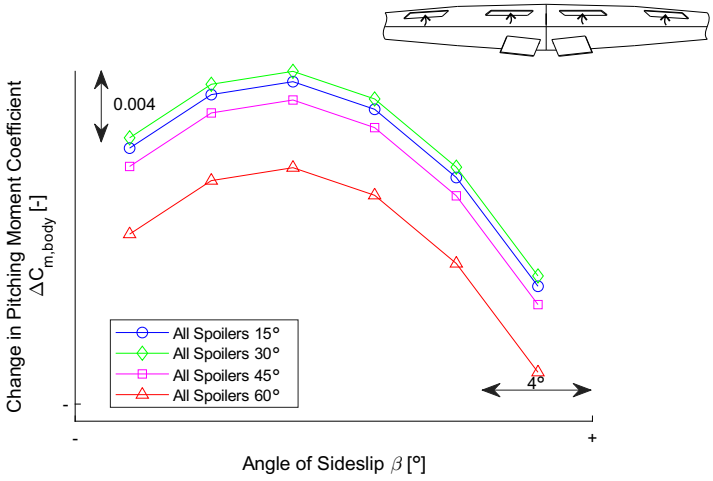

Figure 5.22: Predicted ΔC_m at $\alpha = 17°$ for fixed $\delta_f = 60°$ varying spoiler deflection, and varying sideslip

As the Flying V yaws, the ΔC_m at $\alpha = 17°$ is predicted to switch from negative to positive around $\beta = -2.5°$ for the maximum spoiler and flap deflection, negating any potential derotating assistance deploying the spoilers at $\alpha = 17°$ might provide when there's even a small amount of sideslip. However, this trend of changing pitching moment due to combined flap and spoiler deflections with sideslip is called into question when considering the sideslip validation sweeps in Appendix C, where the validation data measured for the change in pitching moment at zero sideslip appears to differ sharply from the rest of the sideslip trend. As a result, whether the change in ΔC_m with sideslip increases or decreases is unclear.

5.5. Specific Configurations

Some of the specific configurations available were analyzed in detail, including configurations that were explicitly tested during the experiment. In each configuration, sweeps at fixed angle of attack or sideslip are considered, highlighting the trends in lift and drag coefficient, the location of the pitch break, and

the changes in the lateral-directional moments. All plots in this section, apart from the clean aircraft and the spoiler differential cases, are created using measured data points and not with model predictions. The set-point order of the measurement sweeps shown was randomized.

It is important to again note that all data presented and used is uncorrected for any wind tunnel corrections, including strut effects, Reynolds effects, and wind tunnel wall effects. Therefore, especially in the case of the lateral-directional derivatives, the results may not be truly indicative of the Flying V's performance.

After the clean aircraft discussion in subsection 5.5.1, the full flap deflection and half flap deflection results are presented in subsection 5.5.2 and subsection 5.5.3, respectively. Then, the combined full flap and spoiler deflection results are presented in subsection 5.5.4. The half spoiler deflection case is discussed in subsection 5.5.5, and then a discussion on the predicted spoiler differential roll control is given in subsection 5.5.6.

5.5.1. Clean Aircraft

Some notes are needed about the Flying V's forces and moments before moving on to a discussion about how those forces and moments are affected by subsequent flap and spoiler deflections. The next two subsections highlight some unique behavior observed.

Drag

As is shown in the following subsections, the drag of the clean Flying V model actually decreases with sideslip at higher angles of attack. One example can be seen in Figure 5.26. In a conventional transport aircraft, the opposite trend is expected in flight. An aircraft's most streamline orientation is at zero sideslip as it has the smallest frontal area at that orientation. As an aircraft slips, it's frontal area increases, resulting in greater pressure drag. The increased friction drag due to increased separation over the leeward wing also increases the overall drag.

For the Flying V measurements, however, it appears that the drag is largest at zero sideslip at higher angles of attack. The reason for why the drag is a maximum at zero sideslip at higher angles of attack is likely associated with the corresponding loss in lift for that same orientation. The lift reduction leads to a corresponding reduction in drag due to lift. To bank the aircraft in free flight while maintaining a constant level, the aircraft would need to pitch up at sideslip to produce the same amount of lift. Thus, when using the models to plot C_D for constant C_L and varying sideslip at high angles of attack, the drag increases with sideslip as expected. This is illustrated in Figure 5.23.

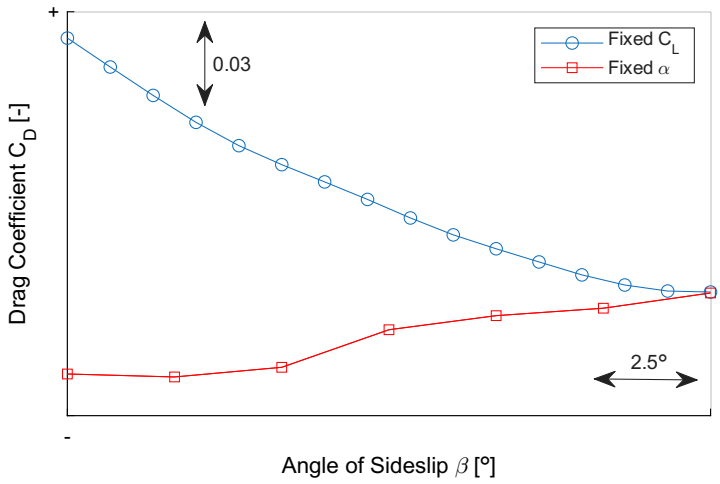

Figure 5.23: Change in drag coefficient with sideslip for clean Flying V at fixed angle of attack $\alpha = 17.8°$ and fixed C_L

The same decrease in drag at high angles of attack with increasing sideslip for fixed angle of attack was also predicted by Jorge in his numerical research [15], and the same trend in drag was observed for a different flying wing design in other wind tunnel studies [69].

Lateral-Directional Stability

The lateral-directional stability derivatives for the clean model with only winglets installed were calculated and shown for reference in Figure 5.24. Note again that these derivatives are calculated using moment values that are influenced by and not corrected for the significant vertical aft strut used to position the model. For these lateral-directional stability derivatives, the forward-differencing scheme was used to turn the rolling and yawing moment coefficients, fit using a thin plate spline, into derivatives. No models were fitted to the calculated stability derivative data; models were used to predict the moment values needed to calculate the derivatives for plotting.

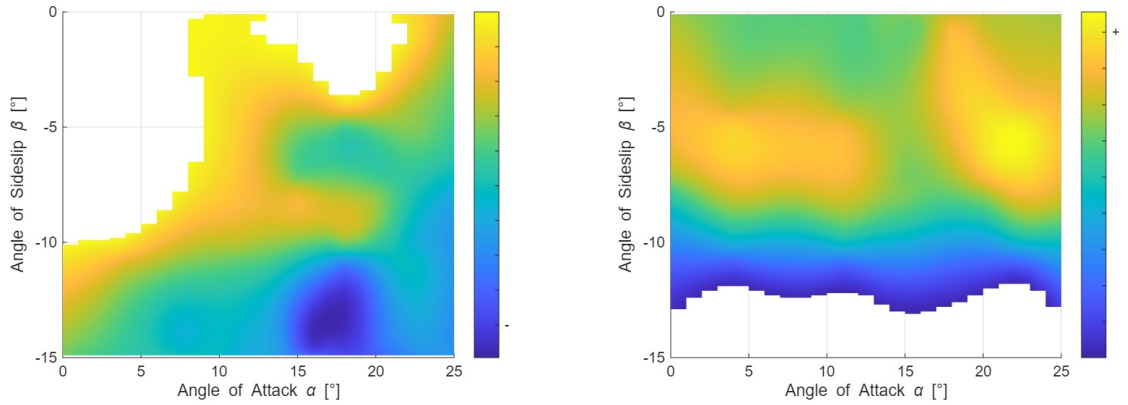

(a) Clean model $C_{l,\beta}$ surface plot

(b) Clean model $C_{n,\beta}$ surface plot

Figure 5.24: $C_{l,\beta}$ and $C_{n,\beta}$ with clean model, unstable derivatives shown as NaN

In Figure 5.24a, it is seen that for low angles of attack, the uncorrected wind tunnel data shows the Flying V has positive, unstable $C_{l,\beta}$ values. Stable lateral derivatives take the conventional form of $C_{l,\beta} < 0$. As the angle of attack is increased for the clean model, the derivative becomes stable before becoming unstable again at low sideslips. The Flying V's $C_{n,\beta}$ values are positive and stable for all angles of attack up to around $\beta = -12.5°$ sideslip, as seen in Figure 5.24b. Past $\beta = -12.5°$ sideslip, the derivatives are effectively zero, indicating neutral directional stability. The scaled flight test studies done on the Flying V show the Flying V is laterally-directionally statically stable for all angles of attack and sideslip tested, demonstrating the limited usefulness of the full rolling and yawing moment coefficients from this research in their present state shown in Figure 5.24 [70].

The reason for the inconsistency between flight test results and these wind tunnel results is again due to the lack of strut effect corrections. As seen in Figure 3.15b, the vertical aft strut effectively acts as a vertical tail extending below the aircraft with respect to the aircraft's fixed reference frame. Therefore, a positive sideslip would result in a sizeable positive rolling moment contributed by the vertical aft strut, counteracting any laterally statically stable aircraft response that might exist apart from it. However, as the aircraft is pitched nose up, the aft strut becomes smaller as it is retracted into the test section ceiling. This decreases the wet area of the strut and the counteracting rolling moment it provides.

Additionally, the Flying V is expected to increase in lateral stability with increasing angle of attack and sideslip, which is seen to some extent in Figure 5.24a. The Flying V has some geometric dihedral combined with effective dihedral due to its high sweep angle. Using vector analysis, these design features and the new winglets all should result in increasing lateral stability with increasing angle of attack.

For the low angles of attack, it is suspected that the aft strut destabilizing contribution to the rolling moment opposes the stabilizing rolling moment in sideslip produced by the Flying V body and winglets, making it appear that the entire aircraft is laterally unstable. As the Flying V is pitched up, there is a point at which the increasing stabilizing rolling moment of the aircraft surpasses the decreasing destabilizing rolling moment from the strut, resulting in a stable $C_{l,\beta}$ for the angles of attack greater than $\alpha > 7°$.

While the derivatives shown in Figure 5.24a show most values of $C_{l,\beta}$ increasing in magnitude with

increasing angle of attack as expected, the trend reverses briefly at low sideslips with neutrally stable or even unstable derivatives for around $\alpha = 15° - 20°$. This change from the expected trend is observed in literature for other highly swept wings.

Johnson Jr. *et. al.* experimentally tested the effects of vortex-bursting over highly swept wings on their lateral-directional stability, showing that the vortex break down at high angles of attack resulted in a sharp change in lateral stability away from the theoretical vector analysis results [71]. From these results, it is suggested that, though the Flying V geometry differs from that tested in [71], the Flying V's decrease in lateral stability with increasing angle of attack despite its effective dihedral effect could be due to changes in vortex breakdown and flow separation. Additionally, a different experimental investigation on a flying wing configuration showed statically stable lateral moments for low angles of attack but then lateral divergence past around 15 degrees angle of attack with a corresponding break in the pitching moment trend [72]. Though the vortex breakdown isn't specifically identified as the underlying phenomenon in that study, the similar trend and geometry to the Flying V suggests the trends observed in this experiment are representative of the Flying V design and not artifacts of the experimental setup.

Regarding the directional stability derivative in Figure 5.24b, the static stability requirement of $C_{n,\beta} > 0$ is met for all sideslip up to around the highest sideslip angles. For the directional stability, the vertical aft strut is expected to amplify the model's yawing moment; the yawing moment increment due to the strut should be in the same direction as the yawing moment generated by the winglets. In this case, then, the directional static stability is likely less than reported here. For the uppermost sideslip range, the slope of C_n flattens out and may drop below zero for sideslips greater than $\beta = -12.5°$. This could be due to separation onset over the winglets and maybe also the strut with respect to the angle of sideslip, resulting in little added yawing moment for increased sideslip and a corresponding zero-magnitude derivative.

From these uncorrected wind tunnel results and conceptually considering the strut contributions, it appears the Flying V is laterally-directionally stable or at least neutrally stable for most angles of attack and sideslip. Literature suggests that sharp changes in laterally stability can be seen over highly swept wings when pitch break occurs, which is typically a result of a sudden change in the vortex flow development and breakdown. Therefore, there might be orientations at high angles of attack where the lateral stability of the Flying V diverges from the theoretical predictions. In the following configurations considered, the effects of the flaps and spoilers on the rolling and yawing moment trends will be highlighted, as these effects are likely unchanged by the struts.

5.5.2. Full Flap Deflections

The full flap deflection configuration refers to the maximum flap deflection possible: $\delta_f = 60°$. The data measured with this configuration is displayed alongside the clean-model baseline data to illustrate the flap effects in the following sections.

Lift and Drag

The change in lift coefficient with full flap deflections can be seen in Figure 5.25. At zero sideslip and at low angles of attack, the lift increment is roughly constant. Then, about halfway up the angle of attack sweep, the flap effectiveness decreases until it is negligible at the top of the sweep. However, at a fixed, nonzero sideslip, the flap effectiveness is relatively constant throughout the entire angle of attack sweep. As the Flying V is yawed, the flaps' effectiveness decreases slightly. The apparent C_L peak at the nonzero sideslip for the $\alpha = 12.7°$ case may be nonphysical as it is the same as the zero sideslip value within the estimated experimental uncertainty.

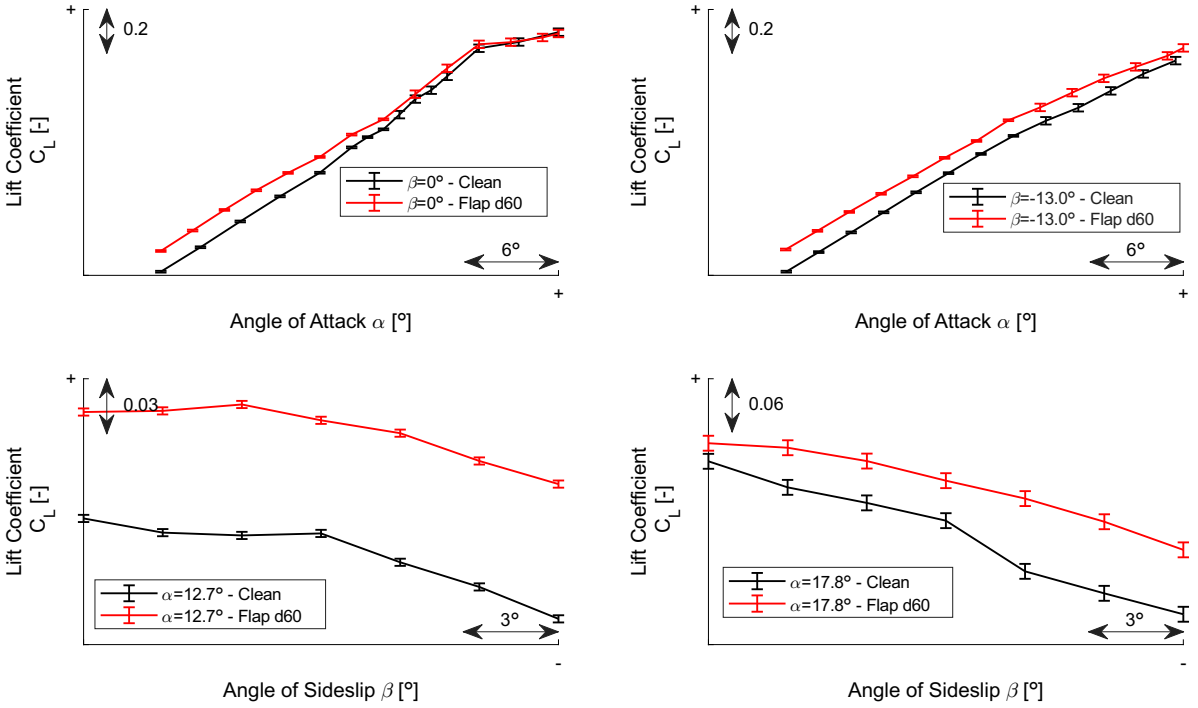

Figure 5.25: C_L with winglets alone and flaps = 60°

The change in drag coefficient due to full flap deflections is not surprising: a split flap deflection increases the drag, as seen in Figure 5.26. The offset is roughly constant across angles of attack and sideslip, though the drag increment decreases due to the flaps at the higher angles of attack at zero sideslip.

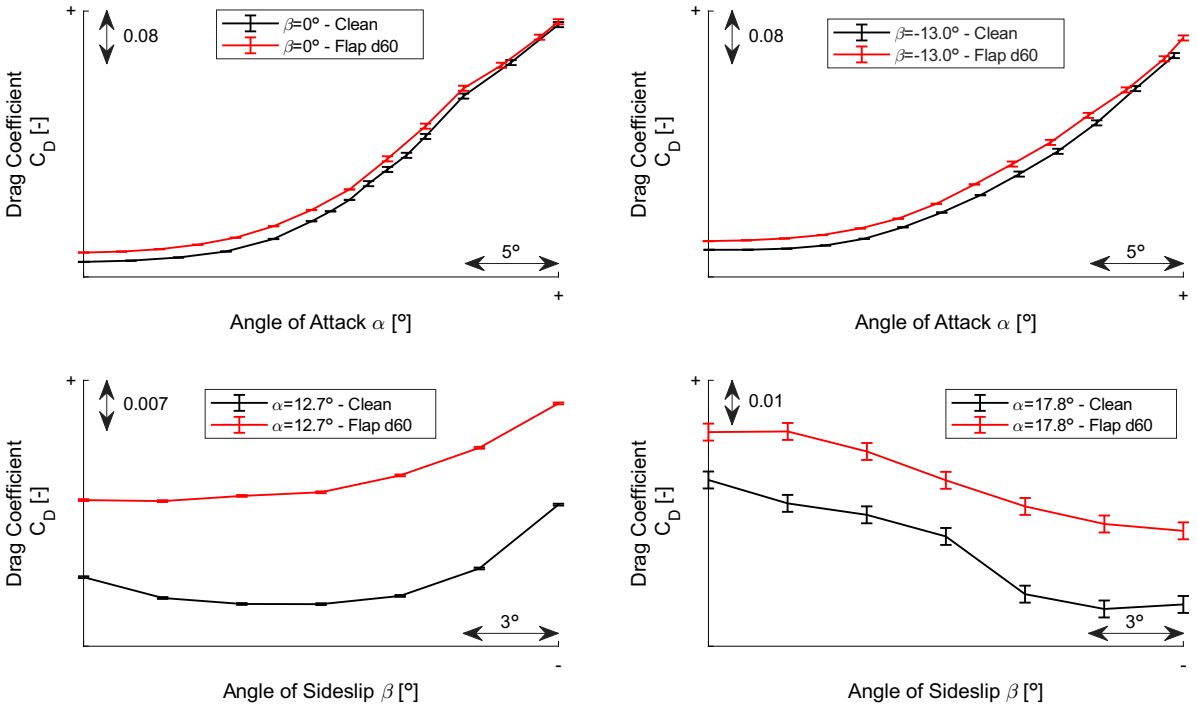

Figure 5.26: C_D with winglets alone and flaps = 60°

Pitch Break

Deflecting the flaps to the maximum $60°$ does not change the location of the pitch break at either the zero sideslip condition or at $\beta = -13°$ sideslip. For both conditions, however, the flap deflection does show to decrease C_{m_0} and also decrease the magnitude of C_{m_α} for the stable region. The implications of the positive shift in C_m due to the $\delta_f = 60°$ flap deflection at the middle range of angles of attack means that deflecting the flaps in final approach configuration would introduce a nose-up pitching moment component. This makes sense considering the flaps are located forward of the MRC and cause an increase in pressure on the pressure side at that location, resulting in an positive increment in pitching moment.

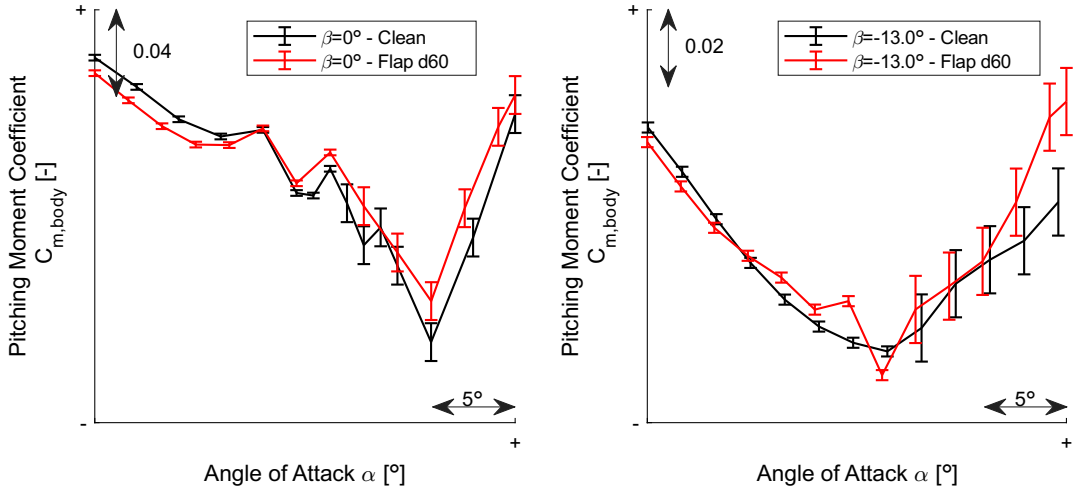

Figure 5.27: $C_{m,\text{body}}$ with winglets alone and flaps = 60°

Lateral-Directional Moments

The effects on the lateral-directional moments due to full flap deflections can be seen in Figure 5.28 and Figure 5.29. Looking first at ΔC_l, it can be seen that the flap deflections cause an opposite effect at $\alpha = 12.7°$ than at $\alpha = 17.8°$. There is an increase in the rolling moment at low sideslips for the lower angle of attack, and the change decreases to about zero at the higher sideslips. There is statistically no difference in rolling moment at the higher angle of attack at the low sideslips but then an increase in rolling moment at the higher sideslip angles.

Most interesting is the offset in rolling moment at zero sideslip. This is unexpected, as symmetric flap deflections in an ostensibly symmetric flow condition should not result in a change in rolling moment. As discussed earlier in subsection 5.4.1, an asymmetrical flow topology can be introduced over both wings in ostensibly symmetric conditions by small misalignments. It is possible a the flow asymmetry is triggered by a slight misalignment in the flap installation. The fact that the zero sideslip rolling moment offset only occurs at the lower angle of attack presented and not at the $\alpha = 17.8°$ angle goes to show that the vortices over the Flying V dominate the response behavior and are easily disturbed. Overall, the net trend to increase the rolling moment with flap deflection for a negative sideslip would indicate an improving of the lateral static stability in Figure 5.28, where $C_{l,\beta} < 0$ indicates static stability. However, for the $\alpha = 12.7°$ data, the flap deflections cause the rolling moment to flatten out for the low sideslip angles. This changes the otherwise laterally stable derivative to neutrally stable.

The flaps' impact on the yawing moment is seen in Figure 5.29: the net increase in ΔC_n due to the flap deflections for most negative sideslip doesn't change the positive $C_{n,\beta}$ derivative. The positive yawing moment increment for high negative sideslip could make sense considering the flaps extend below the model centerline and in front of the MRC, resulting in a positive increment in yawing moment for a negative sideslip.

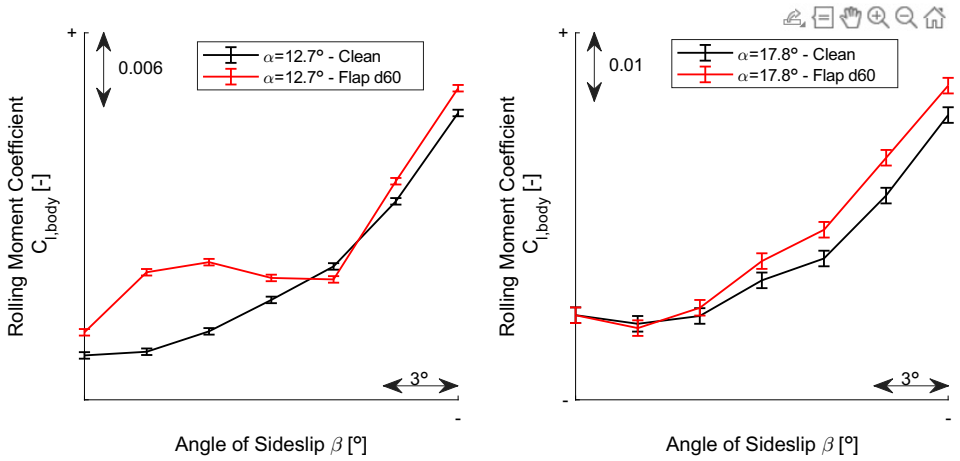

Figure 5.28: C_l with flaps = 60°

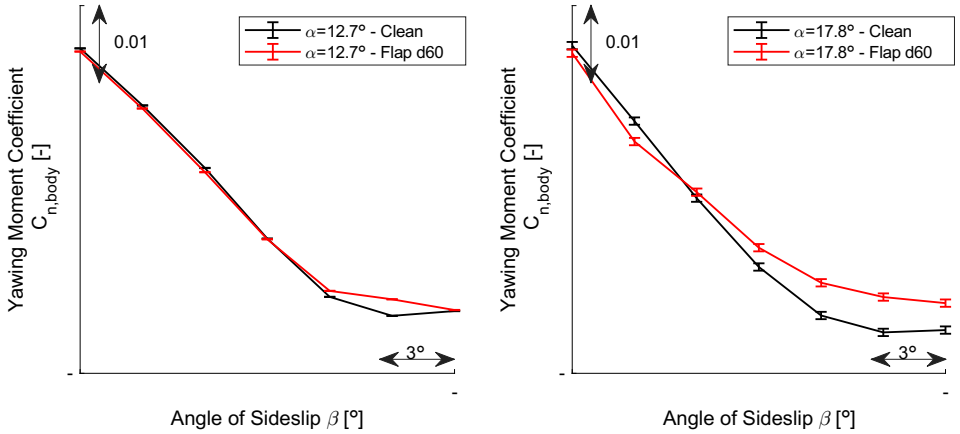

Figure 5.29: C_n with flaps = 60°

5.5.3. Half Flap Deflections

The half flap deflection configuration refers not to a half-sized flap but to a flap deflected halfway through its possible range: $\delta_f = 30°$. In the following subsections, the data measured with the maximum flap deflection possible is also shown to illustrate the how the flap effects develop with increasing flap deflection.

Lift and Drag

Considering the lift and drag added by the $30°$ deflection flaps, it appears the half deflection provides more than half of the added lift for less than half of the added drag of the full flap deflections, as seen in Figure 5.30 and Figure 5.31. This means the $\Delta(L/D)$ due to flap deflection is greater for the half deflections than the full deflections.

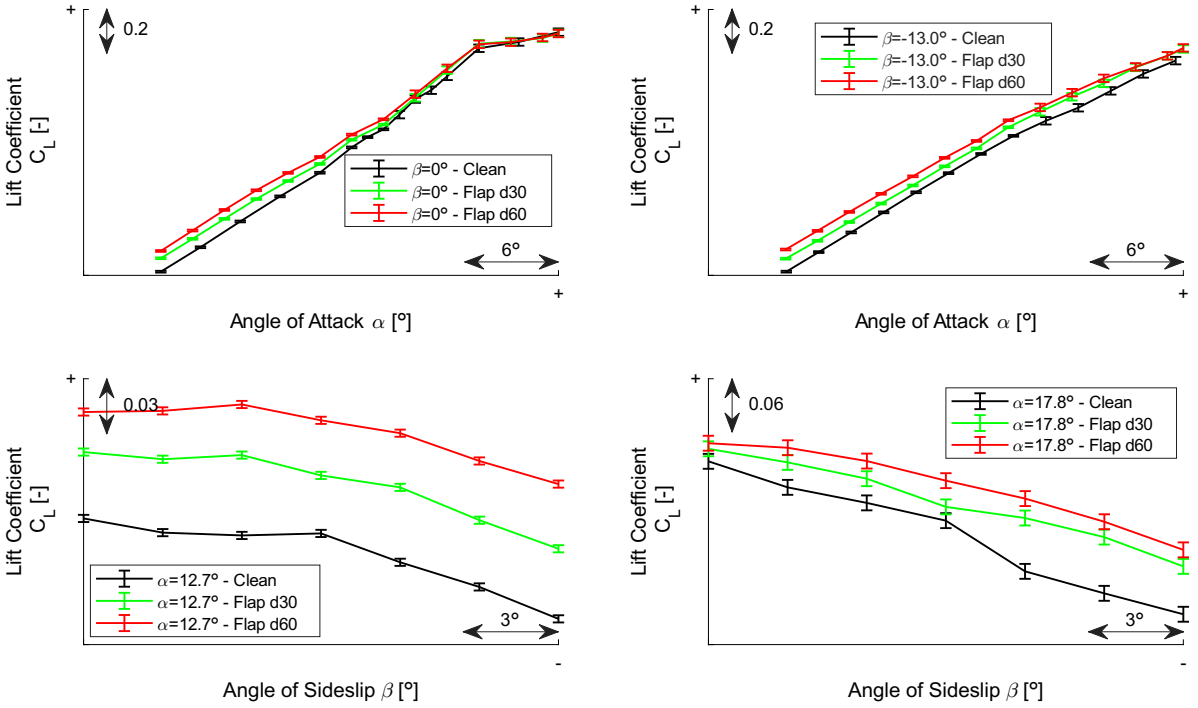

Figure 5.30: C_L with winglets alone, flaps = 30°, and flaps = 60°

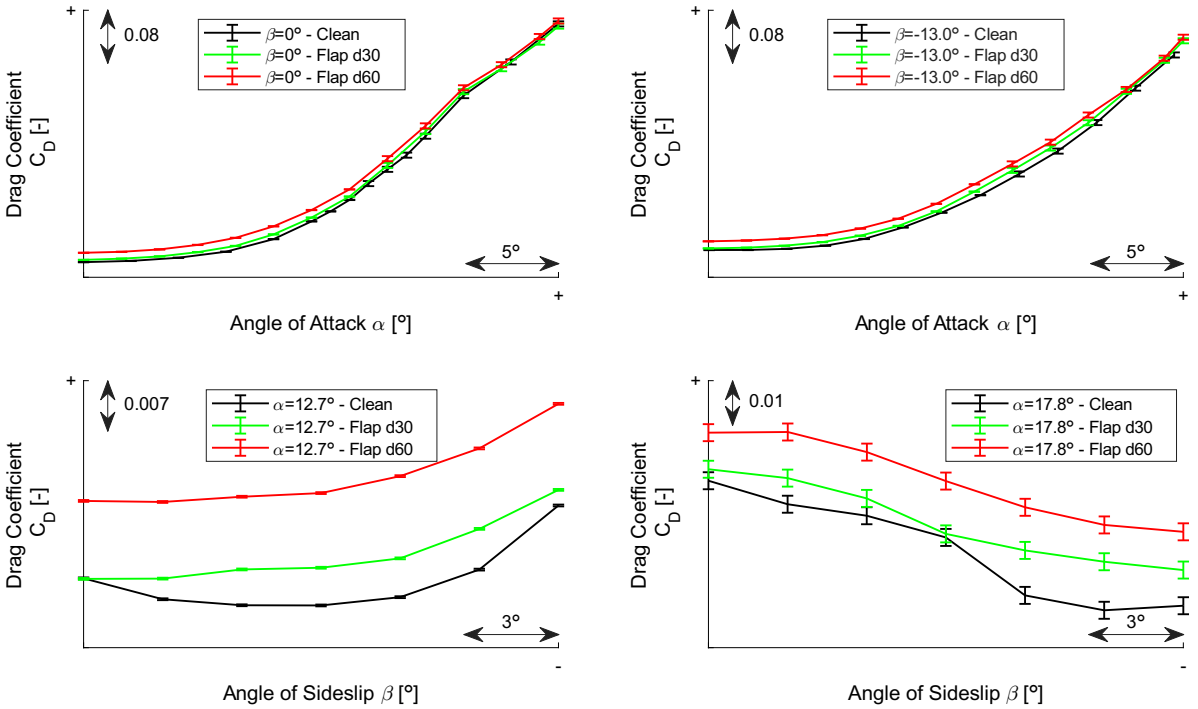

Figure 5.31: C_L with winglets alone, flaps = 30°, and flaps = 60°

Pitch Break

Deflecting the flaps to their half deflection of $30°$ doesn't appear to change the orientation at which the pitch break occurs, as seen in Figure 5.32. This indicates that as the flaps are deflected over their whole range, the pitch break location doesn't change, but the pitching moment slope increases slightly and the C_{m_0} decreases. In general, the magnitude of the Flying V pitching moment coefficient doesn't

drastically change with increasing flap deflection at zero sideslip for the mid range of angles of attack. This behavior is kept from the OJF results, where a change in pitching moment with flap deflection was unwanted as it could mitigate the flap's benefits due to losing lift through trim. The upwards increment of pitching moment due to flap deflection from around $\alpha = 12° - 17°$ is thus beneficial in potentially lessening the amount of trim needed.

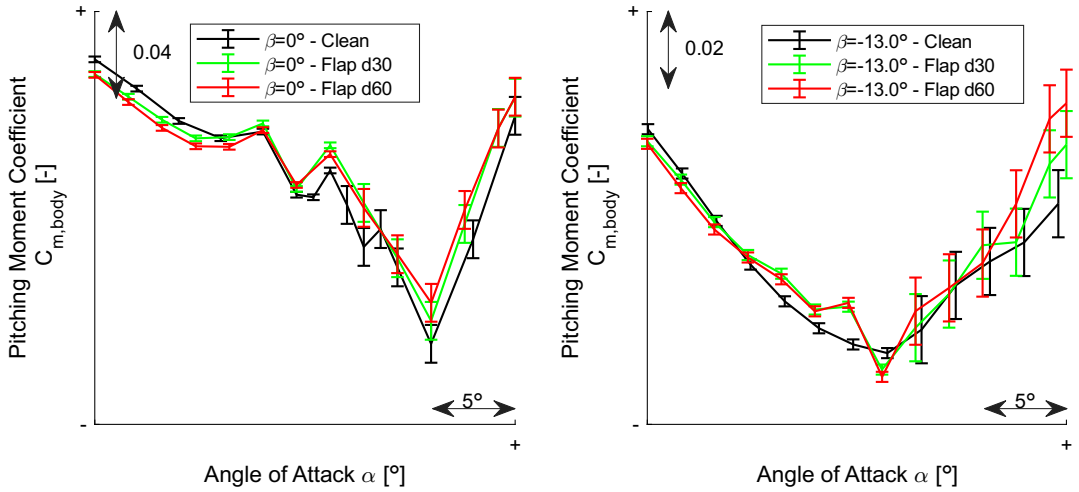

Figure 5.32: $C_{m,\ \text{body}}$ with winglets alone, flaps = 30°, flaps = 60°

Lateral-Directional Moments

The effects on lateral and directional moments are close to the same for the $30°$ flap deflection as they are for the $60°$ flap deflections, as seen in Figure 5.33 and Figure 5.34. The main exceptions being a decrease in the rolling moment trend for the $30°$ flap deflection compared to the $60°$ flap deflection. In other words, increasing the flap deflection from low to high deflections has a nonlinear change in rolling moment. The change in yawing moment due to flap deflection looks roughly the same between the two deflection cases. The effects on lateral-directional stability for the half flap deflection is to make $C_{l,\beta}$ positive (unstable) for around $\beta = -3°$ to $\beta = -7.5°$ at $\alpha = 12.7°$. The same occurs at low sideslip for $\alpha = 17.8°$. The half flap deflections have the same effect on directional stability as the full flaps.

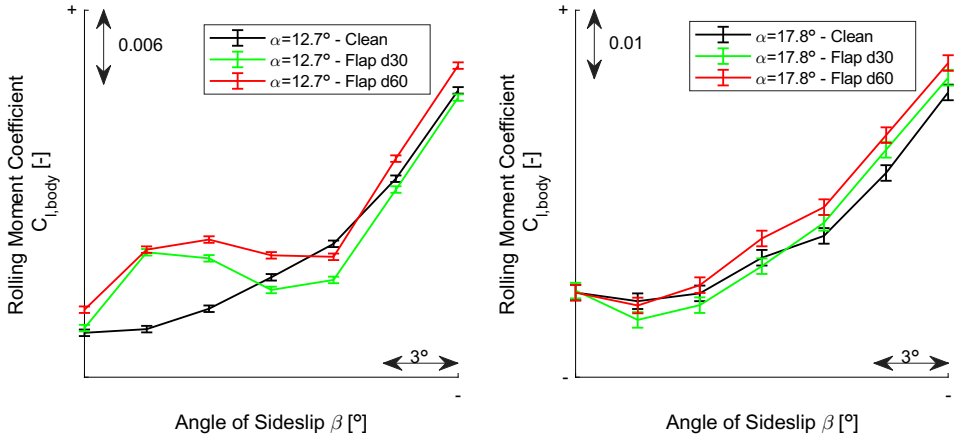

Figure 5.33: C_l with flaps = 30° deflection

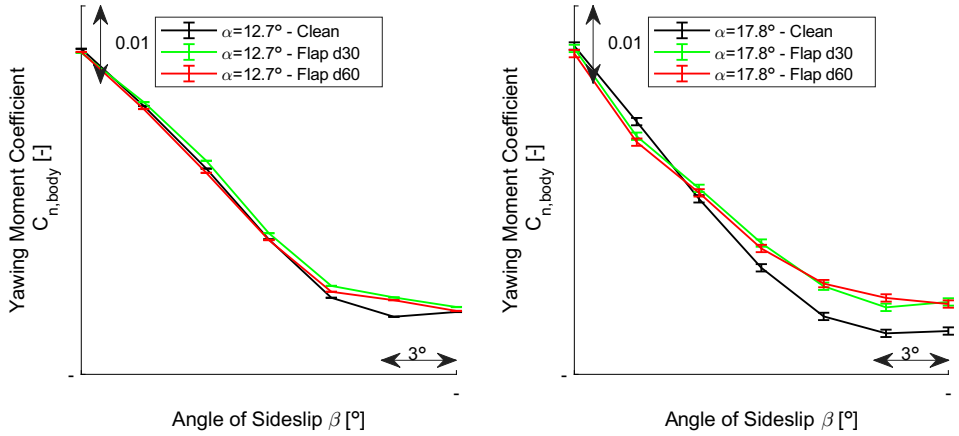

Figure 5.34: C_n with flaps = 30° deflection

5.5.4. Full Flap and Spoiler Deflections

The full flap and spoiler deflections refers to the tested configuration where all flap, inboard spoiler, and outboard spoiler surfaces were deflected to the maximum value of $60°$, which corresponds to the full range of deflection. This configuration could be used in derotation upon touchdown, using the maximum spoiler deflections to dump lift and add drag for a shorter rolling distance, as suggested by [5].

Lift and Drag

When all spoilers are deflected in combination with the flaps to their maximum $60°$ deflection, the spoilers decrease the maximum amount of lift achieved. Moreover, at $\alpha = 17.8°$, the added spoiler deflection spoils the flaps' effectiveness and more, bringing the lift coefficient below the clean model level. This suggests the vortices at $\alpha = 17.8°$ without the flaps deployed are susceptible to the spoiler deflections. This also looks to be the case at the higher end of the angle of attack sweep at zero sideslip in Figure 5.35, though the results seem to fall closer within the estimated experimental uncertainty. At the lower angles of attack, the spoilers are most effective, spoiling roughly two-thirds of the lift generated by the flaps. Elsewhere, the spoiler deflection serves to reduce the lift generated by the split flap deflection by a roughly constant offset for all other angles of attack and sideslip.

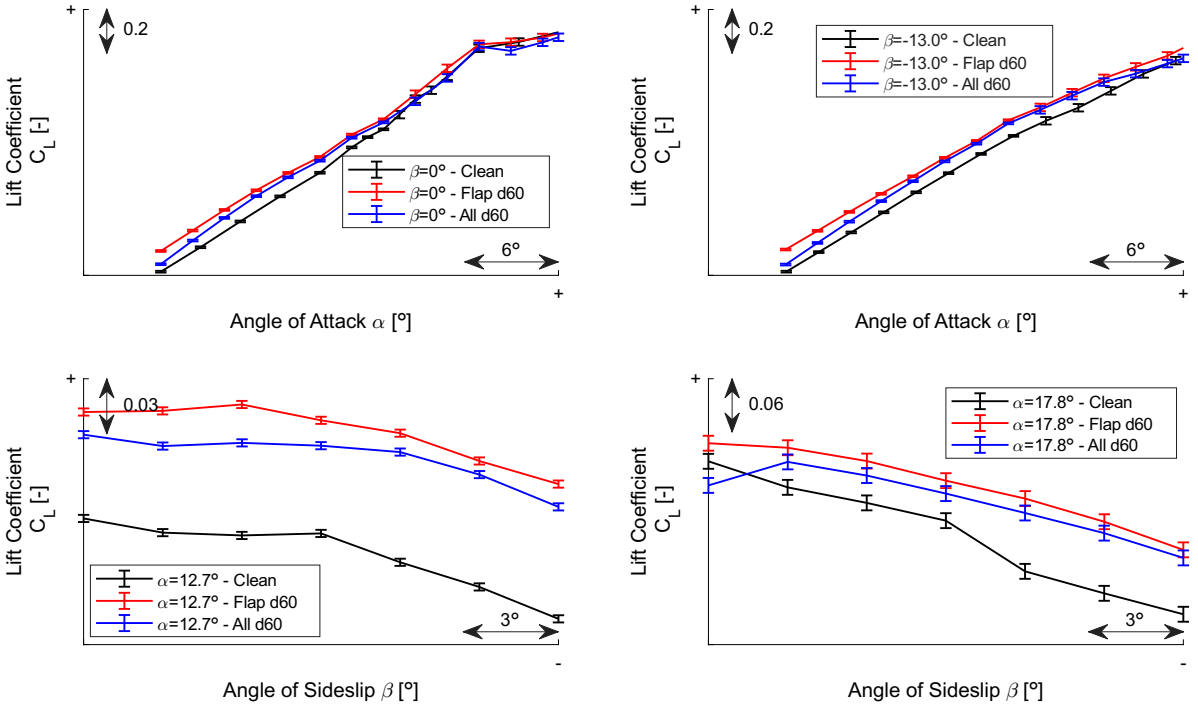

Figure 5.35: C_L with winglets alone, flaps = 60°, and combined spoilers and flaps = 60°

The added drag due to spoilers deflected in addition to deployed flaps is greatest at the lower angles of attack across the sideslip range, as shown in Figure 5.36. This is likely because the flow is the most attached and thus the most affected by the spoilers' presence. For the zero sideslip $\alpha = 17.8°$ case, the spoiler deflection actually causes the drag to decrease. Full flap and spoiler deflections at zero sideslip and $\alpha = 17.8°$ leads to a reduction in drag when compared to the clean model. This is again likely due to the disrupted vortical flow over the Flying V when the spoilers are deflected at this orientation. The spoiler deployment contributes some increased pressure drag due to the induced separation, but the simultaneous decrease in overall pressure drag due to the reduced blockage that occurs when the vortices are disrupted may surpass the spoiler drag increment. This also appears to be the case at the upper range of angles of attack at $\beta = -13°$, presumably for the same reason, though it may also fall within the estimated experimental uncertainty.

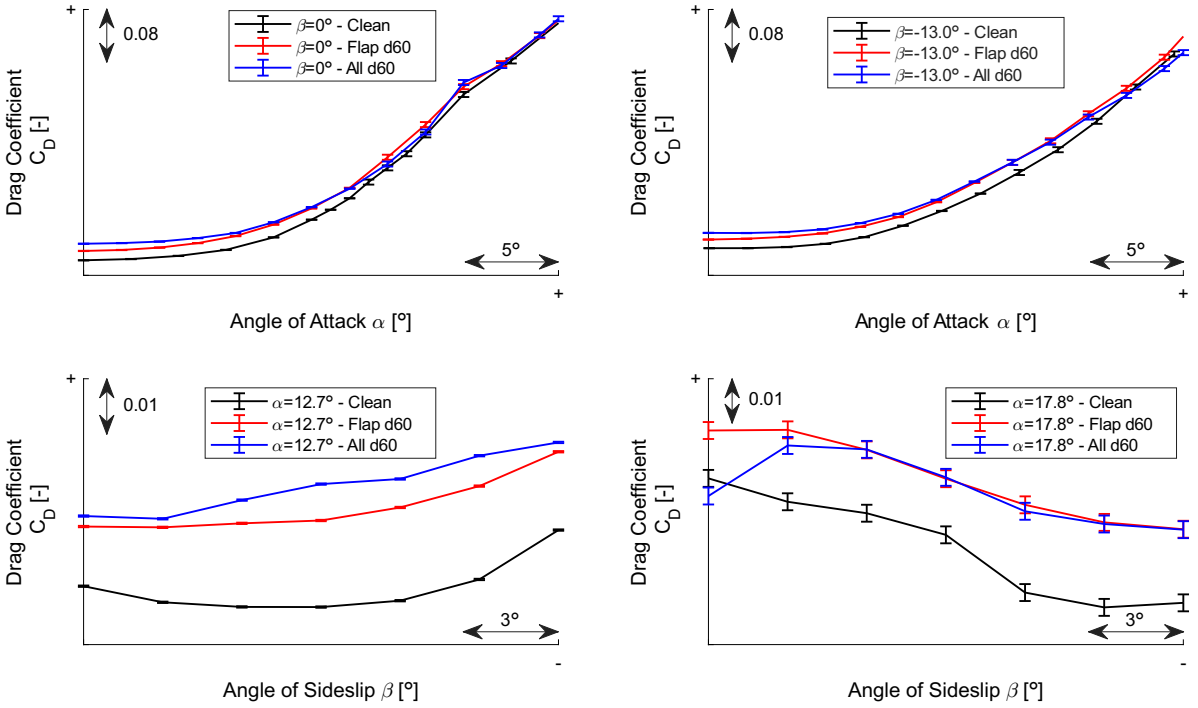

Figure 5.36: C_D with winglets alone, flaps = 60°, and combined spoilers and flaps = 60°

Pitch Break

The pitch break location does not change from flaps = $60°$ to combined flaps and spoilers = $60°$, as shown in Figure 5.37. What does change is the C_{m_0} and the magnitude of C_{m_α} for the stable region. Deflecting the spoilers when the flaps are already deployed cause the C_{m_0} to increase past the clean value. Additionally, for the first 10 degrees of angle of attack, the C_{m_α} also increases in magnitude.

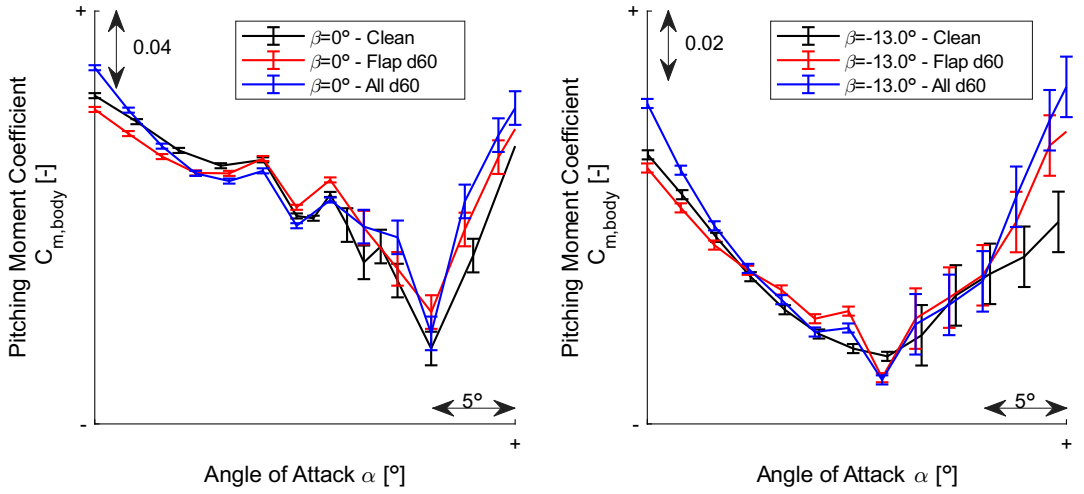

Figure 5.37: $C_{m,\ \text{body}}$ with winglets alone, flaps = 60°, and combined spoilers and flaps = 60°

Lateral-Directional Moments

Figure 5.38 and Figure 5.39 show the changes in lateral and directional moments for the combined max flap and spoiler deflections configuration. The results from Figure 5.5.2 are also included so that the effects of deflecting the spoilers when the flaps are already deployed can be seen.

The overall trend of the ΔC_l is the same for the $60°$ flap case and the $60°$ flap and spoilers case with an overall increase in rolling moment for all sideslip at both angles of attack. However, the combined flap

and spoilers introduce two places where the sign changes on $C_{l,\beta}$. The ΔC_l might become negative with spoiler deflection due to the windward spoilers, as with increasing sideslip they become more perpendicular with the flow and thus more effective. The lift that is then dumped over the windward wing results in an increase in rolling moment towards that wing, which is a negative rolling moment increment when at negative sideslip.

Deflecting the spoilers in addition to the flaps reduces the magnitude of the yawing moment even more. Except for at the high angles of sideslip at $\alpha = 12.7°$, it doesn't look like the combined flap and spoiler deflections change the sign of $C_{n,\beta}$. The center of the larger inboard spoilers sit just forward of the MRC. Deflecting them likely causes the positive ΔC_n increment seen in the same way the flap deflections do.

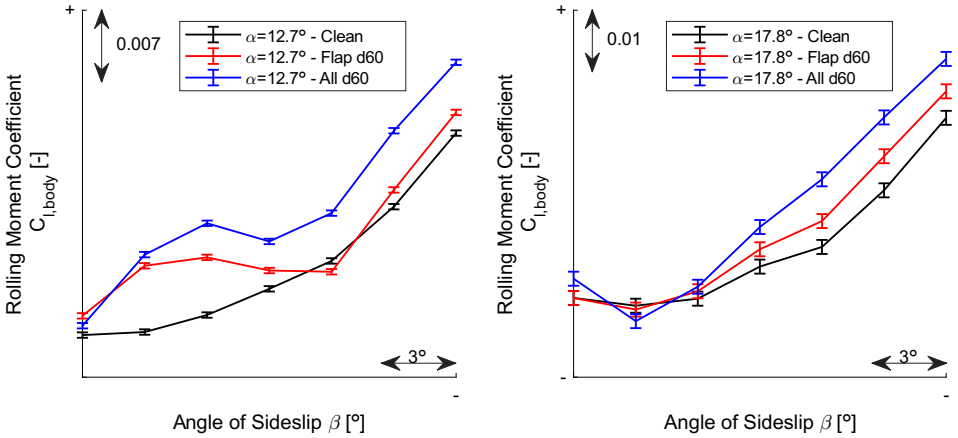

Figure 5.38: C_l with all flaps and spoilers at full 60° deflection

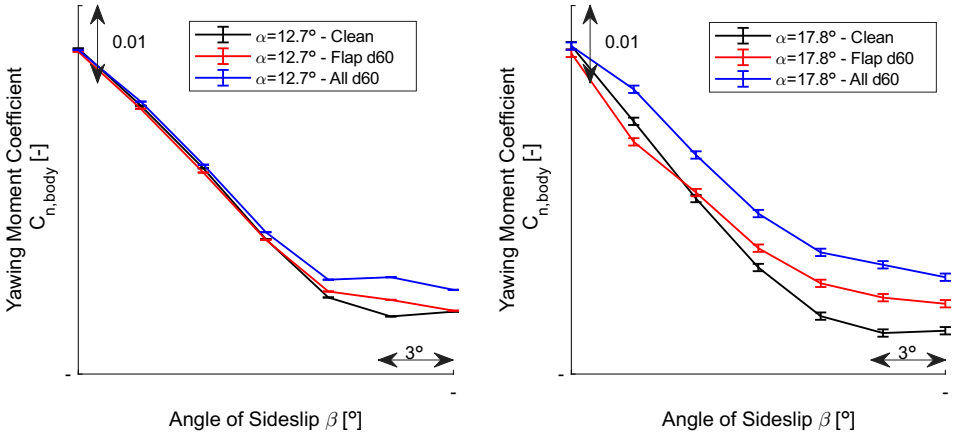

Figure 5.39: C_n with all flaps and spoilers at full 60° deflection

Looking at Figure 5.40, it can be seen how the rolling and yawing moment increment due to full flap and spoiler deflection changes with angles of attack and sideslip. These plots were created using thin plate splines fitted to the measurement data gathered. Figure 5.40a shows that the increase in rolling moment for all negative sideslip remains positive for almost all angles of attack. Figure 5.40b, however, shows that the yawing moment increment flips sign for low angles of attack, suggesting that the directional stability might increase with combined flap and spoiler deflections at low angles of attack.

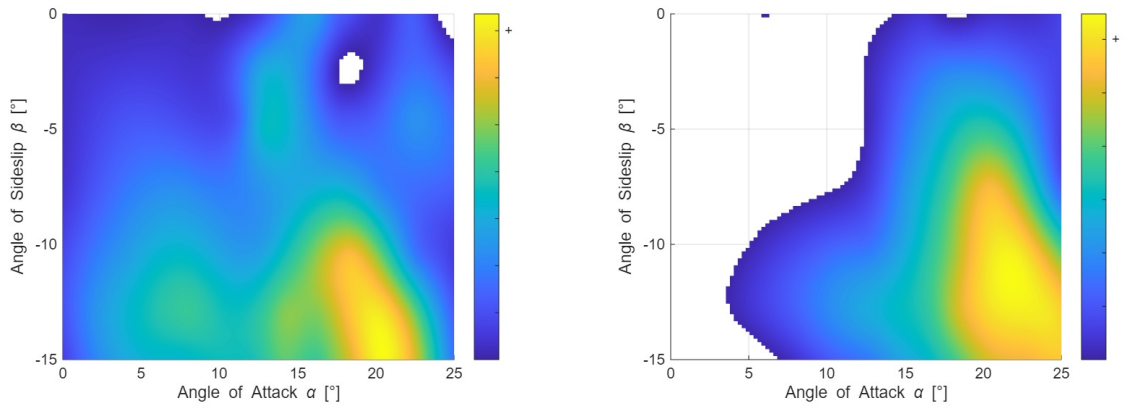

(a) ΔC_l surface plot

(b) ΔC_n surface plot

Figure 5.40: $\Delta C_{l,\text{ body}}$ and $\Delta C_{n,\text{ body}}$ with all flaps and spoilers at full 60° deflection, negative values not shown

5.5.5. Half Spoilers Deflections

Similarly to the half flap deflections, the half spoiler deflection configuration refers not to spoiler surface size but to the value at which all of the spoilers are deflected to. The forces and moments generated by the simultaneous deployment of all inboard and outboard spoilers at 30° are unexpected. The following subsections highlights the unusual behavior in each category.

Lift and Drag

As seen in Figure 5.41, the spoilers at half deflection dump surprisingly little lift at zero sideslip, surprising when compared to the results of Erdinçler in [5]. In this experiment, a very small amount of lift is dumped at $\alpha = 0^\circ, \beta = 0^\circ$, and there is virtually no lift dumped for most of the angle of attack range, with notable exceptions at $\alpha = 12.7^\circ$, where lift is generated due to spoilers deflected to 30°. The same is seen at $\beta = -13^\circ$ for part of the upper range of angles of attack and in the sideslip sweep at fixed $\alpha = 17.8^\circ$.

The 30° spoiler deflection data was not gathered until the final day of the experiment, and this interesting behavior was not processed, analyzed, and identified during the experiment. As a result, this configuration was not closely investigated, and there are not yet any definitive explanations for the peculiar behavior. However, there is surely some interaction occurring between the spoiler surfaces and the vortices over the Flying V due to the spoiler positions and the identified vortex locations [65]. It is possible key vortices are being strengthened by the half spoiler deflection through the change in the pressure distribution caused by the spoilers. Stronger vortices could lead to less flow separation and thus more lift and less drag. There could even be smaller vortices caused by the sharp edges of the highly swept spoilers themselves. As of now, there is no definitive explanation for the reverse spoiler effectiveness at 30° deflection, though there are some clues as to which regions might be affected by the spoilers as discussed below.

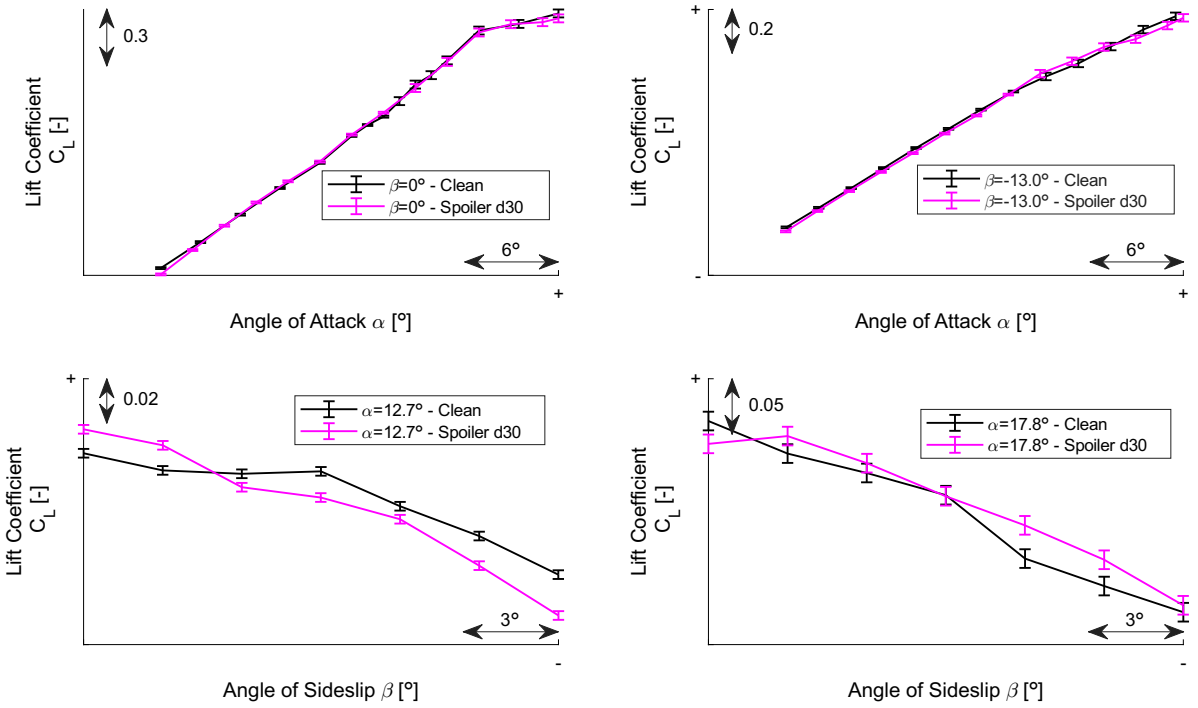

Figure 5.41: C_L with winglets alone, spoilers = 30°

Strengthening the argument for the possible vortex-spoiler interaction being the source for the reversed spoiler effectiveness is the drag coefficient trends seen in Figure 5.42. Especially in the sideslip sweep at fixed $\alpha = 12.7°$, it is seen how more than just increasing lift, deflecting the spoilers can actually decrease the drag, further indicating that the flow separation at the trailing edge of the Flying V and over the outboard wing is somehow being reduced.

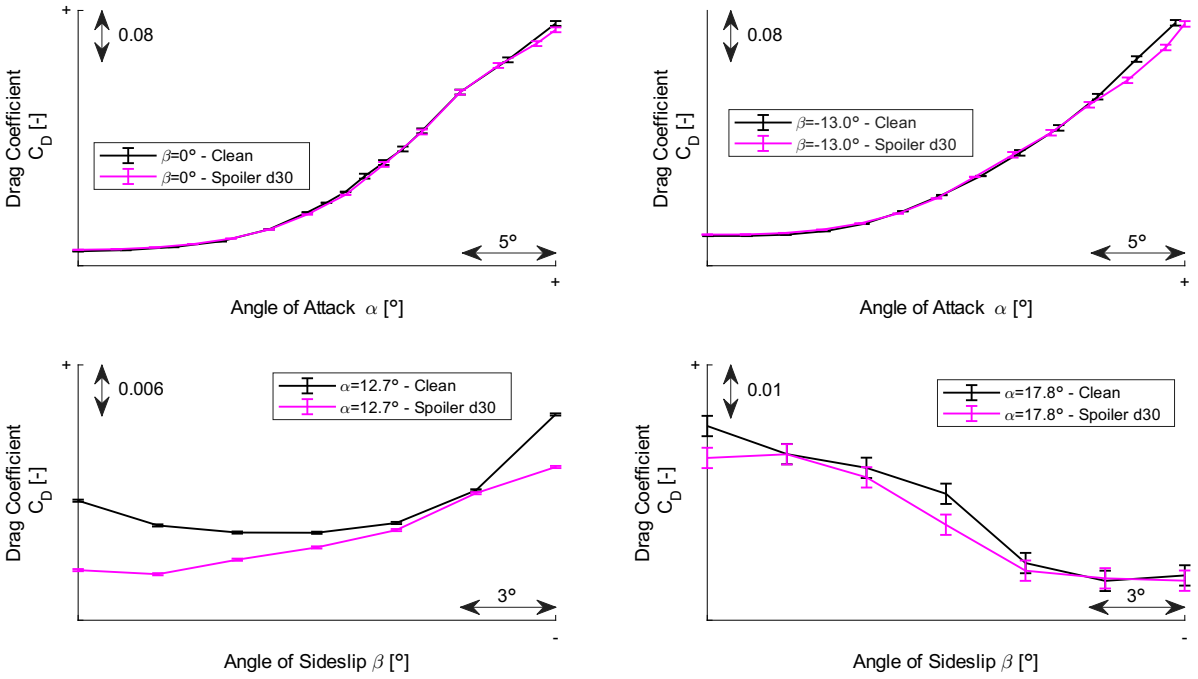

Figure 5.42: C_D with winglets alone, spoilers = 30°

As indicated in the Background in section 2.1, Erdinçler identified some spoiler designs that resulted

in an increase in lift for low deflections. These spoilers were placed at the 90% local chord line and extended to the wing trailing edge. As such, he hypothesized that there was no room for the flow to separated over the spoiler trailing edge and reattach before the wing trailing edge and create a region of low pressure [5]. This flow separation bubble is identified by Erdinçler as being a common culprit, but it appears that there are other phenomena at work here. Looking at the tuft images from Erdinçler's test in Figure 5.43, it is seen that there that the tufts in front of the most outboard spoiler are turned more streamwise with the low spoiler deflections and that there is an indication of less flow separation over the outboard wing area. This shows the most outboard spoiler affects regions of the wing further along the span and not just behind the spoiler itself. Furthermore, every spoiler tested in Erdinçler's campaign reduced the drag coefficient from the clean baseline at angles of attack greater than $\alpha > 15°$.

Additionally, bio-inspired passive separation control "flaps" or high-lift-enhancing-effectors (LEEs) have been experimentally assessed in a number of sources to effectively extend the maximum lift coefficient achieved at high angles of attack by delaying flow separation and thereby decreasing the drag [73]–[75]. The LEE devices resemble the spoilers tested in this report in chord size, and they work by preventing the flow separation from progressing upstream over the suction side of the wing. It is possible that the spoiler devices designed for the Flying V to dump lift at landing might be unintentionally acting as a high-lift device similar to these LEEs at low spoiler deflections.

Again, it is not known for certain what phenomena are causing the lift increase and drag decrease observed in the LTT Flying V model, but it is expected that there is a spanwise effect introduced by the low spoiler deflections on the LTT Flying V model that reduces the amount of flow separation experienced at the trailing edge near the trailing edge kink.

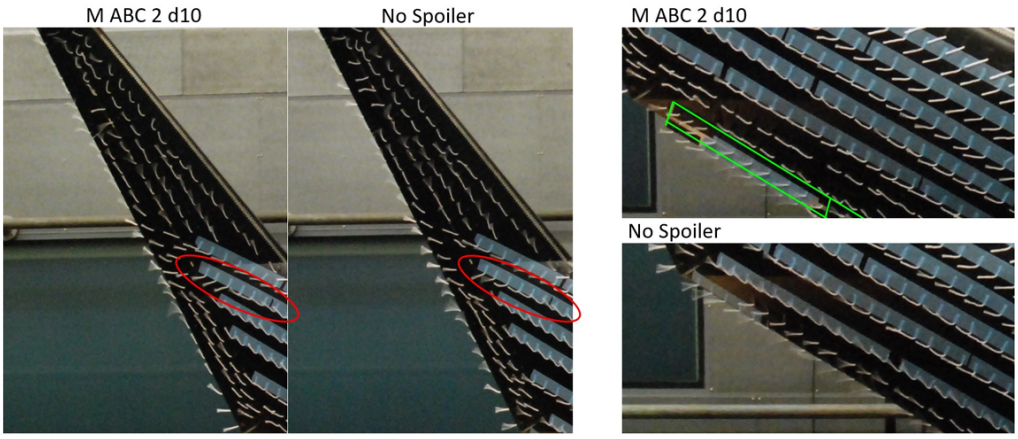

Figure 5.43: Low spoiler deflection effect on tuft orientation on OJF 4.8% Flying V model with at $\alpha = 17°$ [5]

Pitch Break

Surprisingly, the pitch break location is extended when the spoilers are deflected at $30°$ deflection at nonzero sideslip, as seen in Figure 5.44. As the sudden change in pressure distribution over the Flying V's surface due to vortices bursting and forming is the cause for the sharp pitch break around $\alpha = 18° - 20°$, it would follow that a disruption to how those vortices are forming and bursting would also disrupt the pitch break conditions. However, which vortex specifically is being affected and how that delays the pitch break exactly is unknown.

For the zero sideslip case, there is not a spike in the pitching moment coefficient when the spoilers are deflected. This spike is speculated to occur due to the start of outboard flow separation [65]. It is unclear if the spoilers effectively prevent the outboard separation or if they instead counteract the pitching moment imbalance by inducing trailing edge separation inboard and upstream of the CG as well. It is possible that the introduced cross-flow strengthens the primary vortices and delay their breakdown downstream, which would in turn prevent the outboard separation. The exact mechanism by which the spoilers affect the pressure distribution over the Flying V should be examined via oil flow in future experiments.

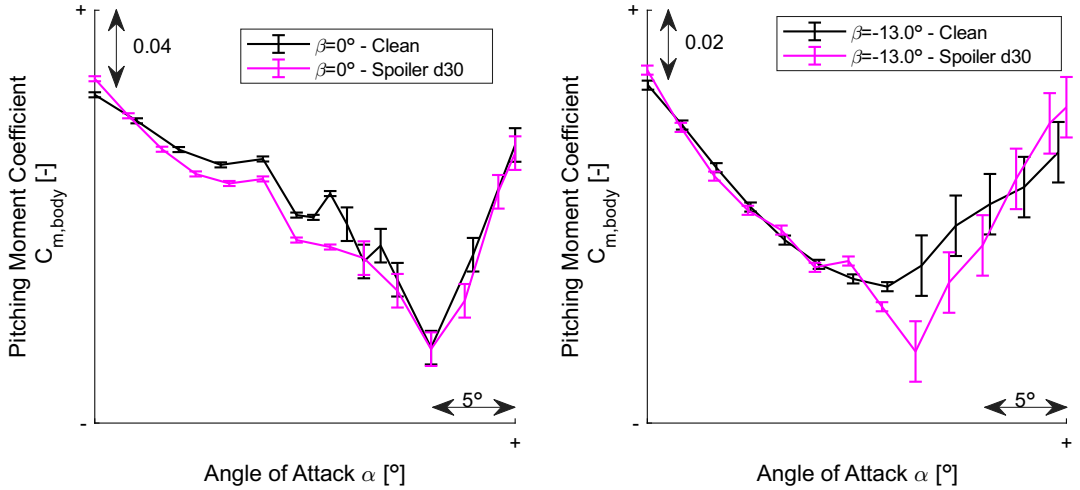

Figure 5.44: $C_{m,\text{ body}}$ with winglets alone and apoilers = 30°

Lateral-Directional Moments

The spoilers in Figure 5.45, when deflected alone at $30°$, impact the rolling moment much in the same way as the flap-alone effects do for the $\delta_f = 60°$ flap deflection in Figure 5.28, adding roll stiffness at low sideslip. For change in yawing moment due to spoiler deflection, it isn't surprising to see that the spoilers increase the yawing moment for all angles presented. This is because the same positive increase due to spoiler deflection was observed for the combined maximum deflection of flap and spoilers in Figure 5.39.

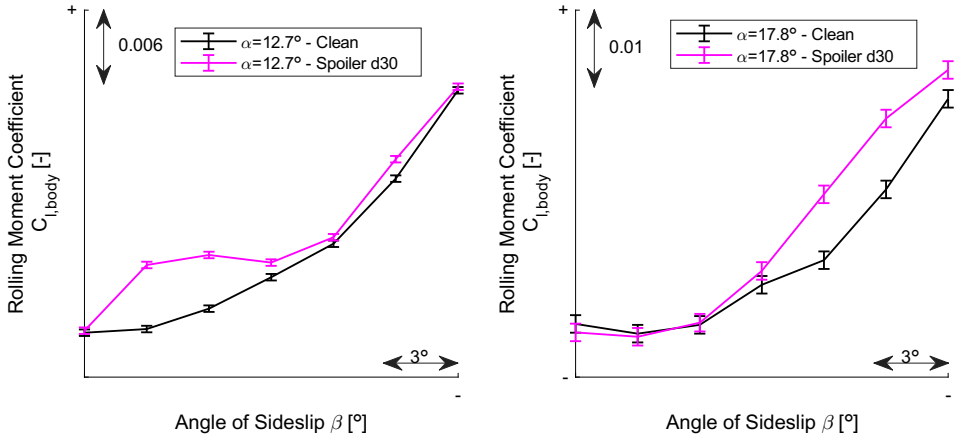

Figure 5.45: C_l with spoilers = 30° deflection

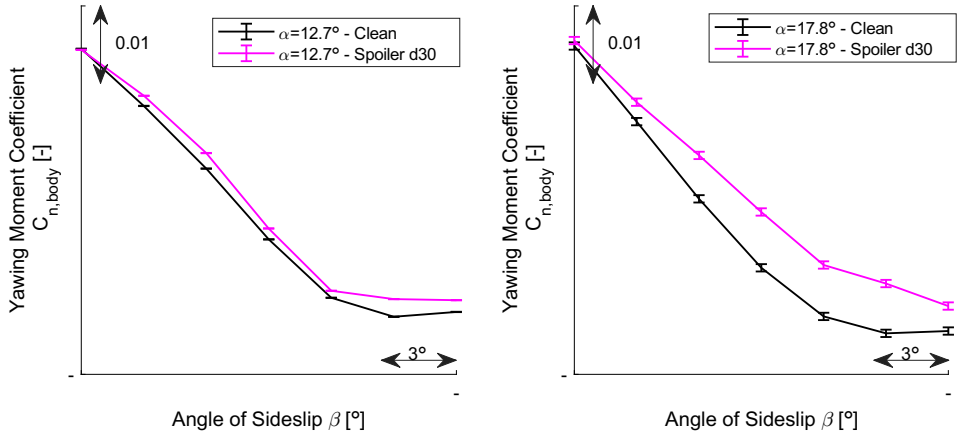

Figure 5.46: C_n with spoilers = 30° deflection

5.5.6. Outboard Spoiler Differential

The spoiler differential configuration used to generate a rolling moment at cruise conditions, where aileron roll control reversal is possible, was predicted using the fitted regression models at the cruise angle of attack. Although past predictions put the Flying V cruise angle of attack at around $\alpha = 3°$, the cruise lift coefficient in this experiment was reached around $\alpha = 5°$. The difference in angles is likely due to the lack of corrections, such as blockage, compressibility, and Reynolds effects. Regardless, the outboard spoiler lateral control effectiveness was assessed at $\alpha = 3°$, at zero sideslip, as the trends here are more clear to describe.

When using the models to predict the roll control effectiveness of differential outboard spoiler deflection, Figure 5.47 shows that the there is roll control reversal for the low spoiler deflections. After the reversal, the rolling moment increases with a starboard spoiler deflection and it decreases with a port spoiler deflection as expected. For the low spoiler deflections, however, the reversal likely occurs for the same reasons discussed above in subsection 5.5.5: lift generated by small spoiler differential results in the opposite rolling moment response than when the spoiler differential dumps lift. The reversal in spoiler lift effects causes a corresponding roll control effectiveness. This is problematic as outboard spoilers are usually used for roll control to compensate for the roll reversal ailerons normally experience at cruise conditions. These model prediction results in Figure 5.47 suggests the current outboard spoiler design would also exhibit roll reversal.

Furthermore, as is clearly seen in the figure, the confidence interval of the model's predictions are quite large relative to the predictions, and the interval includes $\Delta C_{l,\text{ body}} = 0$ for all deflections for both spoilers past around $\delta_{sp,2} = 15°$. This means the predicted response is not distinguishable from zero with statistical confidence. The $\delta_{sp,2\ell}$ model predictions also include the $\delta_{sp,2r}$ within its confidence interval, further limiting the usefulness of these results.

The reason for this model uncertainty is that the specific configurations predicted are predicted through extrapolation. Considering the sample space of configurations as a four-dimensional hypersphere, the center of such a space is located at the configuration where all flaps and spoilers are at half deflection. The edges of the configuration sample space are at the configurations where one surface is deflected to $0°$ and to $60°$ and all the other surfaces are deflected to $30°$. To predict a configuration where all surfaces are held at $0°$ or no deflection while one surface is deflected lies outside of the sampled space of configurations. If the sample space hypersphere lay circumscribed within a hypercube, the predicted differential configurations shown here would exist in the empty space in a corner of the hypercube. The specific configurations tested can be seen in Appendix A.

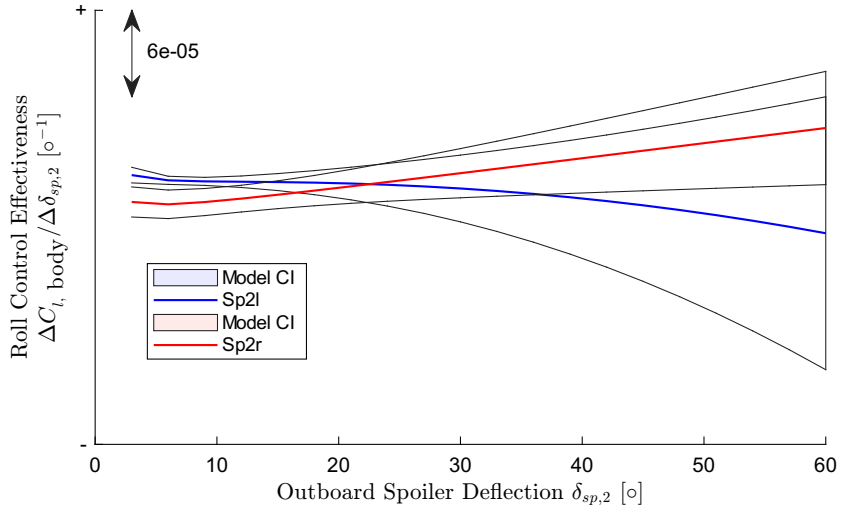

Figure 5.47: Predicted $\frac{\Delta C_\ell}{\Delta\delta_{sp,2}}$ with outboard spoiler differential with $\pm 2\sigma$ model confidence interval; $(\alpha, \beta) = (3^\circ, 0^\circ)$

Using the data measured for the model fitting, a single data point exists for varying a single outboard spoiler while holding all other variables constant. In addition to the half deflections configuration, two isolated right outboard spoiler deflections, shown in Figure 5.48, were measured at the middle of both Range 1 and Range 2. Therefore, a crude approximation of $\frac{\Delta C_\ell}{\Delta\delta_{sp,2}}$ can be calculated for this orientation, using a change in spoiler deflection of $\Delta\delta_{sp,2} = 30^\circ$ to approximate the derivative.

The approximation is distorted by the presence of the deflected flap, inboard spoiler, and the opposite outboard spoiler, and the approximation is limited to the single orientation of $(\alpha, \beta) = (7.5^\circ, -7.5^\circ)$. Moreover, the propagated balance uncertainty is around the same magnitude as the estimated derivatives, and for the higher $\delta_{sp,2\ell}$ deflection it encompasses 0. The roll control derivative for the $\delta_{sp,2\ell}$ spoiler is statistically indistinguishable from zero at the orientation of $(\alpha, \beta) = (7.5^\circ, -7.5^\circ)$ and with the flap and inboard spoilers deployed. The change in rolling moment due to outboard spoiler deflection is shown in Table 5.14.

(a) Outboard right spoiler up:
$\delta_f = \delta_{sp,1} = \delta_{sp,2l} = 30^\circ, \delta_{sp,2r} = 60^\circ$

(b) Outboard right spoiler down:
$\delta_f = \delta_{sp,1} = \delta_{sp,2l} = 30^\circ, \delta_{sp,2r} = 0^\circ$

Figure 5.48: Roll control estimate configurations, back view

Derivative	Outboard Spoiler Deflections	Range	Value
$\frac{\Delta C_\ell}{\Delta\delta_{sp,2\ell}}$	(0°, 30°)	1	$(19 \pm 5) \times 10^{-5}$ [-]
$\frac{\Delta C_\ell}{\Delta\delta_{sp,2\ell}}$	(30°, 60°)	1	$(0.3 \pm 5) \times 10^{-5}$ [-]
$\frac{\Delta C_\ell}{\Delta\delta_{sp,2r}}$	(0°, 30°)	1	$(-9 \pm 5) \times 10^{-5}$ [-]
$\frac{\Delta C_\ell}{\Delta\delta_{sp,2r}}$	(30°, 60°)	1	$(16 \pm 5) \times 10^{-5}$ [-]

Table 5.14: Outboard spoilers roll control estimates at $(\alpha, \beta) = (7.5^\circ, -7.5^\circ)$, half flap and inboard spoiler deflections, and different outboard spoiler deflections.
Reported with $\pm\sigma = \pm 5 \times 10^{-5}$, and normalized with a confidential deflection

The model predictions and these hand-calculated approximations indicate there may be roll control reversal for small $\delta_{sp,2r}$ spoiler deflections but for larger $\delta_{sp,2\ell}$ deflections the expected roll control

could be achieved. This is again likely due to the reversal of expected spoiler effects for the low spoiler deflections. For the $\delta_{sp,2\ell}$ spoiler, the same reversal is predicted, and at the higher spoiler differential, the model uncertainty is so large that it is statistically indistinguishable from the $\delta_{sp,2r}$ predictions.

5.6. Synthesis

From the results in section 5.5, some general remarks can be made about the flap and spoiler effects on the Flying V and the Flying V's lateral-directional stability based on these wind tunnel results.

First, it appears that the current Flying V design might be statically directionally stable or neutrally stable up to the maximum sideslip angle. However, this result is confounded with the effects of the aft vertical strut, which acts as a vertical tail behind the moment reference point and thus benefits directional stability. Furthermore, Barlow, Rae, and Pope suggest that most wind tunnels tend to overestimate the directional stability of an aircraft. These qualifying remarks must be taken into account when considering the data presented.

Second, the wind tunnel results suggest the current Flying V design is laterally stable for most sideslip and angles of attack past $\alpha = 7^\circ$, though there is a small range of neutral stability or unstable behavior at mid angles of attack and low sideslip. It is possible the aircraft is laterally stable for all angles of attack, but without removing the destabilizing effect of the aft strut, it is hard to make such a conclusion from the wind tunnel results alone. However, it is known that the scaled flight test results indicate static lateral-directional stability for the Flying V [70], so it is assumed that removing the aft strut contribution would reveal laterally stable behavior.

Using the wind tunnel data and regression models from this research, though, the flap and spoiler effects on the rolling and yawing moment trends have been quantified. Flap, spoiler, and combined flap and spoiler deflections seem to add a positive increment to both the rolling moment and yawing moment for negative sideslip. There are some configurations at high angles of attack around $\alpha = 12.5^\circ$ where the flap and spoilers might make the Flying V neutrally laterally stable or even laterally unstable for small sideslips.

Third, it appears the maximum ΔC_L achieved by the full flap deflection is about $\Delta C_L = 80\% \times \Delta C_{L,\,\text{OJF, max}}$ at a $C_L \approx 0.25$. The maximum ΔC_L dumped by the spoilers in the touchdown configuration is about $\Delta C_{L,\delta_{sp}} = 45\% \times \Delta C_{L,\,\delta_{sp},\,\text{OJF}}$ at $\alpha = 0^\circ$ and $\Delta C_{L,\delta_{sp}} = 55\% \times \Delta C_{L,\,\delta_{sp},\,\text{OJF}}$ without the flaps deflected at the same angle. However, the Flying V is pitched nose down when the landing gear makes contact with the runway, so the maximum lift dumping achieved by the current spoiler design is likely higher. Erdinçler's experimental results suggest a maximum $\Delta C_{L,\,\delta_{sp},\,\text{OJF}} = -0.16$ at $\alpha = -2.5^\circ$ with no flap deflections [5].

Fourth, rather than acting as lift dumping devices, the spoilers have reversed lift dumping, i.e. they increase the lift and decrease drag, at half deflection for some orientations. This suggests at low deflections the spoilers are not spoiling the flow over the wing and thus the lift generated by the wing but instead are affecting some other aerodynamic phenomenon. There is likely a significant interaction between the half spoiler deflections and the vortical flow generated by the Flying V.

6

Conclusions and Recommendations

This chapter highlights the conclusions of the study of Combined Spoiler and Split Flap Effects On The Flying V in section 6.1. Based on the results, limitations, and experience gained through this research, a list of recommendations for next steps and further research is provided in section 6.2.

6.1. Conclusions

This report highlights the research conducted to meet the research objective stated in the introduction:

Experimentally characterize the Flying V's split flap and spoiler aerodynamic and interaction effects in sideslip conditions using Modern Design of Experiment techniques in a wind tunnel.

In the experiment, 29 distinct configurations were tested, 244 unique data points were measured for model fitting, and the test was completed nearly four hours ahead of schedule due to planned margin and assistance from other researchers. Through the successful planning and execution of the wind tunnel test using MDOE techniques, the data gathered was used to characterize the Flying V's split flap and spoiler effects for a variety of conditions through the fitting of numerous polynomial regression models. Through a process of verification and validation, these regression models and the gathered data were then used to answer the research questions put forth by this report.

The primary research question was

What is the combined effect of split flap and spoiler deflection on the Flying V's forces and moments, and how does that effect change in sideslip conditions?

The combined maximum split flap and spoiler deflections add a net increase in lift and drag at zero sideslip with respect to the baseline configuration, except for certain high angles of attack, such as $\alpha = 17.8°$, where the combined deflections lead to a loss in lift and drag compared to the baseline performance. For low angles of attack, the lift added from combined flap and spoiler deflections is constant with increasing sideslip for most angles of attack. The combined drag increment stays relatively constant for increasing sideslip for most angles of attack.

The combined maximum split flap and spoiler deflections add a net increase in the pitching moment around the leading edge of the MAC at for low angles of attack at all sideslips. The combined deflections do not change the location of the pitch break, neither worsening or improving the pitch break behavior observed on the Flying V. At zero sideslip, the combined flap and spoilers at the low angles of attack of around $\alpha \approx 5° - 10°$ result in a decrease in pitching moment. The combined flap and spoiler deflections add a positive increment in rolling moment for most of the negative sideslips tested, with a few small exceptions at low sideslip and high angles of attack. For yawing moment, the positive increment is largest at high sideslips, and it appears the flap and spoiler effect reverses at lower angles of attack, providing a negative yawing moment increment. These effects on the moments are not expected to change much once the data is corrected for the strut effects.

The identified trends above answer the primary research question in part, but the answers to the secondary research questions serve to answer the primary one more fully. The first sub question was

- What is the mathematical relationship between flap deflection angle, inboard spoiler deflection angle, outboard spoiler deflection angle, angle of attack, and sideslip angle on each of the Flying V's forces and moments?

This is answered by observing the identified model structures that were fit using the RSM methodology. Using only 128 data points for the full models and 141 points for the effects models, the polynomial models were fitted and used to identify the significant relationships each design variable had on the Flying V's forces and moments. Due to the sheer number of models and the number of terms included in each, the models' mathematical structures are provided in Appendix B. Most model structures were cubic, with pure cubic terms and up to three-way interactions.

The second sub questions was

- To what extent is the spoiler effectiveness changed when combined with flap deflections?

This sub question is answered when observing the trends in the data and those predicted by the models. Additionally, it is answered notationally when looking at the significant interactions identified in the model terms, comparing the significant interaction groups and the sign on their group coefficient indicates how the effects of spoiler deflections on any of the forces or moments change with a flap deflection, and vice versa. All interaction term coefficients are not presented in this report due to confidentiality constraints.

Some observed changes in spoiler and flap effects due to the combined deflections take place in $\Delta C_{D,1}$, ΔC_S, $\Delta C_{l,\text{ body}}$, and $\Delta C_{n,\text{ body}}$. The implications of these findings suggest that research on the lift and pitching moment behavior of the Flying V need not include the flap and spoiler deflections together in order to accurately predict the lift or pitching moment response. However, when validating the pitching moment model, it was found that there was poor accuracy at zero sideslip and that the model failed to predict some configurations well, leading to a R^2_{adj} value of 0.67 and 0.46 for Range 1 and 2, respectively. The validation data suggests there may be a change in the flap or spoiler pitching moment contribution when deflected together. For accurate predictions for the landing configuration in any of the forces or moments, then, the measurements should be made with both the flaps and spoilers deployed.

The last sub question was

- How do full-span flap and spoiler effects compare with the semi-span flap and spoiler effects?

This question is answered when comparing the flap and spoiler predictions from previous research with the results in this report. The trends of the lift generated or dumped by the flaps and spoilers respectively follows the same trends identified with the semi-span model in the OJF, but the magnitude of the effects differ. The uncorrected LTT data presented indicates an overall reduction in both flap and spoiler effectiveness when considering the present flap and spoiler designs on the new full-span, 1.84% Flying V geometry, though this conclusion is obscured by the fact that both the data measured in the LTT and presented in this report and the OJF data from previous reports are uncorrected and use different reference geometries.

Having answered the sub questions and the primary research question using the results from, the research objective was successfully met. There are limitations to the results and answers presented, however, so recommendations are provided to improve the usefulness and accuracy of the results provided.

6.2. Recommendations

It is recommended that the data gathered in this experiment is further analyzed. The usefulness of the fitted models and the raw data is by no means exhausted, and the methods used to process and analyze it can be improved upon. First, it is highly recommended to exploit the designed nature of the dataset to improve the precision with which the model terms are estimated. There are many ways in which the data can be presented, such as centering and encoding the design variable levels, expressing the design variables in different ways (such as treating the difference in outboard spoiler levels as a variable instead of treating each surface separate), and analyzing the data using more of the available

variables, such as temperature, relative time within a wind-on block, or time of day. Any of these approaches could potentially explain the data better, providing improved estimates of the residual error, identifying and removing systematic error instead of grouping it all as a block effect, and identifying the fixed effects terms more accurately and precisely. Codifying the design variables before model fitting is highly recommended as doing so can leverage the orthogonal design of the experiment.

It is recommended that more robust model regression algorithms are implemented for fitting linear mixed models on the data. There are plenty of examples in literature of algorithms used in stepwise regression, following different goodness-of-fit criteria such as AIC/BIC, PRESS residuals, and more [21], [60]. More effective algorithms could be developed and implemented with the dataset presented in this research to not only improve on the models presented here but to also prepare for the analysis of future tests. Better algorithms promise improved insight in identifying the true significant effects in a dataset.

It is recommended to explore designing future wind tunnel experiments with the Flying V for the purpose of fitting splines. The Flying V has many discontinuities in it's flight envelope due to the complicated vortical flow development and breakdown over it. Low order polynomials are suitable for screening the sample space and identifying regions of interest, but splines should be carefully constructed for higher accuracy interpolation and aerodynamic model capabilities. Using the results from this report, anyone seeking to gather experimental data for spline fitting should carefully consider the different sources of experimental error inherent in wind tunnel testing and should select a spline-fitting procedure that can handle such multi-level stochasticity in the data.

It is recommended to closely investigate and diagnose the aerodynamic phenomena over the Flying V in the LTT with spoilers alone deflected, whether with fluorescent oil flow, PIV, or pressure readings. Understanding better the interactions between the vortical flow and the spoilers can inform any design changes needed to be made to the spoilers. A few different phenomena have been identified from Erdinçler's research and other literature that provide suggestions for the next steps of investigation. Namely, the flow separation alleviation outboard of the most outboard spoiler at low deflections and the possibility of the low spoiler deflections acting as a lift enhancing effector are identified as starting points for further research. It is recommended that both the spoilers and flaps be more carefully investigated to see if design modifications should be made to improve their performance on the new Flying V geometry.

It is highly recommended to robustly quantify the LTT wind tunnel effects on the Flying V, especially the effects of the model struts. Without removing the strut effects from the data, it is hard to estimate the true lateral-directional stability of the Flying V. Furthermore, assessing the wind tunnel effects on the Flying V sooner rather than later will decrease the amount of backwards-facing post-processing needed to be done on the already-gathered data. For assessing the strut effects, it is recommended to follow the procedure detailed in Chapter 7 of Barlow, Rae, and Pope for determining the tare and interference effects of model struts [40]. This is not trivial to do, as the 1.84% model will need to be modified to permit both upright and inverted installation, and images of the struts will also need to be manufactured. However, characterizing these effects will greatly increase the usefulness of any data measured with this model.

It is recommended to carefully inspect the current fore struts used to hang the model in the test section. Concerns have been raised that the nonmetric fairings shielding much of the load-bearing struts can deform under sideslip loading and bridge the strut. This interferes with the measured data, especially in the measured drag and sideslip. Time should be allocated to conclusively determine if this bridging is occurring, and if so, a different installation system should be used or manufactured.

The aft strut that interfaces with the trailing edge of the wind tunnel model likely interacts and effects the flow around the flaps when deflected, especially at low flap deflection angles. This may in part explain the decrease in flap effectiveness seen from the OJF test to the results presented in this report. It is recommended to perform a few Large Eddy Simulation or Lattice Boltzmann Method simulations for one or two low flap deflections with and without the aft strut present. Using the data gathered in this experiment for the 30° flap alone deflection, the simulation can be calibrated for the aft-strut case. If the change in flap effectiveness observed when removing the presence of the aft strut is on the order of the difference between OJF and LTT results, then the aft strut influences the flap effectiveness and should be seen as a limitation for any investigations done in that area of the model.

Due to the limited range provided by the aft strut, as discussed in section 3.1 and subsection 3.4.2, the nose-wheel touchdown angle of $\alpha = -2.5^\circ$ was not measured in this experiment and the estimated spoiler effectiveness at this orientation was not explicitly measured. The models fitted can be used to extrapolate to this orientation, but only with great uncertainty. In order to properly compare the change in spoiler effectiveness from the old Flying V geometry to the new Flying V geometry, a change in the model installation should be made to allow for this touchdown angle of $\alpha = -2.5^\circ$ to be explicitly measured.

It is recommended to gather data for the positive sideslip range to verify the assumption that the flap and spoiler effects are symmetric across the longitudinal plane of symmetry.

It is recommended to explicitly measure the spoilers alone at $\delta_{sp} = 60^\circ$ maximum deflection. This configuration was not extensively tested, and not enough data was gathered to make definitive comparisons of the maximum spoiler effectiveness with that which was measured in the OJF test.

It is recommended that when surface effects models are to be fit in the future, the data measured to validate the fitted model ought to have clean model data measured for every data point. This can greatly help identify the true trends of the surface effects. Without a matching clean data point for every validation data point, one relies on a model to interpolate between the available clean data points. This can average out, approximate, or miss entirely the true behavior of the effects data, leading to incorrect conclusions when using the wrongly-calculated effects validation data to validate the fitted models. This is especially true when the validation data is measured over a fine sweep but the clean data is measured sparsely.

It is recommended to go back over the fitted models and examine where models might benefit from added data. The models fitted in this research could potentially be useful for more than just screening purposes but could actually be used as a reliable aerodynamic model if the models are seen to be valid. In some cases, it was observed that areas in which the models failed to predict the validation data simply failed because of a lack of fitting data in that region; adding even a single validation point to the model often corrected the behavior. As such, combing through the available data and attempting to refine the models can increase their usefulness. Alternatively, future experiments could be done to measure more data that could be added to the existing models and dataset, rather than starting afresh. However, this is not necessarily recommended, because as soon as the engine integration takes place, the spoiler effects will likely change and need remodeled. Thus, one should weigh the pros and cons of gathering more data on the Flying V spoilers alone for the sole purpose of improving the existing prediction models.

It is recommended that future experiments done in the LTT using MDOE techniques carefully consider how the text matrix randomization be conducted. The turntable and balance in the LTT can easily be put into a position where they move independently of each other, putting the model, balance, and wind tunnel infrastructure at risk and bringing the test to a halt. As such, it is recommended to yaw the synced turntable and balance as little as possible. It may be possible to introduce sideslip angle as a second grouping variable, held constant for variations in alpha measurements within a run, and added to a resulting Linear Mixed Effects model as a random grouping effect.

References

[1] D. P. Raymer, *Aircraft Design: A Conceptual Approach*, 6th. Reston, VA: American Institute of Aeronautics and Astronautics (AIAA), 2018, pp. 834–839, ISBN: 978-1624104909.

[2] J. Benad, "The flying v: A new aircraft configuration for commercial passenger transport," Airbus Operations GmbH, Technical Report, 2015.

[3] F. Faggiano, "Aerodynamic design optimization of a flying v aircraft," MSc Thesis, Delft University of Technology, Delft, The Netherlands, Nov. 2016. [Online]. Available: https://resolver.tudelft.nl/uuid:0b1472a5-3aad-433c-9a64-242c84b114fd.

[4] S. Eftekhar, "High lift split flaps for the flying-v," MSc Thesis, Delft University of Technology, Delft, The Netherlands, Jan. 2024. [Online]. Available: https://resolver.tudelft.nl/uuid:0ad3c088-b6a6-472b-b60b-4b424a08e15c.

[5] O. Erdinçler, "Aerodynamic and performance analysis of ground spoilers on the flying v," MSc Thesis, Delft University of Technology, Delft, The Netherlands, Sep. 2021. [Online]. Available: https://resolver.tudelft.nl/uuid:d8176c14-f3e1-4a6a-99b0-55c7251f9762.

[6] G. J. de Zoeten, "Comparative flight performance evaluation of the flying-v and a reference aircraft," MSc Thesis, Delft University of Technology, 2022. [Online]. Available: https://resolver.tudelft.nl/uuid:3a5999b2-1bd9-4b38-86be-fb65c5087880.

[7] W. J. Oosterom, "Flying-v family design," MSc Thesis, Delft University of Technology, 2021. [Online]. Available: https://resolver.tudelft.nl/uuid:9e8f9a41-8830-405d-8676-c46bf6b07891.

[8] N. van Luijk, "Constrained aerodynamic shape optimisation of the flying v outer wing," MSc Thesis, Delft University of Technology, Delft, Netherlands, Mar. 2023. [Online]. Available: https://resolver.tudelft.nl/uuid:fc2bbe10-6796-4337-81cc-5971b324d50e.

[9] Y. A. Laar, "Aerodynamic design of a flying v aircraft in transonic conditions," MSc Thesis, Delft University of Technology, Delft, The Netherlands, Jun. 2023. [Online]. Available: https://resolver.tudelft.nl/uuid:591093b2-5cdc-41c5-b564-3786f43d51db.

[10] M. R. V. D. Toorn, "Flying-v family design for stability & control," MSc Thesis, Delft University of Technology, 2021. [Online]. Available: https://resolver.tudelft.nl/uuid:c9c1ded2-a0a0-4e95-9d81-5d93e9f54ad2.

[11] J. Benad, *Design of a commercial aircraft for high-subsonic speed as a flying wing configuration*, Berlin, Mar. 2015. [Online]. Available: https://filelist.tudelft.nl/LR/Subsites/Flying%20V/Publications/2015%20-%20Justus%20Benad%20-%20Design%20of%20a%20commercial%20aircraft%20for%20high-subsonic%20speed%20as%20a%20flying%20wing%20configuration%20%282015%29.pdf.

[12] R. de Voogt, "Flying-v design optimisation for the global warming impact and operating cost," MSc Thesis, Delft University of Technology, Delft, The Netherlands, Feb. 2024. [Online]. Available: https://resolver.tudelft.nl/uuid:f1147217-55af-4779-850a-87e80bf7d2f1.

[13] M. Palermo, "The longitudinal static stability and control characteristics of a flying v scaled model: An experimental and numerical investigation," MSc Thesis, Delft University of Technology, 2019. [Online]. Available: https://resolver.tudelft.nl/uuid:6286f9e2-c24a-430c-a4fa-9fb67b9558b4.

[14] R. A. Viet, "Analysis of the flight characteristics of a highly swept cranked flying wing by means of an experimental test," MSc Thesis, Delft University of Technology, 2019. [Online]. Available: https://resolver.tudelft.nl/uuid:90de4d9e-70ae-4efc-bd0a-7426a0a669c3.

[15] A. M. C. M. Jorge, “Quantifying wind tunnel effects on the flying v,” MSc Thesis, Delft University of Technology, Delft, The Netherlands, Dec. 2023. [Online]. Available: https://resolver.tudelft.nl/uuid:b9076ade-2d6e-4faf-882c-1f6115a1317a.

[16] C. E. Jobe, “Vortex breakdown location over 65° delta wings: Empiricism and experiment,” *The Aeronautical Journal*, vol. 108, no. 1087, pp. 475–482, 2004. DOI: 10.1017/S0001924000000294. [Online]. Available: https://doi.org/10.1017/S0001924000000294.

[17] M. Hillen, “Parametrisation of the flying-v outer mould line,” MSc Thesis, Delft University of Technology, Delft, Netherlands, 2020. [Online]. Available: http://resolver.tudelft.nl/uuid:f4863ae4-2792-4335-b929-ff9dfdb6fed5.

[18] T. Nieuwenhuizen, “Conceptual design optimisation of a flying v aircraft,” MSc Thesis, Delft University of Technology, Delft, Netherlands, Aug. 2021. [Online]. Available: https://resolver.tudelft.nl/uuid:ec1cbf97-f795-476a-87e3-066c3736b618.

[19] J. Horwitz, “Parametric design of the flying-v winglets for improved lateral-directional stability and control,” MSc Thesis, Delft University of Technology, Delft, Netherlands, 2021. [Online]. Available: http://resolver.tudelft.nl/uuid:d7513b36-b9fd-4f8a-8726-f5c7ee7f3a6b.

[20] F. Granata, “Aerodynamic optimization of a flying v aircraft using a vortex lattice method,” MSc Thesis, Delft University of Technology, Delft, Netherlands, Sep. 2023. [Online]. Available: https://resolver.tudelft.nl/uuid:35d70826-c242-4eb1-a10a-2a61955b7182.

[21] A. Garcia, “Aerodynamic model identification of the flying v using wind tunnel data,” MSc Thesis, Delft University of Technology, 2019. [Online]. Available: https://resolver.tudelft.nl/uuid:79e01f29-1789-4501-8556-ca2bcf06f3ab.

[22] A. Świderski, “Automating the handling qualities predictions of the flying-v,” MSc Thesis, Delft University of Technology, 2023. [Online]. Available: http://resolver.tudelft.nl/uuid:e9b906e8-2a7b-4464-9c78-dd0d9ecde137.

[23] S. van Overeem, X. Wang, and E. J. van Kampen, “Modelling and handling quality assessment of the flying-v aircraft,” in *AIAA Science and Technology Forum and Exposition, AIAA SciTech Forum 2022*, American Institute of Aeronautics and Astronautics Inc, AIAA, 2022, ISBN: 9781624106316. DOI: 10.2514/6.2022-1429.

[24] J. J. D. van Uitert, “Experimental investigation into the effect of aerodynamic add-ons on the aerodynamic characteristics of the flying v,” MSc thesis, Delft University of Technology, Delft, The Netherlands, Jan. 2021. [Online]. Available: https://resolver.tudelft.nl/uuid:fdfff622-792c-4d54-a048-b59abf477a11.

[25] A. V. Meenen, “Vortex flow control using fillets and fences on the flying v,” MSc Thesis, Delft University of Technology, 2024. [Online]. Available: http://resolver.tudelft.nl/uuid:3e29a737-5944-4149-aa26-b326a72698a5.

[26] A. J. Santosh, “Influence of ground effect on the flying v aircraft: A numerical investigation,” MSc Thesis, Delft University of Technology, May 2020. [Online]. Available: https://resolver.tudelft.nl/uuid:d34e14b2-fed5-4e4f-a448-aa0fb92e0331.

[27] P. K. C. Rudolph, “High-lift systems on commercial subsonic airliners,” NASA Langley Research Center, Hampton, VA, NASA Contractor Report NASA CR-4746, 1996.

[28] G. J. de Zoeten, C. Varriale, and R. Vos, “Flight performance evaluation of the flying-v,” in *AIAA Aviation and Aeronautics Forum and Exposition, AIAA AVIATION Forum 2023*, American Institute of Aeronautics and Astronautics Inc, AIAA, 2023, ISBN: 9781624107047. DOI: 10.2514/6.2023-3484. [Online]. Available: https://resolver.tudelft.nl/uuid:355db742-8b4c-422d-8640-23ead6d15125.

[29] A. M. O. Smith, “High-lift aerodynamics,” *Journal of Aircraft*, vol. 12, pp. 501–530, 6 1975. DOI: 10.2514/3.59830.

[30] A. D. Young, “The aerodynamic characteristics of flaps,” Royal Aircraft Establishment, Farnborough, UK, Technical Report R.A.E. Report No. Aero 2153, 1953.

[31] E. Obert, *Aerodynamic Design of Transport Aircraft*. IOS Press, 2009, pp. 433–440, ISBN: 978-1-58603-970-7.

[32] M. D. Mack, H. C. Seetharam, W. G. Kuhn, and J. T. Bright, “Aerodynamics of spoiler control devices,” in *AIAA Aircraft Systems and Technology Meeting*, New York, NY: American Institute of Aeronautics and Astronautics, Aug. 1979. DOI: 10.2514/6.1979-1873.

[33] R. Vos and S. Farokhi, *Introduction to Transonic Aerodynamics*, 2nd. Cham, Switzerland: Springer, 2015, ISBN: 978-94-017-9746-7.

[34] W. Wentz, H. Seetharam, and J. Calhoun, “Wind tunnel and flight development of spoilers for general aviation aircraft,” SAE International, SAE Technical Paper 750523, 1975. DOI: 10.4271/750523. [Online]. Available: https://doi.org/10.4271/750523.

[35] J. D. Anderson Jr., *Introduction to Flight*, 9th. New York, NY: McGraw-Hill Education, 2021, pp. 324–326, ISBN: 978-1-260-57985-1.

[36] W. W. H. Yeung, C. Xu, and W. Gu, “Reduction of transient adverse effects of spoilers,” *Journal of Aircraft*, vol. 34, no. 4, pp. 479–484, 1997. DOI: 10.2514/2.2216.

[37] W. Wentz., C. Ostowari, and H. Seetharam, “Effects of design variables on spoiler control effectiveness, hinge moments and wake turbulence,” in *AIAA 19th Aerospace Sciences Meeting*, American Institute of Aeronautics and Astronautics, Missouri, 1981. [Online]. Available: https://arc.aiaa.org/doi/pdf/10.2514/6.1981-72.

[38] M. M. Abdelrahman, M. A. Ghazi, I. A. Olwi, and A. M. Al-Bahi, “Aircraft spoiler effects under wind shear,” *Journal of Aircraft*, vol. 31, no. 1, pp. 154–160, 1994. DOI: 10.2514/3.46468.

[39] European Union Aviation Safety Agency (EASA), *Certification Specifications for Large Aeroplanes (CS-25)*, Accessed: 2025-04-04, 2025. [Online]. Available: https://www.easa.europa.eu/en/document-library/certification-specifications.

[40] J. B. Barlow, W. H. Rae, and A. Pope, *Low-speed wind tunnel testing*. Wiley, 1999, pp. 19–22, 230–232, 239, 266–267, 328, 428, 445–461, ISBN: 0471557749.

[41] D. C. Montgomery, *Design and Analysis of Experiments*, 8th. Hoboken, NJ: John Wiley & Sons, 2013, pp. 68–75, 523, 462–466, 473–475, 479, 320–325, ISBN: 978-1-118-14692-7.

[42] G. E. P. Box, W. G. Hunter, and J. S. Hunter, *Statistics for Experimenters: An Introduction to Design, Data Analysis, and Model Building*. New York, USA: John Wiley & Sons, 1978, pp. 173, 17–48, ISBN: 978-0-471-09315-7.

[43] R. DeLoach, “The modern design of experiments: A technical and marketing framework,” in *21st AIAA Advanced Measurement Technology and Ground Testing Conference*, American Institute of Aeronautics and Astronautics (AIAA), Denver, CO, 2000. DOI: 10.2514/6.2000-2691. [Online]. Available: https://arc.aiaa.org/doi/10.2514/6.2000-2691.

[44] R. DeLoach, *Analysis of variance in the modern design of experiments*, Presented at the 48th AIAA Aerospace Sciences Meeting and Exhibit, Orlando, FL, January 4–7, 2010, 2010. DOI: 10.2514/6.2010-1111. [Online]. Available: https://arc.aiaa.org/doi/10.2514/6.2010-1111.

[45] R. DeLoach and J. R. Micol, “Analysis of wind tunnel polar replicates using the modern design of experiments (invited),” in *27th AIAA Aerodynamic Measurement Technology and Ground Testing Conference*, Paper presented at the conference, American Institute of Aeronautics and Astronautics (AIAA), Jun. 2010. DOI: 10.2514/6.2010-4927. [Online]. Available: https://arc.aiaa.org/doi/pdf/10.2514/6.2010-4927.

[46] J. M. Reichert, “Statistical design of aircraft wind tunnel experiments application of modern design of experiments,” MSc Thesis, Delft University of Technology, Mar. 2012.

[47] A. A. Giunta, S. F. W. Jr., and M. S. Eldred, “Overview of modern design of experiments methods for computational simulations,” in *41st AIAA Aerospace Sciences Meeting and Exhibit*, Sandia National Laboratories, Albuquerque, NM, American Institute of Aeronautics and Astronautics, Reno, NV, USA: AIAA, Jan. 2003. DOI: 10.2514/6.2003-649. [Online]. Available: https://doi.org/10.2514/6.2003-649.

[48] R. H. Myers, D. C. Montgomery, and C. M. Anderson-Cook, *Response Surface Methodology: Process and Product Optimization Using Designed Experiments*, 4th. Hoboken, NJ: Wiley, 2016, pp. 1–7, 13–17, 24–30, 161–167, 393–417, 488–499, ISBN: 978-1-118-91601-8.

[49] R. DeLoach and G. Erickson, “Low-order response surface modeling of wind tunnel data over truncated inference subspaces,” in *41st Aerospace Sciences Meeting and Exhibit*, American Institute of Aeronautics and Astronautics (AIAA), Reno, Nevada, 2003. DOI: 10.2514/6.2003-456. [Online]. Available: https://doi.org/10.2514/6.2003-456.

[50] R. DeLoach and J. R. Micol, “Comparison of resource requirements for a wind tunnel test designed with conventional vs. modern design of experiments methods,” in *49th AIAA Aerospace Sciences Meeting including the New Horizons Forum and Aerospace Exposition*, American Institute of Aeronautics and Astronautics (AIAA), Orlando, FL, 2011. DOI: 10.2514/6.2011-1260. [Online]. Available: https://arc.aiaa.org/doi/10.2514/6.2011-1260.

[51] N. Gumedze F. and T. Dunne T., “Parameter estimation and inference in the linear mixed model,” *Linear Algebra and Its Applications*, vol. 435, no. 8, pp. 1920–1944, 2011. DOI: 10.1016/j.laa.2011.04.015.

[52] P. Goos, “Optimal versus orthogonal and equivalent-estimation design of blocked and split-plot experiments,” *Statistica Neerlandica*, vol. 60, no. 3, pp. 361–378, 2006. DOI: 10.1111/j.1467-9574.2006.00344.x.

[53] R. Dowgwillo and R. DeLoach, “Using modern design of experiments to create a surface pressure database from a low speed wind tunnel test,” in *24th AIAA Aerodynamic Measurement Technology and Ground Testing Conference*, Jun. 2004. DOI: 10.2514/6.2004-2200. [Online]. Available: https://arc.aiaa.org/doi/abs/10.2514/6.2004-2200.

[54] P. Goos, B. Jones, and U. Syafitri, “I-optimal design of mixture experiments,” *Journal of the American Statistical Association*, vol. 111, no. 514, pp. 899–911, 2016. DOI: 10.1080/01621459.2015.1136632.

[55] R. DeLoach, “Improved quality in aerospace testing through the modern design of experiments,” *AIAA Paper*, 2002. DOI: 10.2514/6.2000-825. [Online]. Available: https://arc.aiaa.org/doi/abs/10.2514/6.2000-825.

[56] R. DeLoach, “Blocking: A Defense Against Long-Period Unexplained Variance in Aerospace Ground Testing,” in *41st AIAA Aerospace Sciences Meeting and Exhibit*, American Institute of Aeronautics and Astronautics, Jan. 2003. DOI: 10.2514/6.2003-650. [Online]. Available: https://arc.aiaa.org/doi/10.2514/6.2003-650.

[57] R. A. Fisher, *The Design of Experiments*. Edinburgh, UK: Oliver and Boyd, 1935.

[58] D. Landman, J. Simpson, R. Mariani, F. Ortiz, and C. Britcher, “A high performance aircraft wind tunnel test using response surface methodologies,” in *U.S. Air Force Test and Evaluation Days*, Nashville, TN, USA: American Institute of Aeronautics and Astronautics (AIAA), 2005. DOI: 10.2514/6.2005-7602. [Online]. Available: https://arc.aiaa.org/doi/10.2514/6.2005-7602.

[59] J. Luner and M. Healey, “Modern design of experiments techniques to optimize a leading edge extension fence,” in *41st Aerospace Sciences Meeting and Exhibit*, Reno, NV, USA: American Institute of Aeronautics and Astronautics (AIAA), 2003. DOI: 10.2514/6.2003-655. [Online]. Available: https://arc.aiaa.org/doi/abs/10.2514/6.2003-655.

[60] N. Ulbrich, “Regression model optimization for the analysis of experimental data,” in *47th AIAA Aerospace Sciences Meeting and Exhibit*, Orlando, Florida: American Institute of Aeronautics and Astronautics (AIAA), Jan. 2009. [Online]. Available: https://arc.aiaa.org/doi/10.2514/6.2009-1344.

[61] R. DeLoach, “The modern design of experiments for configuration aerodynamics: A case study,” in *44th AIAA Aerospace Sciences Meeting and Exhibit*, Paper presented at the conference, American Institute of Aeronautics and Astronautics (AIAA), Jan. 2006. DOI: 10.2514/6.2006-923. [Online]. Available: https://arc.aiaa.org/doi/10.2514/6.2006-923.

[62] G. G. Vining, S. M. Kowalski, and D. C. Montgomery, “Response surface designs within a split-plot structure,” *Journal of Quality Technology*, vol. 37, no. 2, pp. 115–129, 2005. DOI: 10.1080/00224065.2005.11980310.

[63] TU Delft. “Low turbulence tunnel.” Accessed: 2025-01-09. (n.d.), [Online]. Available: https://www.tudelft.nl/en/ae/organisation/departments/flow-physics-and-technology/facilities/low-speed-wind-tunnels/low-turbulence-tunnel.

[64] Y. A. Laar, D. Atherstone, J. Benad, and R. Vos, “Aerodynamic design of a flying v aircraft in transonic conditions,” in *AIAA SCITECH 2024 Forum*, Orlando, Florida: American Institute of Aeronautics and Astronautics (AIAA), Jan. 2024. DOI: 10.2514/6.2024-2669.

[65] N. van Luijk and R. Vos, “Experimental investigation of vortex flow over a flying v subsonic transport,” in *AIAA SCITECH 2025 Forum*. American Institute of Aeronautics and Astronautics (AIAA), 2025. DOI: 10.2514/6.2025-0258. [Online]. Available: https://arc.aiaa.org/doi/abs/10.2514/6.2025-0258.

[66] C. Varriale, “Flight mechanics and performance of direct lift control applying control allocation methods to a staggered box-wing aircraft configuration,” Accessed: 2025-04-01, Ph.D. dissertation, Delft University of Technology, Delft, The Netherlands, 2022. [Online]. Available: https://resolver.tudelft.nl/uuid:8b868c52-f34f-4307-8fc0-b1176eaf9d04.

[67] MathWorks, *Estimating parameters in linear mixed-effects models*, https://www.mathworks.com/help/stats/estimating-parameters-in-linear-mixed-effects-models.html, Accessed: 2025-07-02, 2024.

[68] S. Pfnür and C. Breitsamter, “Leading-edge vortex interactions at a generic multiple swept-wing aircraft configuration,” *AIAA Journal*, vol. 57, no. 9, pp. 3833–3845, 2019. DOI: 10.2514/1.C035491. [Online]. Available: https://doi.org/10.2514/1.C035491.

[69] V. Kumar, A. C. Mandal, and K. Poddar, “Effect of sideslip on the aerodynamic characteristics of a non-slender flying wing configuration,” in *AIAA Aviation 2020 Forum*, American Institute of Aeronautics and Astronautics, 2020. DOI: 10.2514/6.2020-3064. [Online]. Available: https://doi.org/10.2514/6.2020-3064.

[70] A. R. Garcia, M. Brown, D. Atherstone, N. v. Arnhem, and R. Vos, “Aerodynamic model identification of the flying v from sub-scale flight test data,” in *AIAA SCITECH 2022 Forum*, 2022. DOI: 10.2514/6.2022-0713. eprint: https://arc.aiaa.org/doi/pdf/10.2514/6.2022-0713. [Online]. Available: https://arc.aiaa.org/doi/abs/10.2514/6.2022-0713.

[71] J. L. Johnson Jr., S. B. Grafton, and L. P. Yip, “Exploratory investigation of the effects of vortex bursting on the high angle-of-attack lateral-directional stability characteristics of highly-swept wings,” NASA Langley Research Center, Hampton, VA, NASA Technical Memorandum NASA-TM-85778, 1983.

[72] G. Stenfelt and U. Ringertz, “Lateral stability and control of a tailless aircraft configuration,” *Journal of Aircraft*, vol. 46, no. 6, pp. 2216–2219, Nov. 2009. DOI: 10.2514/1.41092.

[73] N. Osterberg, “Investigation of self-deploying high-lift effectors applied to membrane wings,” *The Aeronautical Journal*, vol. 121, no. 1239, pp. 660–679, May 2017. DOI: 10.1017/aer.2017.10.

[74] G. Bramesfeld and M. D. Maughmer, “Experimental investigation of self-actuating, upper-surface, high-lift-enhancing effectors,” *Journal of Aircraft*, vol. 39, no. 1, pp. 120–124, Jan. 2002. DOI: 10.2514/2.2905.

[75] L. W. Traub and L. Jaybush, “Experimental investigation of separation control using upper-surface spoilers,” *Journal of Aircraft*, vol. 47, no. 2, pp. 714–717, Mar. 2010. DOI: 10.2514/1.45434.

A

Test Matrix

The test matrix used for the execution of the wind tunnel experiment is shown in this appendix. Table A.1 shows the high-level overview of the test matrix with respect to when in the test each configuration was tested and for what purpose. The levels of the design variables used to measure the force and moment responses were fed in to the model regression using the model design matrix shown in Table A.2.

A.1. Wind Tunnel Test Matrix

Run Type	**Run**	**Whole Plot**	**ST**	**Flap** (deg)	**IB SP** (deg)	**OB SP L** (deg)	**OB SP R** (deg)
Shake Down	999	-		60	60	60	60
Repeats	201	200	1202, 1203	0	0	0	0
Shake Down	998	0	1202, 1203	0	0	0	0
Flow Angularity	401	0	1401	0	0	0	0
Boundary Check	301	0	1301	0	0	0	0
Shake Down	999	101	1301	60	60	60	60
Validation Data	1	101	1101	60	60	60	60
RSM Data	2	22	1022	30	30	60	30
RSM Data	3	9	1009	42.5	17.5	17.5	17.5
RSM Data	4	3	1003	17.5	17.5	42.5	17.5
RSM Data	5	11	1011	42.5	17.5	42.5	17.5
RSM Data	6	15	1015	42.5	42.5	42.5	17.5
RSM Data	7	19	1019	30	0	30	30
RSM Data	8	23	1023	30	30	30	0
RSM Data	9	17	1017	0	30	30	30
RSM Data	10	18	1018	60	30	30	30
RSM Data	11	12	1012	42.5	17.5	42.5	42.5
RSM Data	12	10	1010	42.5	17.5	17.5	42.5
RSM Data	13	4	1004	17.5	17.5	42.5	42.5
Validation Data	14	102	1102	42.5	30	30	17.5
RSM Data	15	24	1024	30	30	30	60
RSM Data	16	21	1021	30	30	0	30
RSM Data	17	20	1020	30	60	30	30
RSM Data	18	25	1025	30	30	30	30

Run Type	Run	Whole Plot	ST	Flap (deg)	IB SP (deg)	OB SP L (deg)	OB SP R (deg)
RSM Data	19	5	1005	17.5	42.5	17.5	17.5
RSM Data	20	14	1014	42.5	42.5	17.5	42.5
RSM Data	21	13	1013	42.5	42.5	17.5	17.5
RSM Data	22	7	1007	17.5	42.5	42.5	17.5
RSM Data	23	16	1016	42.5	42.5	42.5	42.5
RSM Data	24	8	1008	17.5	42.5	42.5	42.5
RSM Data	25	6	1006	17.5	42.5	17.5	42.5
RSM Data	26	2	1002	17.5	17.5	17.5	42.5
RSM Data	27	1	1001	17.5	17.5	17.5	17.5
Sample Time Test	28	1	1001	17.5	17.5	17.5	17.5
Hysteresis Test	29	1	1001	17.5	17.5	17.5	17.5
RSM Data	30	98	1098	60	60	60	60
RSM Data	31	99	1099	0	0	0	0
Flow Angularity	402	0	1402	0	0	0	0
Flow Angularity	403	0	1402	0	0	0	0
R301 Repeat	302	0	1302	0	0	0	0
FA Check	303	0	1302	0	0	0	0
Hysteresis	304	0	1302	0	0	0	0
RSM Data	9b	17	1017b	0	30	30	30
RSM Data	9c	17	1017c	0	30	30	30
Validation Data	32	103	1103	0	30	30	30
Validation Data	33	104	1104	30	30	30	30
Validation Data	34	105	1105	30	0	0	0
Validation Data	35	106	1106	60	0	0	0

Table A.1: High-level configuration test matrix

A.2. Model Design Matrix

AoA	AoS	Flap	Sp1	Sp2l	Sp2r	WP
7.6	-7.5	30	30	60	30	22
-0.0	0	42.5	17.5	17.5	17.5	9
15.3	0	42.5	17.5	17.5	17.5	9
4.0	-10.5	42.5	17.5	17.5	17.5	9
-0.0	-15	42.5	17.5	17.5	17.5	9
11.2	-4.5	42.5	17.5	17.5	17.5	9
15.3	-15	42.5	17.5	17.5	17.5	9
4.0	-10.5	17.5	17.5	42.5	17.5	3
15.3	0	17.5	17.5	42.5	17.5	3
15.3	-15	17.5	17.5	42.5	17.5	3
-0.0406	0	17.5	17.5	42.5	17.5	3
-0.0406	-15	17.5	17.5	42.5	17.5	3
11.1937	-4.5	17.5	17.5	42.5	17.5	3

AoA	AoS	Flap	Sp1	Sp2l	Sp2r	WP
-0.0406	0	42.5	17.5	42.5	17.5	11
-0.0406	-14.995	42.5	17.5	42.5	17.5	11
15.2779	-14.995	42.5	17.5	42.5	17.5	11
11.1937	-10.505	42.5	17.5	42.5	17.5	11
15.2779	0	42.5	17.5	42.5	17.5	11
4.0426	-4.5	42.5	17.5	42.5	17.5	11
11.1937	-4.5	42.5	42.5	42.5	17.5	15
15.2799	-14.995	42.5	42.5	42.5	17.5	15
15.2789	0	42.5	42.5	42.5	17.5	15
-0.0406	-15	42.5	42.5	42.5	17.5	15
4.0446	-10.505	42.5	42.5	42.5	17.5	15
-0.0406	0	42.5	42.5	42.5	17.5	15
7.6232	-7.5	30	0	30	30	19
7.6232	-7.5	30	30	30	0	23
7.6232	-7.505	0	30	30	30	17.1
7.6232	-7.5	60	30	30	30	18
4.0446	-10.5	42.5	17.5	42.5	42.5	12
15.2799	-15	42.5	17.5	42.5	42.5	12
15.2799	0	42.5	17.5	42.5	42.5	12
-0.0406	0	42.5	17.5	42.5	42.5	12
-0.0406	-15	42.5	17.5	42.5	42.5	12
11.1937	-4.5	42.5	17.5	42.5	42.5	12
15.2779	-14.995	42.5	17.5	17.5	42.5	10
-0.0406	0	42.5	17.5	17.5	42.5	10
15.2789	0	42.5	17.5	17.5	42.5	10
11.1927	-10.5	42.5	17.5	17.5	42.5	10
4.0446	-4.5	42.5	17.5	17.5	42.5	10
-0.0406	-15	42.5	17.5	17.5	42.5	10
-0.0406	-15	17.5	17.5	42.5	42.5	4
4.0446	-4.5	17.5	17.5	42.5	42.5	4
15.2799	-15	17.5	17.5	42.5	42.5	4
15.2799	0	17.5	17.5	42.5	42.5	4
11.1917	-10.5	17.5	17.5	42.5	42.5	4
-0.0406	0	17.5	17.5	42.5	42.5	4
7.6181	-7.5	30	30	30	60	24
7.6171	-7.5	30	30	0	30	21
7.6232	-7.505	30	60	30	30	20
7.6192	-15	30	30	30	30	25
7.6192	-7.505	30	30	30	30	25
7.6232	-7.5	30	30	30	30	25
15.2789	-7.505	30	30	30	30	25
7.6232	0	30	30	30	30	25
7.6232	-7.505	30	30	30	30	25
7.6232	-7.505	30	30	30	30	25
-0.0406	-7.505	30	30	30	30	25

AoA	AoS	Flap	Sp1	Sp2l	Sp2r	WP
7.6192	-7.505	30	30	30	30	25
4.0446	-10.5	17.5	42.5	17.5	17.5	5
-0.041621	0	17.5	42.5	17.5	17.5	5
15.2748	-14.995	17.5	42.5	17.5	17.5	5
15.2789	0	17.5	42.5	17.5	17.5	5
11.1947	-4.5	17.5	42.5	17.5	17.5	5
-0.041621	-15	17.5	42.5	17.5	17.5	5
11.1937	-4.5	42.5	42.5	17.5	42.5	14
-0.0406	0	42.5	42.5	17.5	42.5	14
15.2789	-15	42.5	42.5	17.5	42.5	14
4.0446	-10.505	42.5	42.5	17.5	42.5	14
-0.0406	-15	42.5	42.5	17.5	42.5	14
15.2789	0	42.5	42.5	17.5	42.5	14
4.0456	-4.5	42.5	42.5	17.5	17.5	13
-0.039579	0	42.5	42.5	17.5	17.5	13
-0.039579	-14.995	42.5	42.5	17.5	17.5	13
15.2799	-15	42.5	42.5	17.5	17.5	13
11.1947	-10.505	42.5	42.5	17.5	17.5	13
15.2748	0	42.5	42.5	17.5	17.5	13
-0.039579	0	17.5	42.5	42.5	17.5	7
15.2799	-15	17.5	42.5	42.5	17.5	7
15.2779	0	17.5	42.5	42.5	17.5	7
-0.0406	-15	17.5	42.5	42.5	17.5	7
4.0436	-4.5	17.5	42.5	42.5	17.5	7
11.1957	-10.505	17.5	42.5	42.5	17.5	7
15.2799	-15	42.5	42.5	42.5	42.5	16
15.2799	0	42.5	42.5	42.5	42.5	16
-0.0406	0	42.5	42.5	42.5	42.5	16
4.0456	-4.505	42.5	42.5	42.5	42.5	16
-0.041621	-15	42.5	42.5	42.5	42.5	16
11.1917	-10.5	42.5	42.5	42.5	42.5	16
-0.0406	0	17.5	42.5	42.5	42.5	8
4.0456	-10.5	17.5	42.5	42.5	42.5	8
15.2769	-15	17.5	42.5	42.5	42.5	8
15.2769	0	17.5	42.5	42.5	42.5	8
-0.039579	-15	17.5	42.5	42.5	42.5	8
11.1906	-4.505	17.5	42.5	42.5	42.5	8
4.0426	-4.505	17.5	42.5	17.5	42.5	6
15.2789	0	17.5	42.5	17.5	42.5	6
15.2789	-15	17.5	42.5	17.5	42.5	6
11.1937	-10.495	17.5	42.5	17.5	42.5	6
-0.0406	-15	17.5	42.5	17.5	42.5	6
-0.0406	0	17.5	42.5	17.5	42.5	6
-0.039579	-14.995	17.5	17.5	17.5	42.5	2
-0.039579	0	17.5	17.5	17.5	42.5	2

AoA	AoS	Flap	Sp1	Sp2l	Sp2r	WP
15.2789	-14.995	17.5	17.5	17.5	42.5	2
11.1937	-4.505	17.5	17.5	17.5	42.5	2
4.0456	-10.5	17.5	17.5	17.5	42.5	2
15.2748	0	17.5	17.5	17.5	42.5	2
11.1957	-10.5	17.5	17.5	17.5	17.5	1
4.0436	-4.5	17.5	17.5	17.5	17.5	1
15.2769	0	17.5	17.5	17.5	17.5	1
-0.039579	0	17.5	17.5	17.5	17.5	1
-0.039579	-14.995	17.5	17.5	17.5	17.5	1
15.2779	-14.995	17.5	17.5	17.5	17.5	1
7.6192	-7.505	0	30	30	30	17.2
7.6192	-7.505	0	30	30	30	17.3
4.0426	-4.505	60	60	60	60	98
11.1957	-10.5	60	60	60	60	98
-0.039579	0	60	60	60	60	98
15.2779	0	60	60	60	60	98
-0.039579	-15	60	60	60	60	98
15.2789	-15	60	60	60	60	98
4.0456	-10.5	60	60	60	60	98
11.1927	-4.495	60	60	60	60	98
7.6232	-7.495	60	60	60	60	98
-0.0406	-7.495	60	60	60	60	98
15.2789	-7.495	60	60	60	60	98
7.6232	0	60	60	60	60	98
7.6232	-15	60	60	60	60	98

Table A.2: Model design matrix

B

Regression Model Terms

This appendix displays the force and moments model structures of the Flying V as functions of flap and spoiler deflections and orientation angles. Due to confidentiality constraints, the coefficient estimates found for each term are not presented in this report. Section B.1 shows the model structures for the wind axis force and moment models which provide the effects of the flaps and spoilers. Section B.2 and section B.3 provide the full model structures which provide the full coefficients of the Flying V in the wind and body axes, respectively.

B.1. Wind Axis Flap and Spoiler Effects Model Structures

This section displays the wind axis force and moments effects models of the Flying V as functions of flap and spoiler deflections and orientation angles. These models were fitted to the difference between the clean model data and the data gathered with different configurations. Due to confidentiality constraints, the coefficient estimates found for each term are not presented in this report. In practice, each term presented in the model structure is multiplied by some coefficient and sign to scale that term. As there is no change in a force or moment in the null condition–all variables set to zero–there is no intercept for these effects models.

$$\begin{aligned}\Delta C_{L,1} = {} & \alpha + \delta_f + \alpha \cdot \delta_{sp,1} \\ & + \delta_{sp,1} \cdot \delta_{sp,2\ell} + \delta_{sp,2\ell} \cdot \delta_{sp,2r} + \alpha^2 \\ & + \alpha \cdot \beta \cdot \delta_{sp,1} + \alpha \cdot \delta_{sp,1} \cdot \delta_{sp,2\ell} + (\alpha^2) \cdot \delta_{sp,1} \\ & + \alpha^3\end{aligned}$$

$$\begin{aligned}\Delta C_{L,2} = {} & \delta_f + \delta_{sp,1} + (\alpha^2) \cdot \delta_f \\ & + (\beta^2) \cdot \delta_f + \delta^3_{sp,2r}\end{aligned}$$

$$\begin{aligned}\Delta C_{D,1} = {} & \delta_{sp,2\ell} \cdot \delta_{sp,2r} + \delta_f^2 + \delta_{sp,1}^2 \\ & + \alpha \cdot \delta_f \cdot \delta_{sp,1} + \alpha \cdot \delta_{sp,2\ell} \cdot \delta_{sp,2r} + (\alpha^2) \cdot \delta_{sp,1} \\ & + \beta^3 + \delta_f^3\end{aligned}$$

$$\begin{aligned}\Delta C_{D,2} = {} & \delta_{sp,2\ell} + \delta_{sp,2r} + \delta_f^2 \\ & + \alpha \cdot \beta \cdot \delta_{sp,1} + (\alpha^2) \cdot \beta + (\beta^2) \cdot \delta_{sp,1} \\ & + \alpha^3\end{aligned}$$

$$\begin{aligned}\Delta C_{Y,1} = {} & \delta_{sp,2r} + \alpha \cdot \delta_{sp,2\ell} + \delta_f \cdot \delta_{sp,2\ell} \\ & + \alpha \cdot \beta \cdot \delta_f + \alpha \cdot (\beta^2) + (\alpha^2) \cdot \delta_{sp,1} \\ & + (\alpha^2) \cdot \delta_{sp,2r}\end{aligned}$$

$$\begin{aligned}\Delta C_{Y,2} = {} & \alpha \cdot \beta + \alpha \cdot \delta_{sp,1} + \delta_{sp,2\ell}^2 \\ & + \alpha \cdot \beta \cdot \delta_f + \alpha \cdot \delta_f \cdot \delta_{sp,2r} + \beta \cdot (\delta_f^2) \\ & + \beta^3\end{aligned}$$

$$\Delta C_{l,\text{wind},1} = \beta \cdot \delta_f + \alpha \cdot \beta \cdot \delta_{sp,2\ell} + (\alpha^2) \cdot \delta_{sp,2\ell}$$

$$\begin{aligned}\Delta C_{l,\text{wind},2} = {} & \delta_f + \alpha \cdot \delta_f + \beta \cdot \delta_f \cdot \delta_{sp,1} \\ & + (\alpha^2) \cdot \delta_f + (\delta_f^2) \cdot \delta_{sp,2r} + \alpha^3\end{aligned}$$

$$\begin{aligned}\Delta C_{m,\text{wind},1} = {} & \beta + \alpha \cdot \delta_{sp,2\ell} + \delta_{sp,1}^2 \\ & + \delta_{sp,2\ell}^2 + \delta_{sp,2r}^2 + \alpha \cdot \beta \cdot \delta_{sp,2\ell} \\ & + (\alpha^2) \cdot \beta + (\alpha^2) \cdot \delta_{sp,2\ell} + \alpha \cdot (\delta_{sp,2\ell}^2)\end{aligned}$$

$$\begin{aligned}\Delta C_{m,\text{wind},2} = {} & \beta \cdot \delta_f + \delta_f \cdot \delta_{sp,1} + (\alpha^2) \cdot \delta_f \\ & + (\beta^2) \cdot \delta_f + \alpha \cdot (\delta_{sp,1}^2)\end{aligned}$$

$$\begin{aligned}\Delta C_{n,\text{wind},1} = {} & \alpha \cdot \beta + \delta_f \cdot \delta_{sp,2\ell} + \alpha \cdot \delta_{sp,2r} \\ & + \beta \cdot \delta_{sp,2r} + \delta_{sp,2\ell} \cdot \delta_{sp,2r} + \alpha \cdot \beta \cdot \delta_f \\ & + (\alpha^2) \cdot \beta + (\alpha^2) \cdot \delta_{sp,1} + (\alpha^2) \cdot \delta_{sp,2\ell} \\ & + (\beta^2) \cdot \delta_{sp,2\ell}\end{aligned}$$

$$\begin{aligned}\Delta C_{n,\text{wind},2} = {} & \delta_{sp,1} + \alpha \cdot \beta + \beta \cdot \delta_f \\ & + \alpha \cdot \delta_{sp,1} + \beta \cdot \delta_{sp,1} + \beta^2 \\ & + \delta_{sp,2\ell}^2 + \alpha \cdot \delta_f \cdot \delta_{sp,1} + \beta \cdot \delta_f \cdot \delta_{sp,2\ell} \\ & + \beta \cdot \delta_{sp,1} \cdot \delta_{sp,2r} + (\alpha^2) \cdot \beta + \alpha \cdot (\beta^2) \\ & + (\beta^2) \cdot \delta_f + (\alpha^2) \cdot \delta_{sp,1} + (\beta^2) \cdot \delta_{sp,1} \\ & + \alpha \cdot (\delta_{sp,2\ell}^2) + \delta_{sp,1} \cdot (\delta_{sp,2r}^2) + \beta^3 \\ & + \delta_f^3\end{aligned}$$

B.2. Wind Axis Full Force and Moment Model Structures

This section displays the full wind axis force and moments models of the Flying V as functions of flap and spoiler deflections and orientation angles. Due to confidentiality constraints, the coefficient estimates found for each term are not presented in this report. In practice, each term presented in the model structure is multiplied by some coefficient and sign to scale that term.

$$\begin{aligned}C_{L,1} = {} & 1 + \alpha + \delta_f \\ & + \delta_{sp,2\ell} \cdot \delta_{sp,2r} + \alpha^2 + \alpha \cdot \beta \cdot \delta_f \\ & + \alpha \cdot \delta_{sp,2\ell} \cdot \delta_{sp,2r} + \delta_{sp,1} \cdot \delta_{sp,2\ell} \cdot \delta_{sp,2r} + \alpha \cdot (\beta^2) \\ & + (\alpha^2) \cdot \delta_f + \alpha \cdot (\delta_f^2) + \alpha^3\end{aligned}$$

$$\begin{aligned}C_{L,2} = {} & 1 + \alpha + \delta_f \\ & + \alpha^2 + \alpha \cdot (\beta^2) + \alpha \cdot (\delta_f^2) \\ & + (\alpha^2) \cdot \delta_{sp,1} + \alpha^3\end{aligned}$$

$$\begin{aligned}C_{D,1} = {} & 1 + \alpha + \delta_{sp,1} \\ & + \alpha \cdot \delta_f + \beta^2 + \delta_f^2 \\ & + \alpha \cdot \beta \cdot \delta_f + \alpha \cdot \delta_{sp,2\ell} \cdot \delta_{sp,2r} + \beta \cdot \delta_{sp,2\ell} \cdot \delta_{sp,2r} \\ & + \alpha \cdot (\beta^2) + (\beta^2) \cdot \delta_f + \beta \cdot (\delta_f^2) \\ & + (\alpha^2) \cdot \delta_{sp,1} + \alpha^3 + \delta_{sp,1}^3\end{aligned}$$

$$\begin{aligned}C_{D,2} = {} & 1 + \delta_f + \alpha \cdot \beta \\ & + \alpha \cdot \beta \cdot \delta_f + (\alpha^2) \cdot \beta + \alpha \cdot (\beta^2) \\ & + (\beta^2) \cdot \delta_f + (\alpha^2) \cdot \delta_{sp,1} + \alpha^3 \\ & + \beta^3\end{aligned}$$

$$\begin{aligned}C_{Y,1} = {} & 1 + \alpha + \beta \\ & + \delta_{sp,1} \cdot \delta_{sp,2r} + \beta^2 + \alpha \cdot \beta \cdot \delta_f \\ & + \alpha \cdot \beta \cdot \delta_{sp,1} + \beta \cdot \delta_f \cdot \delta_{sp,2\ell} + (\alpha^2) \cdot \beta \\ & + \alpha \cdot (\beta^2) + (\beta^2) \cdot \delta_f + \beta \cdot (\delta_{sp,1}^2) \\ & + (\alpha^2) \cdot \delta_{sp,2\ell} + (\alpha^2) \cdot \delta_{sp,2r} + \beta^3 \\ & + \delta_f^3\end{aligned}$$

$$\begin{aligned}C_{Y,2} = {} & 1 + \beta + \delta_{sp,1} \\ & + \delta_{sp,2\ell} + \alpha \cdot \beta + \beta^2 \\ & + \alpha \cdot \beta \cdot \delta_f + \beta \cdot \delta_f \cdot \delta_{sp,2\ell} + \alpha \cdot \delta_{sp,1} \cdot \delta_{sp,2r} \\ & + (\alpha^2) \cdot \beta + \alpha \cdot (\beta^2) + \alpha^3 \\ & + \beta^3\end{aligned}$$

$$C_{l,\text{wind},1} = 1 + \alpha\cdot\beta + \alpha\cdot\delta_{sp,2\ell} + \beta^2 + \delta_{sp,2\ell}^2 + \alpha\cdot\beta\cdot\delta_{sp,2\ell} + (\beta^2)\cdot\delta_f + \alpha^3$$

$$C_{l,\text{wind},2} = 1 + \beta + \beta\cdot\delta_f + \beta^2 + \alpha\cdot\beta\cdot\delta_f + (\alpha^2)\cdot\beta + \alpha\cdot(\beta^2) + (\beta^2)\cdot\delta_{sp,1} + \beta\cdot(\delta_{sp,1}^2) + \beta^3$$

$$C_{m,\text{wind},1} = 1 + \alpha + \delta_{sp,1} + \alpha\cdot\beta + \alpha^2 + \beta^2 + \delta_{sp,2\ell}^2 + (\alpha^2)\cdot\beta + \alpha\cdot(\beta^2) + \alpha\cdot(\delta_{sp,2\ell}^2) + \beta\cdot(\delta_{sp,2\ell}^2) + \alpha^3 + \beta^3$$

$$C_{m,\text{wind},2} = 1 + \alpha + \beta + \delta_f + \alpha^2 + \beta^2 + \alpha\cdot\beta\cdot\delta_f + (\alpha^2)\cdot\delta_f + \alpha^3 + \beta^3$$

$$C_{n,\text{wind},1} = 1 + \alpha\cdot\beta + \delta_f\cdot\delta_{sp,2\ell} + \alpha^2 + \beta^2 + \alpha\cdot\beta\cdot\delta_f + \alpha\cdot\beta\cdot\delta_{sp,1} + \beta\cdot\delta_f\cdot\delta_{sp,1} + \alpha\cdot\beta\cdot\delta_{sp,2\ell} + \alpha\cdot\beta\cdot\delta_{sp,2r} + (\alpha^2)\cdot\beta + \alpha\cdot(\beta^2) + (\alpha^2)\cdot\delta_{sp,2\ell} + (\alpha^2)\cdot\delta_{sp,2r} + (\delta_{sp,2\ell}^2)\cdot\delta_{sp,2r} + \alpha^3 + \beta^3$$

$$C_{n,\text{wind},2} = 1 + \beta + \delta_{sp,2\ell} + \beta\cdot\delta_f + \beta^2 + \delta_{sp,2r}^2 + \alpha\cdot\delta_f\cdot\delta_{sp,1} + \alpha\cdot\beta\cdot\delta_{sp,2\ell} + \alpha\cdot(\beta^2) + (\beta^2)\cdot\delta_f + (\alpha^2)\cdot\delta_{sp,2\ell} + \alpha^3 + \beta^3 + \delta_f^3$$

B.3. Body Axis Full Force and Moment Model Structures

This section displays the full body axis force and moments models of the Flying V as functions of flap and spoiler deflections and orientation angles. Due to confidentiality constraints, the coefficient estimates found for each term are not presented in this report. In practice, each term presented in the model structure is multiplied by some coefficient and sign to scale that term.

$$C_{N,1} = 1 + \alpha + \delta_f + \alpha\cdot\beta + \alpha\cdot\delta_{sp,2\ell} + \alpha^2 + \delta_f^2 + \delta_{sp,2\ell}^2 + \alpha\cdot\beta\cdot\delta_f + \alpha\cdot\delta_{sp,2\ell}\cdot\delta_{sp,2r} + \delta_{sp,1}\cdot\delta_{sp,2\ell}\cdot\delta_{sp,2r} + (\alpha^2)\cdot\beta + \alpha\cdot(\beta^2) + \alpha\cdot(\delta_f^2) + \alpha^3 + \delta_f^3$$

$$C_{N,2} = 1 + \beta + \delta_f + \alpha\cdot\beta + \alpha^2 + \beta\cdot\delta_f\cdot\delta_{sp,1} + (\alpha^2)\cdot\beta + \alpha\cdot(\beta^2) + \alpha\cdot(\delta_f^2) + (\alpha^2)\cdot\delta_{sp,1} + \alpha^3 + \beta^3$$

$$C_{T,1} = 1 + \alpha + \beta + \alpha\cdot\delta_f + \beta\cdot\delta_{sp,2r} + \alpha^2 + \beta^2 + \delta_f^2 + \beta\cdot(\delta_f^2) + (\alpha^2)\cdot\delta_{sp,2\ell} + \alpha\cdot(\delta_{sp,2\ell}^2) + (\alpha^2)\cdot\delta_{sp,2r} + \alpha^3 + \beta^3 + \delta_{sp,1}^3$$

$$C_{T,2} = 1 + \alpha + \alpha^2 + \beta^2 + \delta_{sp,2\ell}^2 + \alpha\cdot\beta\cdot\delta_f + \alpha\cdot\beta\cdot\delta_{sp,1} + \alpha\cdot\delta_{sp,1}\cdot\delta_{sp,2\ell} + (\beta^2)\cdot\delta_{sp,2\ell} + \alpha^3 + \beta^3$$

$$
\begin{aligned}
C_{S,1} = 1 &+ \alpha + \beta \\
&+ \beta^2 + \alpha \cdot \beta \cdot \delta_f + \alpha \cdot \beta \cdot \delta_{sp,1} \\
&+ \beta \cdot \delta_f \cdot \delta_{sp,1} + \beta \cdot \delta_f \cdot \delta_{sp,2\ell} + \alpha \cdot \beta \cdot \delta_{sp,2r} \\
&+ \delta_f \cdot \delta_{sp,1} \cdot \delta_{sp,2r} + \alpha \cdot (\beta^2) + (\beta^2) \cdot \delta_f \\
&+ (\alpha^2) \cdot \delta_{sp,2\ell} + (\delta_f^2) \cdot \delta_{sp,2\ell} + (\alpha^2) \cdot \delta_{sp,2r} \\
&+ \beta^3 + \delta_f^3
\end{aligned}
$$

$$
\begin{aligned}
C_{S,2} = 1 &+ \beta + \delta_{sp,1} \\
&+ \delta_{sp,2\ell} + \beta \cdot \delta_f + \beta \cdot (\delta_f^2) \\
&+ \delta_{sp,1} \cdot (\delta_{sp,2r}^2) + \beta^3
\end{aligned}
$$

$$
\begin{aligned}
C_{l,\text{body},1} = 1 &+ \alpha \cdot \beta + \alpha \cdot \delta_{sp,2\ell} \\
&+ \delta_{sp,2\ell} \cdot \delta_{sp,2r} + \beta^2 + \alpha \cdot \beta \cdot \delta_f \\
&+ \alpha \cdot \beta \cdot \delta_{sp,1} + \beta \cdot \delta_f \cdot \delta_{sp,2\ell} + \alpha \cdot \delta_{sp,2\ell} \cdot \delta_{sp,2r} \\
&+ (\alpha^2) \cdot \beta + (\beta^2) \cdot \delta_f + (\beta^2) \cdot \delta_{sp,1} \\
&+ \beta^3
\end{aligned}
$$

$$
\begin{aligned}
C_{l,\text{body},2} = 1 &+ \delta_f + \alpha \cdot \beta \\
&+ \alpha^2 + \beta \cdot \delta_f \cdot \delta_{sp,1} + (\alpha^2) \cdot \delta_f \\
&+ \alpha^3 + \beta^3
\end{aligned}
$$

$$
\begin{aligned}
C_{m,\text{body},1} = 1 &+ \alpha + \delta_{sp,1} \\
&+ \alpha^2 + \delta_{sp,2\ell}^2 + (\alpha^2) \cdot \beta \\
&+ \alpha \cdot (\beta^2) + \alpha \cdot (\delta_{sp,2\ell}^2) + \beta \cdot (\delta_{sp,2\ell}^2) \\
&+ \alpha^3
\end{aligned}
$$

$$
\begin{aligned}
C_{m,\text{body},2} = 1 &+ \alpha + \alpha \cdot \beta \\
&+ \alpha^2 + \beta \cdot \delta_f \cdot \delta_{sp,1} + \alpha^3
\end{aligned}
$$

$$
\begin{aligned}
C_{n,\text{body},1} = 1 &+ \beta + \alpha \cdot \beta \\
&+ \alpha \cdot \delta_f + \beta \cdot \delta_f + \delta_f \cdot \delta_{sp,2\ell} \\
&+ \alpha \cdot \delta_{sp,2r} + \delta_{sp,2\ell} \cdot \delta_{sp,2r} + \beta^2 \\
&+ \alpha \cdot \beta \cdot \delta_f + \alpha \cdot \beta \cdot \delta_{sp,1} + \alpha \cdot \delta_f \cdot \delta_{sp,2\ell} \\
&+ \beta \cdot \delta_f \cdot \delta_{sp,2\ell} + \alpha \cdot \beta \cdot \delta_{sp,2r} + (\alpha^2) \cdot \beta \\
&+ \alpha \cdot (\beta^2) + \beta \cdot (\delta_f^2) + \beta^3
\end{aligned}
$$

$$
\begin{aligned}
C_{n,\text{body},2} = 1 &+ \beta + \delta_{sp,2\ell} \\
&+ \beta \cdot \delta_f + \delta_f \cdot \delta_{sp,2\ell} + \beta^2 \\
&+ \delta_{sp,2r}^2 + \alpha \cdot \beta \cdot \delta_f + \alpha \cdot \beta \cdot \delta_{sp,2\ell} \\
&+ (\alpha^2) \cdot \beta + \alpha \cdot (\beta^2) + (\beta^2) \cdot \delta_f \\
&+ \beta \cdot (\delta_f^2) + (\alpha^2) \cdot \delta_{sp,1} + \beta \cdot (\delta_{sp,2r}^2) \\
&+ \beta^3
\end{aligned}
$$

C

Model Validation Plots

The plots shown in this Appendix are the plots of the effects models predictions versus the measured validation data. These plots illustrate the models' capability at predicting new data and interpolating between the fitted regression points. Included at the top of each figure is the flap and spoiler configuration used to gather the validation data in the figure and a visual cue for which surfaces were deflected. For more information on the visual cue provided, see Figure 3.3.

Due to confidentiality constraints, the tick marks have been removed from all plots and substitute reference lengths are provided. The model predictions are plotted with $\pm 2\sigma$ confidence intervals, indicating a 95% confidence range, and the validation data is plotted with $\pm 2\sqrt{2}\sigma_{exp}$ error bars to account for the error propagated when taking the difference:

$$\Delta C_L = C_L(\delta_f, \delta_{sp}) - C_{L,\text{ clean}}$$

The resulting uncertainty for the validation deltas data is found using:

$$\sigma_{\text{propagated}} = \sqrt{{\sigma_a}^2 + {\sigma_b}^2} = \sqrt{{\sigma_{exp}}^2 + {\sigma_{exp}}^2} = \sqrt{2}\sigma_{exp}$$

As described in section 3.1, Range 1 corresponds to the sub plot variable range of angles of attack and sideslip $\alpha = [0°, 15°], \beta = [-15°, 0°]$, and Range 2 corresponds to angles of attack and sideslip $\alpha = [15°, 25°], \beta = [-15°, 0°]$.

Note that the flap alone configurations 5 and 6 are not true validation configurations but are extrapolation cases. They are included in this appendix, however, because it is useful to see how well the fitted regression models can extrapolate to and predict the flap alone configurations.

C.1. Validation Plots for ΔC_L

Range 1 Model

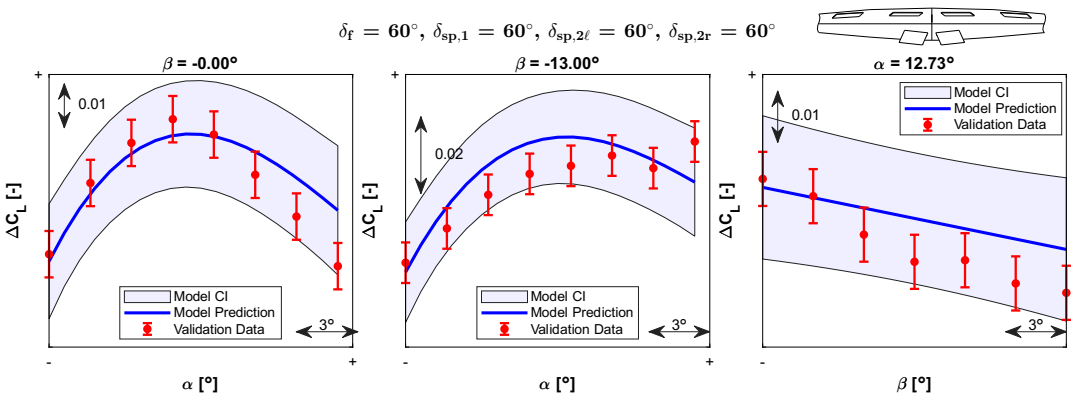

Figure C.1: Range 1 ΔC_L effects model validation plot: validation config 1

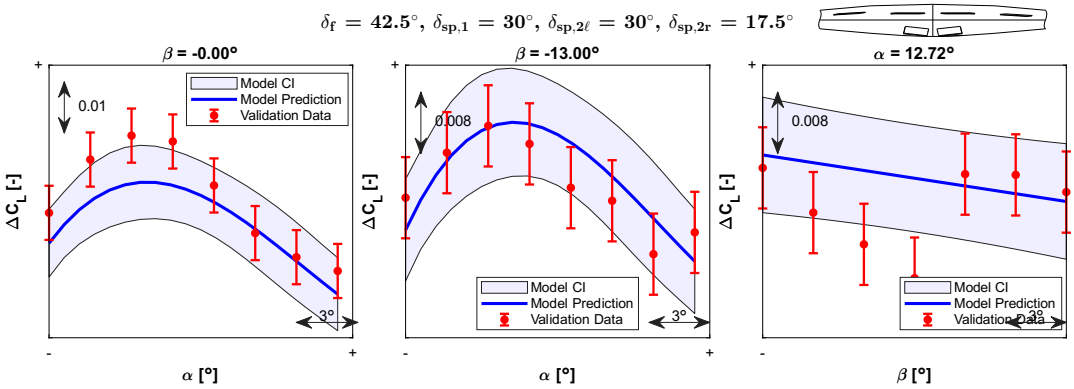

Figure C.2: Range 1 ΔC_L effects model validation plot: validation config 2

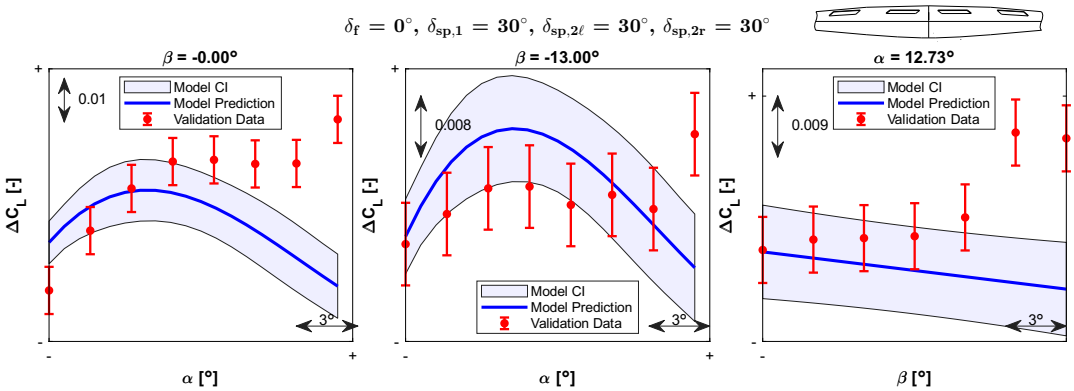

Figure C.3: Range 1 ΔC_L effects model validation plot: validation config 3

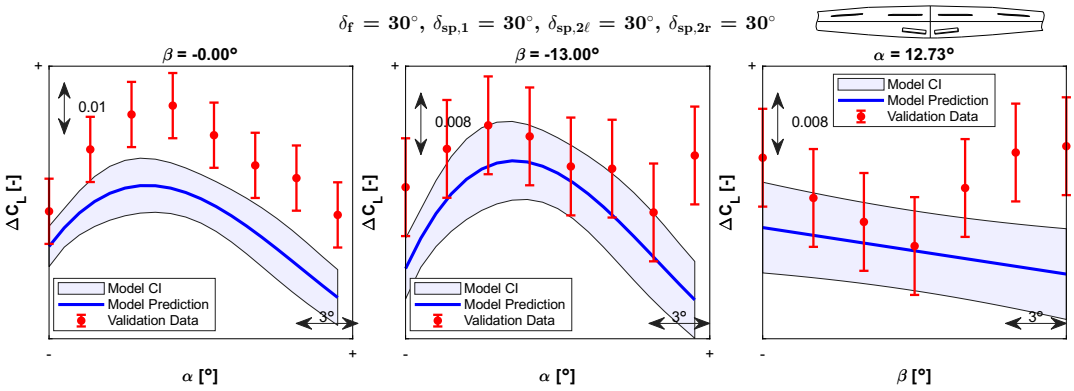

Figure C.4: Range 1 ΔC_L effects model validation plot: validation config 4

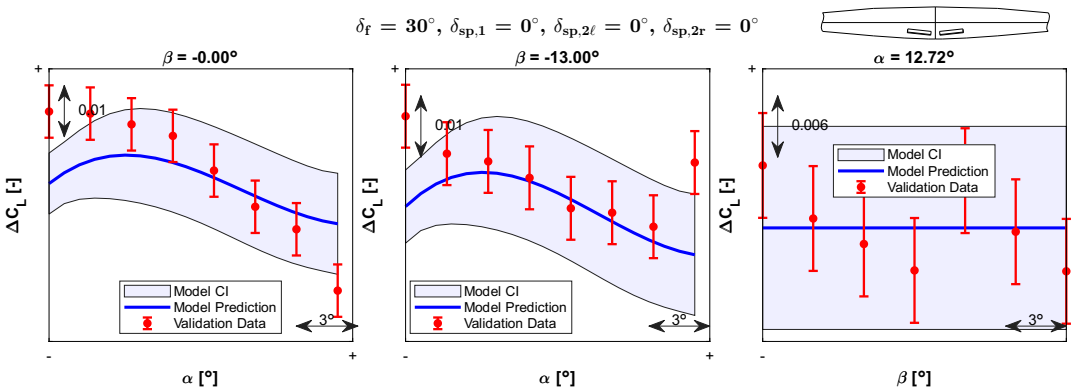

Figure C.5: Range 1 ΔC_L effects model validation plot: validation config 5

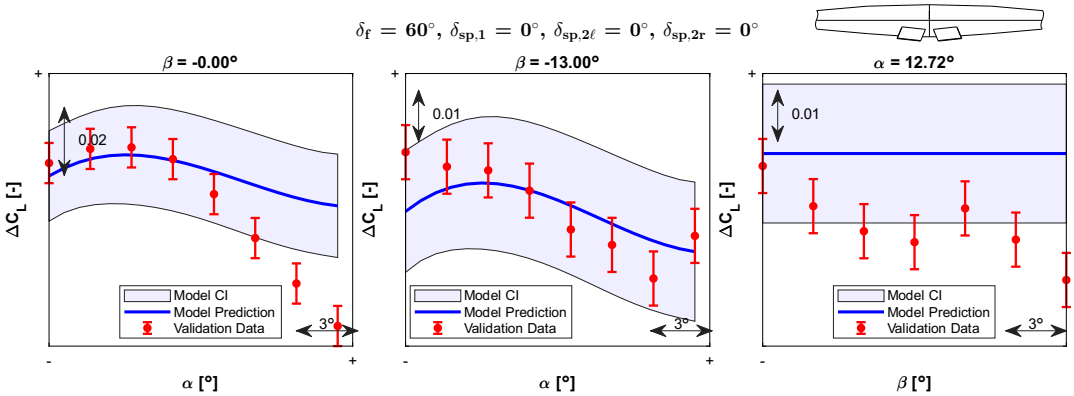

Figure C.6: Range 1 ΔC_L effects model validation plot: validation config 6

Range 2 Model

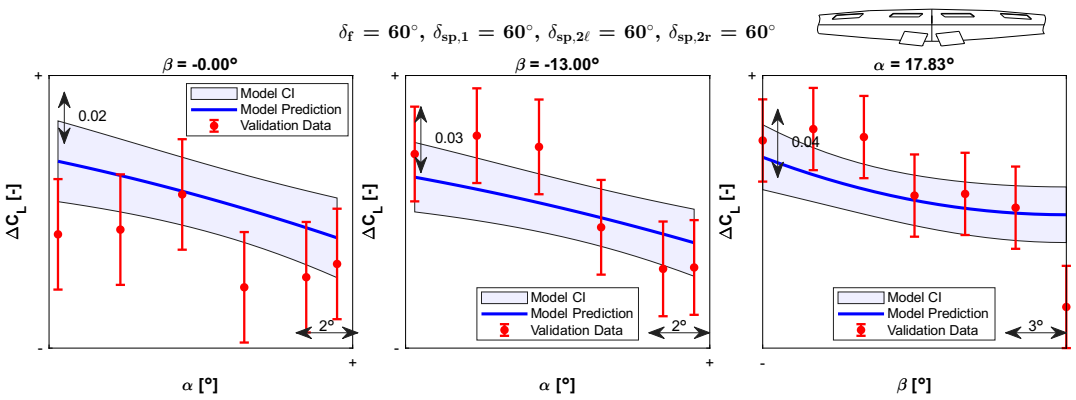

Figure C.7: Range 2 ΔC_L effects model validation plot: validation config 1

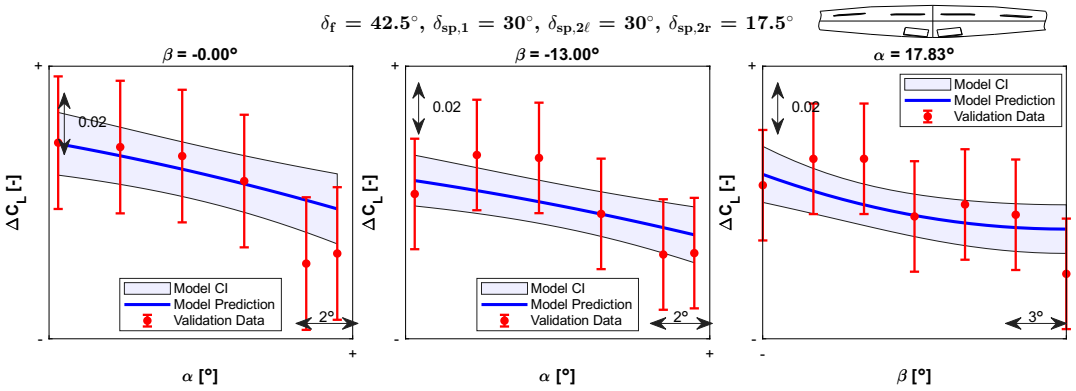

Figure C.8: Range 2 ΔC_L effects model validation plot: validation config 2

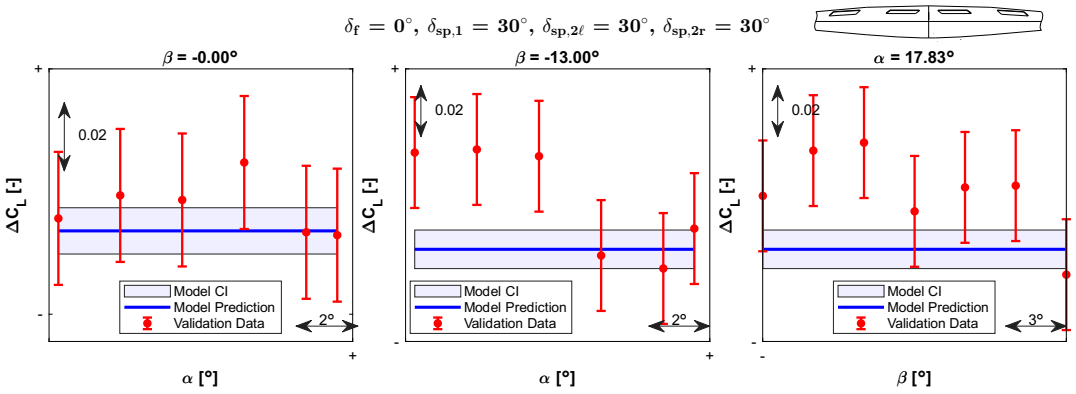

Figure C.9: Range 2 ΔC_L effects model validation plot: validation config 3

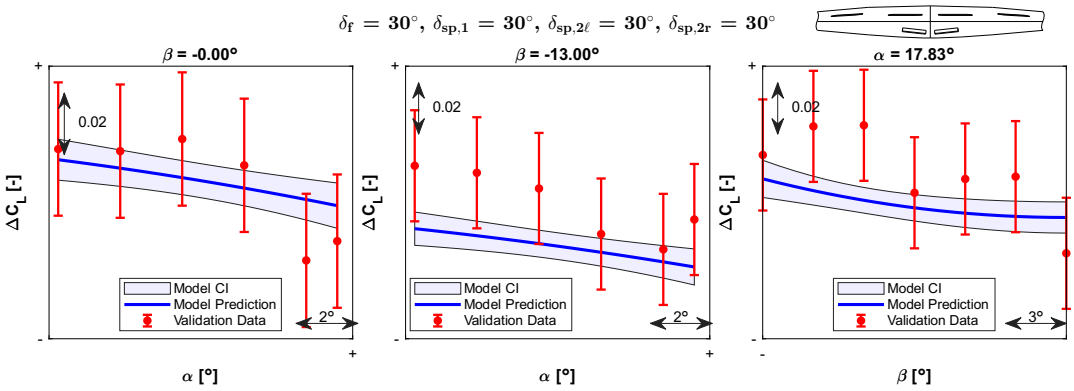

Figure C.10: Range 2 ΔC_L effects model validation plot: validation config 4

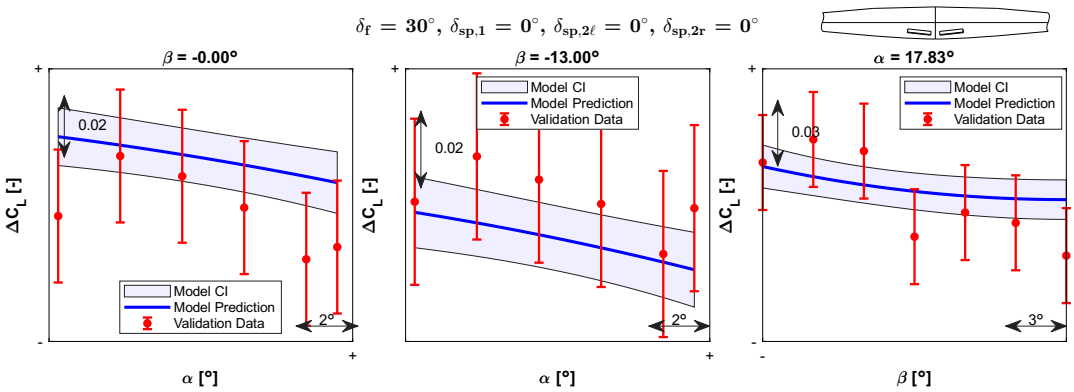

Figure C.11: Range 2 ΔC_L effects model validation plot: validation config 5

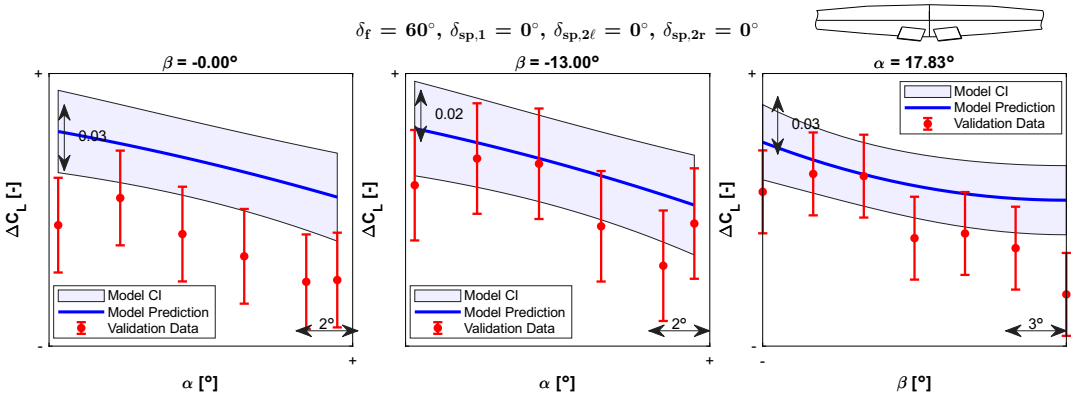

Figure C.12: Range 2 ΔC_L effects model validation plot: validation config 6

C.2. Validation Plots for ΔC_D

Range 1 Model

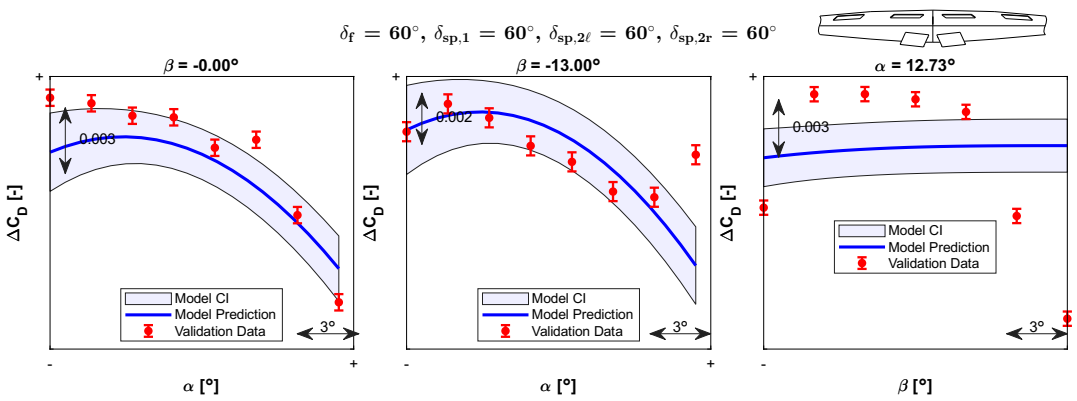

Figure C.13: Range 1 ΔC_D effects model validation plot: validation config 1

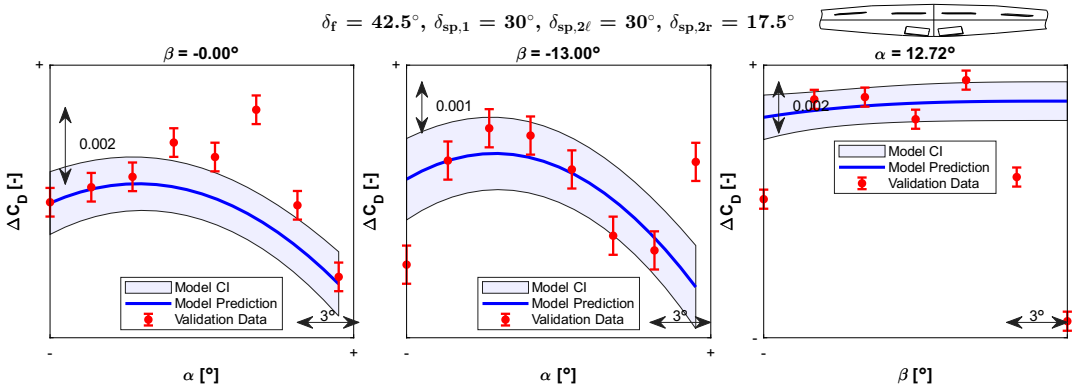

Figure C.14: Range 1 ΔC_D effects model validation plot: validation config 2

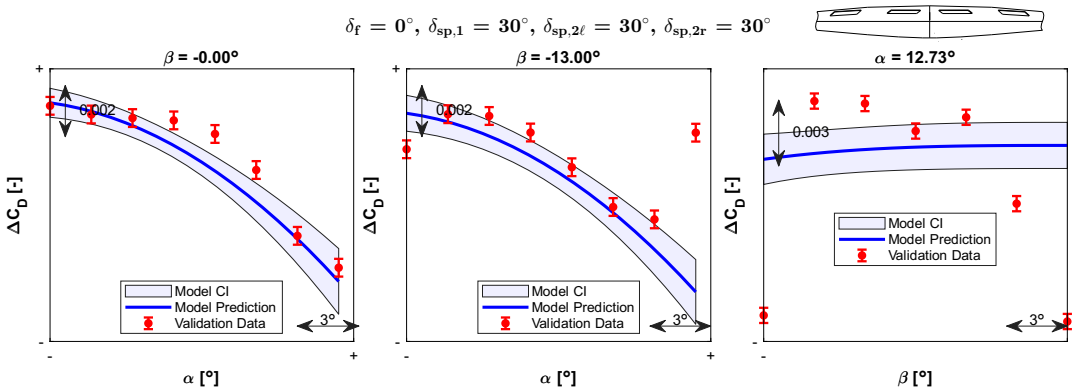

Figure C.15: Range 1 ΔC_D effects model validation plot: validation config 3

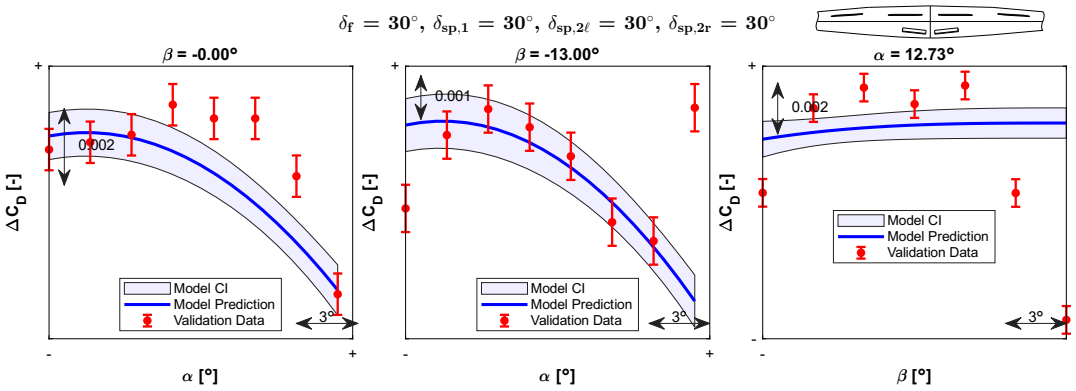

Figure C.16: Range 1 ΔC_D effects model validation plot: validation config 4

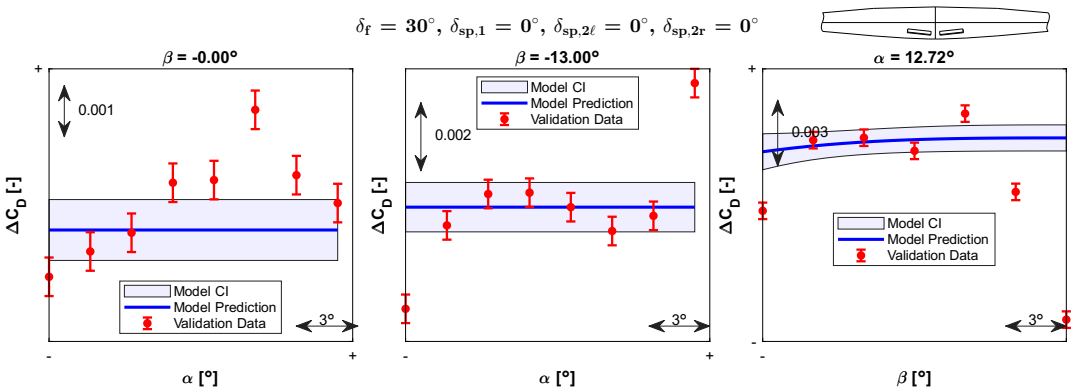

Figure C.17: Range 1 ΔC_D effects model validation plot: validation config 5

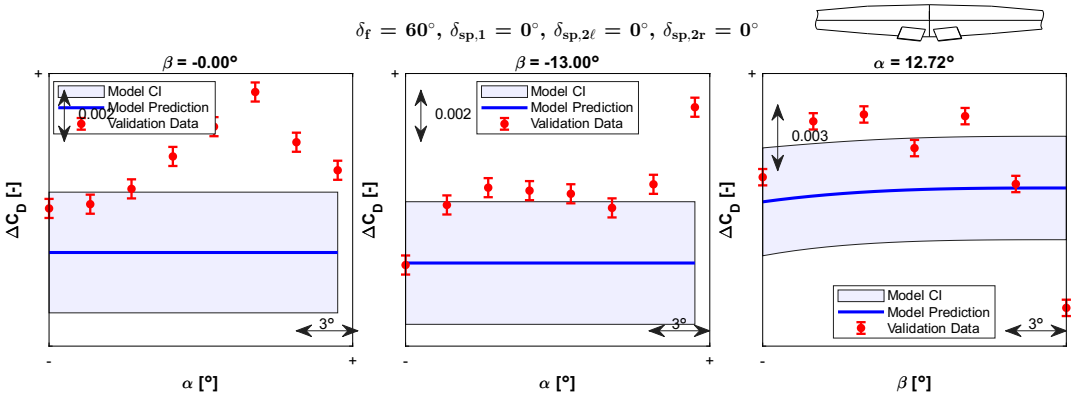

Figure C.18: Range 1 ΔC_D effects model validation plot: validation config 6

Range 2 Model

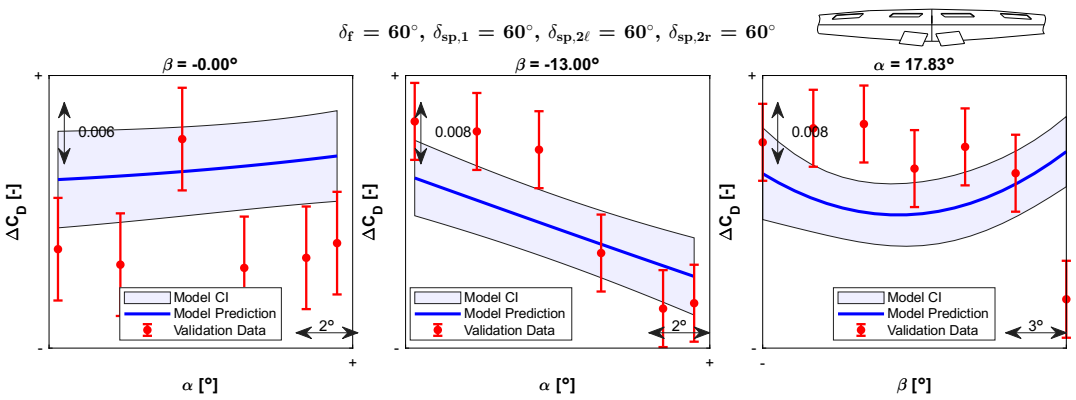

Figure C.19: Range 2 ΔC_D effects model validation plot: validation config 1

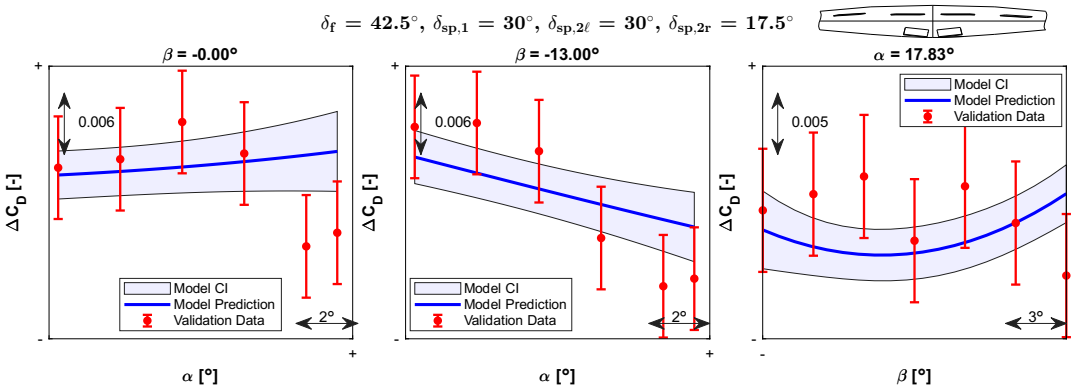

Figure C.20: Range 2 ΔC_D effects model validation plot: validation config 2

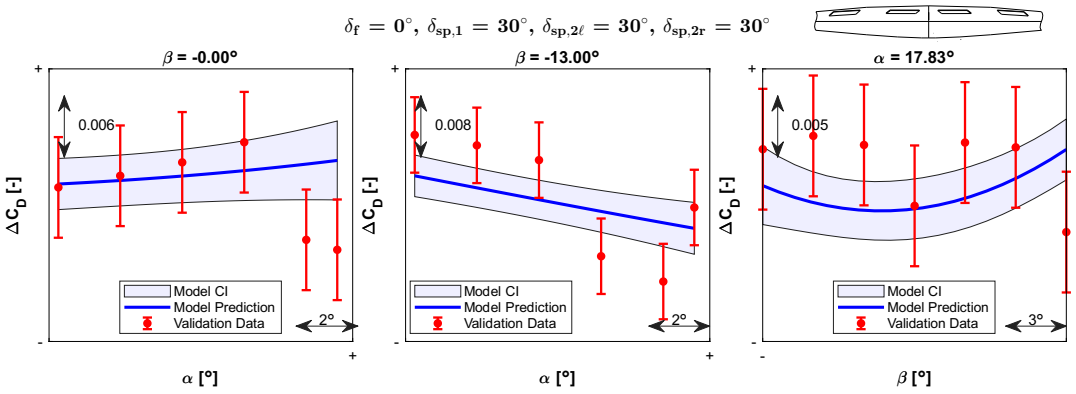

Figure C.21: Range 2 ΔC_D effects model validation plot: validation config 3

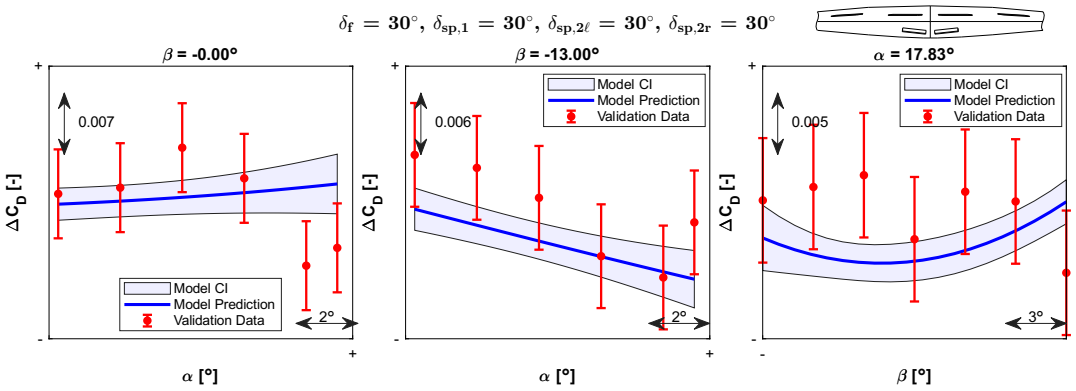

Figure C.22: Range 2 ΔC_D effects model validation plot: validation config 4

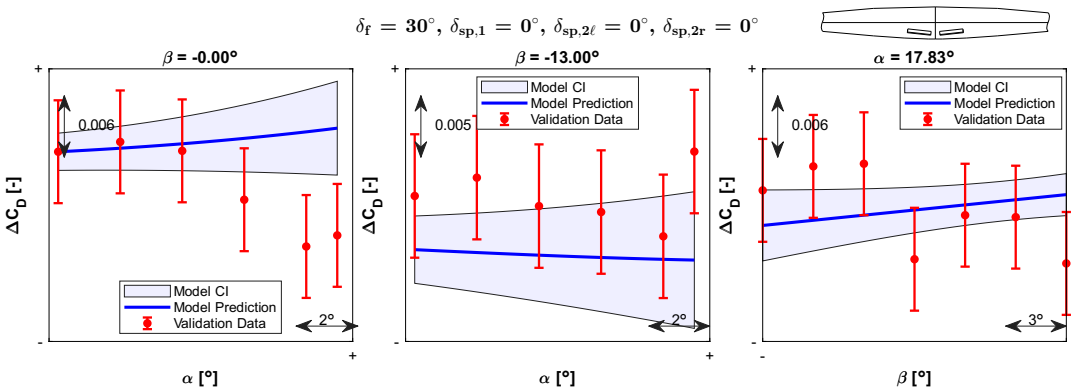

Figure C.23: Range 2 ΔC_D effects model validation plot: validation config 5

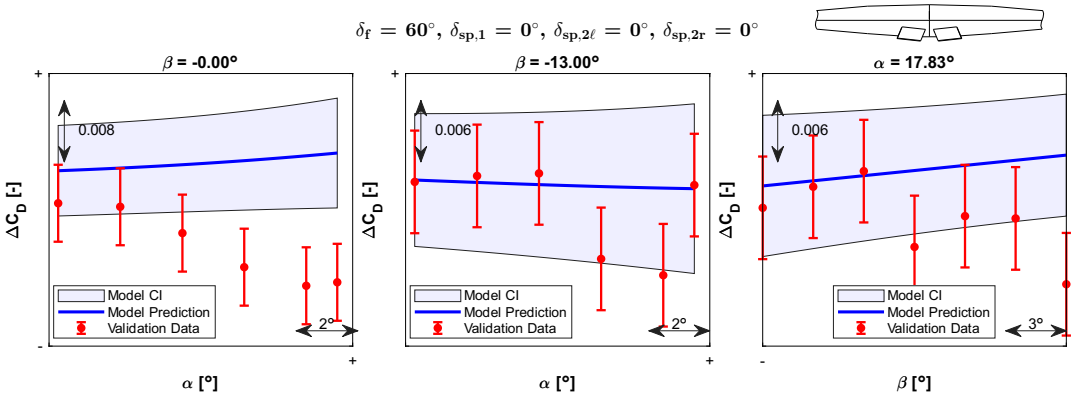

Figure C.24: Range 2 ΔC_D effects model validation plot: validation config 6

C.3. Validation Plots for ΔC_Y

Range 1 Model

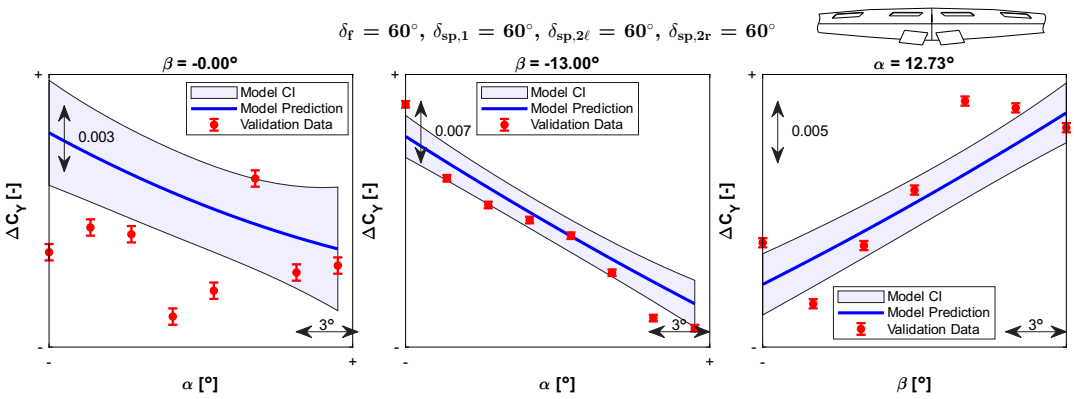

Figure C.25: Range 1 ΔC_Y effects model validation plot: validation config 1

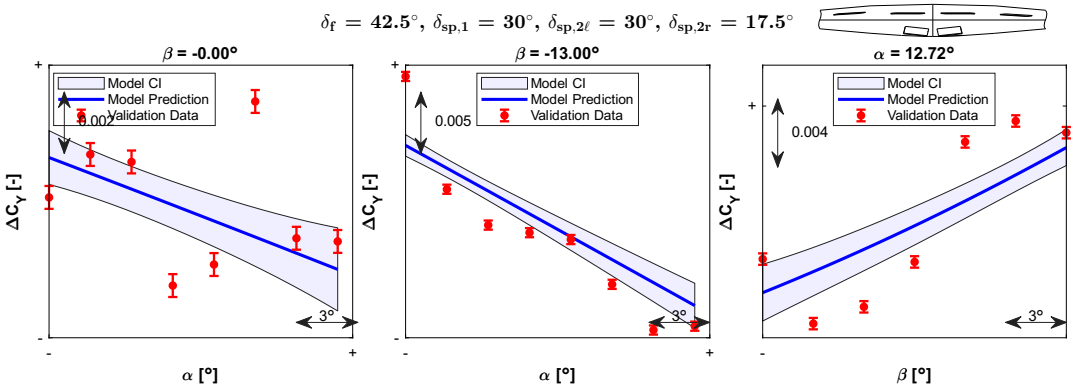

Figure C.26: Range 1 ΔC_Y effects model validation plot: validation config 2

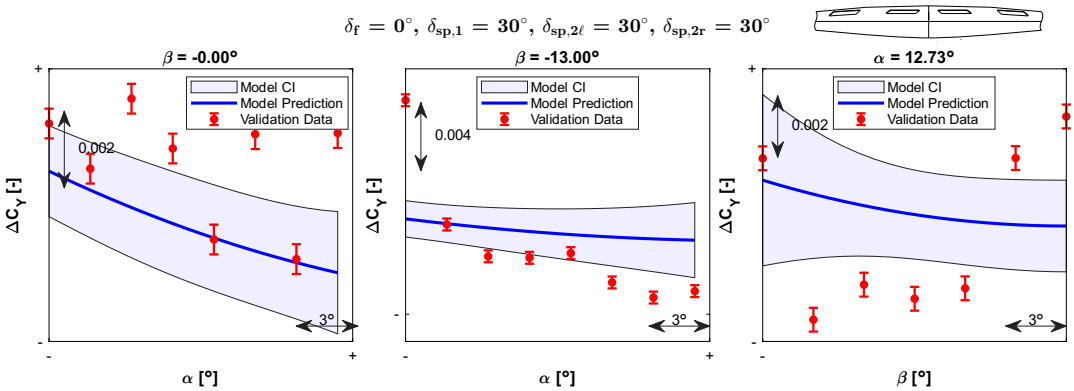

Figure C.27: Range 1 ΔC_Y effects model validation plot: validation config 3

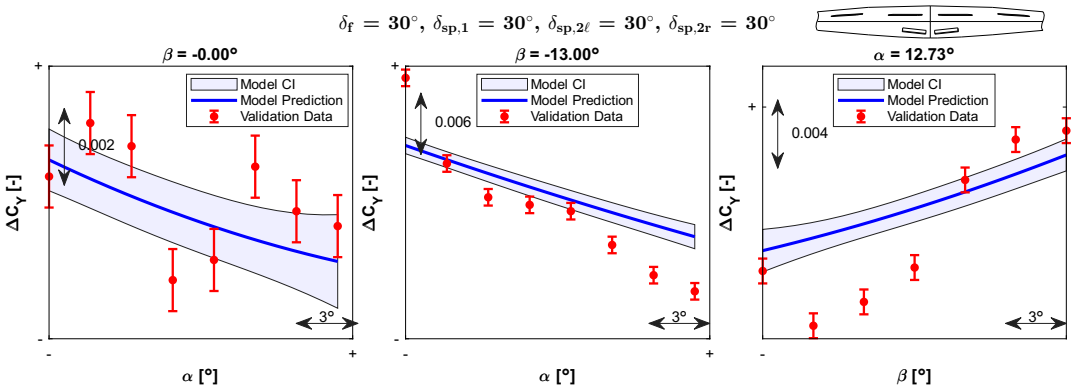

Figure C.28: Range 1 ΔC_Y effects model validation plot: validation config 4

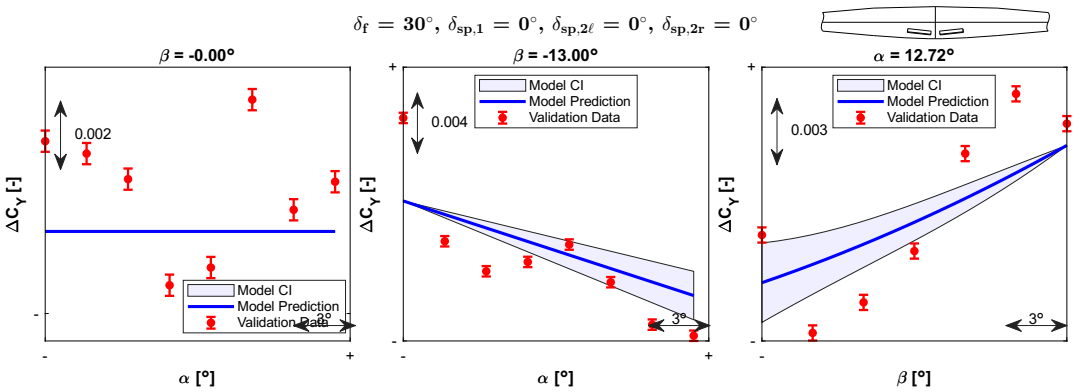

Figure C.29: Range 1 ΔC_Y effects model validation plot: validation config 5

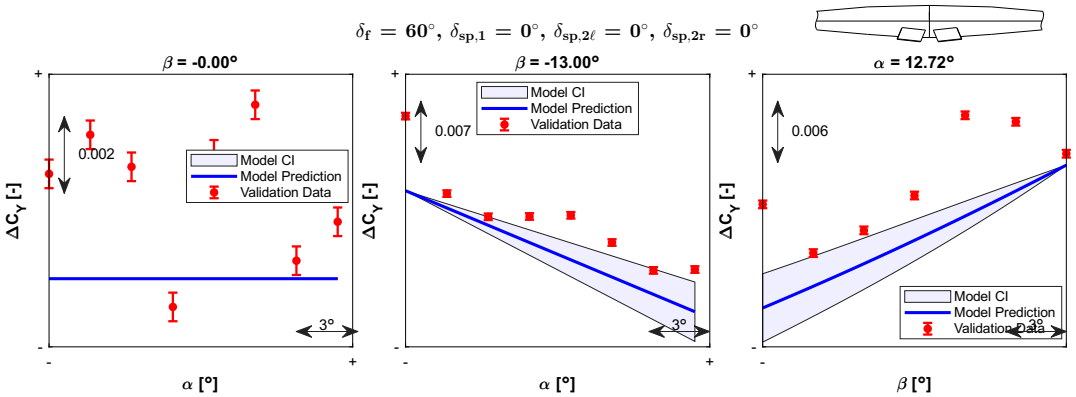

Figure C.30: Range 1 ΔC_Y effects model validation plot: validation config 6

Range 2 Model

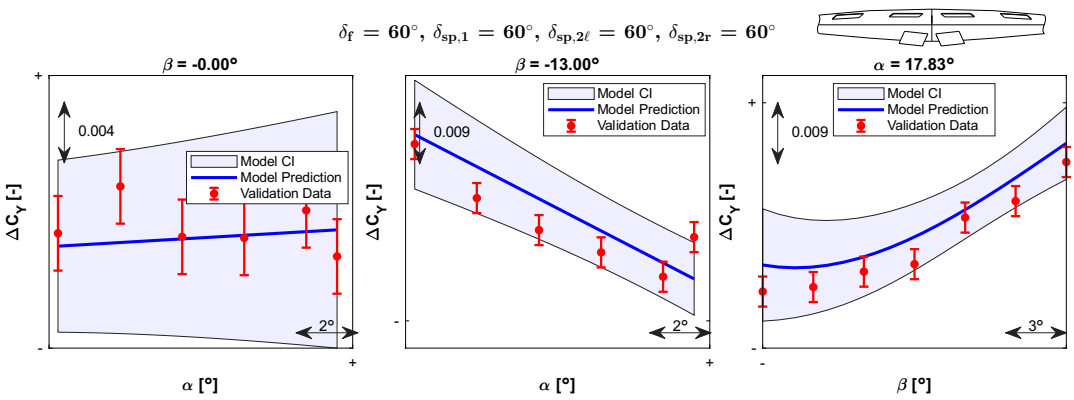

Figure C.31: Range 2 ΔC_Y effects model validation plot: validation config 1

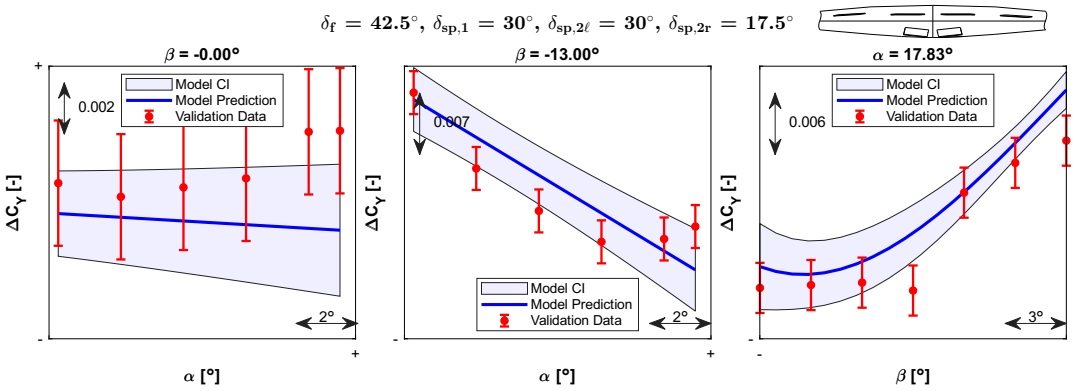

Figure C.32: Range 2 ΔC_Y effects model validation plot: validation config 2

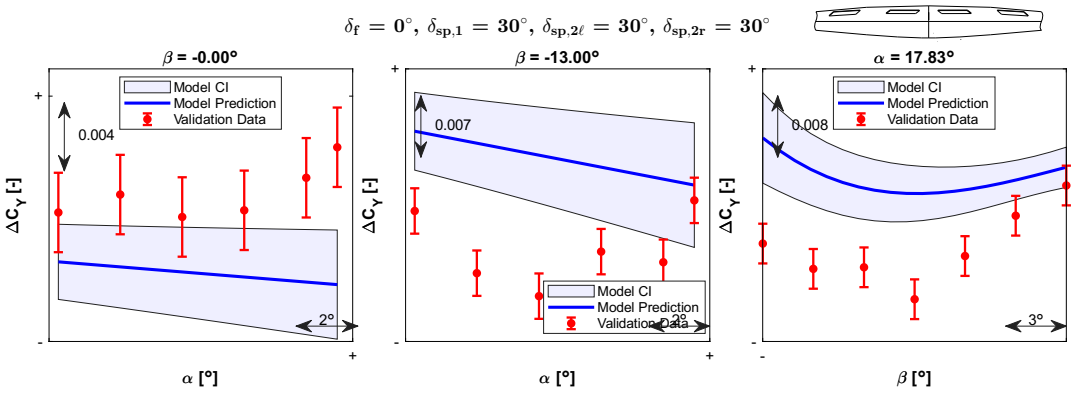

Figure C.33: Range 2 ΔC_Y effects model validation plot: validation config 3

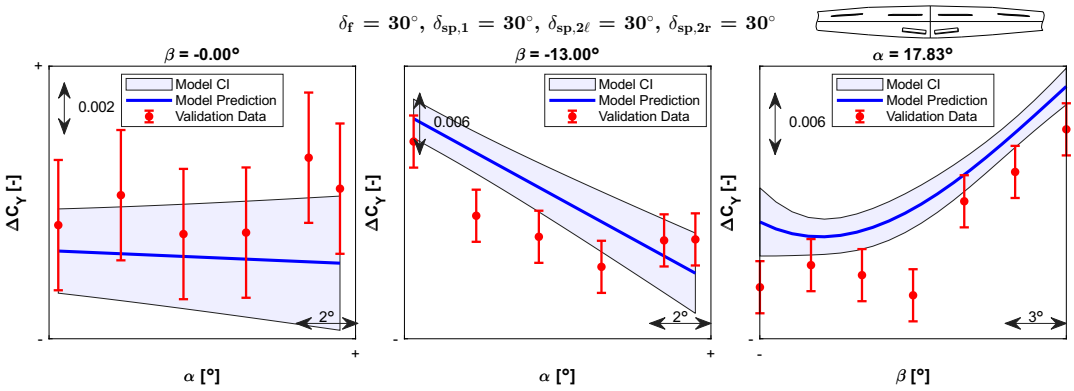

Figure C.34: Range 2 ΔC_Y effects model validation plot: validation config 4

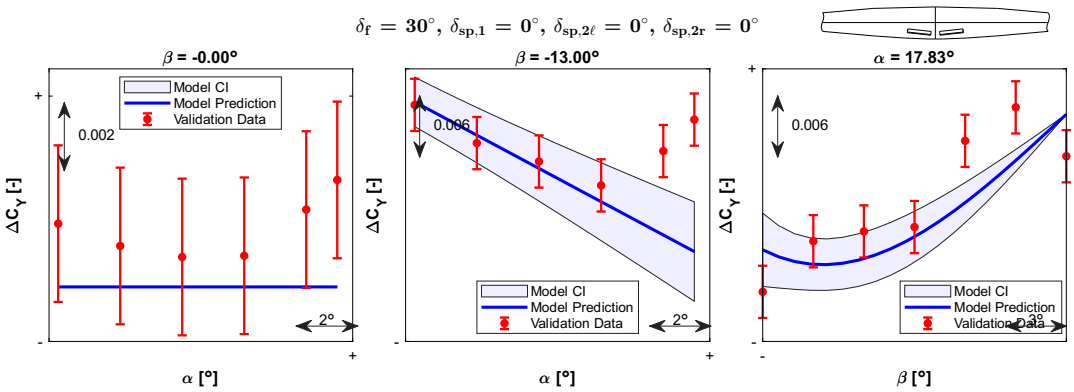

Figure C.35: Range 2 ΔC_Y effects model validation plot: validation config 5

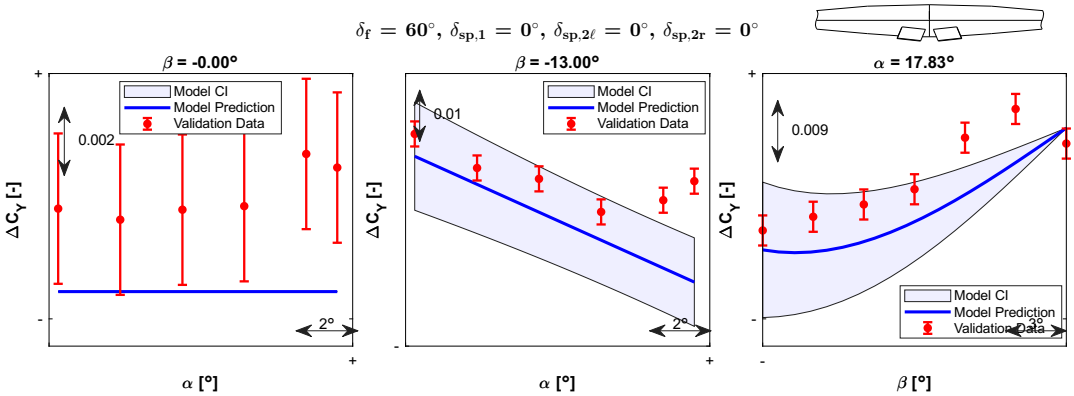

Figure C.36: Range 2 ΔC_Y effects model validation plot: validation config 6

C.4. Validation Plots for $\Delta C_{l,body}$

Range 1 Model

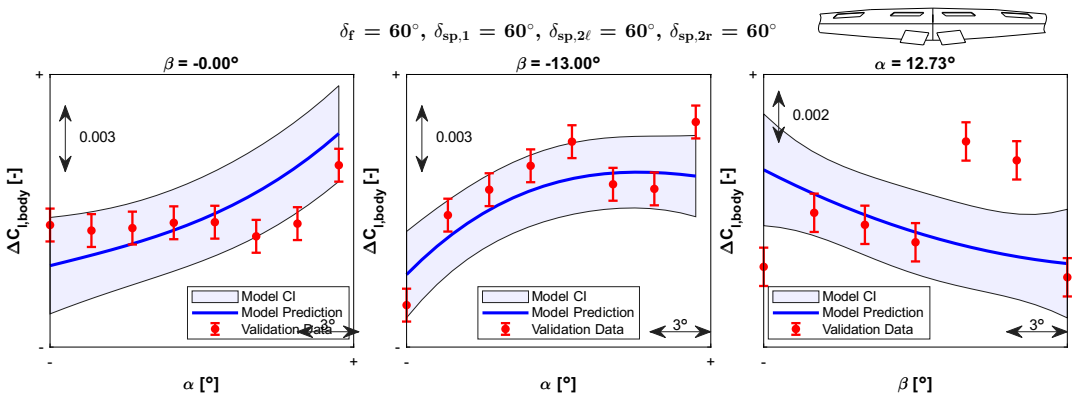

Figure C.37: Range 1 $\Delta C_{l,body}$ effects model validation plot: validation config 1

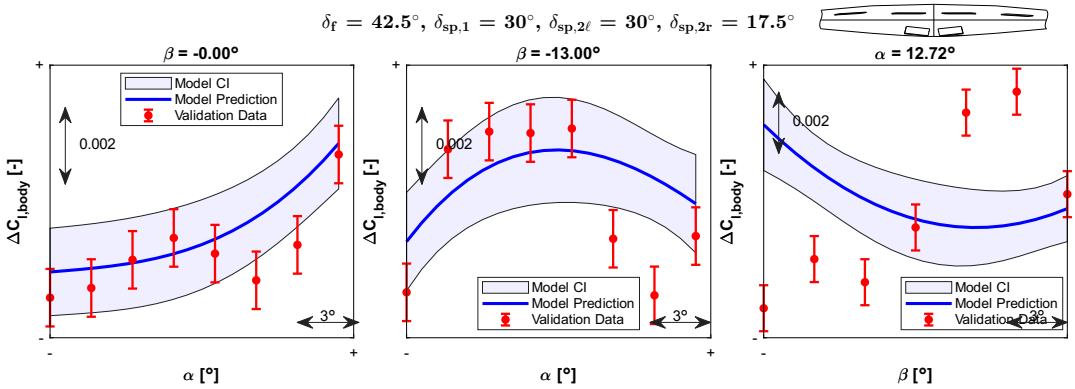

Figure C.38: Range 1 $\Delta C_{l,body}$ effects model validation plot: validation config 2

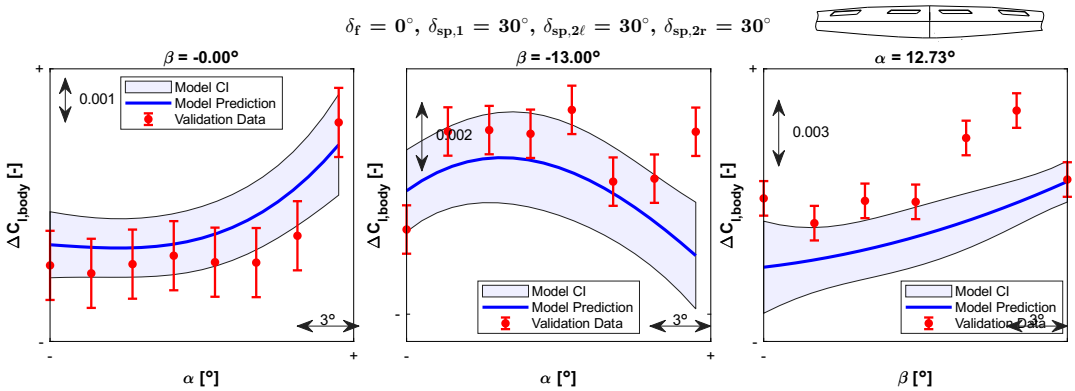

Figure C.39: Range 1 $\Delta C_{l,body}$ effects model validation plot: validation config 3

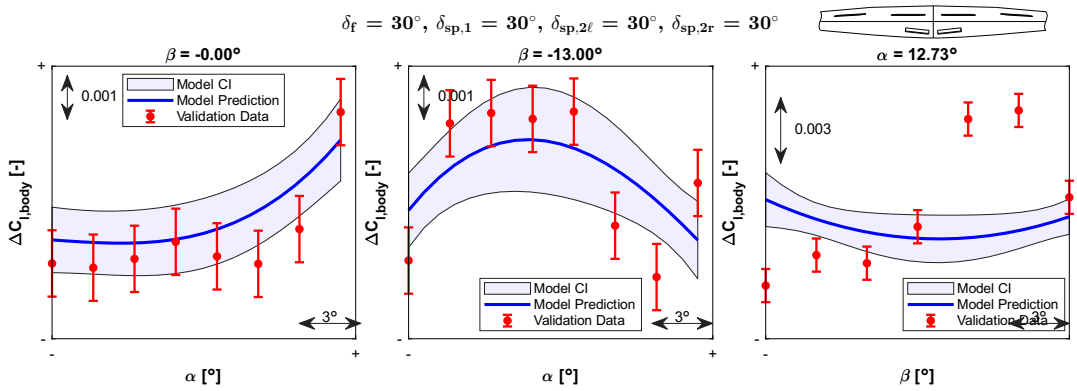

Figure C.40: Range 1 $\Delta C_{l,body}$ effects model validation plot: validation config 4

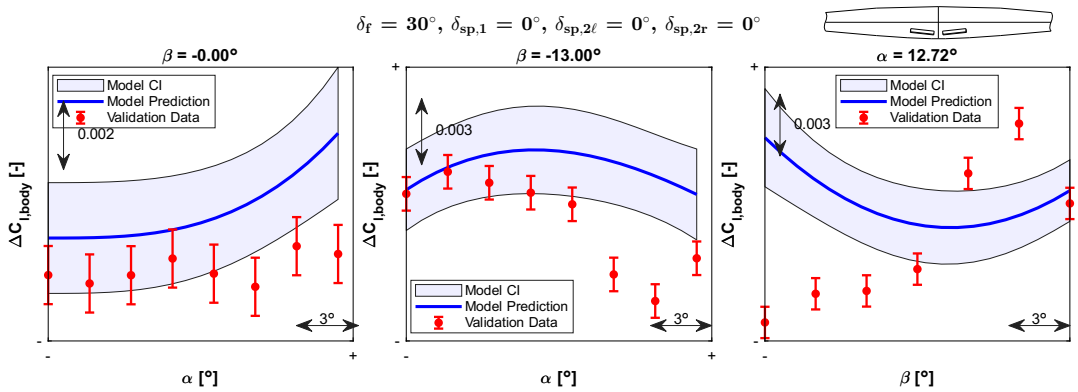

Figure C.41: Range 1 $\Delta C_{l,body}$ effects model validation plot: validation config 5

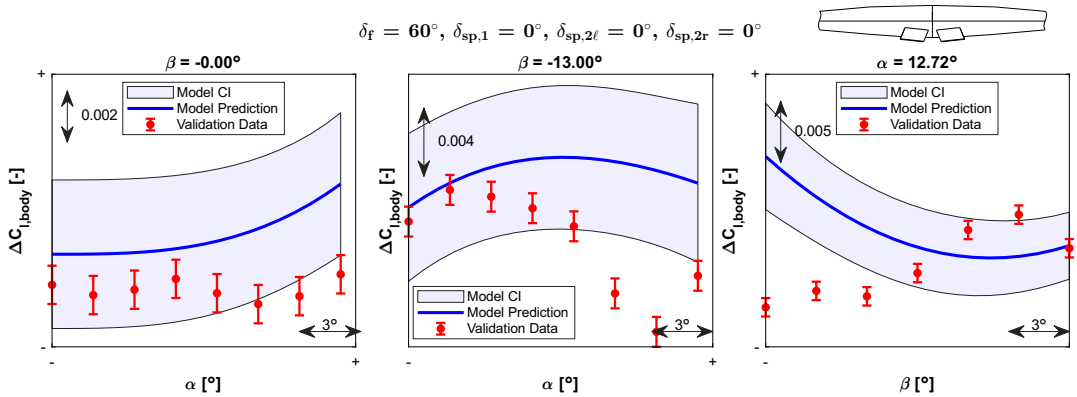

Figure C.42: Range 1 $\Delta C_{l,body}$ effects model validation plot: validation config 6

Range 2 Model

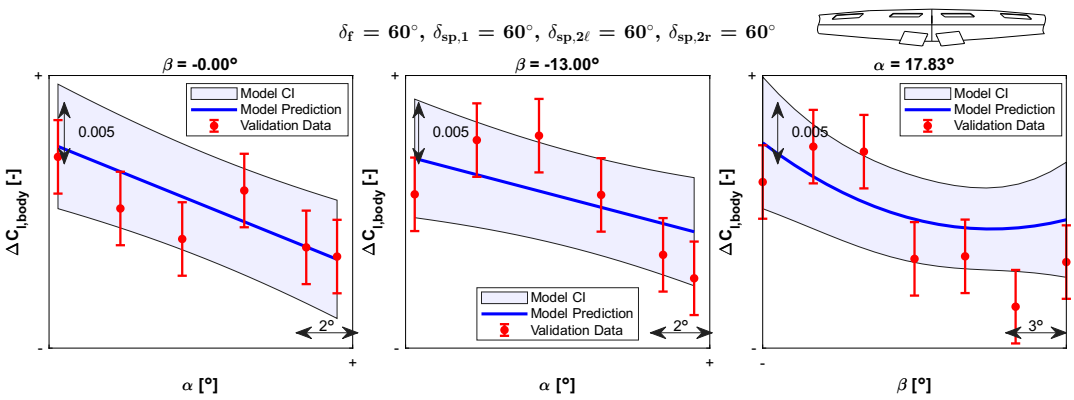

Figure C.43: Range 2 $\Delta C_{l,body}$ effects model validation plot: validation config 1

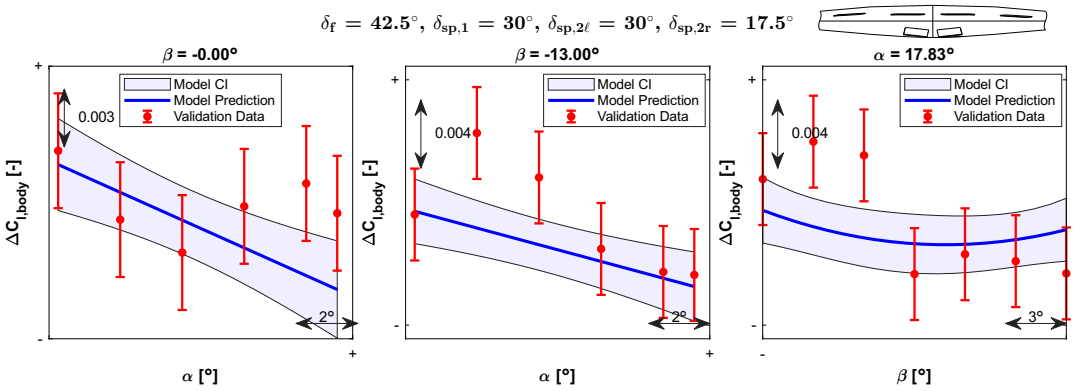

Figure C.44: Range 2 $\Delta C_{l,body}$ effects model validation plot: validation config 2

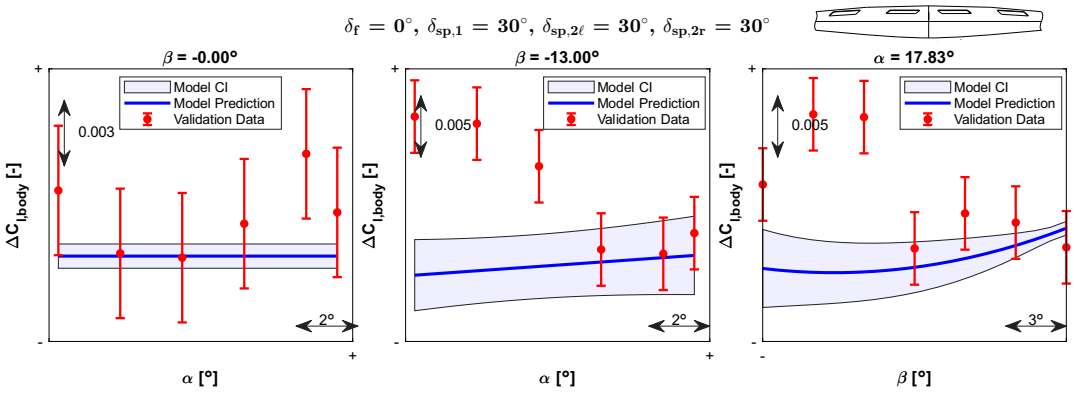

Figure C.45: Range 2 $\Delta C_{l,body}$ effects model validation plot: validation config 3

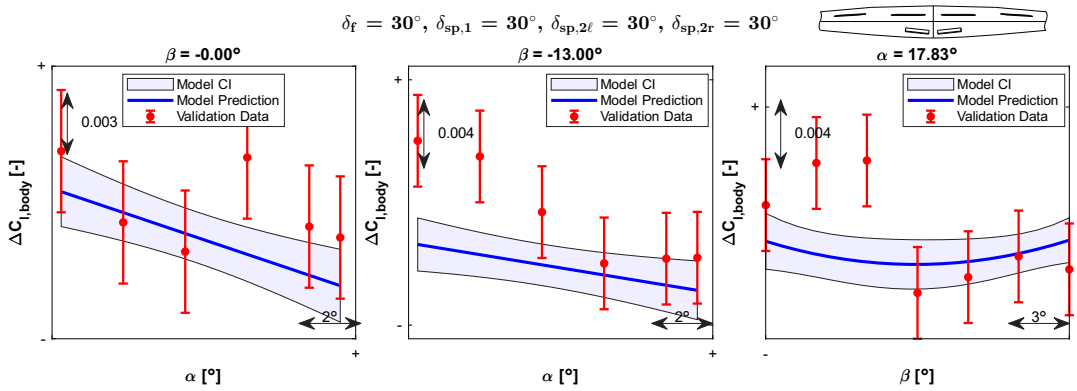

Figure C.46: Range 2 $\Delta C_{l,body}$ effects model validation plot: validation config 4

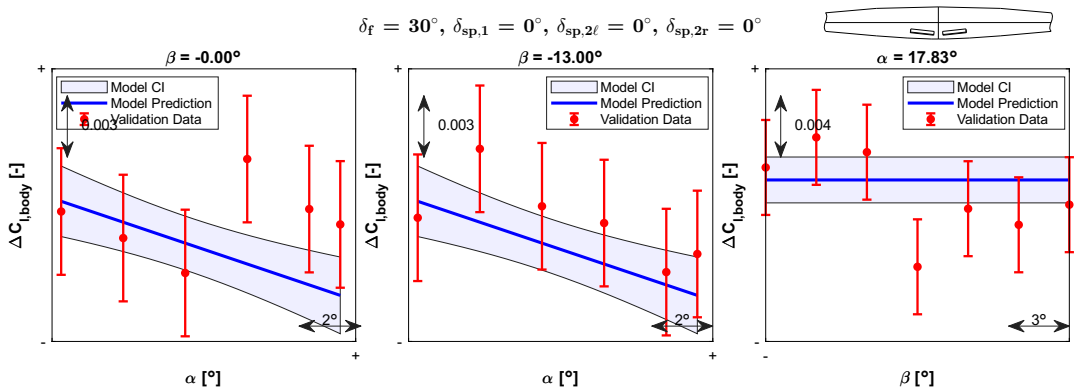

Figure C.47: Range 2 $\Delta C_{l,body}$ effects model validation plot: validation config 5

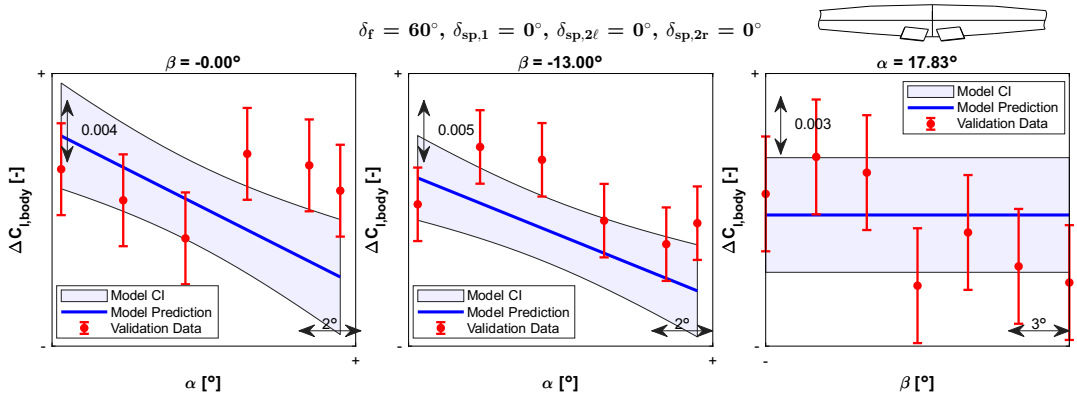

Figure C.48: Range 2 $\Delta C_{l,body}$ effects model validation plot: validation config 6

C.5. Validation Plots for $\Delta C_{m,body}$

Range 1 Model

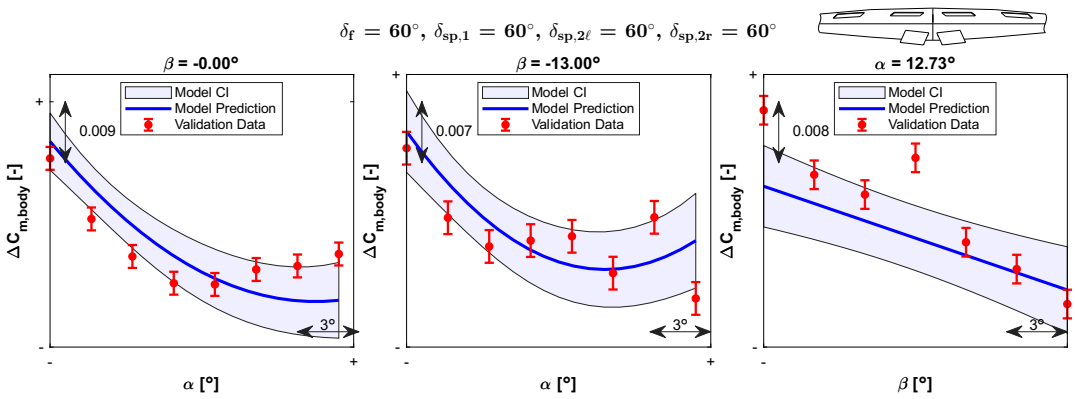

Figure C.49: Range 1 $\Delta C_{m,body}$ effects model validation plot: validation config 1

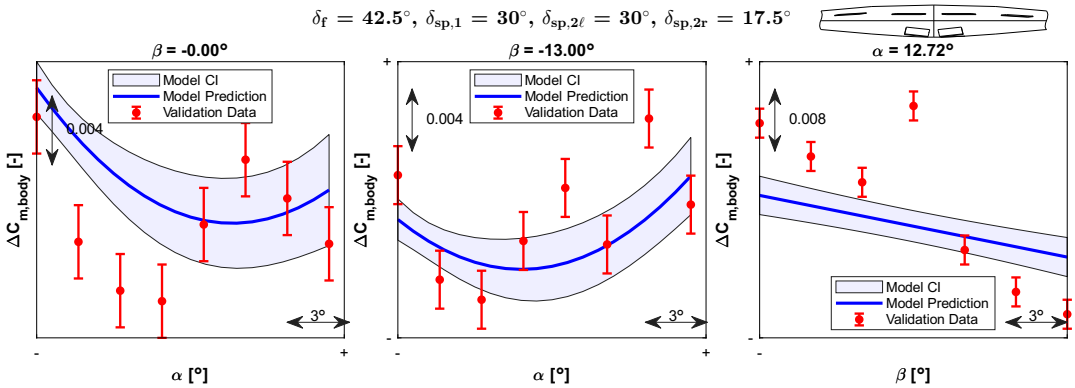

Figure C.50: Range 1 $\Delta C_{m,body}$ effects model validation plot: validation config 2

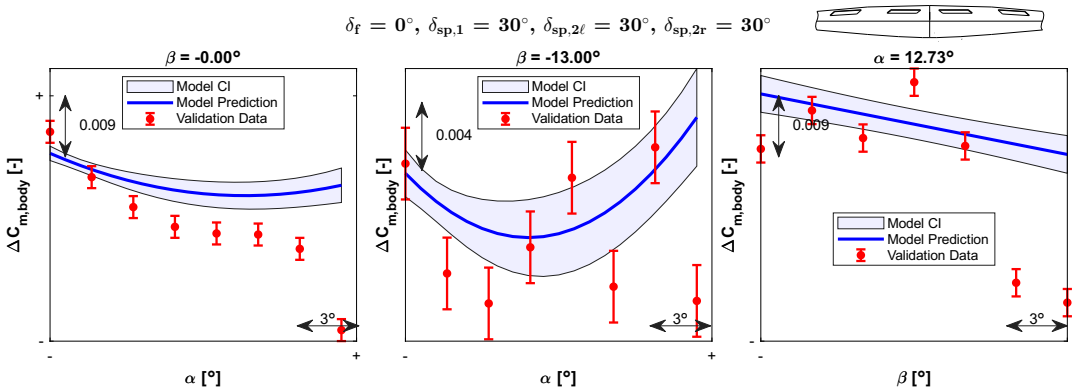

Figure C.51: Range 1 $\Delta C_{m,body}$ effects model validation plot: validation config 3

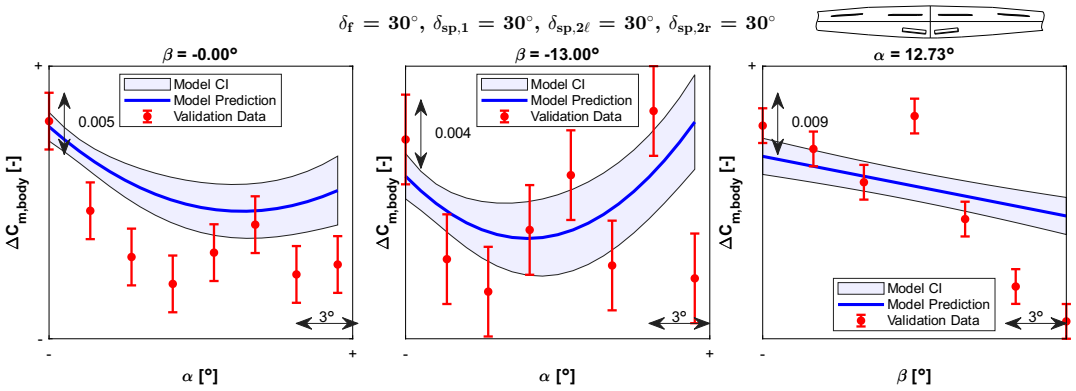

Figure C.52: Range 1 $\Delta C_{m,body}$ effects model validation plot: validation config 4

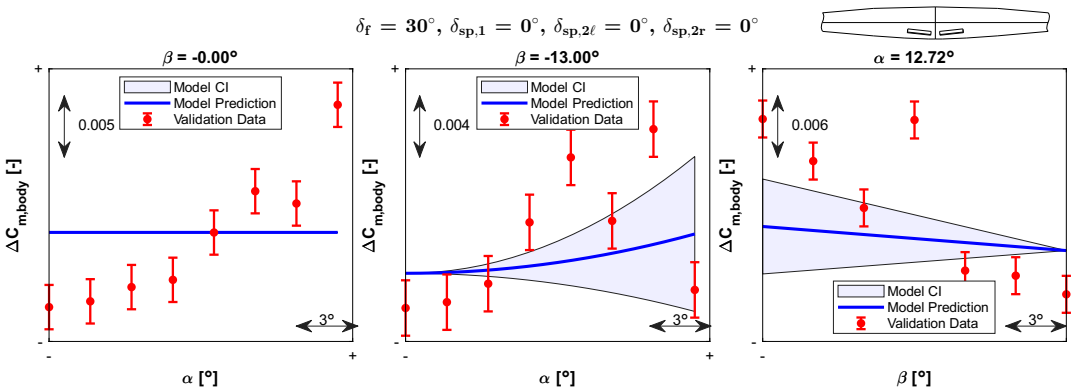

Figure C.53: Range 1 $\Delta C_{m,body}$ effects model validation plot: validation config 5

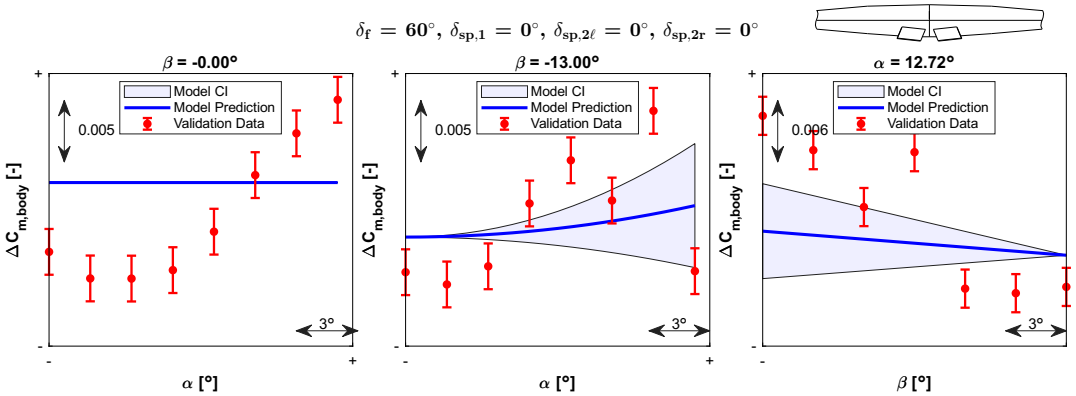

Figure C.54: Range 1 $\Delta C_{m,body}$ effects model validation plot: validation config 6

Range 2 Model

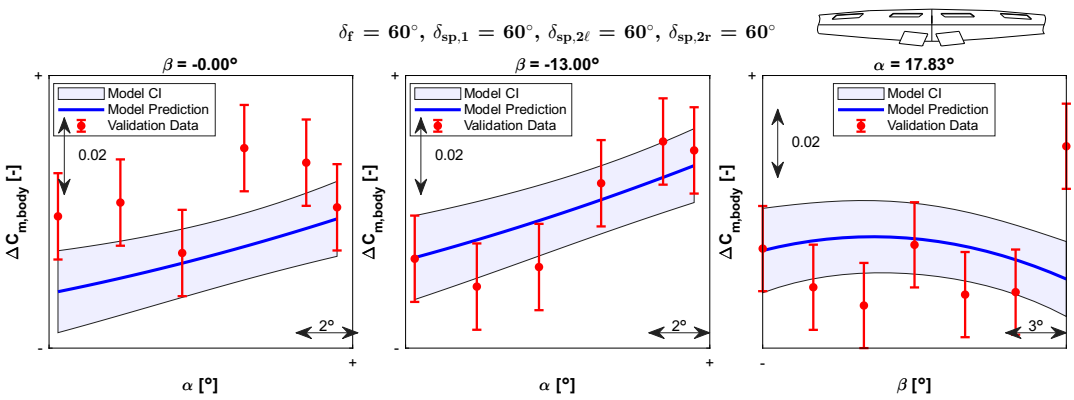

Figure C.55: Range 2 $\Delta C_{m,body}$ effects model validation plot: validation config 1

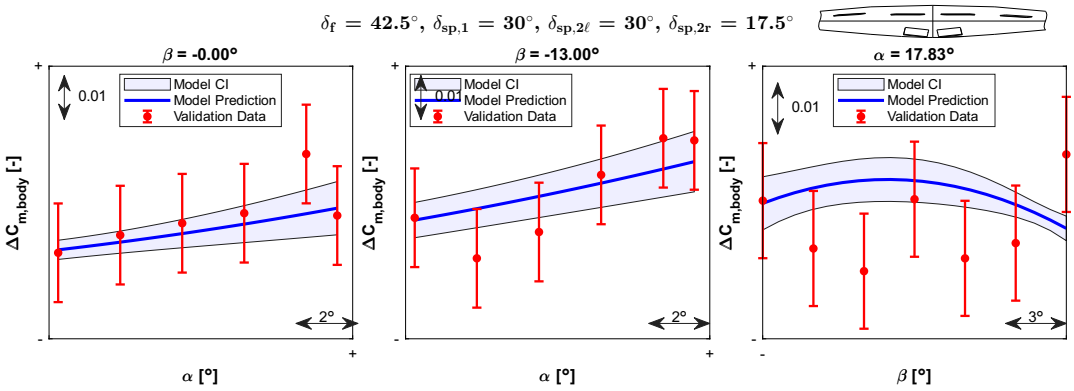

Figure C.56: Range 2 $\Delta C_{m,body}$ effects model validation plot: validation config 2

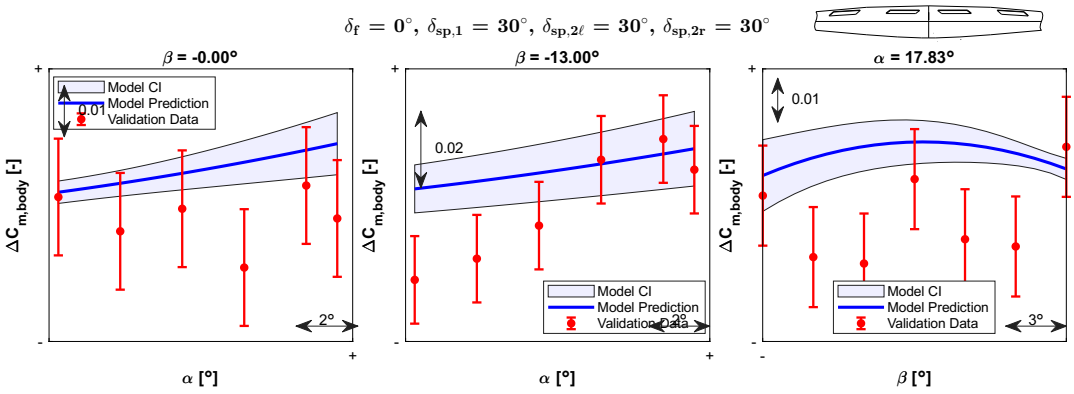

Figure C.57: Range 2 $\Delta C_{m,body}$ effects model validation plot: validation config 3

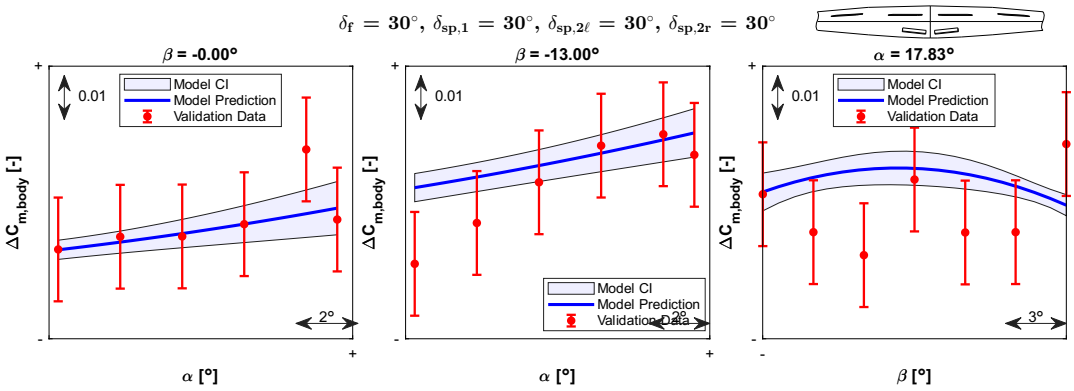

Figure C.58: Range 2 $\Delta C_{m,body}$ effects model validation plot: validation config 4

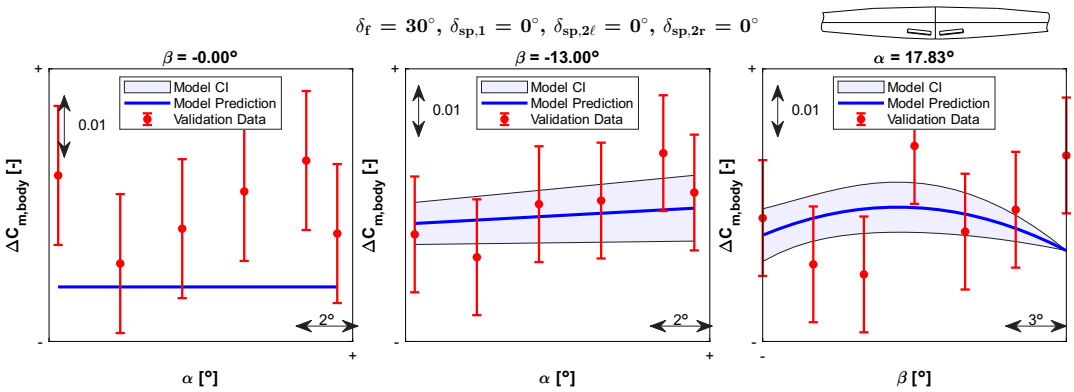

Figure C.59: Range 2 $\Delta C_{m,body}$ effects model validation plot: validation config 5

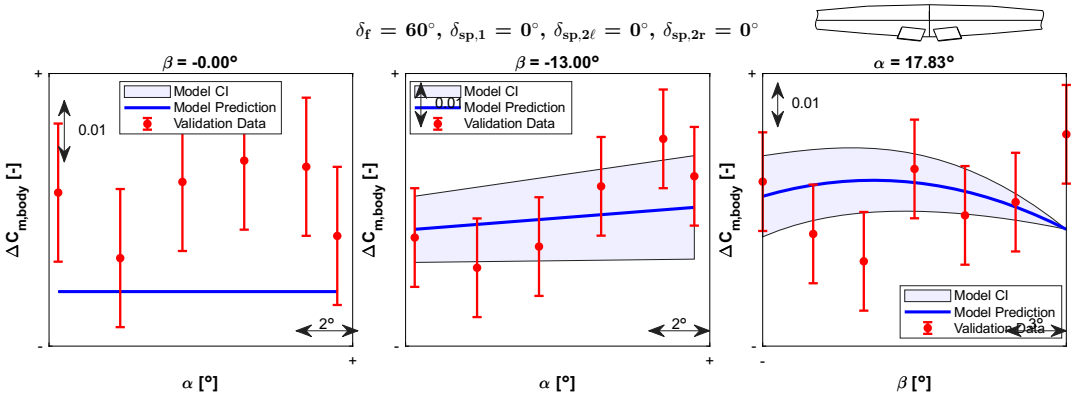

Figure C.60: Range 2 $\Delta C_{m,body}$ effects model validation plot: validation config 6

C.6. Validation Plots for $\Delta C_{n,body}$

Range 1 Model

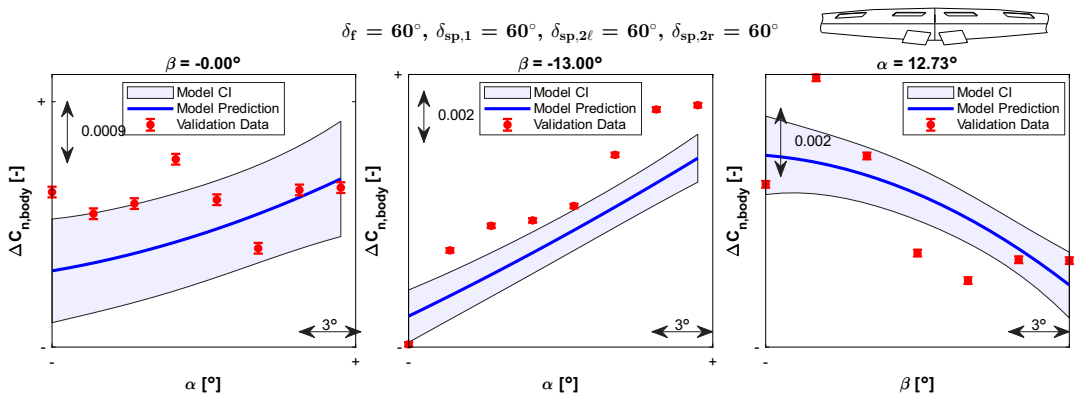

Figure C.61: Range 1 $\Delta C_{n,body}$ effects model validation plot: validation config 1

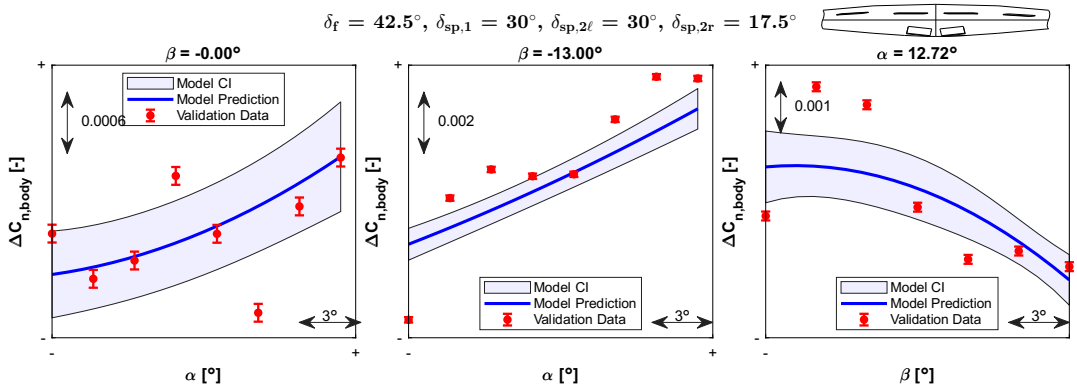

Figure C.62: Range 1 $\Delta C_{n,body}$ effects model validation plot: validation config 2

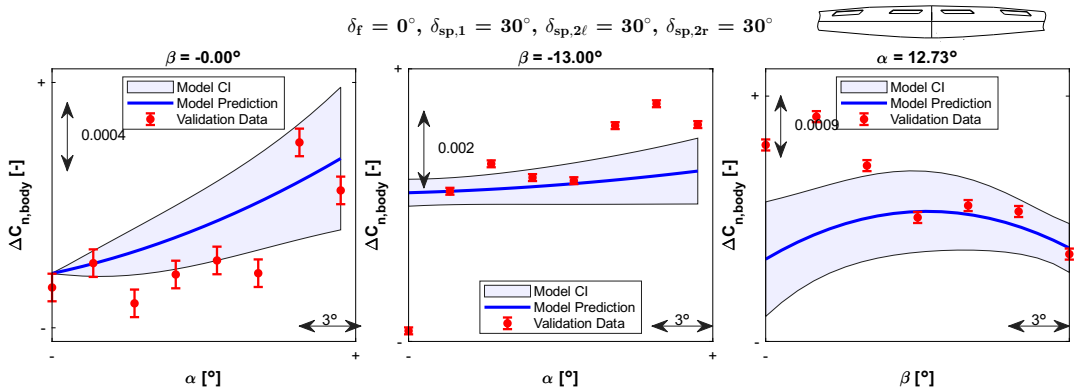

Figure C.63: Range 1 $\Delta C_{n,body}$ effects model validation plot: validation config 3

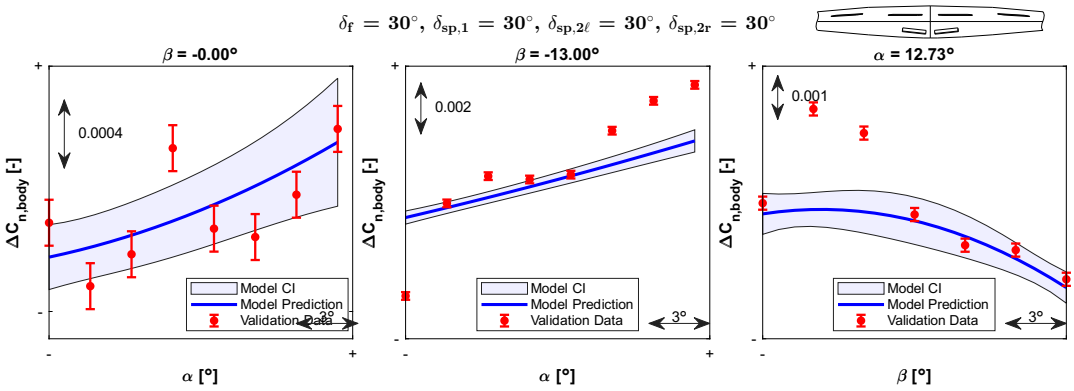

Figure C.64: Range 1 $\Delta C_{n,body}$ effects model validation plot: validation config 4

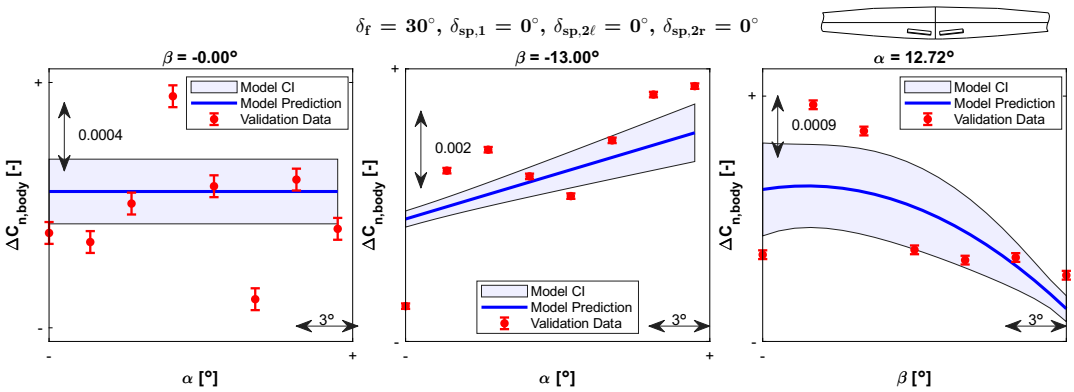

Figure C.65: Range 1 $\Delta C_{n,body}$ effects model validation plot: validation config 5

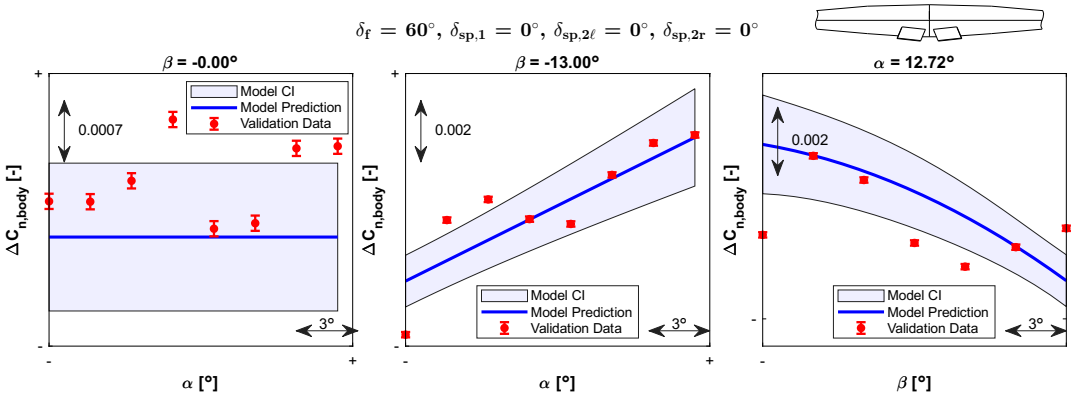

Figure C.66: Range 1 $\Delta C_{n,body}$ effects model validation plot: validation config 6

Range 2 Model

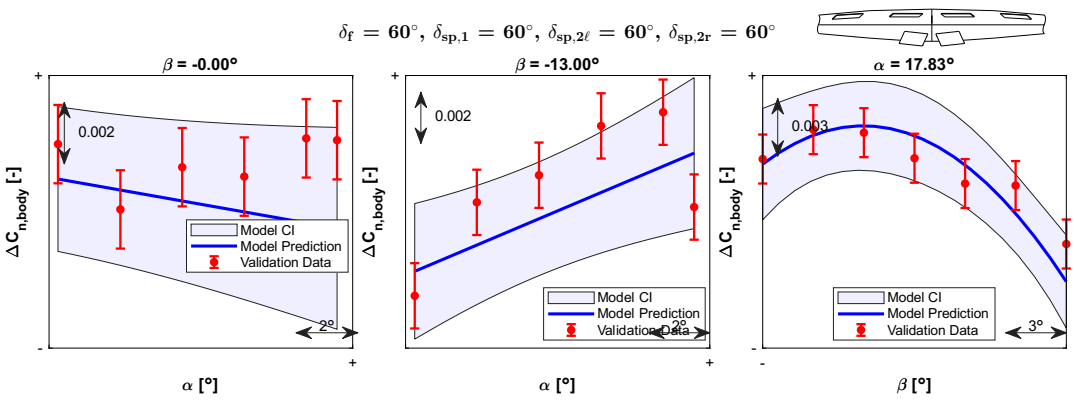

Figure C.67: Range 2 $\Delta C_{n,body}$ effects model validation plot: validation config 1

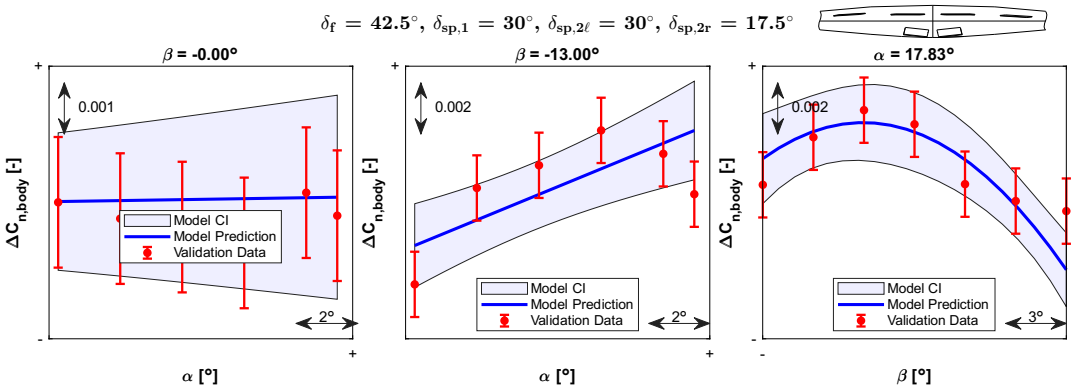

Figure C.68: Range 2 $\Delta C_{n,body}$ effects model validation plot: validation config 2

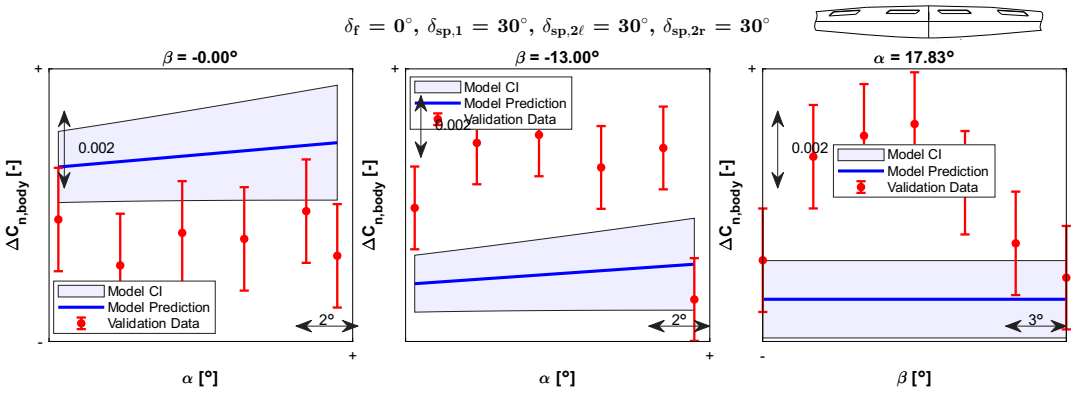

Figure C.69: Range 2 $\Delta C_{n,body}$ effects model validation plot: validation config 3

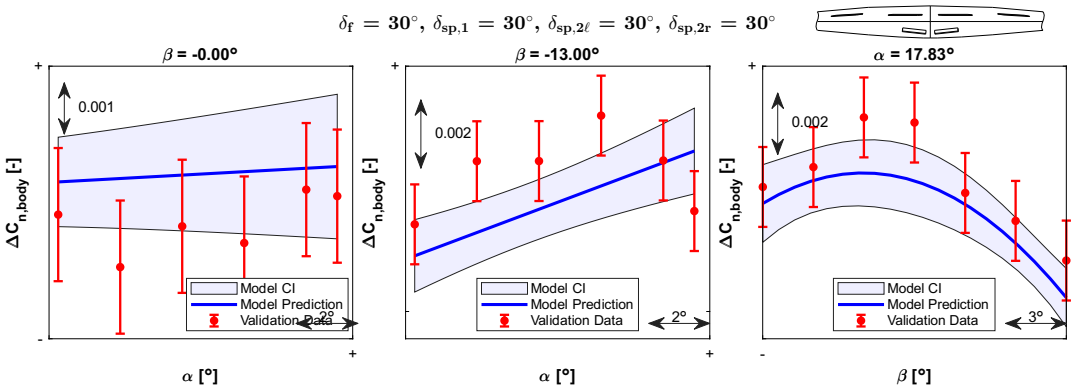

Figure C.70: Range 2 $\Delta C_{n,body}$ effects model validation plot: validation config 4

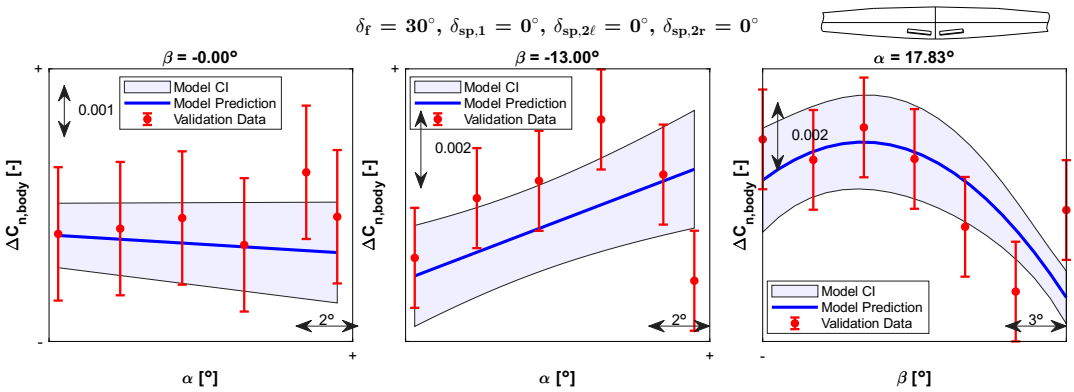

Figure C.71: Range 2 $\Delta C_{n,body}$ effects model validation plot: validation config 5

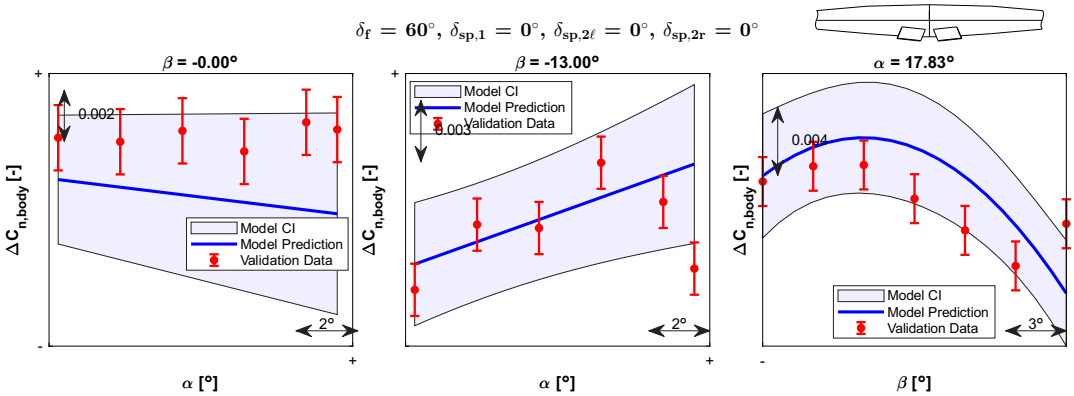

Figure C.72: Range 2 $\Delta C_{n,body}$ effects model validation plot: validation config 6